NASA Contractor Report 174952

LIFE PREDICTION AND CONSTITUTIVE MODELS FOR ENGINE HOT SECTION ANISOTROPIC MATERIALS PROGRAM

Annual Status Report

G.A. Swanson, I. Linask, D.M. Nissley,
P.P. Norris, T.G. Meyer, and K.P. Walker

Contract NAS3-23939
February 1986

NASA

1.REPORT NO. NASA CR-174952	2. GOVERNMENT AGENCY	3.RECIPIENT'S CATALOG NO.
4.TITLE AND SUBTITLE LIFE PREDICTION AND CONSTITUTIVE MODELS FOR ENGINE HOT SECTION ANISOTROPIC MATERIALS PROGRAM		5. REPORT DATE February, 1986 6. PERFORMING ORG. CODE
7.AUTHOR(S) G.A. Swanson, I. Linask, D.M. Nissley, P.P. Norris, T.G. Meyer, and K.P. Walker		8. PERFORMING ORG. REPT. NO. PWA-5968-19
9.PERFORMING ORG. NAME AND ADDRESS UNITED TECHNOLOGIES CORPORATION Pratt & Whitney, Engineering Division 400 Main St., East Hartford, CT 06108		10. WORK UNIT NO. 11. CONTRACT OR GRANT NO. NAS3-23939
12. SPONSORING AGENCY NAME AND ADDRESS National Aeronautics and Space Administration Lewis Research Center Project Manager, R. C. Bill, MS 49-7 21000 Brookpark Road, Cleveland, OH 44135		13. TYPE REPT./PERIOD COVERED Annual Status Report 14. SPONSORING AGENCY CODE
15. SUPPLEMENTARY NOTES		

16. ABSTRACT

This report presents the results of the first year of a program designed to develop life prediction and constitutive models for two coated single crystal alloys used in gas turbine airfoils. The two alloys are PWA 1480 and Alloy 185. The two oxidization resistant coatings are PWA 273, an aluminide coating, and PWA 286, an overlay NiCoCrAlY coating. To obtain constitutive and/or fatigue data, tests were conducted on coated and uncoated PWA 1480 specimens tensilely loaded in the <100>, <110>, <111> and <123> directions. A literature survey of constitutive models was completed for both single crystal alloys and metalic coating materials; candidate models were selected. One constitutive model under consideration for single crystal alloys applies Walker's micromechanical viscoplastic formulation to all slip systems participating in the single crystal deformation. Results from initial calibrations and comparisons with test data are encouraging. The constitutive models for the overlay coating correlate the viscoplastic data well. For the aluminide coating, a unique test method is under development. A literature search of single crystal fatigue module was completed. LCF and TMF tests are underway. The two coatings caused a significant drop in fatigue life, and each produced a much different failure mechanism.

17. KEY WORDS (SUGGESTED BY AUTHOR(S))	18. DISTRIBUTION STATEMENT
Life Prediction, Constitutive Models, Single Crystal Alloys, Anisotropic Materials, Gas Turbine Engine, Airfoils	Unclassified Unlimited

19. SECURITY CLASS THIS (REPT)	20. SECURITY CLASS THIS (PAGE)	21. NO. PGS	22. PRICE *
Unclassified	Unclassified		

* For sale by the National Technical Information Service, Springfield, VA 22161

PREFACE

This first Annual Report covers the initial effort on the NASA HOST (Hot Section Technology) program titled "Life Prediction and Constitutive Models for Engine Hot Section Anisotropic Materials" conducted under Contract NAS3-23939. The NASA Program Manager for this project is Dr. Robert C. Bill. The Pratt & Whitney Program Manager is Mr. Gustav A. Swanson. Contributors include Messrs. Indrik Linask, David M. Nissley, Paul P. Norris, and Thomas G. Meyer at Pratt & Whitney and Dr. Kevin P. Walker, Consultant.

Table of Contents

Table of Contents (continued)

List of Figures

List of Figures (continued)

List of Figures (continued)

List of Figures (continued)

List of Figures (continued)

List of Tables

SECTION 1.0

INTRODUCTION

One of the more important recent developments in gas turbine blade materials has been the introduction of directionally solidified and single crystal castings. This casting process has matured to the level where it is now routinely used in the production of commercial and military aircraft jet engine turbine blades. Among the advantages of these materials are the following:

- By eliminating grain boundaries, the high temperature creep strength is substantially increased.
- The elastic modulus in the direction of solidification is lowered, reducing thermally induced stresses and, thereby, increasing low cycle fatigue life.
- Corrosion and oxidation resistance are enhanced by the absence of grain boundaries.
- Eliminating grain boundary strenthening elements raises the melting temperature and permits greater heat treatment flexibility.

Unfortunately, these metallurgical and processing advances have not been matched by corresponding advancements in the knowledge and understanding of the mechanics of these materials, their failure mechanisms, and methods for life predictions. In order to realize the full potential of these materials, it is necessary to have a complete knowledge of the full envelope of life limiting parameters. Anisotropy introduces many life prediction questions especially for stresses which are not parallel to the direction of solidification. Oxidation resistant coating adds another layer of complexity to these questions. All of these issues are addressed in this HOST program.

The program is divided into a base program which covers a duration of forty-two months and two optional programs which are to be exercised at the discretion of NASA. In the base program a primary and alternative coated single crystal material, operating at relevant turbine airfoil temperatures, are being investigated. In Option 1 the same two single crystal materials, in an uncoated condition and operating at root attachment temperatures and notched conditions, will be studied. In Option 2 a directionally solidified or recrystallized material, in a coated and uncoated condition, will be studied at temperatures occurring at the airfoil and root attachment, respectively.

In the base and optional programs, candidate constitutive and life prediction models are being developed concurrent with laboratory specimens which will be tested under a variety of mechanical and thermal load histories to provide data for the final model selections. The models will be incorporated into a computer code which will be checked for operability on a representative turbine blade section.

The first year effort of the contract has involved material selection, specimen preparation, basic material tests, literature searches of appropriate constitutive and life prediction models, initial formulation of constitutive models, and initial constitutive and fatigue tests. The specific accomplishments are listed in Section 5.0 and are expanded upon throughout this report.

During the second year, the Task III, Level I, experiments will be completed on the primary single crystal alloy and the two coatings. Metallurgical evaluation of the results, together with constitutive and life prediction modeling, will continue in parallel with these tests.

SECTION 2.0

TASK I - MATERIAL/COATING SELECTION AND ACQUISITION

2.1 Material Selection

A survey was conducted of the single crystal materials and surface protection coating systems currently in use or in an advanced state of development for use in turbine blade applications. Two single crystal materials and two coating systems have been selected for this program.

2.1.1 Single Crystal Airfoil Material

The trend toward improved engine efficiency and improved durability has placed increasing demands on materials for turbine airfoils that operate in the hot section of the gas turbine engine. To meet these demands, nickel-base superalloys have been designed specifically for use in single crystal form, which offers greater creep fatigue resistance at elevated temperatures and reduced susceptibility to corrosion or oxidation than conventionally cast alloys. Table 2-I lists some of the single crystal alloys that have been developed for gas turbine engines. These alloys do not contain grain boundary strengthening elements such as carbon, boron, and zirconium; therefore, the incipient melting temperatures are higher than those of conventionally cast alloys. This allows for a higher temperature solution heat treatment, which, in turn, further improves alloy strength by providing a high volume fraction (approximately 65 percent) of fine, cuboidal, homogeneously distributed gamma prime precipitate.

Table 2-I

Single Crystal Superalloys Used in Gas Turbine Industry

	Alloy Composition (Weight Percent)												
	Ta	W	Mo	Cr	Al	Ti	Cb	Co	Hf	C	B	Zr	Ni
PWA 1480	12	4	--	10	5	1.5	--	5	--	--	--	--	Bal*
Rene N4	4	6	1.5	9.2	3.7	4.2	0.5	7.5	--	--	--	--	Bal*
CM SX-2	6	8	0.6	8	5.6	1	--	4.6	--	--	--	--	Bal*
CM SX-3	6	8	0.6	8	5.6	1	--	4.6	0.1	--	--	--	Bal*

*Balance

PWA 1480 was selected as the primary single crystal superalloy. It was the first superalloy designed specifically for use in single crystal form and was developed with the goal of achieving an optimum balance of creep strength, thermal fatigue strength, and oxidation and hot corrosion resistance. PWA 1480 is the most widely used single crystal alloy in gas turbine engines today and the most advanced turbine airfoil material utilized in Pratt & Whitney production engines. PWA 1480 was certified for commercial use in the JT9D-7R4D/E engine in late 1981 and has since been certified for use in the JT9D-7R4G/H and PW2037 engines.

Two heats of PWA 1480 have been procured for this program from the Howmet Turbine Components Corporation, Alloy Division, Dover, New Jersey. The primary heat, identified by Howmet as 200A14824, has been designated P9866. The secondary heat, identified by Howmet as 200B14773, has been designated P9867. The chemical compositions for the heats are compared to the nominal specifications in Table 2-II. The typical solution heat treated microstructure is illustrated in Figure 2-1(A).

Table 2-II

Single Crystal Superalloys to be Studied in Contract

		Alloy Composition (Weight Percent)								
		Elements								
Alloy	Heat Code	Ni	Cr	Co	Ti	Al	Ta	W	Mo	C
PWA 1480	Nominal	Bal*	10.0	5.0	1.5	5.0	12.0	4.0	--	--
	P9866 (Heat A)	Bal*	10.35	5.5	1.44	4.95	12.2	3.9	--	0.01
	P9867 (Heat B)	Bal*	10.3	5.3	1.44	4.9	10.3	4.0	--	0.004
Alloy 185	Nominal	Bal*	--	--	--	6.8	--	6.0	14.0	0.04
	P9921	Bal*	--	--	0.001	6.82	--	6.10	13.85	0.04

*Balance

A

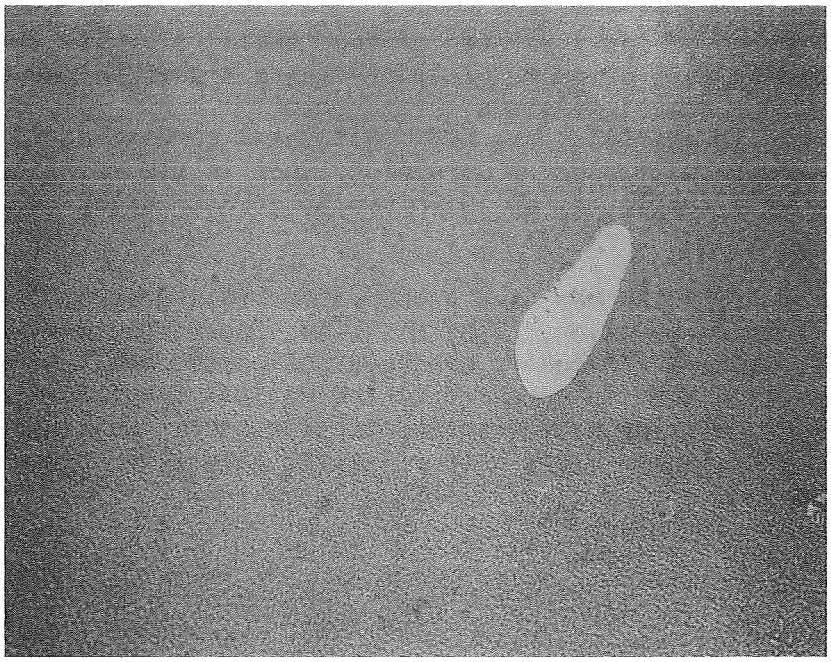

B

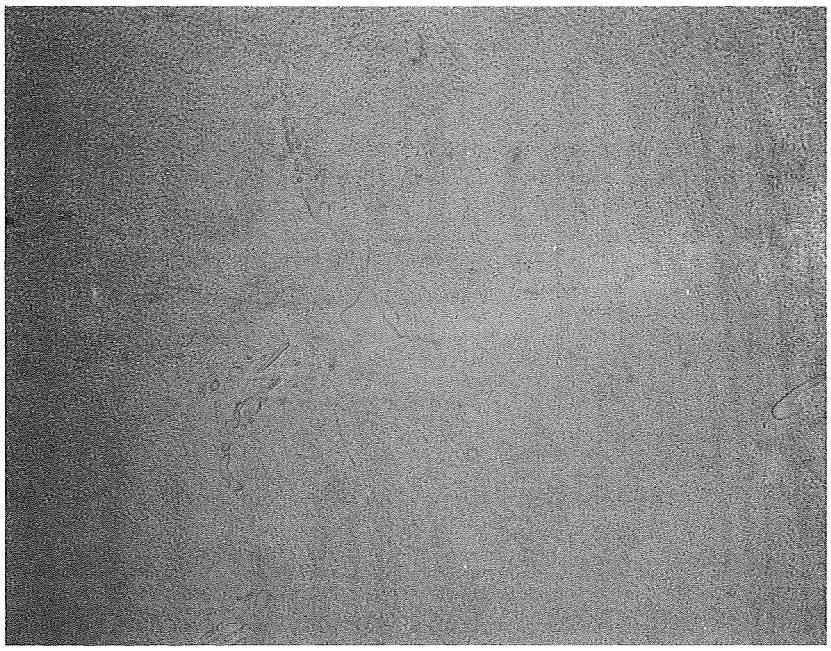

Figure 2-1 Typical Solution Heat Treated Microstructure Illustrating Gamma/Gamma Prime Eutectic Islands in Gamma Matrix With Fine Unresolved Gamma Prime Precipitates of: A) PWA 1480, and B) Alloy 185. (500X Mag., Etchant: Mixed Acids)

Alloy 185 was selected as the secondary single crystal alloy with the intent of testing the range of applicability of the constitutive and life prediction models developed in this program. Alloy 185 has a higher volume fraction (approximately 70 percent) of gamma prime compared to PWA 1480 due to a higher aluminum content. In addition, the high molybdenum content and high volume fraction of gamma prime produce a morphology that is semi-continuous rather than cuboidal. As a result, Alloy 185 exhibits greater creep anisotropy than PWA 1480.

A single heat of Alloy 185 has been procured for this program from the Howmet Turbine Components Corporation, Alloy Division, Dover, New Jersey. This heat, identified by Howmet as 242A15847, has been designated P9921. The chemical composition for this heat is compared to the nominal specifications in Table 2-II. The typical solution heat treated microstructure is illustrated in Figure 2-1(B). Tensile and creep properties for this alloy are given in Figures 2-2 and 2-3.

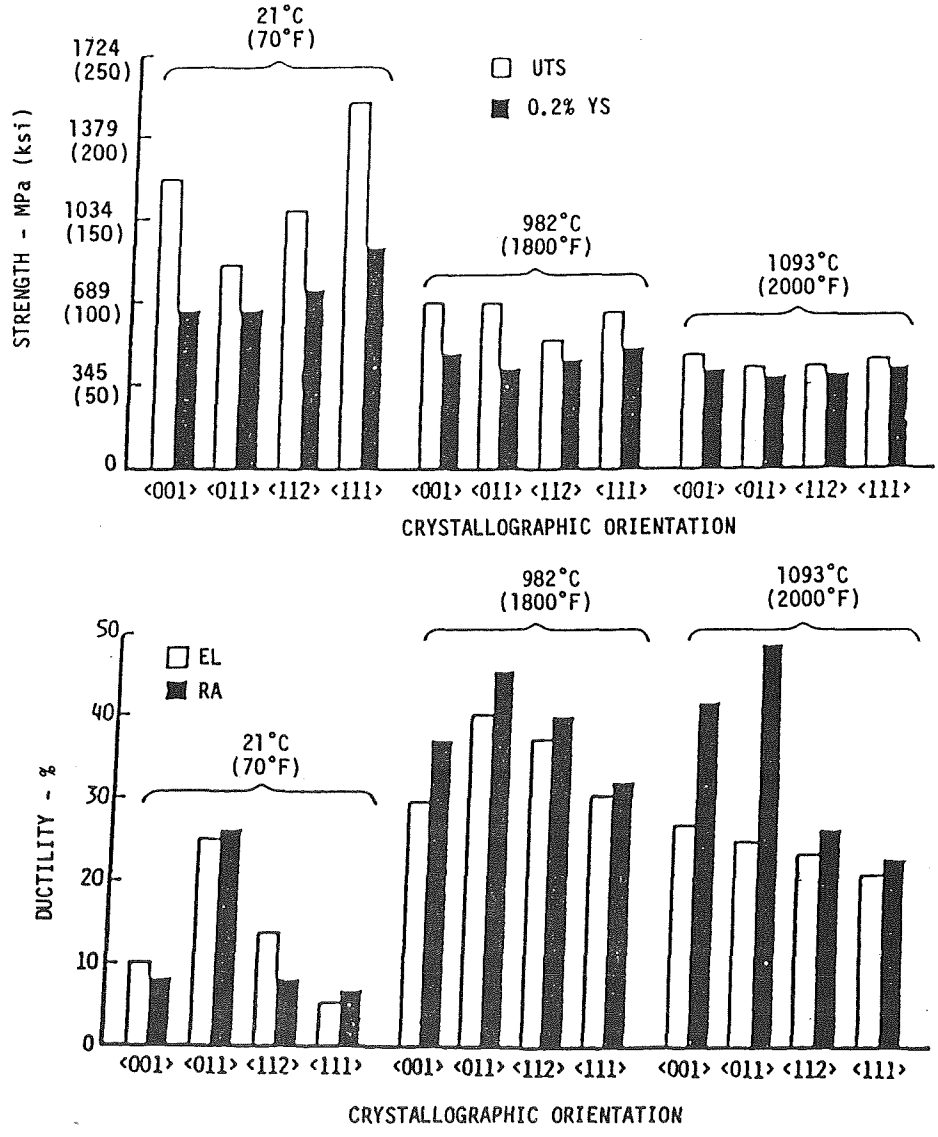

Figure 2-2 Tensile Properties of Cast Single Crystal Alloy 185

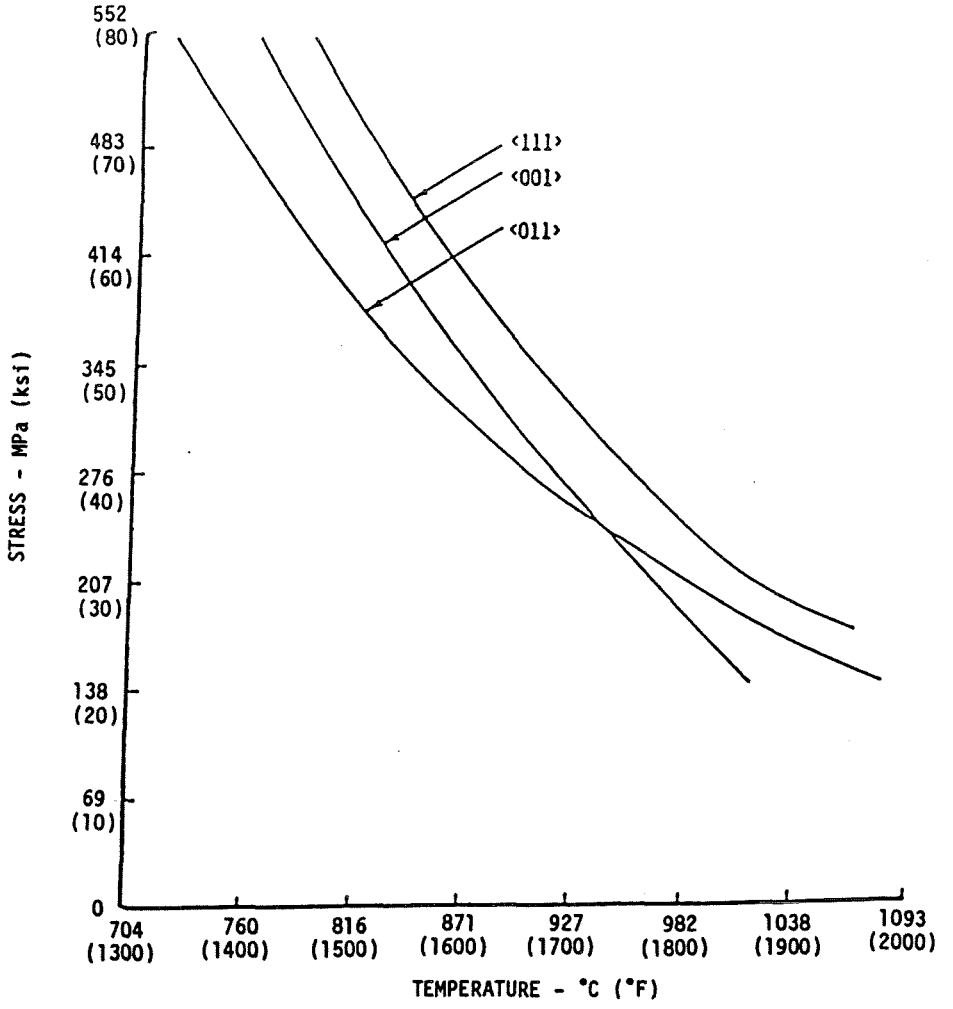

Figure 2-3 500-Hour Rupture Life of Cast Single Crystal Alloy 185

2.1.2 Coatings

For gas turbine applications of high temperature alloys, the use of protective coatings is required to achieve practical lives for components which are designated to operate in oxidizing environments at elevated temperatures. One overlay and one diffusion coating were selected for this program to be representative of those employed in actual gas turbine engines.

PWA 286 was selected as the overlay coating. It offers enhanced oxidation and corrosion resistance for turbine blades and vanes. The composition and deposition process are provided in Table 2-III. The typical microstructure for this coating is illustrated in Figure 2-4(A).

Table 2-III

Coating Compositions and Processes

Coating	Type	Composition	Deposition Process
PWA 286	Overlay	NiCoCrAlY+Si+Hf	Vacuum Plasma Spray
PWA 273	Aluminide (Outward Diffusion)	NiAl	Pack Cementation

PWA 273 was selected as the diffusion coating. It is an outward diffusion aluminide coating for nickel-base turbine blades and vanes. The composition and deposition process are given in Table 2-III. The typical microstructure for this coating is illustrated in Figure 2-4(B).

2.2 Specimen Preparation

2.2.1 Casting

The superalloys employed for this program have been cast using the directional solidification process which is schematically illustrated in Figure 2-5. The molten metal, initially freezing on the chill plate, has a very fine polycrystalline structure. As the solidification front moves vertically, elongated grains (or columns) are formed. The dynamics of solidification are such that grains with a [001] crystal orientation parallel to the direction of heat flux grow preferentially compared to grains with other orientations. To produce a single crystal casting, a helix is used to act as a filter constricting the growth of the many columnar grains that grow from the water cooled chill plate. The helix permits a single <001> oriented grain to pass through. For orientations other than <001> (i.e., <111>, <110>, and <123>), a seed crystal of the desired orientation is employed in the mold to override the natural tendency for growth in the <001> direction. When molten alloy is poured into the mold, the seed crystal acts as a starting block for solidification. Directional solidification proceeds with the crystallographic growth direction dictated by the orientation of the seed crystal producing a single crystal casting of the desired orientation.

Cylindrical single crystal bars with nominal 15.2 cm (6.0 in) lengths and 2.54 cm (1.0 in) and 1.59 cm (0.625 in) diameters have been cast. The standard <100> crystallographic direction along with the <111>, <110>, and <123> directions have been chosen as the primary orientations for single crystal casting.

A

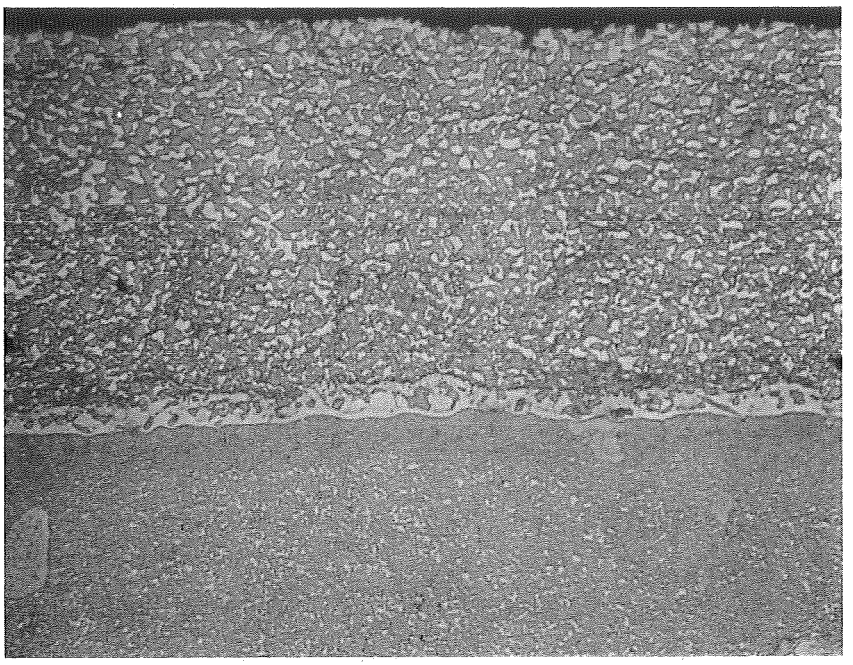

B

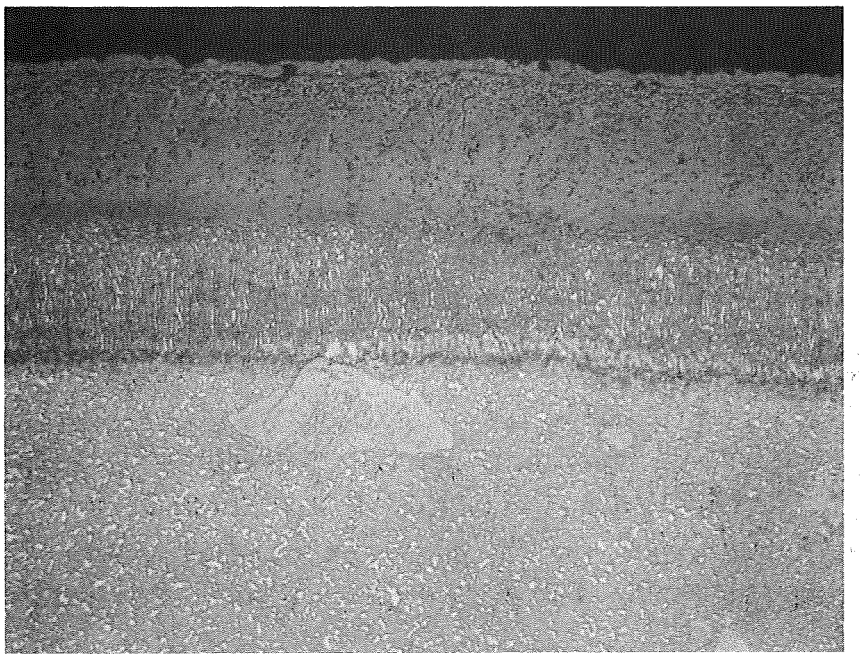

Figure 2-4 Typical Micrographs of: A) PWA 286 Overlay Coating, and B) PWA 273 Diffusion Coating Illustrating the Microstructural Differences Between the Coatings. Note the small interdiffusion zone associated with the overlay coating compared to that of the diffusion coating. The substrate is PWA 1480. (500X Mag., Etchant: Mixed Acids)

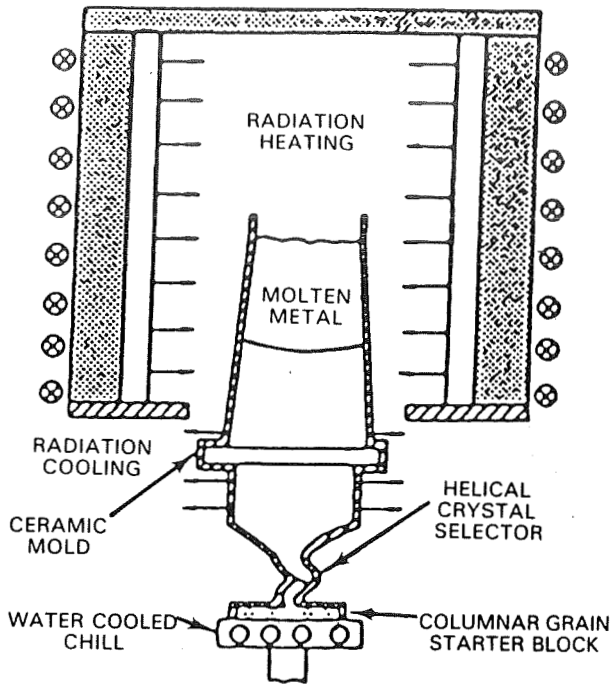

Figure 2-5 Schematic Representation of Single Crystal Casting Process

After casting, the bars were solution heat treated employing a step-temperature cycle with a thirty-minute hold at the 1293°C (2360°F) maximum temperature, followed by a forced gas cool to obtain the desired microstructure of fine gamma prime precipitate homogeneously distributed in the gamma matrix without the onset of incipient melting. The following inspection procedure was employed to ensure the quality of the castings prior to specimen fabrication:

1) Grain etch - visual inspection for surface defects.

2) Laue back reflection x-ray diffraction to determine the deviation from the primary crystallographic orientation and the presence of any low angle grain boundaries.

3) Metallographic examination of the heat treated microstructure to ensure complete gamma prime solutioning without incipient melting or excessive porosity.

Table 2-IV lists the matrix for the number of acceptable bars cast to date.

Table 2-IV

Matrix for the Number of Acceptable Cast Bars Based on Crystallographic Orientation and Bar Diameter

	Number of 2.54 cm (1.0 in) Diameter Bars				Number of 1.59 cm (0.625 in) Diameter Bars			
Alloy	<100>	<111>	<110>	<123>	<100>	<111>	<110>	<123>
PWA 1480 (P9866)	82	28	73	69	53	42	37	31
PWA 1480 (P9867)	28	3	3	--	--	8	--	--
Alloy 185	15	--	--	--	15	--	--	--

2.2.2 Specimen Fabrication

Specimen geometries were chosen to allow conditions comparable to those found in actual turbine blades to be produced during testing. PWA 1480 specimens (and, in the future, Alloy 185 specimens) were machined from 2.54 cm (1.0 in) and 1.59 cm (0.625 in) diameter bars. For coated property testing, the specimens were coated using the standard methods as listed in Table 2-III. Specimens for determining coating material properties of the overlay coating were fabricated from ingots of hot isostatically pressed (HIP) powder. Diffusion aluminide coating specimens were prepared by applying the coating to specially designed specimens of PWA 1480. Additional details on the specimens are as follows:

- Physical Property Specimens - The determination of the thermal conductivity, thermal expansion, and specific heat for the materials chosen for this project has been contracted to the Southern Research Institute, Birmingham, Alabama. Figure 2-6 illustrates the specimen geometries required for two of the physical property tests. The specification for the specific heat specimen is that a minimum volume of 16.4 cubic cm (1.0 cubic in) of material be supplied. Six specimens (two for each property) of each material are to be tested.

- Single Crystal Alloy and Single Crystal Alloy/Casting Mechanical Property Specimens - Figure 2-7(A) and 2-7(B) illustrate the specimen geometries employed for coated and uncoated tensile and creep testing, and uncoated cyclic constitutive testing. Figure 2-7(C) is a diagram of the current standard strain-controlled thermomechanical fatigue (TMF) specimen used at Pratt & Whitney. The specimen was employed to determine the feasibility of using external extensometry (which would eliminate the need for internal ridges in the specimen) instead of the standard internal extensometry by performing direct comparison TMF testing trials. Table 2-V lists the number of specimens prepared to date.

A) THERMAL CONDUCTIVITY SPECIMEN

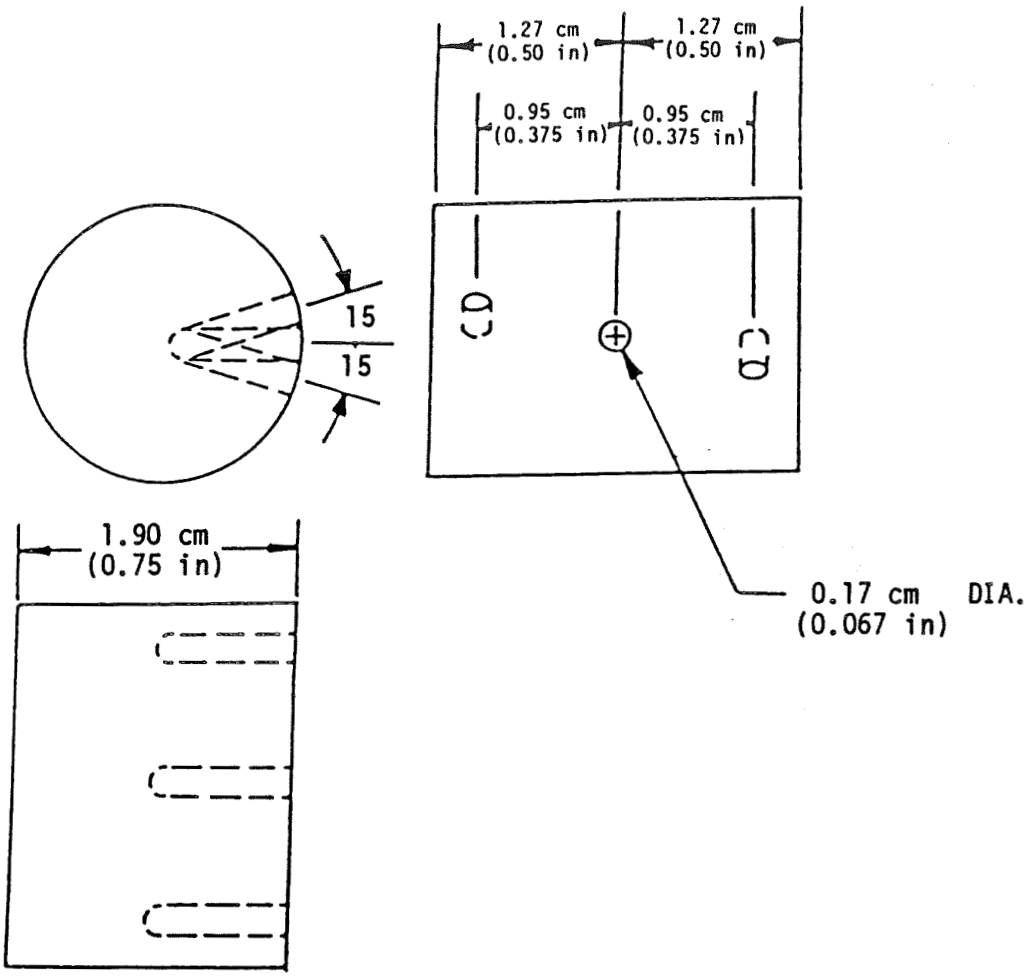

B) THERMAL EXPANSION SPECIMEN

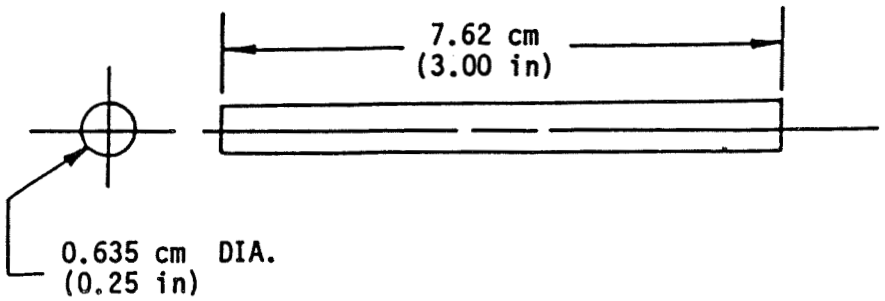

Figure 2-6 Specimen Designs for Determining Physical Properties

A) TENSILE AND CREEP TEST SPECIMEN

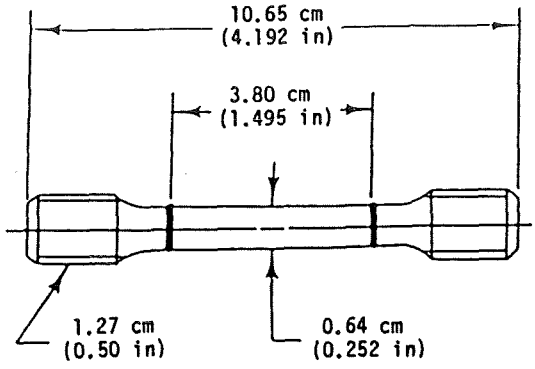

B) CYCLIC CONSTITUTIVE TEST SPECIMEN

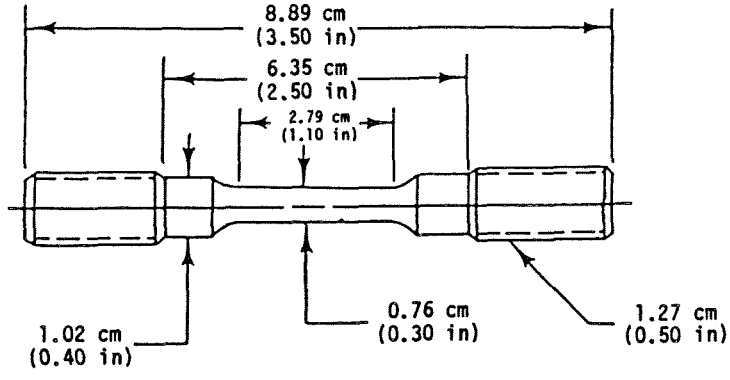

C) INITIAL THERMOMECHANICAL FATIGUE SPECIMEN

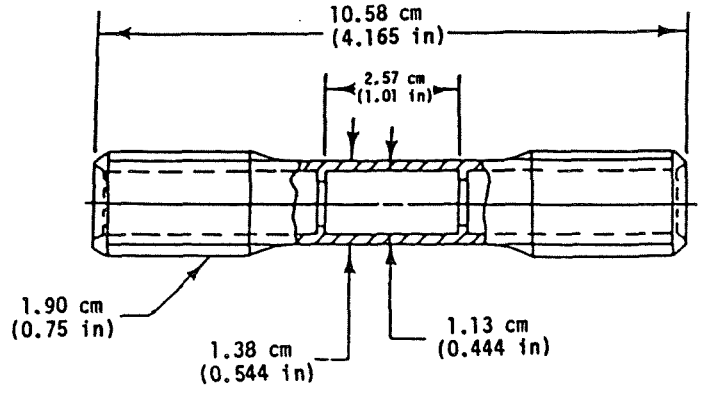

Figure 2-7 Specimen Designs for Single Crystal Alloy and Single Crystal Alloy/Coating Mechanical Property Tests

Table 2-V

Number of PWA 1480 Mechanical Property Test Specimens Fabricated to Date

Type of Specimen	Coating	Number of Specimens <100>	<111>	<110>	<123>
Tensile and Creep Test Specimens	Uncoated	14	12	14	14
	PWA 286	10	9	--	--
	PWA 273	10	9	--	--
Cyclic Constitutive Test Specimens	Uncoated	11	11	11	11
Thermomechanical Fatigue Test Specimens	PWA 286	12	--	--	--
	PWA 273	12	--	--	--

- Coated Material Mechanical Property Specimens- Figure 2-8 illustrates the specimen geometries employed for testing the mechanical properties of bulk PWA 286 overlay coating material. The specimen diagrammed in Figure 2-8(A) was machined from PWA 286 ingots of hot isostatically pressed (HIP) powder. Figure 2-8(B) illustrates specimens fabricated from thick sheets of plasma sprayed PWA 286. The thick sheets were produced of plasma spraying thick layers of PWA 286 onto substrates. The substrates were subsequently removed by machining.

  Figure 2-9 illustrates the specimens employed for determining coating material properties when applied to PWA 1480 substrates. Figure 2-9(A) diagrams the substrate for the PWA 273 coated specimen for tensile and creep testing. Two coating thicknesses will be used. The reasons for this particular configuration selection is discussed in Section 4.1. Figure 2-9(B) illustrates the substrate for the four-point bend coated fatigue specimens. Both coating materials will be employed for testing. Table 2-VI lists the number of specimens fabricated to date.

A) TENSILE, RELAXATION, AND STRESS-RUPTURE SPECIMEN FABRICATED FROM HOT ISOSTATICALLY PRESSED POWDER

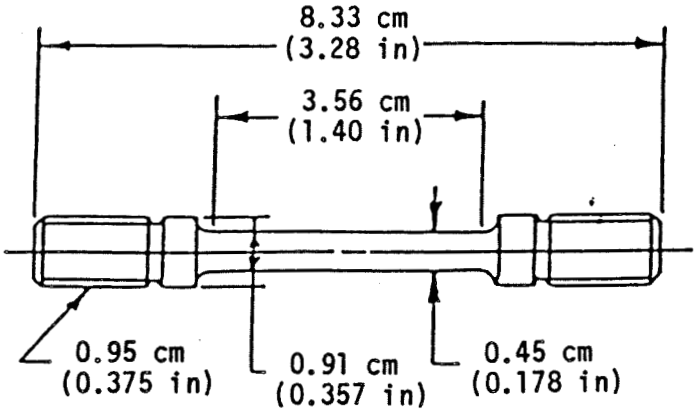

B) TENSILE, RELAXATION, AND STRESS-RUPTURE SPECIMEN FABRICATED FROM PLASMA SPRAYED SHEETS

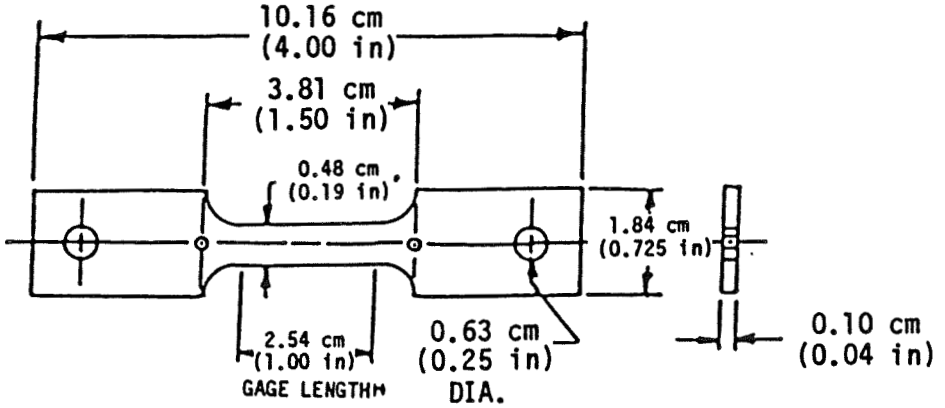

Figure 2-8 Specimen Designs for Bulk PWA 286 Coating Material Mechanical Property Tests

A) TENSILE AND CREEP DIFFERENCE METHOD TEST SPECIMEN

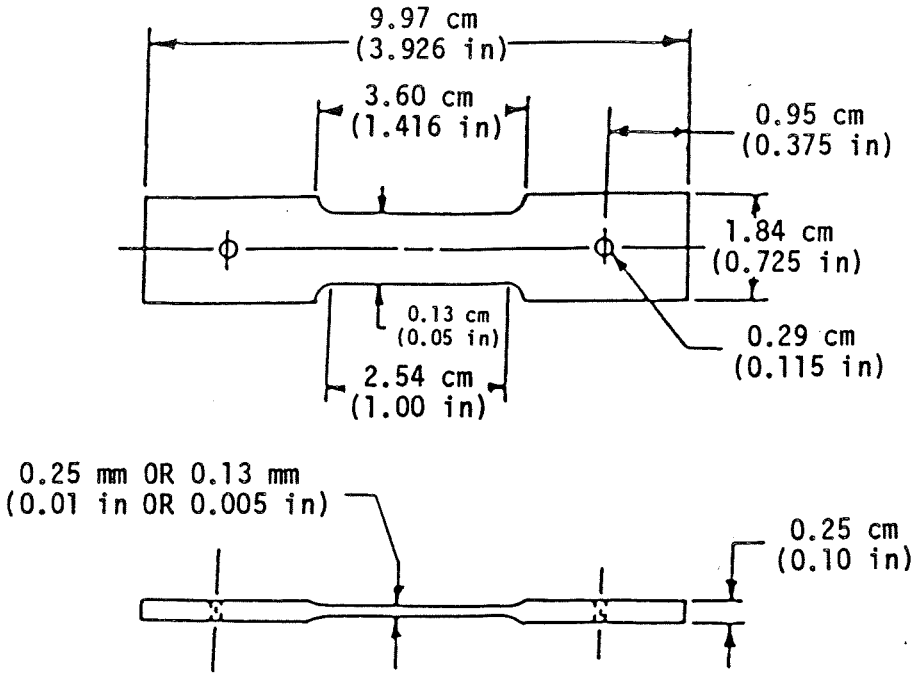

B) FOUR-POINT BEND FATIGUE TEST SPECIMEN

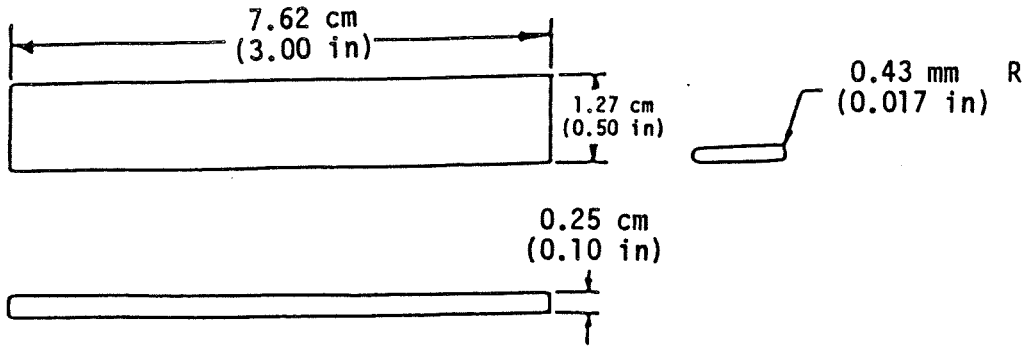

Figure 2-9 Specimen Designs of the Substrates for Coating Material Mechanical Property Tests

Table 2-VI

Number of Coating Material Mechanical
Property Test Specimens Fabricated to Date

Type of Specimen	Material	Number	Comments
Cylindrical Tensile, Relaxation and Stress-Rupture Specimen	Bulk PWA 286	29	Fabricated from HIPed powder
Flat Tensile, Relaxation and Stress-Rupture Specimen	Bulk PWA 286	16	Fabricated from plasma sprayed sheets
Tensile and Creep Difference Method Specimen	Bulk PWA 273	21	0.25 mm (0.010 in) substrate thickness
	Bulk PWA 273	17	0.13 mm (0.005 in) substrate thickness
Four-Point Fatigue Specimen	Bulk PWA 273	15	---

2.3 Physical, Thermal and Monotonic Mechanical Properties

2.3.1 PWA 1480 Physical and Thermal Properties

Physical and thermal property tests of PWA 1480 have been run at Southern Research Institute. Data on thermal conductivity, thermal expansion, specific heat and density have been obtained and the results are being reviewed.

2.3.2 Tensile Properties

2.3.2.1 PWA 1480 Single Crystal

A total of forty monotonic tensile tests were conducted on PWA 1480 single crystal specimens with orientations of <100>, <110>, <111>, and <123>. All tests were run at the ASTM (American Society for Testing Materials) standard strain rate of 0.005 min^{-1}. Additional tests are planned at other strain rates. Tests included uncoated and aluminide diffusion and NiCoCrAlY overlay coated <100> and <111> oriented specimens. A summary of all test conditions and observed material properties is presented in Table 2-VII.

Table 2-VII

Summary of PWA 1480 Tensile Testing

Temp. °C(°F)	Spec. ID	Orient	Coat Type	Ex10^{-3} MPa(KSI)	.2% Yield MPa(KSI)	Ult. MPa(KSI)	Elong %	RA %
427(800)	JA-16	100	---	113.8(16.5)	989.4(143.5)	1118.4(162.2)	5.7	3.2
	KA-2	110	---	221.3(32.1)	921.9(133.7)	957.0(138.8)	14.3	23.2
	LA-36	111	---	239.3(34.7)	897.0(130.1)	1393.5(202.1)	11.7	11.9
	MA-1	123	---	198.6(28.8)	837.7(121.5)	1218.3(176.7)	19.1	18.2
649(1200)	JA-33	100	---	POROSITY FAILURE				
	KA-3	110	---	176.5(25.6)	929.4(134.8)	1081.1(156.8)	4.7	5.6
	LA-51	111	---	253.7(36.8)	849.5(123.2)	1245.2(180.6)	23.7	25.6
	MA-3	123	---	193.7(28.1)	824.0(119.5)	1082.5(157.0)	22.7	25.1
760(1400)	JA-34	100	---[1,2]	101.4(14.7)	1177.0(170.7)	1324.5(192.1)	14.1	13.0
	JA-22		273[1,2]	103.4(15.0)	1159.7(168.2)	1293.5(187.6)	4.8	7.3
	JA-11		286[1,3]	94.5(13.7)	1163.2(168.7)	1290.1(187.1)	8.0	15.1
	KA-4	110	---	174.4(25.3)	948.1(137.5)	1108.7(160.8)	10.5	23.9
	LA-52	111	---[1,2]	200.0(29.0)	879.8(127.6)	1093.5(158.6)	22.1	24.2
	LA-25		273[1,2]	220.6(32.0)	920.5(133.5)	1030.1(149.4)	16.8	20.9
	LA-13		286[1,3]	171.7(24.9)	908.1(131.7)	1106.6(160.5)	21.4	29.7
	MA-4	123	---	180.0(26.1)	891.5(129.3)	985.3(142.9)	17.8	18.5
871(1600)	JA-36	100	---[1,2]	102.0(14.8)	715.0(103.7)	1021.1(148.1)	13.7	23.6
	JA-24		273[1,2]	92.4(13.4)	756.4(109.7)	991.5(143.8)	18.7	25.4
	JA-12		286[1,3]	91.7(13.3)	755.7(109.6)	961.9(139.5)	21.7	26.2
	KA-6	110	---	149.6(21.7)	786.0(114.0)	910.1(132.0)	13.1	26.0
	LA-53	111	---[1,2]	190.3(27.6)	696.4(101.0)	819.8(118.9)	19.0	22.1
	LA-26		273[1,2]	201.3(29.2)	682.6(99.0)	812.2(117.8)	20.3	24.4
	LA-14		286[1,3]	181.3(26.3)	671.6(97.4)	812.2(117.8)	22.1	22.1
	MA-5	123	---	179.3(26.0)	626.1(90.8)	764.7(110.9)	18.0	21.1
982(1800)	JA-37	100	---[1,2]	88.3(12.8)	452.3(65.6)	695.0(100.8)	23.0	32.5
	JA-25		273[1,2]	92.4(13.4)	437.1(63.4)	659.9(95.7)	24.0	34.3
	JA-13		286[1,3]	102.0(14.8)	428.9(62.2)	642.6(93.2)	22.9	35.4
	KA-8	110	---	133.1(19.3)	519.9(75.4)	628.8(91.2)	16.7	36.1
	LA-54	111	---[1,2]	189.6(27.5)	427.5(62.0)	557.8(80.9)	22.2	28.0
	LA-28		273[1,2]	175.1(25.4)	448.2(65.0)	575.7(83.5)	18.3	26.3
	LA-16		286[1,3]	120.0(17.4)	455.1(66.0)	557.1(80.8)	23.7	28.2
	MA-6	123	---	164.8(23.9)	431.6(62.6)	539.9(78.3)	25.9	25.0
1093(2000)	JA-38	100	---[1,2]	72.4(10.5)	275.1(39.9)	371.6(53.9)	30.0	53.8
	JA-26		273[1,2]	52.4(7.6)	272.4(39.5)	368.2(53.4)	31.3	56.8
	JA-14		286[1,3]	68.9(10.0)	269.6(39.1)	353.7(51.3)	43.0	59.2
	KA-9	110	---	91.7(13.3)	315.8(45.8)	385.4(55.9)	18.7	28.1
	LA-55	111	---[1,2]	132.4(19.2)	259.9(37.7)	328.9(47.7)	41.7	35.5
	LA-29		273[1,2]	97.9(14.2)	253.0(36.7)	315.1(45.7)	28.0	42.1
	LA-18		286[1,3]	85.5(12.4)	262.7(38.1)	321.3(46.6)	29.2	46.6
	MA-9	123	---	125.5(18.2)	273.0(39.6)	319.2(46.3)	24.9	35.3

1 X-sectional area used to calculate stress excludes coating area
2 Aluminide diffusion
3 NiCoCrAlY overlay

Some of the trends can be understood by examining the fracture surfaces of some of these specimens shown in Figure 2-10. Note that the faceting is quite pronounced at 760°C (1400°F), but as the temperature is increased to 1093°C (2000°F), the number of faceting planes increases dramatically and the fracture surface appears more normal to the tensile load. Also note that necking and the ductility of the specimens increase with temperature. All of these trends can be explained by the increase in the number of active slip systems with temperature.

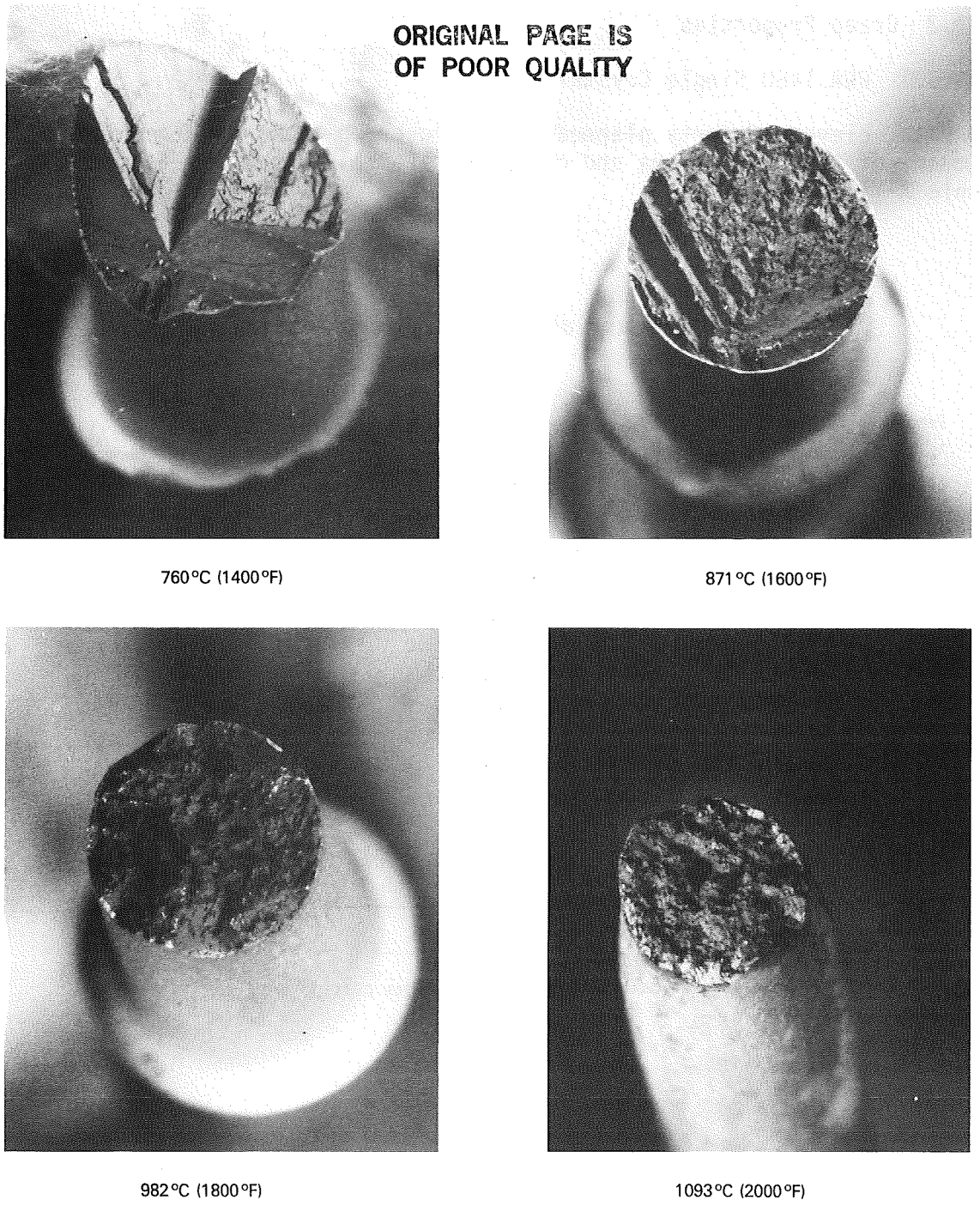

Figure 2-10 Fracture Surfaces of <001> PWA 1480 Tensile Specimens. Note the pronounced faceting at 760°C (1400°F) is reduced with increased temperature.

Test specimen JA-33, with orientation <100>, exhibited extremely low elongation. Upon metallurgical evaluation, the specimen was found to contain large porosity sites along the fracture surface. Such porosity is considered noncharacteristic of PWA 1480 material. For actual turbine hardware, the standard part inspection practices would detect this type of defect prior to installation into an engine.

2.3.3 Creep Properties

2.3.3.1 PWA 1480 Single Crystal

To date, eleven of forty planned monotonic creep tests have been completed. A summary of test conditions and observed material properties is presented in Table 2-VIII.

Table 2-VIII

Summary of PWA 1480 Creep Testing

Temp. °C (°F)	Spec. ID	Orient	Coat Type	Stress MPa (KSI)	% Of .2% Yield	Life (Hrs.)	Secondary Creep Rate (Min^{-1})	Elong %	RA %
871(1600)	JA-40	100	---	413.7(60)	57.8	462.9	8.84 E-07	12.0	20.1
	JA-41		---	517.1(75)	72.3	79.0	8.28 E-06	15.3	28.9
	LA-57	111	---	482.6(70)	69.3	67.1	2.90 E-05	14.9	22.8
982(1800)	JA-42	100	---	220.6(32)	48.8	STOPPED @ 5.4 HRS. FOR TEM[1]			
	JA-27		273[2,3]	231.7(33.6)	53.0	89.1	3.94 E-06	25.2	44.2
	JA-15		286[2,4]	237.9(34.5)	55.5	105.5	3.65 E-06	20.0	42.3
	JA-45		---	248.2(36)	54.9	80.5	4.74 E-06	20.7	41.4
	JA-28		273[2,3]	260.6(37.8)	59.6	53.3	8.74 E-06	24.3	40.6
	JA-17		286[2,4]	268.2(38.9)	62.5	51.7	8.48 E-06	20.7	36.3
	MA-13	123	---	248.2(36)	57.5	76.6	3.12 E-06	23.5	33.1
1093(2000)	JA-30	100	273[2,3]	122.7(17.8)	45.1	76.4	2.88 E-06	20.6	58.1

1 Transmission Electron Microscopy

2 X-sectional area used to calculate stresses excludes coating area

3 Aluminide diffusion

4 NiCoCrAlY overlay

Transmission electron microscopy (TEM) was conducted on a specimen tested at 982°C/220 MPa (1800°F/32 ksi) to examine the dislocation patterns developed at the end of primary creep. At this stage, the dislocation density is low and inhomogeous in distribution, Figure 2-11(A). Dislocation pairs, one is shown by the arrow in Figure 2-11(B), are observed surrounding the γ'. Using the $g \cdot b = 0$ invisibility criterion, the Burger's vector of the dislocation pairs were found to be of <011> type. Therefore, it is believed that shear of the γ' precipitates by pairs of a/2 <110> dislocations controlled the primary creep deformation in this specimen.

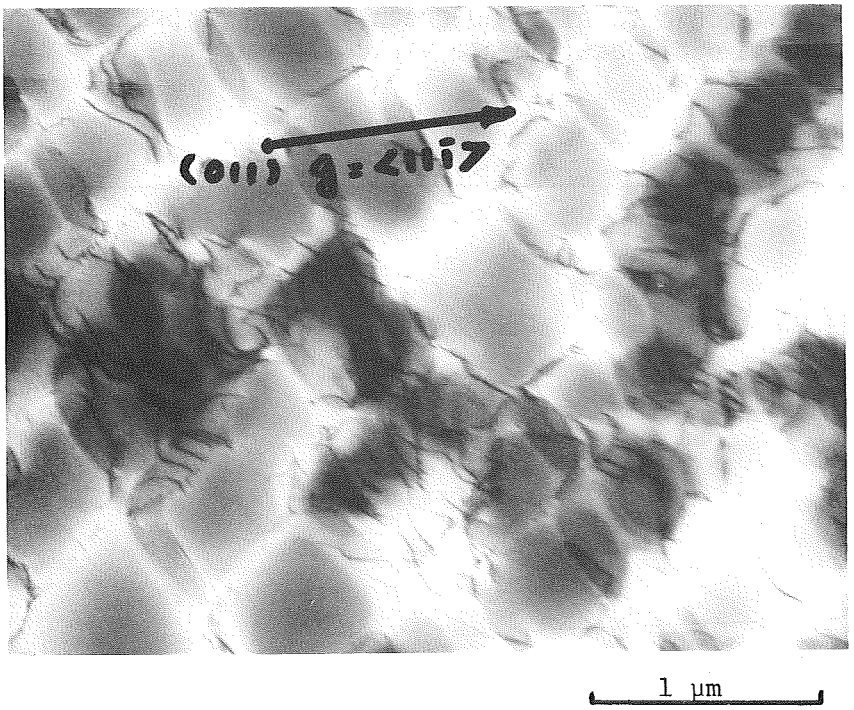

A) FOIL IS CUT PERPENDICULAR TO STRESS AXIS (I.E., PARALLEL TO <001>)

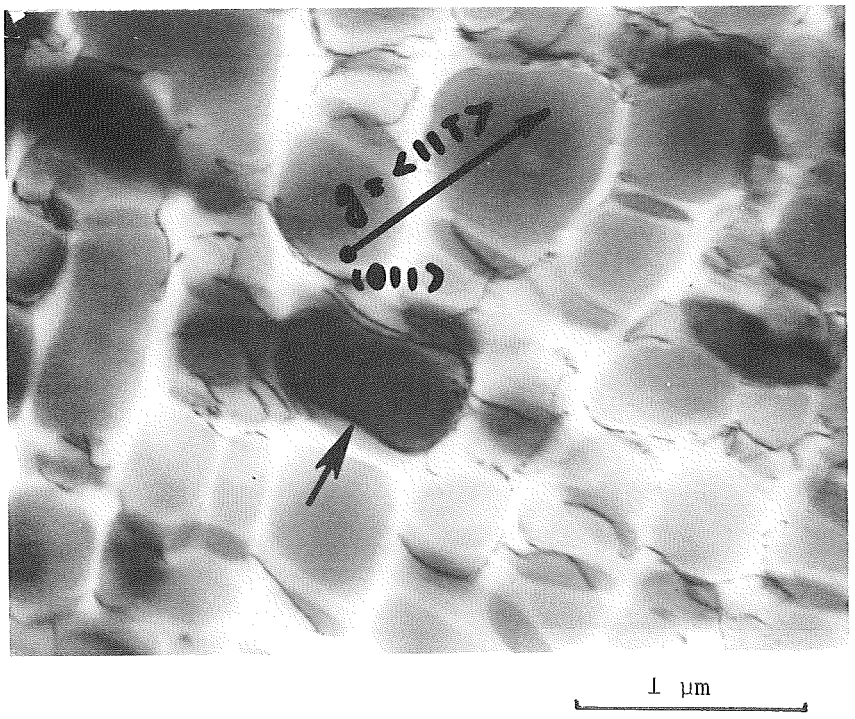

B) FOIL IS CUT PARALLEL TO <111> SLIP PLANE

Figure 2-11 Dislocation Structure After Being Creep Tested at 982°C/220 MPa (1800°F/32 ksi) for 5.4 Hours (Within Primary Creep Stage)

The <123> oriented creep specimen tested at 982°C/248 MPa (1800°F/36 ksi) exhibited virtually no primary creep as compared to the <100> oriented specimen (Figure 2-12). Examination of the fracture surface also indicated more of a cleavage fracture (i.e., stage I cracking) than is usually observed at 982°C (1800°F).

A comparison of the percent elongation observed in uncoated <100> oriented specimens during monotonic tensile and creep testing is presented in Figure 2-13. As shown, the two elongations are virtually equivalent.

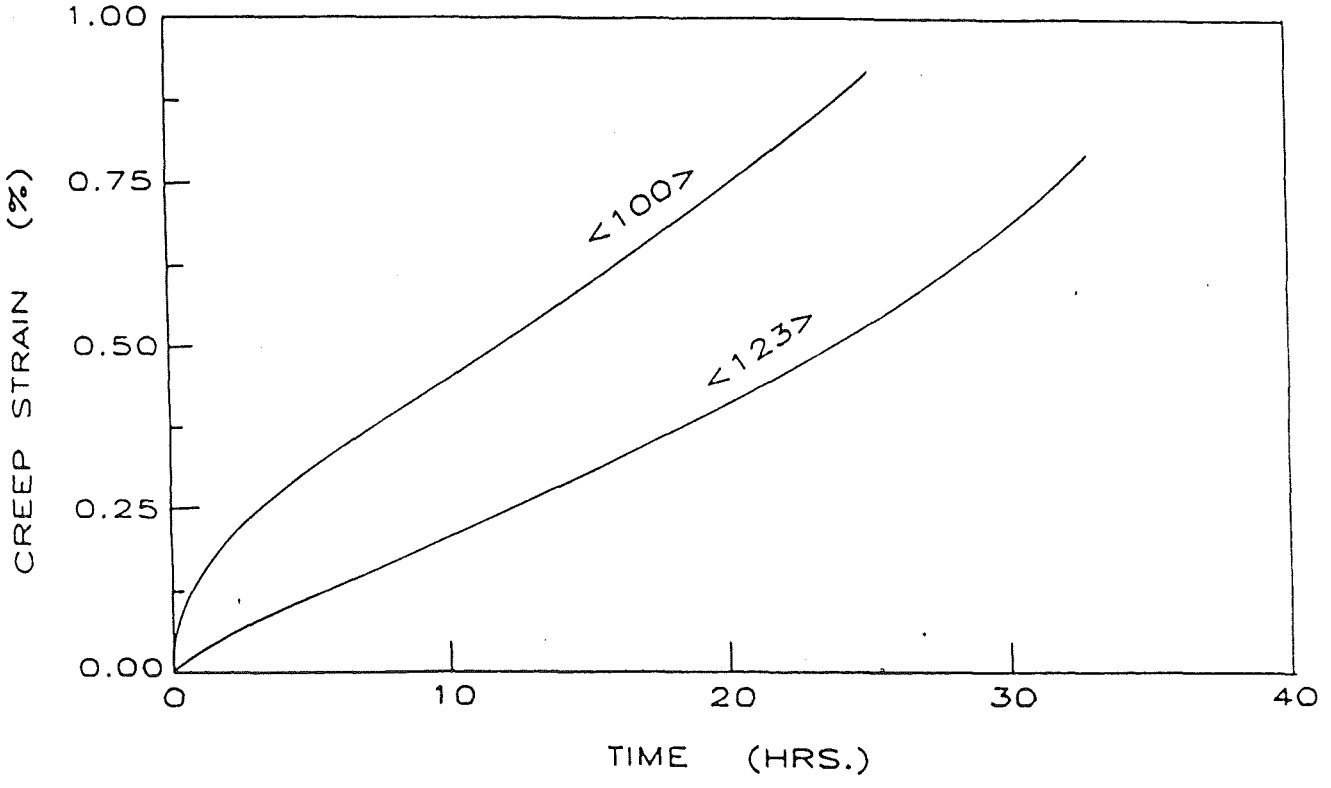

Figure 2-12 Uncoated PWA 1480 Creep 982°C/220 MPa (1800°F/36 ksi)

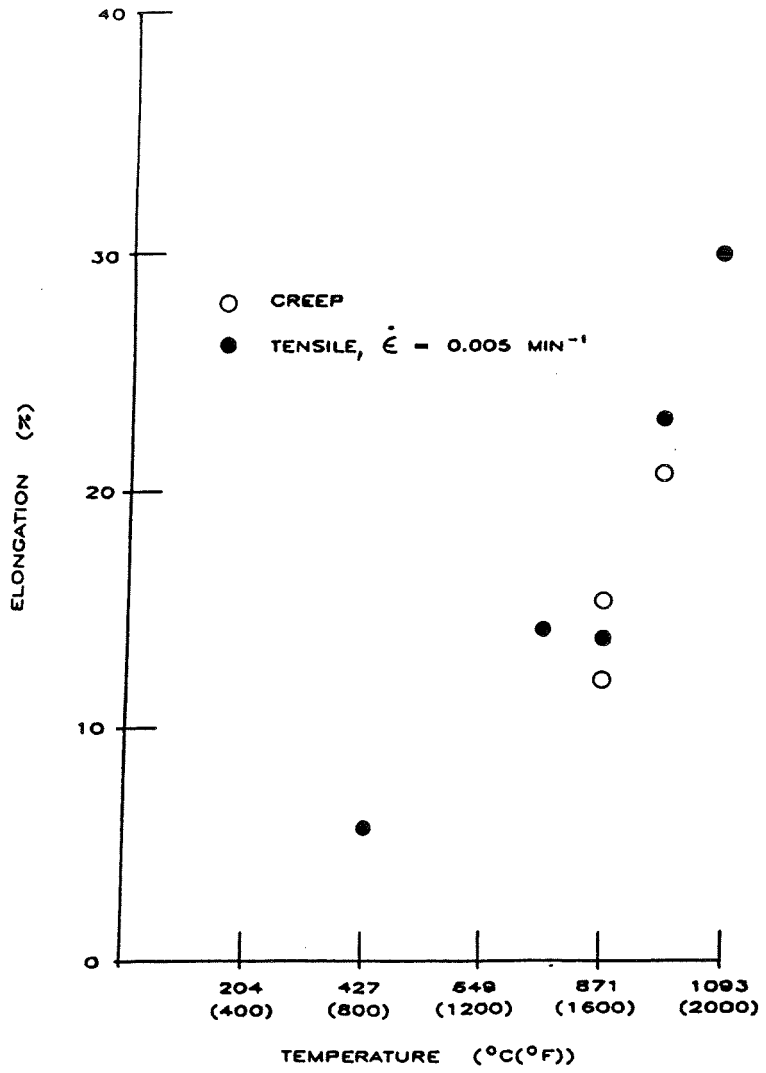

Figure 2-13 Elongation Observed in Uncoated <100> PWA 1480 Tensile and Creep Tests

2.3.3.2 PWA 286 NiCoCrAlY Overlay Coating

A summary of the test conditions and observed material properties is presented in Table 2-IX. No previous creep experience was available with this material. The creep test conditions were set based on the limited stress relaxation tests conducted for the constitutive modeling effort. As a result, most tests required uploading or were discontinued before rupture. Due to the poor success in running these tests and the limited number of bulk hot isostatically pressed PWA 286 specimens remaining for constitutive model development, the balance of the planned creep tests have been postponed until the results of coated PWA 1480 fatigue tests can be used to define new test conditions for PWA 286.

Table 2-IX

Summary of Bulk Hot Isostatically Pressed
PWA 286 Creep Testing

Temp. °C(°F)	Spec. ID	Stress MPa(KSI)	Life (Hrs)	Secondary Creep Rate (Min^{-1})	Elong %	RA %	Comments
649(1200)	9-T	68.9(10)	1700	2.99 E-07	N/A	N/A	Discontinued At 1700 hrs.
	9-B	103.4(15)	1130	1.25 E-06	N/A	N/A	Discontinued At 1130 hrs.
760(1400)	17-T	34.5(5)	446	6.53 E-06	93.2	87.1	
	12-T	20.7/55.2(3/8)	92.1	2.64 E-06/4.60 E-05	166.1	23.7	Uploaded from 20.7 MPa/3 ksi to 55.2 MPa/8 ksi at 48 hrs.
871(1600)	18-B	6.9/13.8(1/2)	280.5	9.38 E-07/2.31 E-05	77.1	84.9	Uploaded from 6.9 MPa/1 ksi to 13.8 MPa/2 ksi at 160 hrs.
	17-B	20.7(3)	26.8	1.40 E-04	206.0	86.7	
982(1800)	15-B	3.45(.5)	---	---	139.1	66.1	Failed on loading

N/A = Not available

SECTION 3.0

TASK II - SELECTION OF CANDIDATE LIFE PREDICTION AND CONSTITUTIVE MODELS

Basic to any life prediction model is a good constitutive model. This is particularly true when predicting lives within the hot section of a gas turbine engine. As a gas turbine part is cycled through a wide range of stresses, strains, and temperatures, deformation and damage accumulate by a variety of mechanisms, all of which could play an important role in the part's ultimate failure. It is the goal of constitutive modeling to predict this stress-strain history and cycle shape, and possibly, the damage history, so that the conditions at fatigue initiation are accurately known. For coated airfoils, fatigue often originates in the coating and, under certain conditions, the coating reduces the fatigue life of the part. Due to this intimate interaction between the coating and substrate in fatigue, both materials must be understood in terms of constitutive and life models. A literature search of numerous such models is reported in this section together with the selection of the most promising candidates.

3.1 Coating Constitutive Models

Unlike the single crystal substrate materials selected for this program, the two coatings are polycrystalline, and, to a first approximation, isotropic. Some anisotropy (Figure 2-4) does exist due to the application process and/or interdiffusion between the coating and the substrate. However, for this program anisotropy will be ignored for the following reasons:

1) Coating properties are very difficult to measure and many of the planned test specimens are machined from billets which are inherently isotropic.

2) The properties parallel to the surface are believed to be most important, while errors in those normal to the surface are inconsequential.

Over this range of complexity five promising models have been selected for evaluation in this program. These are:

1) Classical model,
2) Walker's model,
3) Simplified Walker's model,
4) Simplified unified approach, and
5) Stowell equation.

Each model will be evaluated based on the desirable features which are categorized below:

1) Simplicity

   a) number of model temperature dependent constants
   b) simplicity of test quantity of baseline data required to obtain model constants
   c) ease of implementation into a finite element code

2) Predictive capability

a) accurate representation of baseline data
b) prediction of both isothermal and nonisothermal thermomechanical fatigue verification tests

Priority in ranking the models is depicted graphically in Figure 3-1 together with a qualitative preliminary evaluation of each model. Simple models which exhibit high predictive capability are considered most desirable and are represented by Region I on the figure. Region IV represents the least desirable class of models. Emphasis is placed on prediction capability. Thus, models which are more complex, such as Walker's unified approach, compare favorably to simpler models since the additional complexity should improve predictive capability. Quantification of the tradeoffs will become possible as test data are generated in Tasks III and V.

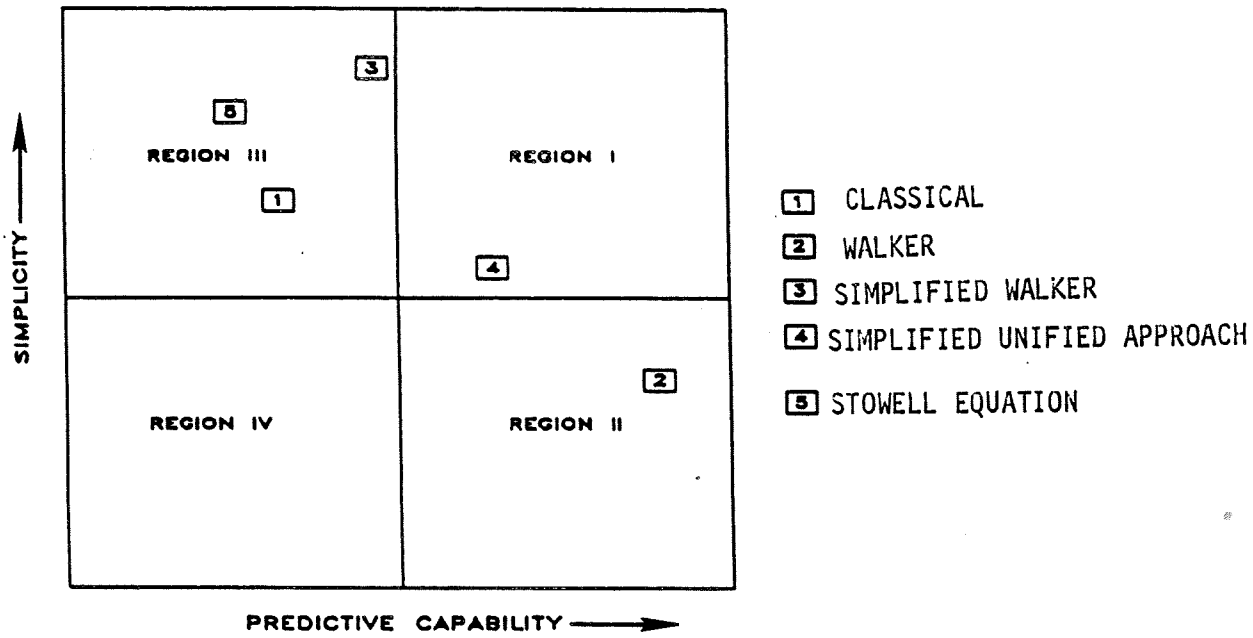

Figure 3-1 Comparison of Constitutive Model Features

To facilitate quantitative assessment, models are regressed and evaluated utilizing a consistent set of isothermal baseline data manipulated by a computer automated regression/prediction system. For regressions, the system calculates a standard deviation for each model constant which is interpreted as a measure of the model's ability to reproduce the baseline data behavioral characteristics.

3.1.1 Classical Model

The classical approach (Reference 1) was one of the first attempts at developing a nonlinear model which recognizes the observed dissimilarity between monotonic tensile and creep inelastic material responses. Time independent plasticity (tensile) and time dependent inelasticity (creep) are considered as uncoupled components of the total inelastic strain.

$$\varepsilon_{inelastic} = \varepsilon_{plastic} + \varepsilon_{creep} \tag{3-1}$$

Thus, the total strain function, neglecting thermal strain, is written:

$$\varepsilon_{total} = \varepsilon_{elastic} + \varepsilon_{plastic} + \varepsilon_{creep} \tag{3-2}$$

or

$$\varepsilon_{total} = \sigma/E + f(\sigma) + g(\sigma,t) \tag{3-3}$$

where: σ = stress,
t = time, and
E = elastic modulus.

Both plastic and creep strain functions [$f(\sigma)$, $g(\sigma,t)$] are chosen to provide adequate duplication of the material behavior. From Task I tests of PWA 286, it has been determined that both functions can be described by simple power law relationships:

$$\varepsilon_{plastic} = \left(\frac{\sigma}{A_1}\right)^{A_2} \tag{3-4}$$

$$\varepsilon_{creep} = \left(\frac{\sigma}{A_3}\right)^{A_4} t \tag{3-5}$$

where: A_1, A_2, A_3, and A_4 are constants.

These forms will be used in the first curve fit of constitutive data and will be modified as necessary as more data become available.

3.1.2 Walker Model

The Walker model (Reference 2) is among a new generation of constitutive models based on a unified viscoplastic approach which considers all nonlinear behavior as time dependent inelasticity. No distinction is made between plastic and creep inelastic action as in the classical model. Walker, from his earlier work on Hastelloy X, has chosen to express inelastic behavior by a power law relationship which can be written one-dimensionally as:

$$\dot{\underset{\sim}{\varepsilon}}_{\text{inelastic}} = \left(\frac{\underset{\sim}{\sigma} - \underset{\sim}{\Omega}}{K} \right)^{n} \tag{3-6}$$

where n is a constant and Ω, back stress, and K, drag stress, are strain history dependent internal state variables which describe kinematic and isotropic cyclic hardening, respectively.

The back stress term, $\underset{\sim}{\Omega}$, is a deviatoric quantity which physically corresponds to the asymptotic stress state under relaxation conditions. Qualitatively, the evolutionary expression for back stress is a sum of opposing nonlinear hardening and thermal and dynamic recovery components which can be characterized as:

$$\mathring{\underset{\sim}{\Omega}} = f\left(\underset{\sim}{\varepsilon}_{in}, \dot{\underset{\sim}{\varepsilon}}_{in}, T, t\right) - f\left(\underset{\sim}{\Omega}, \dot{\underset{\sim}{\varepsilon}}_{in}, T, t\right) \tag{3-7}$$

Hardening Recovery

where: $\underset{\sim}{\varepsilon}_{in}$ = instantaneous inelastic strain,

$\dot{\underset{\sim}{\varepsilon}}_{in}$ = instantaneous inelastic strain rate,

T = temperature, and

t = time.

Drag stress is a scalar quantity which represents a resistance to inelastic flow, and is considered a function of the effective inelastic strain, R.

One-dimensionally:
$$K = K_1 - K_2 \exp\left(- n_7 \underset{\sim}{R}\right) \tag{3-8}$$

where: K = instantaneous drag stress,

K_1 = fully hardened/softened drag stress,

$K_1 - K_2$ = initial drag stress,

n_7 = constant, and

$\underset{\sim}{R} = \sum_{i=1}^{n} \left| \Delta \underset{\sim}{\varepsilon}_{in_i} \right|$; $\Delta \underset{\sim}{\varepsilon}_{in}$ = inelastic strain increment.

Thus, the drag stress function is a monotonically increasing relationship describing isotropic hardening ($K_2 > 0$) or softening ($K_2 < 0$).

The entire set of equations for the Walker model considered in this research effort are provided in Table 3-I. References 2 and 3 provide a detailed discussion of Walker's and other unified approaches.

Table 3-I

A Summary of Walker's Model

$$\dot{c}_{ij} = \left(\frac{\sqrt{2/3\ (3/2\ s_{ij} - \ _{ij})\ (3/2\ s_{ij} - \Omega_{ij})}}{K} \right)^{n} \frac{(3/2\ s_{ij} - \Omega_{ij})}{\sqrt{2/3\ (3/2\ s_{ij} - \Omega_{ij})\ (3/2\ s_{ij} - \Omega_{ij})}} \tag{1}$$

$$\dot{\Omega}_{ij} = \dot{\bar{\Omega}}_{ij} + c_{ij} \frac{\partial n_1}{\partial \theta} \dot{\theta} + n_1 \dot{c}_{ij} + \dot{\Omega}^{(1)}_{ij} + \dot{\Omega}^{(2)}_{ij} \tag{2}$$

$$\dot{\Omega}^{(1)}_{ij} = n_2 c_{ij} - \Omega^{(1)}_{ij} \left(\dot{G}_1 - \frac{1}{n_2} \frac{\partial n_2}{\partial \theta} \dot{\theta} \right) \tag{3}$$

$$\dot{\Omega}^{(2)}_{ij} = n_{11}\, c_{ij} - \Omega^{(2)}_{ij} \left(\dot{G}_2 - \frac{1}{n_{11}} \frac{\partial n_{11}}{\partial \theta} \dot{\theta} \right) \tag{4}$$

$$\dot{G}_1 = \left(n_3 + n_4\, e^{-n_5 R} \right) \dot{R} + n_6 \left(\frac{3}{2}\ \Omega^{(1)}_{ij}\ \Omega^{(1)}_{ij} \right)^{\frac{M-1}{2}} \tag{5}$$

$$\dot{G}_2 = n_9 \dot{R} + n_{10} \left(\frac{2}{3}\ \Omega^{(2)}_{ij}\ \Omega^{(2)}_{ij} \right)^{\frac{M-1}{2}} \tag{6}$$

$$K = K_1 - K_2 e^{-n_7 R} - K_3 e^{-n_8 L} \tag{7}$$

$$\dot{R} = \sqrt{2/3\ \dot{c}_{ij}\ \dot{c}_{ij}} \tag{8}$$

$$\dot{L} = \left| \sqrt{2/3\ \dot{c}_{ij}\ \dot{c}_{ij}} - \left| \sqrt{2/3\ c_{ij}\ c_{ij}} \right| \right| \tag{9}$$

$$s_{ij} = \sigma_{ij} - \frac{1}{3} \delta \sigma_{kk} \tag{10}$$

$$\dot{\bar{\Omega}} = -\delta_{ij}\ \dot{\Omega}_{ij} + 3\, \dot{\Omega}_{ij} \frac{c_{ik}\, c_{kj}}{c_{ij}\, c_{ij}} \tag{11}$$

$$\dot{c}_{ij} = \left[\delta_{ij}\, \lambda\, \dot{c}_{kk} + 2\, \mu\, \dot{c}_{ij} - \dot{\sigma}_{ij} - \delta_{ij}\, (3\lambda + 2\mu) \int_0^t \alpha\, \dot{\theta}\, d \right] / 2\mu \tag{12}$$

Material Constants: λ, μ, $\dot{\Omega}$, n, m, n_1, n_2, n_3, n_4, n_5, n_6, n_7, n_8, n_9, n_{10}, n_{11}, K_1, K_2, and K_3 depend on temperature.

3.1.3 Simplified Walker Model

Preliminary Task II results suggest that the Walker model can be simplified because some terms describing the evolutionary response of back stress are unnecessary for PWA 286 coating material. The simplified Walker model is an extension of this simplification process to the extreme case where all back stress terms are eliminated. This seems justified, at least qualitatively, based on the rapid relaxation/low strength properties of coating materials at moderate temperature levels, $T \geq 871^{\circ}C$ ($1600^{\circ}F$). Thus, any exposure at high temperature can erase the back stress component (Figure 3-2). The inelastic strain rate formulation, equation (3-6), is then reduced to:

$$\dot{\underset{\sim}{\varepsilon}}_{in} = \left(\frac{\underset{\sim}{\sigma}}{K} \right)^{n}, \qquad (3\text{-}9)$$

From a simplicity standpoint this model is very attractive.

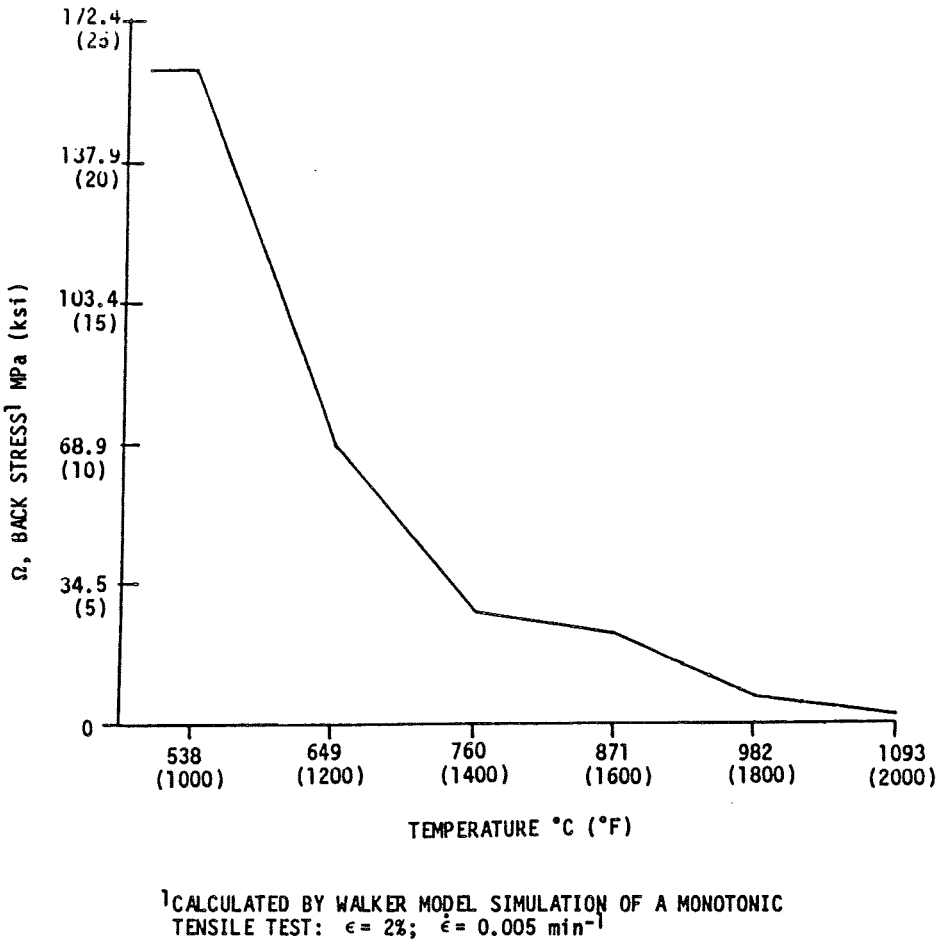

Figure 3-2 Saturated Back Stress Levels for Unexposed PWA 286 Overlay Coating

3.1.4 Simplified Unified Approach

Recently, Moreno (Reference 4) has had success in predicting the constitutive response of Hastelloy X using a hybrid model derived from both classical and unified approaches. Basically, the model assumes that the thermo-elastic response is known from previous analysis from which incremental values of strain, temperature, and time are used to calculate the actual (nonlinear) stress history.

Strain increments are considered as either time independent plastic or thermo-elastic creep.

$$\Delta\varepsilon = \Delta\varepsilon_{plastic} \tag{3-10A}$$

or

$$\Delta\varepsilon = \Delta\varepsilon_{elastic} + \Delta\varepsilon_{creep} \tag{3-10B}$$

Expressed in terms of stress increments:

$$\Delta\sigma = \Delta\sigma_{plastic} \tag{3-11A}$$

or

$$\Delta\sigma = \Delta\sigma_{elastic + creep} \tag{3-11B}$$

The classical yield surface criteria (Figure 3-3) are used to determine the onset of plastic action. Isothermal yield points are calculated from a tri-linear representation of tensile stress/strain information (Figure 3-4), and are assumed to be equal in tension and compression (i.e., the material is perfectly isotropic). No cyclic hardening is considered. Justification for this definition of yielding was based on observations of Hastelloy X cyclic response: 1) at elevated temperatures, little cyclic hardening/softening occurs, and 2) during thermomechanical cycling, exposure to the higher temperatures significantly reduces the amount of cyclic hardening developed at the lower temperatures.

The stress increment associated with time independent plastic action (equation 3-11A) is then calculated as:

$$\sigma_{i+1} - \sigma_i = \Delta\sigma_{plastic} = \sigma_{y_{i+1}} - \sigma_{y_i} \tag{3-12A}$$

for $\sigma_i = \sigma_{y_i}$

$T_{i+1} \geq T_i$

or

$$\sigma_{i+1} - \sigma_i = \Delta\sigma_{plastic} = \frac{E_{p_{i+1}} + E_{p_i}}{2} \Delta\varepsilon \qquad (3\text{-}12B)$$

for

$$\sigma_i = \sigma_{y_i}$$

$$T_{i+t} < T_i$$

and the stress increment associated with time dependent creep behavior (equation 3-11B) is calculated as:

$$\sigma_{i+1} - \sigma_i = \Delta\sigma_{elastic + creep} = E\,(\Delta\varepsilon - \Delta\varepsilon_{creep}) \qquad (3\text{-}13)$$

$$\Delta\varepsilon_{creep} = A\sigma^n \Delta t \qquad (3\text{-}14)$$

where: $\Delta\sigma_{elastic + creep}$ = total thermo-elastic creep stress increment,

$\Delta\sigma_{plastic}$ = total time independent plastic stress increment,

σ_y = yield stress,

$\Delta\varepsilon$ = total strain increment,

$\Delta\varepsilon_{creep}$ = total creep strain increment,

E = elastic modulus,

E_p = strain hardening slope of monotonic σ/ε curve,

T = temperature,

t = time increment,

subscripts: i = beginning of increment, and

$i+1$ = end of increment.

This model has been successful with Hastelloy X, which exhibits some behavioral similarities with overlay coating PWA 286. However, the higher level isothermal cyclic hardening characteristic of PWA 286 may be more difficult to simulate with this simplified model.

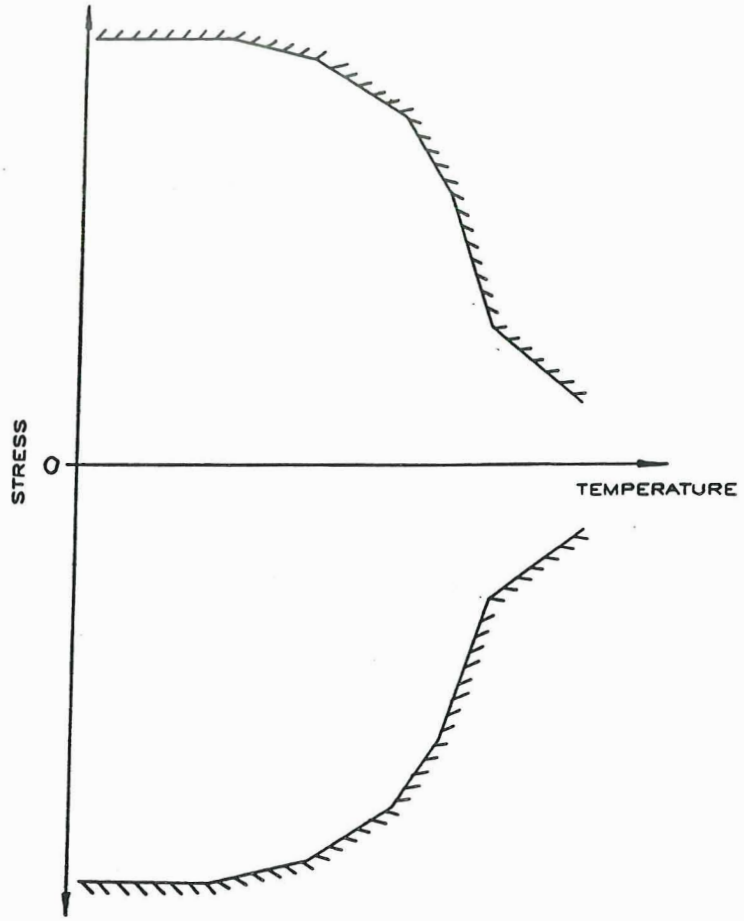

Figure 3-3 Classical Temperature Dependent Yield Surface for Simplified Unified Approach

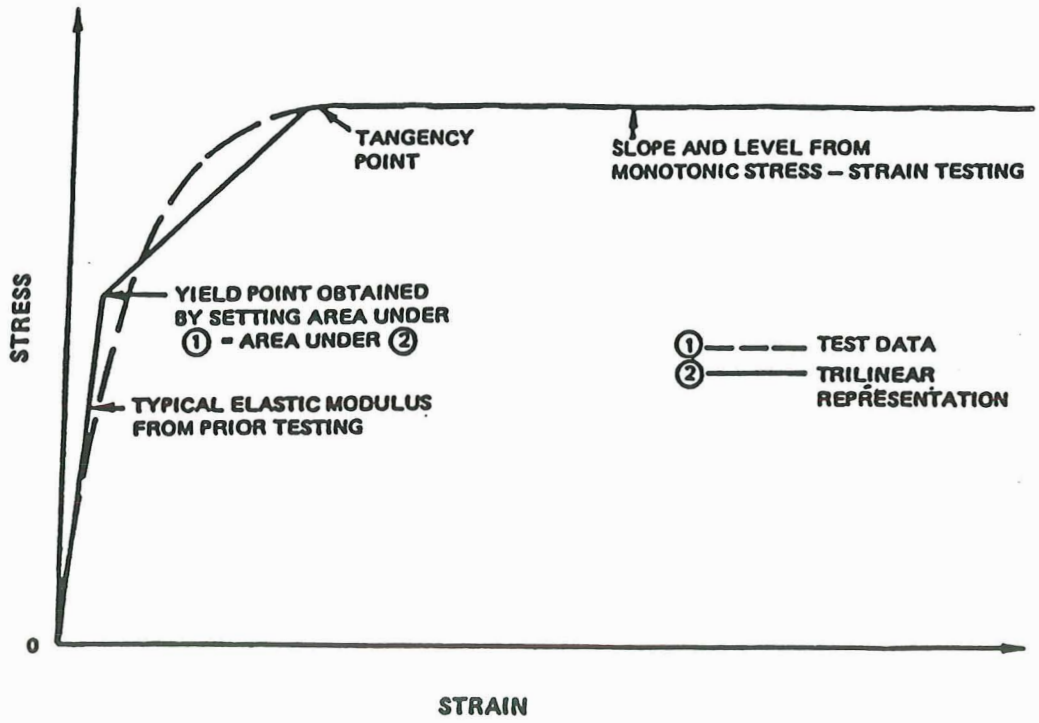

Figure 3-4 Construction of Tri-Linear Stress Strain Curve

3.1.5 Stowell Model

The Stowell model (References 5 through 7) is another form of a unified viscoplastic approach. It considers inelastic action as a diffusion mechanism based upon an apparent activation energy level.

$$\dot{\varepsilon}_{inelastic} = 2S\ T \exp\left(\frac{-\Delta H}{RT}\right) \sinh\left(\frac{\sigma}{\sigma_o}\right) \qquad (3\text{-}15)$$

where: ΔH = apparent activation energy,
σ = applied stress,
T = absolute temperature ($^\circ K$ or $^\circ R$),
R = gas constant, and
S, σ_o = constants.

Since creep deformation is generally thought to be controlled by diffusion processes, this model should perform well at elevated temperatures and/or slow strain rates.

3.2 Single Crystal Airfoil Material Constitutive Model

In Task II, a literature survey (Appendix B) was conducted to identify constitutive models and modeling approaches that are applicable to single crystal and transversely isotropic materials. Two distinct modeling approaches can be identified. The first attempts to model the anisotropic behavior by using the micromechanical processes which occur during deformation as a basis for the mathematical formulation. The second approach ignores the micromechanical processes and attempts to describe the bulk behavior through macroscopic quantities which are made to be functions of material orientation. While some of the earlier macroscopic models can be considered "fully developed", no complete micromechanical models can be considered fully developed.

Three candidate models have been identified for further evaluation. Two of these models use the macroscopic continuum approaches. They are the classical Hill model which is currently coded in general purpose finite element codes (such as MARC and ABAQUS), and a unified viscoplastic formulation of a model presented by Lee and Zaverl, et al. The third model uses a micromechanical approach which is currently under development. Each of these models are discussed in the following sections.

In interpreting the test results extensive use is made of the stereographic projection to display the angular relationships between crystallographic directions. All the planes in a crystal can be represented by a set of plane normals radiating from a single point of origin within the unit cell of the crystal. If a reference sphere is described about this point of origin, the plane normals can be described as the points where the normals intersect the surface of the sphere. This process is illustrated in Figure 3-5 for just the $\{100\}$ planes of the cubic unit cell.

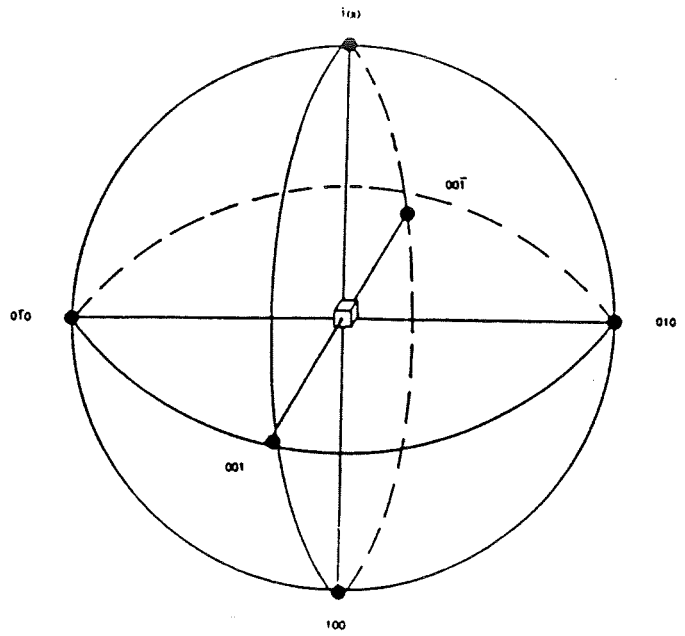

Figure 3-5 The {100} Poles for the Cubic System

The stereographic projection is illustrated in Figure 3-6 which shows a small cube of face centered material located at the center of a sphere. The axes CC is aligned in the Z or [001] direction, while the axes BB and AA are aligned in the y or [010] direction and in the x or [100] direction, respectively. Figure 3-7 shows the orientation ON which is defined by the Euler angles θ and ψ with respect to the cubic crystallographic axes x, y, z. If this direction ON is projected onto the sphere in Figure 3-6, it intersects the spherical surface at point T. The intersection of the line CT with the diametral circle ABAB occurs at point E, the circle ABAB being the stereographic projection with the [001] axes represented as the line OC. The direction OL where $\theta = 45^\circ$ and $\psi = 0^\circ$ in Figure 3-6 intersects the sphere at point P and the line CP, which goes through point L on the corner of the cube, intersects the stereographic projection at point R. This is the [011] direction. Similarly, the direction OM where $\theta = 45^\circ$ and $\psi = 35.26^\circ$ intersects the sphere at point Q and the line CQ intersects the stereographic project at point S. This is the [$\bar{1}$11] direction. The stereographic triangle ORS thus represents all angular orientations with respect to the crystallographic cubic axes. From the symmetry of the cube any other direction outside of the foregoing limits is equivalent to a corresponding direction inside the limits of the stereographic triangle ORS.

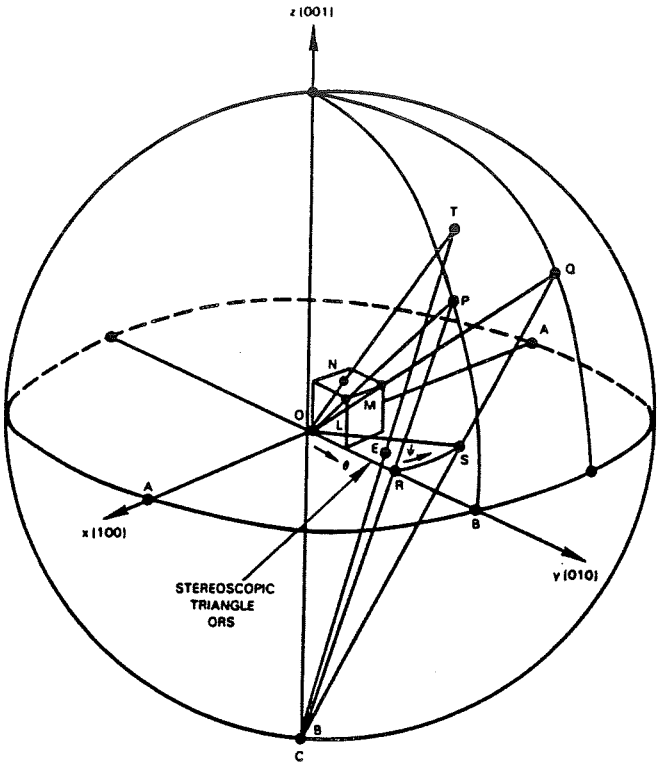

Figure 3-6 A Single Bar Oriented Along the Direction ON With Respect to the Cubic Crystal Axes AA, BB, and CC can be Located in the Stereographic Triangle ORS at Point E. The circular area ABAB is the stereographic projection.

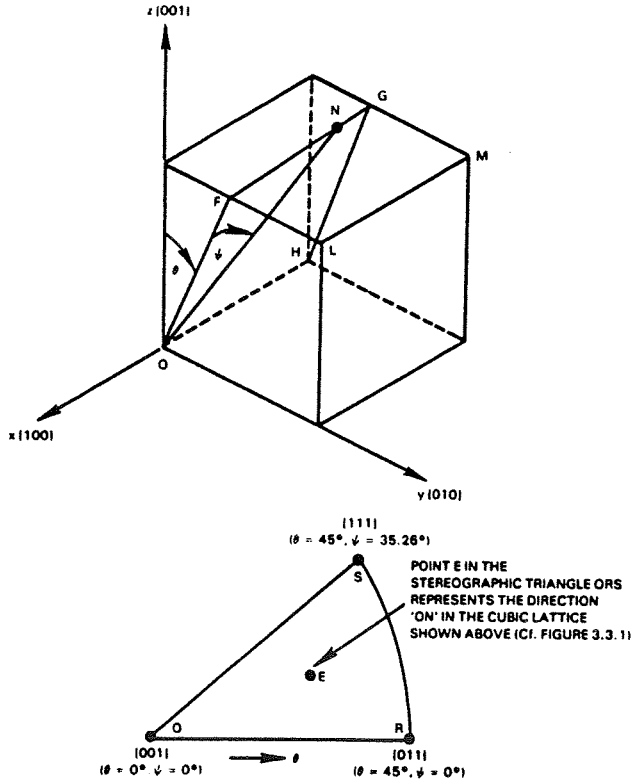

Figure 3-7 A Single Crystal Bar Oriented Along ON at Angles θ and ψ With Respect to the Crystal Axes X, Y, Z is Located at Point E in the Stereographic Triangle ORS.

3.2.1 Classical Hill Model

In 1948, Hill (Reference 8) proposed a generalization of the von Mises yield function for materials having three mutually orthogonal planes of symmetry. This yield function and an associated flow rule are the most widely used formulation for anisotropic materials and has been coded into general purpose nonlinear finite element codes such as MARC and ABAQUS. In this sense, it represents "standard practice" for analyzing structures with anisotropic material. For this reason, it was selected for further evaluation in this contract.

The Hill yield function is most commonly written in the form:

$$\bar{\sigma} = \left(\frac{3}{2}\right)^{1/2} \left(\frac{1}{F+G+H}\right)^{1/2} \Big[F(\sigma_y - \sigma_z)^2 + G(\sigma_z - \sigma_x)^2 + H(\sigma_x - \sigma_y)^2 + 2L\,\tau_{yz}^2 + 2M\,\tau_{zx}^2 + 2N\,\tau_{xy}^2 \Big]^{1/2} \tag{3-16}$$

where $\bar{\sigma}$ is the effective stress and σ_x, σ_y, σ_z, etc. are the stresses referred to the material coordinate system. F, G, H, L, M, and N are constants which in effect permit yielding to occur at different stresses in the different material directions. For single crystals, the material can be assumed to behave identically along the three crystal axes, [100], [010], [001], so that symmetry arguments can be used to show that:

$$F = G = H \text{ and } L = M = N.$$

The effective stress can then be written as:

$$\bar{\sigma} = \left(\frac{3}{2}\right)^{1/2} \left(\frac{1}{3F}\right)^{1/2} \Big[F\left\{(\sigma_y - \sigma_z)^2 + (\sigma_z - \sigma_x)^2 + (\sigma_x - \sigma_y)^2\right\} + 2L\left\{\tau_{yz}^2 + \tau_{zx}^2 + \tau_{xy}^2\right\} \Big]^{1/2} \tag{3-17}$$

or

$$\bar{\sigma} = \left[\sigma_x^2 + \sigma_y^2 + \sigma_z^2 - \sigma_y\sigma_z - \sigma_z\sigma_x - \sigma_x\sigma_y + A\left\{\tau_{yz}^2 + \tau_{zx}^2 + \tau_{xy}^2\right\} \right]^{1/2} \tag{3-18}$$

where A = L/F.

For the case of a simple uniaxial specimen oriented arbitrarily in the crystal, the stresses referred to the crystal axes are:

$$\sigma_x = \cos^2\psi \cos^2\theta\, S \qquad \tau_{xy} = \cos^2\psi \cos\theta \sin\theta\, S$$

$$\sigma_y = \cos^2\psi \cos^2\theta\, S \qquad \tau_{yz} = \cos^2\psi \sin\psi \sin\theta\, S \qquad (3\text{-}19)$$

$$\sigma_z = \cos^2\psi\, S \qquad \tau_{zx} = \cos\psi \sin\psi \cos\theta\, S$$

where θ and ψ are the Eulerian angles shown in Figure 3-7 and S is the uniaxial stress in the specimen.

Substituting, the effective stress equation becomes:

$$\bar{\sigma} = S \left\{ f(\psi, \theta) - g(\psi, \theta) + Ag(\psi, \theta) \right\}^{1/2} \qquad (3\text{-}20)$$

where

$$f(\psi, \theta) = \cos^4\psi\,(\cos^4\theta + \sin^4\theta) + \sin^4\psi$$

$$\text{and } g(\psi, \theta) = \cos^4\psi \cos^2\theta \sin^2\theta + \cos^2\psi \sin^2\psi \qquad (3\text{-}21)$$

Equation (3-20) defines the orientation dependence of the yield stress permitted by the Hill model. For a uniaxial specimen oriented in the [001] direction ($\psi = \theta = 0$), equation (3-20) gives the effective stress at yield:

$$\bar{\sigma} = S_{[001]} \qquad (3\text{-}22)$$

For a specimen oriented in the cube diagonal direction [111] ($\theta = 45°$, $\psi = 35.26°$), the effective stress at yield is:

$$\bar{\sigma} = \left(\frac{A}{3}\right)^{1/2} S_{[111]} \qquad (3\text{-}23)$$

$$A = 3\left(\frac{S_{[100]}}{S_{[111]}}\right)^2 \qquad (3\text{-}24)$$

Substituting equation (3-24) into (3-20) and manipulating gives an expression for the yield strength in any direction S as a function of the yield stress in the [001] and [111] directions.

$$S = S_{[001]} \left\{ f(\psi, \theta) - g(\psi, \theta) + 3 \left(\frac{S_{[001]}}{S_{[111]}} \right)^2 g(\psi, \theta) \right\}^{1/2} \qquad (3\text{-}25)$$

Figure 3-8 shows the permitted variation in yield stress for the hypothetical case where the cube diagonal yield stress is twice the cube axes yield stress. This figure shows that the permitted variation in yield strength changes monotonically from the [001] to the [111] direction which is not in agreement with reported single crystal data. This represents a severe restriction in this classical model.

Further limitations of the Hill formulation have also been identified. The yield function is insensitive to the sign of the stress state so that it cannot properly account for observed differences in tension and compression data (Reference 9). In addition, the state of anisotropy does not change with deformation. In spite of these obvious limitations, the classical Hill model will continue to be evaluated against the body of data being obtained because of the model's widespread use.

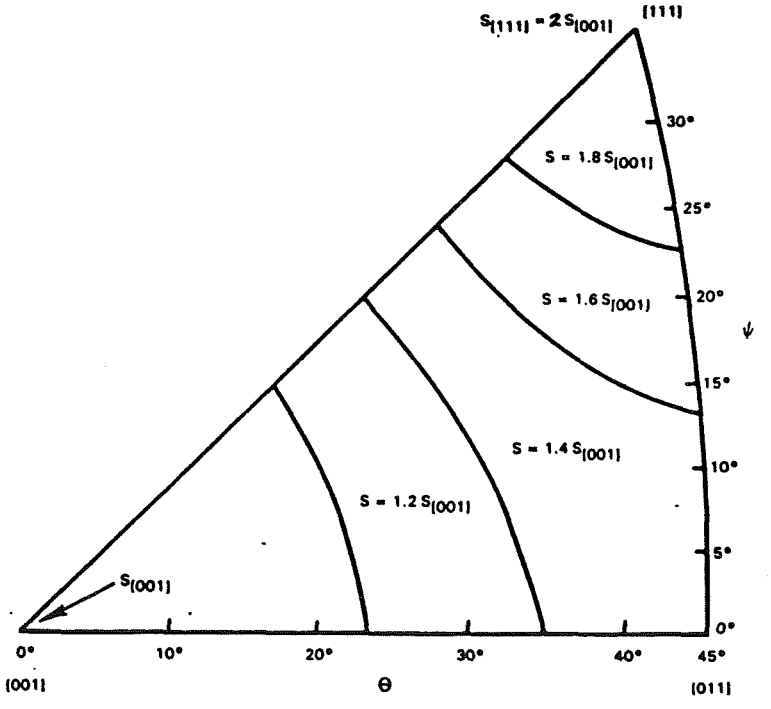

Figure 3-8 The Hill Yield Function Permits Only a Monotonically Changing Yield Strength in the Stereographic Triangle

3.2.2 Macroscopic Viscoplastic Formulation

The second modeling approach selected for evaluation and development is a generalization of the rate-independent yield function proposed by Lee and Zaverl, et al (Reference 10). For application to structural analysis of turbine airfoils, a rate-independent formulation is not as desirable as a unified viscoplastic formulation. Therefore, this second model will imbed the anisotropic matrices D_{ij} and M_{ij} of Lee and Zaverl in a unified viscoplastic framework.

Isotropic unified theories were reviewed in a pre-HOST program in Reference 11; these theories are readily modified to include anisotropy. For example, the unified theories may be modified so that the expression for the inelastic strain rate, c_{ij}, has the form:

$$\dot{c}_{ij} = \left(\frac{\sqrt{M_{ijkl} \, (\sigma_{ij} - \Omega_{ij}) \, (\sigma_{kl} - \Omega_{kl})}}{K} \right)^n \frac{M_{ijkl} \, (\sigma_{ij} - \Omega_{ij}) \, (\sigma_{kl} - \Omega_{kl})}{\sqrt{M_{ijkl} \, (\sigma_{ij} - \Omega_{ij}) \, (\sigma_{kl} - \Omega_{kl})}} \tag{3-26}$$

where Ω_{ij} and K are the equilibrium (back or rest) stress and the drag stress, respectively. The power law expression in equation (3-26) may be replaced by an exponential, hyperbolic sine, or any suitable functional relation according to the particular theory under consideration. The matrix form M_{ij} of the fourth rank tensor M_{ijkl} has two independent components for single crystal materials and three independent components in the case of directionally solidified materials.

The growth law governing the evolution of the equilibrium stress, Ω_{ij}, may be assumed to have the form:

$$\dot{\Omega}_{ij} = \alpha_1 \, c_{ij} - (\Omega_{ij} - \mathring{\Omega}_{ij} - \alpha_2 \, c_{ij}) \, \dot{G}, \tag{3-27}$$

where

$\mathring{\Omega}$ = the initial value of the back stress

$$\dot{G} = \alpha_3 \, \dot{R} \, \alpha_4 \, (M_{ijkl} \, \Omega_{ij} \, \Omega_{kl}) \, \frac{m-1}{2} \tag{3-28}$$

$$\dot{R} = \left(\frac{\sqrt{M_{ijkl} \, (\sigma_{ij} - \Omega_{ij}) \, (\sigma_{kl} - \Omega_{kl})}}{K} \right)^n . \tag{3-29}$$

The drag stress, K, may be assumed to evolve according to the equation:

$$\dot{K} = \alpha_5 \, \dot{R} - \alpha_6 \, K\dot{R} - \alpha_7 \, K^q, \tag{3-30}$$

with $\dot{R}$ defined in equation (3-29).

Calculations may be made with this anisotropic unified theory to construct a theoretical yield surface. For a given point in stress space, a surface surrounding this point may be constructed such that in going from the given point to each point on the surface, the cumulative inelastic strain increment is the same for each point on the surface. If this theoretical construct is called the yield surface, then the model allows the yield surface to translate in stress space by virtue of the presence of the equilibrium stress (similar to kinematic hardening in the isotropic version) and to expand in stress space due to the presence of the drag stress (similar to isotropic hardening in the isotropic version). In addition, the yield surface can distort its shape and rotate in stress space due to the presence of the fourth rank anisotropy tensor M_{ijkl} which might be assumed in the form:

$$\dot{M}_{ijkl} = (\overset{\infty}{M}_{ijkl} - M_{jkl})\,\dot{R} \,, \tag{3-31}$$

where $\overset{\infty}{M}_{ijkl}$ denotes the limiting saturated value of the tensor M_{ijkl} as $R \rightarrow \infty$ under cumulative deformation, with $\overset{\circ}{M}_{ijkl} = M_{ijkl}$ being the initial value of M_{ijkl}. A thermal recovery term may be added to equation (3-31) at high temperatures to allow recovery of the material to its original anisotropic state, viz. $\overset{\circ}{M}_{ijkl}$.

The unified formulations are completed by the specification of the relation:

$$\dot{\sigma}_{ij} = D_{ijkl}\,(\dot{\varepsilon}_{kl} - \dot{c}_{kl}) \,, \tag{3-32}$$

where D_{ijkl} is the fourth rank anisotropic elasticity tensor.

3.2.3 Micromechanical Viscoplastic Formulation

The third constitutive model selected for further development is a micromechanical model based on slip system stresses and strains and imbedded in a unified viscoplastic formulation. Development of a slip system based constitutive model began at Pratt & Whitney in 1982 and continues to be part of a large company effort to develop constitutive models. The slip system model development has continued since 1982 through the combined efforts of Pratt & Whitney's personnel and consultants under the company program and in a complementary NASA grant NAG-512.

The viscoplastic consitutive formulation based on crystallographic slip theory can be written in the form (Reference 12):

For Octahedral Slip

$$\underset{\sim}{m}_1=(\underset{\sim}{i}-\underset{\sim}{k})/\sqrt{2},\ \underset{\sim}{m}_2=(-\underset{\sim}{i}+\underset{\sim}{j})/\sqrt{2},\ \underset{\sim}{m}_3=(-\underset{\sim}{j}+\underset{\sim}{k})/\sqrt{2},\ \underset{\sim}{m}_4=(\underset{\sim}{j}-\underset{\sim}{k})/\sqrt{2}\ ,$$

$$\underset{\sim}{m}_5=(-\underset{\sim}{i}-\underset{\sim}{j})/\sqrt{2},\ \underset{\sim}{m}_6=(\underset{\sim}{i}+\underset{\sim}{k})/\sqrt{2},\ \underset{\sim}{m}_7=(-\underset{\sim}{i}-\underset{\sim}{k})/\sqrt{2},\ \underset{\sim}{m}_8=(\underset{\sim}{i}-\underset{\sim}{j})/\sqrt{2}\ ,$$

$$\underset{\sim}{m}_9=(\underset{\sim}{j}+\underset{\sim}{k})/\sqrt{2},\ \underset{\sim}{m}_{10}=(-\underset{\sim}{j}-\underset{\sim}{k})/\sqrt{2},\ \underset{\sim}{m}_{11}=(\underset{\sim}{i}+\underset{\sim}{j})/\sqrt{2},\ \underset{\sim}{m}_{12}=(-\underset{\sim}{i}+\underset{\sim}{k})/\sqrt{2}\ , \tag{3-33}$$

$$\underset{\sim}{n}_1=\underset{\sim}{n}_2=\underset{\sim}{n}_3=(\underset{\sim}{i}+\underset{\sim}{j}+\underset{\sim}{k})/\sqrt{3},\ \underset{\sim}{n}_4=\underset{\sim}{n}_5=\underset{\sim}{n}_6=(-\underset{\sim}{i}+\underset{\sim}{j}+\underset{\sim}{k})/\sqrt{3}\ ,$$

$$\underset{\sim}{n}_7=\underset{\sim}{n}_8=\underset{\sim}{n}_9=(-\underset{\sim}{i}-\underset{\sim}{j}+\underset{\sim}{k})/\sqrt{3},\ \underset{\sim}{n}_{10}=\underset{\sim}{n}_{11}=\underset{\sim}{n}_{12}=(\underset{\sim}{i}-\underset{\sim}{j}+\underset{\sim}{k})/\sqrt{3}\ ,$$

where $\underset{\sim}{i}$, $\underset{\sim}{j}$, and $\underset{\sim}{k}$ are the unit vectors in the Cartesian coordinate system having axes parallel to the three coordinate axes.

$$\pi^r_{mn}=\underset{\sim}{m}_r\cdot\underset{\sim}{\sigma}\cdot\underset{\sim}{n}_r\ ,\ \pi^r_{mm}=\underset{\sim}{m}_r\cdot\underset{\sim}{\sigma}\cdot\underset{\sim}{m}_r\ ,\ \pi^r_{nn}=\underset{\sim}{n}_r\cdot\underset{\sim}{\sigma}\cdot\underset{\sim}{n}_r\ ,$$

$$\pi^r_{zz}=\underset{\sim}{z}_r\cdot\underset{\sim}{\sigma}\cdot\underset{\sim}{z}_r\ ,\ \pi^r_{mz}=\underset{\sim}{m}_r\cdot\underset{\sim}{\sigma}\cdot\underset{\sim}{z}_r\ ,\ \pi^r_{nz}=\underset{\sim}{n}_r\cdot\underset{\sim}{\sigma}\cdot\underset{\sim}{z}_r\ , \tag{3-34}$$

$$\underset{\sim}{z}_r=\underset{\sim}{m}_r\cdot\underset{\sim}{n}_r\ , \tag{3-35}$$

$$\pi_r=\pi^r_{mn}+\alpha_{mm}\,\pi^r_{mm}+\alpha_{nn}\,\pi^r_{nn}+\alpha_{zz}\,\pi^r_{zz}+2\alpha_{mz}\,\pi^r_{mz}+2\alpha_{nz}\,\pi^r_{nz}\ , \tag{3-36}$$

$$\dot{\gamma}_r=K_r^{-p}\,(\tau_r-\omega_r)\,|\pi_r-\omega_r|^{p-1}\ , \tag{3-37}$$

$$\dot{\omega}=\rho_1\,\dot{\gamma}_r-\rho_2\,|\dot{\gamma}_r|\,\omega_r-\rho_3\,|\omega_r|^{m-1}\,\omega_r\ , \tag{3-38}$$

$$K_r=K_r^o+\rho_4\tanh\left(\frac{\pi^r_{nz}}{\rho_5}\right)+\int_{\xi=0}^{t}\frac{\partial K_r}{\partial\xi}\,d\xi\ , \tag{3-39}$$

$$\dot{K}_r=\sum_{r=1}^{12}h_{rk}\,|\dot{\gamma}_k|\ , \tag{3-40}$$

$$h_{rk} = \beta \left[q + (1 - q)\, \delta_{rk} \right] e - h \sum_{l=1}^{12} \int_0^t \left| \frac{\partial \gamma_l}{\partial \xi} \right| d\xi \ , \tag{3-41}$$

$$\dot{c} = \sum_{k=1}^{12} \frac{1}{2} \dot{\gamma}_k \left(\underset{\sim}{n}_k \underset{\sim}{m}_k + \underset{\sim}{m}_k \underset{\sim}{n}_k \right) , \tag{3-42}$$

$$\dot{\underset{\sim}{\sigma}} = \underset{\sim}{D} : \left(\dot{\underset{\sim}{\varepsilon}} - \dot{\underset{\sim}{c}} \right) . \tag{3-43}$$

For Cube Slip

$$\underset{\sim}{m}_1 = (\underset{\sim}{i} + \underset{\sim}{j})/\sqrt{2},\ \underset{\sim}{m}_2 = (-\underset{\sim}{i} + \underset{\sim}{j})/\sqrt{2},\ \underset{\sim}{m}_3 = (\underset{\sim}{i} + \underset{\sim}{k})/\sqrt{2} ,$$

$$\underset{\sim}{m}_4 = (-\underset{\sim}{i} + \underset{\sim}{k})/\sqrt{2},\ \underset{\sim}{m}_5 = (\underset{\sim}{j} + \underset{\sim}{k})/\sqrt{2},\ \underset{\sim}{m}_6 = (-\underset{\sim}{j} + \underset{\sim}{k})/\sqrt{2} , \tag{3-44}$$

$$\underset{\sim}{n}_1 = \underset{\sim}{n}_2 = \underset{\sim}{k},\ \underset{\sim}{n}_3 = \underset{\sim}{n}_4 = \underset{\sim}{j},\ \underset{\sim}{n}_5 = \underset{\sim}{n}_6 = \underset{\sim}{i} ,$$

The remaining equations are the same as for the octahedral slip except that the summations involving the indices r and l range from 1 to 6 instead of from 1 to 12.

A preliminary evaluation of this model has been made using the 982°C (1800°F) data obtained to date. Figure 3-9 shows the effect of orientation on Young's modulus for PWA 1480 at 982°C (1800°F). The modulus increases from a minimum value of 78.6 x 10^3 MPa (11.4 x 10^6 psi) at the [001] corner of the stereographic triangle and reaches a maximum value of 219.3 x 10^3 MPa (31.8 x 10^6 psi) at the [111] corner of the triangle. The elasticity matrix for a material which exhibits cubic symmetry can be written in the form:

$$[D] = \begin{bmatrix} D_{11} & D_{12} & D_{12} & 0 & 0 & 0 \\ D_{12} & D_{11} & D_{12} & 0 & 0 & 0 \\ D_{12} & D_{12} & D_{11} & 0 & 0 & 0 \\ 0 & 0 & 0 & D_{44} & 0 & 0 \\ 0 & 0 & 0 & 0 & D_{44} & 0 \\ 0 & 0 & 0 & 0 & 0 & D_{44} \end{bmatrix} \tag{3-45}$$

where D_{11} = 206.8 x 10^3 MPa (30 x 10^6 psi),

D_{12} = 151.7 x 10^3 MPa (22 x 10^6 psi), and

D_{44} = 85.5 x 10^3 MPa (12.4 x 10^6 psi)

for PWA 1480 at 982°C (1800°F).

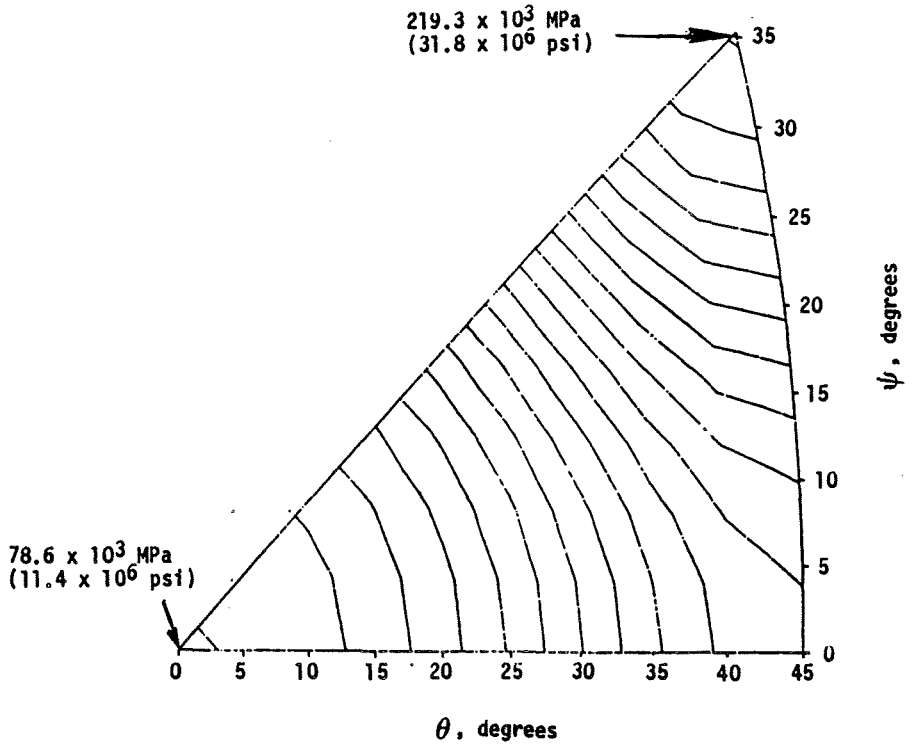

Figure 3-9 Stereographic Contour Plot of Young's Modulus for PWA 1480 at 982°C (1800°F)

To determine the material constants for octahedral slip, the COPES/CONMIN (Control Program for Engineering Synthesis/Constrained Minimization) code (Reference 13) was used. The objective function to be minimized in the COPES/CONMIN code was chosen to be the main square of the difference between the experimental and theoretically predicted cyclic hysteresis loops carried out at strain rates of 10^{-3}, 10^{-4} and 10^{-5} per second in the [111] direction. According to the COPES/CONMIN code, the minimum mean square deviation between the experimental and predicted hysteresis loops occurs for the following values of the material constants:

K_r^Q = 28317 for r=1 to 12,

ρ_1 = 2.49×10^7,

ρ_2 = 2871,

ρ_3 = 10^{-8},

p = 6.34,

m = 2.12,

ρ_4 = 940,

ρ_5 = 10400,

β = 0,

q = 1 (no latent hardening assumed for the present),

h = arbitrary (since β = 0),

D_{11} = 30×10^6,

D_{12} = 22×10^6,

D_{44} = 12.4×10^6, and

$\alpha_{mm} = \alpha_{nn} = \alpha_{zz} = \alpha_{mz} = \alpha_{nz} = 0$.

Figures 3-10 and 3-11 show the experimental and predicted hysteresis loops in the [111] direction for strain rates of 10^{-3}, 10^{-4} and 10^{-5} per second. For octahedral slip, the variation of the constitutive response with respect to direction in the stereographic triangle is now fixed by the preceding values of the material constants. Figures 3-12 and 3-13 show the comparison between the experimental and theoretical cycle hysteresis loops in the [001], [011] and [111] directions at a strain rate of 10^{-3} per second. The variation of peak stress response with direction is reasonable, but the theoretical hysteresis loop in the [001] is "fatter" (i.e., displays a more inelastic response) than the corresponding experimental loop. At this strain range, viz. $\pm$0.3 percent, the experimental [001] loop is almost behaving elastically. At higher strain ranges, the response exhibits an inelastic behavior and the loop becomes "fatter".

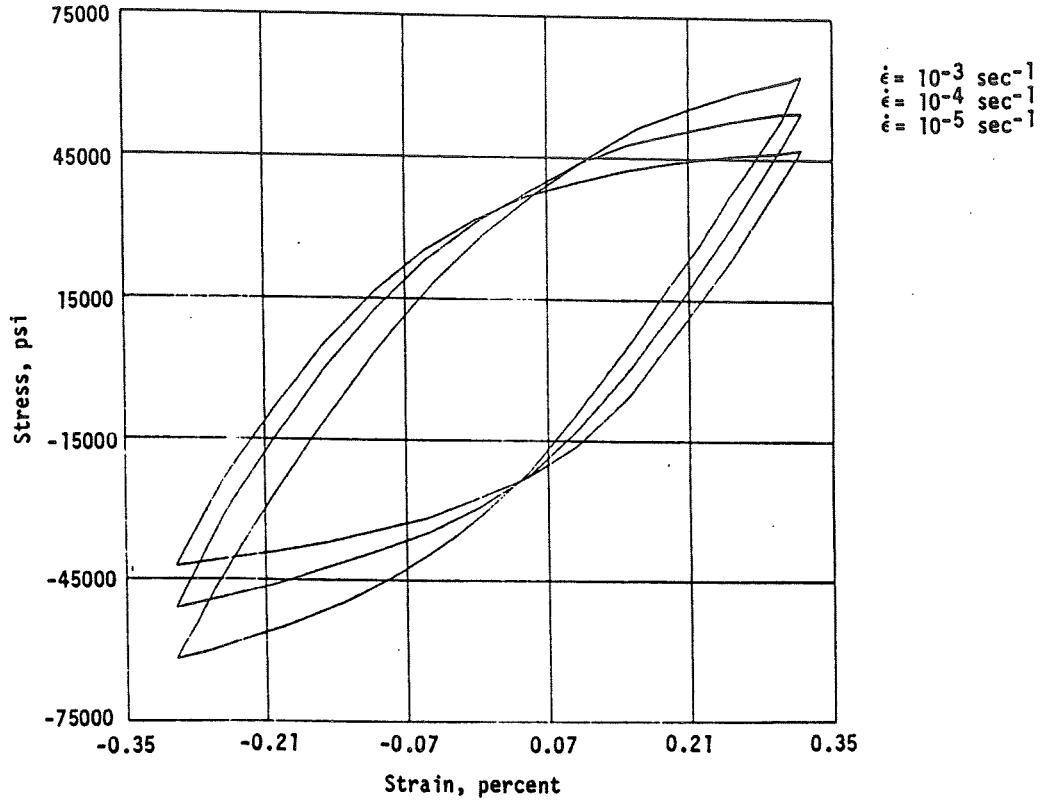

Figure 3-10 Experimental Hysteresis Loops in the [111] Direction for PWA 1480 at 982°C (1800°F)

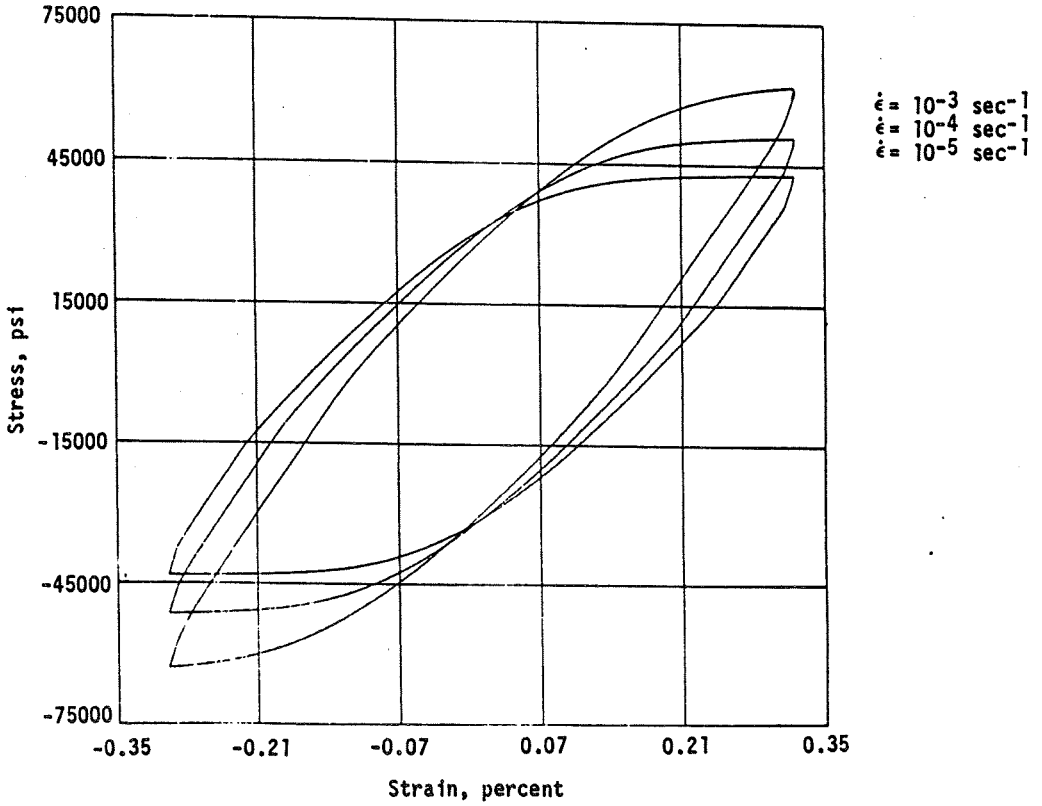

Figure 3-11 Precited Hysteresis Loops in the [111] Direction for PWA 1480 at 982°C (1800°F)

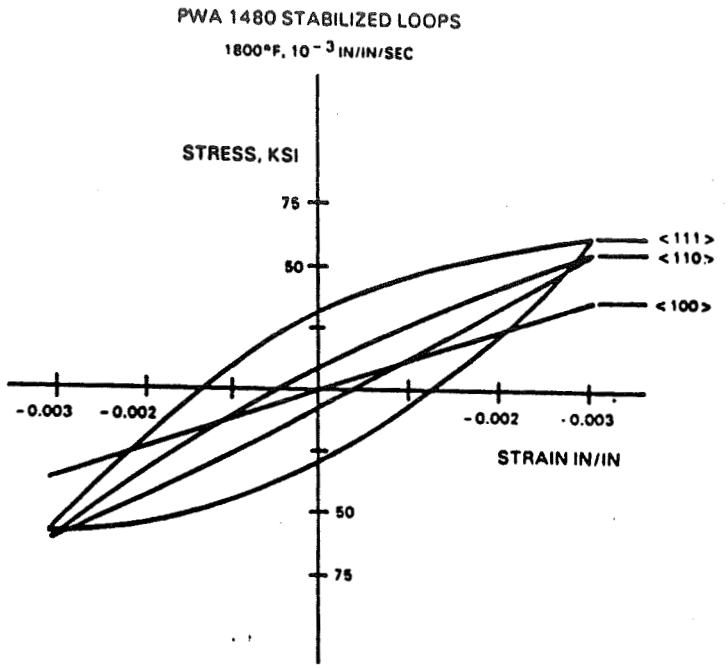

Figure 3-12 Experimental Hysteresis Loops for PWA 1480 at 982°C (1800°F) at 10^{-3} sec^{-1} Strain Rate

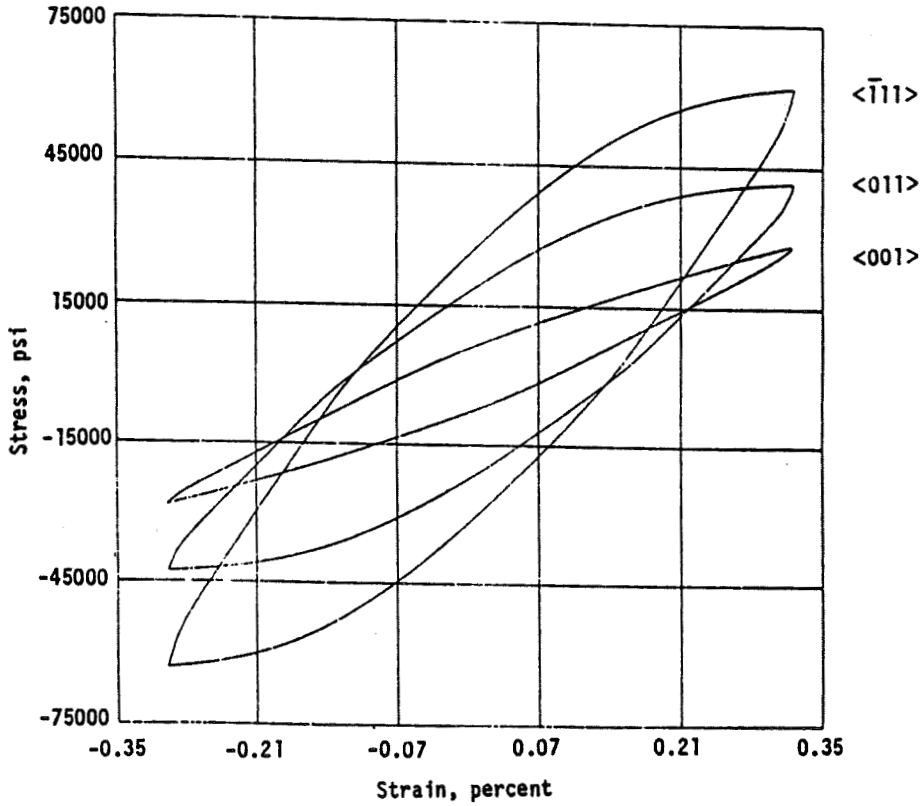

Figure 3-13 Octahedral Slip Predictions of Hysteresis Loops for PWA 1480 at 982°C (1800°F)

Figure 3-14 shows the corresponding predicted loops at a 10^{-3} per second strain rate in the [001], [011] and [111] directions using the cube slip formula. The same constants were used here for the cube slip response as were used for the octahedral response, simply to see the variation of cube slip constitutive response with direction. The material constants are clearly inappropriate but suffice to show that no inelastic response is predicted in the [001] direction. Even for large strain ranges, no inelastic response is predicted in the [001] direction due to the fact that the resolved shear stress r_{mn} is zero in each of the six slip directions when the bar specimen is pulled in the [001] direction. Clearly a mixture of octahedral and cube slip will improve the correlation between the theoretical model and the experimental results shown in Figures 3-12 and 3-13.

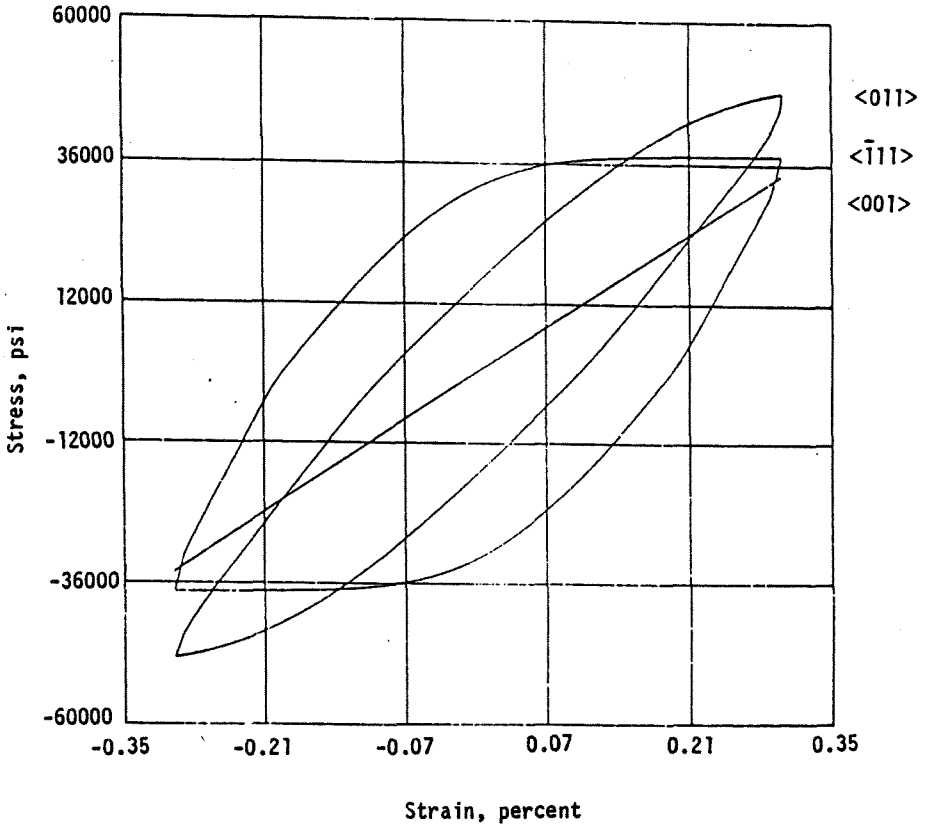

Figure 3-14 Cube Slip Predictions of Hysteresis Loops for PWA 1480 at 982°C (1800°F)

The octahedral slip formulation was used to predict the response during a tensile test at 982°C (1800°F) and 10^{-3} sec^{-1} strain rate. The results are presented in Figures 3-15 through 3-17.

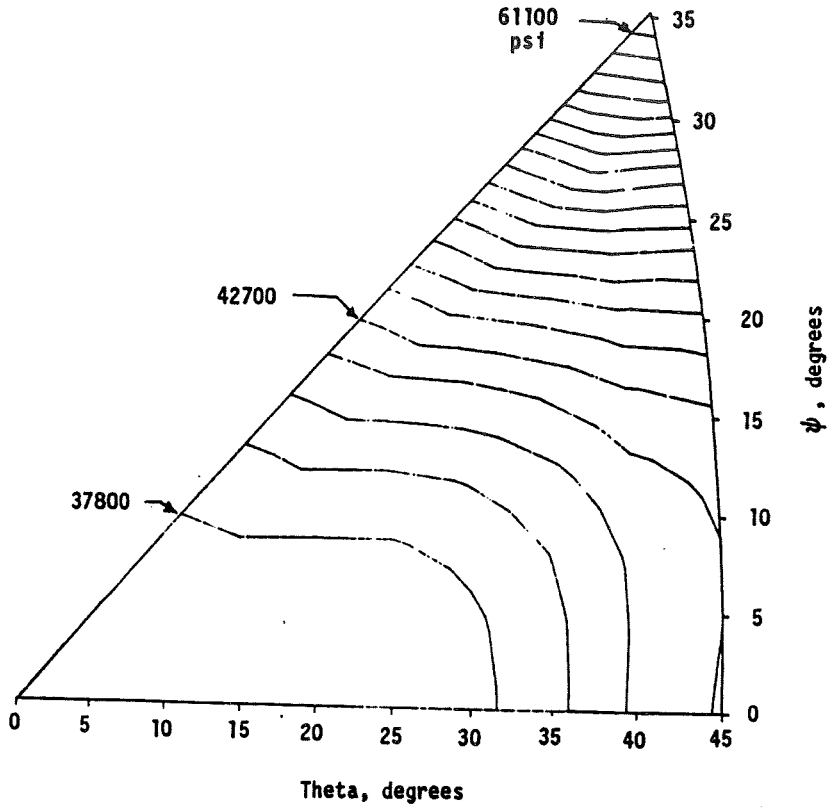

Figure 3-15 Stereographic Contours of Two-Tenths Yield Stress for PWA 1480 at 982°C (1800°F)

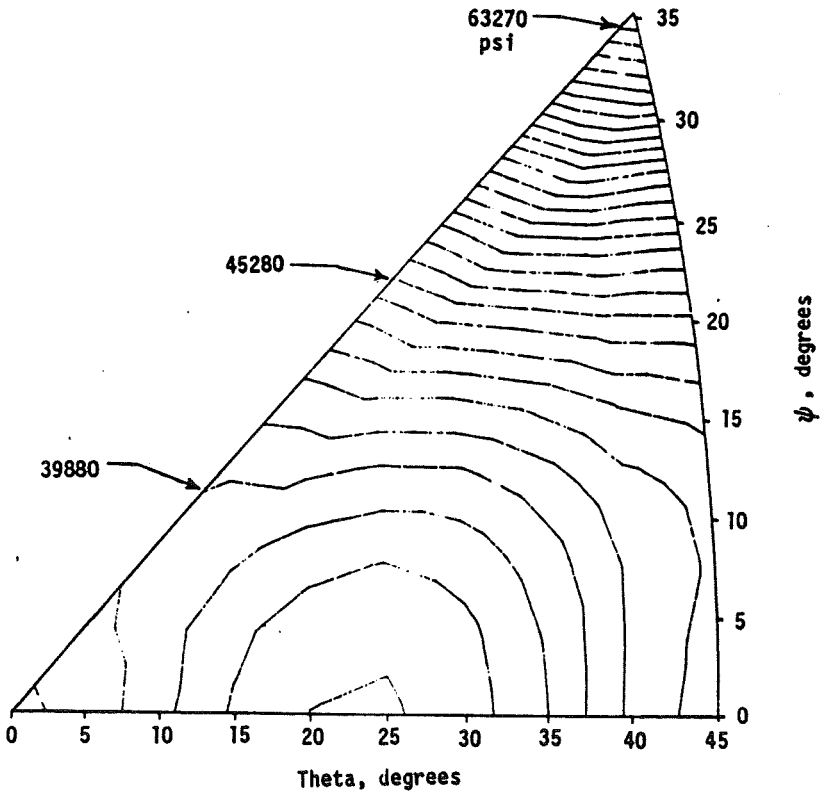

Figure 3-16 Stereographic Stress Contours at Two Percent Inelastic Strain

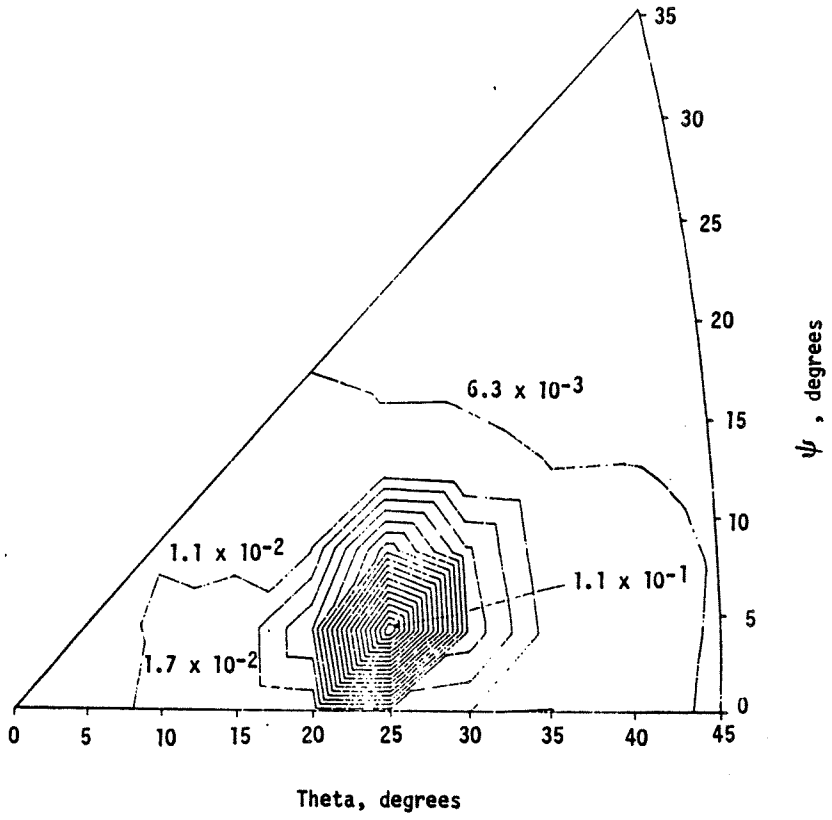

Figure 3-17 Stereographic Contours of Inelastic Strain at 50 ksi Stress

The stereographic contours of the two-tenths offset strain are shown in Figure 3-15, while Figure 3-16 depicts the stress contours at the large offset strain value of two percent. The two percent offset stress contours have an appearance which is similar to the variation of the octahedral Schmid stress over the [001], [011] and [111] stereographic triangle. When the inelastic strain contours corresponding to a load of 50,000 psi on the uniaxial bar specimen are plotted out in Figure 3-17, it is evident that they follow the Schmid stress variation exactly. This is to be expected since an octahedral slip theory is being used. However, at low values of the offset strain the contours do not follow the Schmid pattern since the state variables ω_r and K_r are in a growth phase. In Figure 3-18, the stress contours corresponding to a two-tenths offset strain are plotted for the cube slip model where it is evident that the stress values decrease from the [001] vertex, where the "yield" stress is infinite, towards the [111] vertex.

Further work will address the constitutive modeling of the 427°C, 760°C and 871°C (800°F, 1400°F and 1600°F) data using a mixture of octahedral and cube slip. Work is progressing under NASA grant NAG-512 to determine if the material constants can be obtained without the use of the COPES/CONMIN code. A symbolic computer algebra program called MUMATH, which operates on the IBM PC-X and Apple personal computers, is being employed for this work. If the material constants can be determined by this approach, the COPES/CONMIN code can be used to "fine-tune" these material constants. At present, the constants are simply guessed and fed to the COPES/CONMIN optimization code, which operates on the IBM PC-XT computer. If the guesses are not close to the optimum values, the optimization code will use a large amount of computer time in determining the material constants.

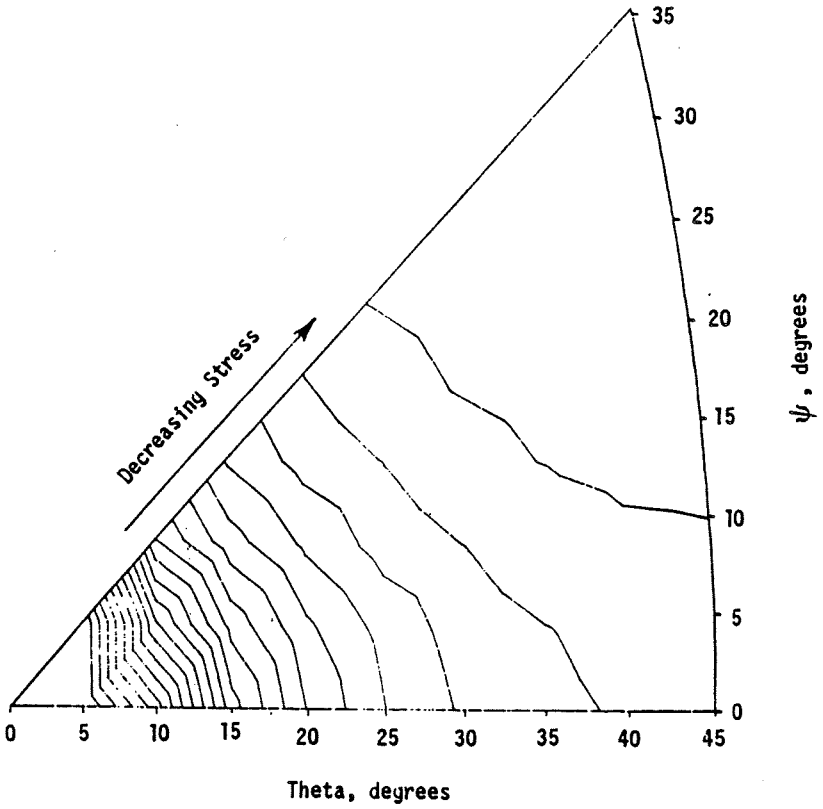

Figure 3-18 Stereographic Contours of Cube Slip Stress Corresponding to Two-Tenths Offset Strain

References - Section 3.0

1. Kraus, H., Creep Analysis, John Wiley & Sons, Inc., New York, Chapter 2, 1980.

2. Walker, K. P., "Research and Development Program for Nonlinear Structural Modeling with Advanced Time-Temperature Dependent Constitutive Relationships," NASA CR-165533, Nov. 1981.

3. Lindholm, U. S., et al, "Constitutive Modeling for Isotropic Materials (HOST)," NASA CR-174718, May 1984.

4. Moreno, V., "Development of a Simplified Analytical Method for Representing Material Cyclic Response," NASA CR-168100, Jan. 1983.

5. Stowell, E. Z., et al, "Predicted Behavior of Rapidly Heated Metal in Compression," NASA TR R-59, 1960.

6. Stowell, E. Z., "The Properties of Metals Under Rapid Heating Conditions," J. Aeron. Sci., pp. 922-923, Dec. 1957.

7. Stowell, E. Z., "A Phenomenological Relation Between Stress, Strain Rate, and Temperature for Metals at Elevated Temperature," NASA TR-R1343, Feb. 1957.

8. Hill, R., "A Theory of the Yielding and Plastic Flow of Anisotropic Metals," Proc. Royal Society of London, Ser. A, Vol. 193, pp. 281-297, 1948.

9. Shah, D. M. and Duhl, D. N., "The Effect of Orientation, Temperature and Gamma Prime Size on the Yield Strength of a Single Crystal Nickel Base Superalloy," Superalloys 1984, Ed. by M. Gell et al., Met. Soc. AIME, 1984.

10. Lee, D., Zaverl, F., Shih, C. F. and German, M. D., "Plasticity Theories and Structural Analysis of Anisotropic Metals," Report No. 77CRD285, General Electric Corporate Research and Development Center, Schenedtady, New York, 1977.

11. Walker, K. P., "Research and Development Program for Nonlinear Structural Modeling with Advanced Time-Temperature Dependence Constitutive Relationships," NASA CR-165533, November 1981.

12. Walker, K. P. and Jordan, E., "First-Annual Report on NASA Grant NAG-512," 1985.

13. Vanderplaats, G. N., NASA TM X-62, 282, 1973.

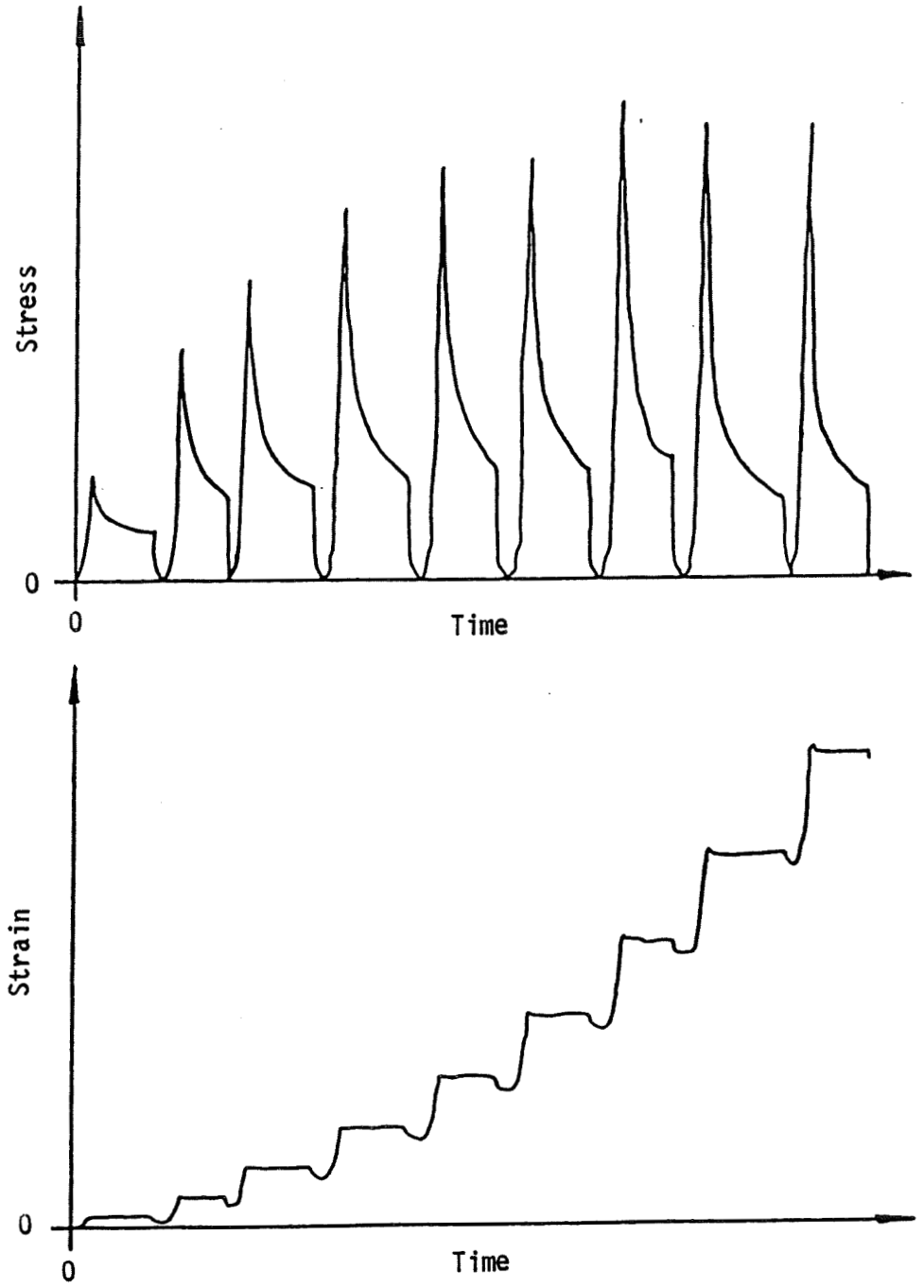

Figure 4-2 Typical Cyclic Relaxation Stress Strain Responses of PWA 286

PRECEDING PAGE BLANK NOT FILMED

4-1, 4-2

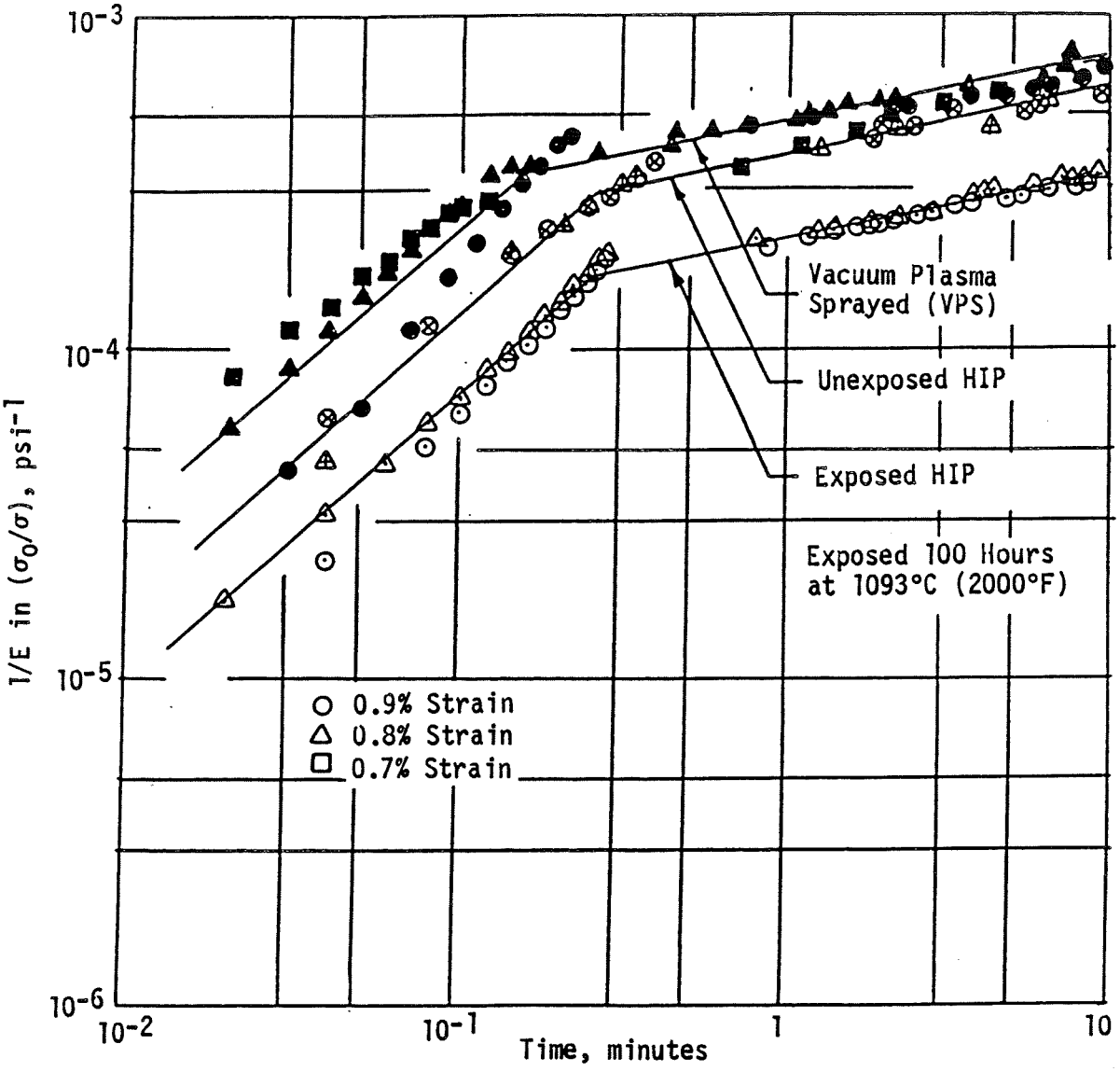

Figure 4-3 Short Time Creep Behavior of PWA 286 at 871°C (1800°F)

Table 4-I

Summary of Baseline Stress Relaxation Tests for PWA 286
NiCoCrAlY+Si+Hf Overlay Coating

Exposed ≡ 100 hours at 1093°C (2000°F)

Test Number	Virgin (V) or Exposed (E)	Temperature °C (°F)	HIP PWA 286	Low Plasma Spray PWA 286
1	V[1]	538 (1000)	X[2]	
2	V[1]	760 (1400)	X	
3	E	760 (1400)	X	
4	V[1]	871 (1600)	X	X
5	E	871 (1600)	X	X
6	V[1]	982 (1800)	X	X
7	E	982 (1800)	X	X
8	V	1038 (1900)	X	
9	E	1038 (1900)		X
10	V[1]	1093 (2000)	X	X

[1]Used for constitutive model evaluations
[2]Each "X" represents a single test specimen

Table 4-II

Summary of Baseline Constitutive Tests for PWA 273
Aluminide Diffusion Coating

Exposed ≡ 100 hours at 1093°C (1900°F)

Test Number	Virgin (V) or Exposed (E)	Temperature °C (°F)
1	V[1]	538 (1000)
2	V[1]	649 (1200)
3	V[1]	760 (1400)
4	E	760 (1400)
5	V[1]	871 (1600)
6	E	871 (1600)
7	V[1]	982 (1800)
8	V[1]	1093 (2000)
9	E	1093 (2000)

[1]Used for constitutive model evaluations
The tests will consist of either monotonic or cyclic waveforms. Specimen design is shown in Figure 2-9(A).

Model constants were determined for the unexposed PWA 286 overlay coating from stress relaxation tests run at 538, 760, 871, 982, and 1093°C (1000, 1400, 1600, 1800, and 2000°F) (see Appendix A). For the model discussions, 538°C (1000°F) and 982°C (1800°F) data are presented as being representative of the low and high temperature material response. PWA 273 diffusion coating baseline constitutive tests are pending.

4.1.1 Classical Model

$$\varepsilon_t = \varepsilon_e + \varepsilon_p + \varepsilon_c$$

$$\varepsilon_t = \frac{\sigma}{E} + \left(\frac{\sigma}{A_1}\right)^{A_2} + \left(\frac{\sigma}{A_3}\right)^{A_4} t$$

where: ε_t = total strain

ε_e = elastic strain

ε_p = plastic (time independent inelastic) strain

ε_c = creep (time dependent inelastic) strain

σ = stress

E = elastic modulus

t = time

A_1, A_2, A_3, and A_4 are constants.

Baseline data regressions for unexposed PWA 286 utilizing the classical model given above are presented in Figure 4-4. As expected, time independent plasticity dominates the inelastic response at lower temperatures, while creep dominates at higher temperatures. Figure 4-4 also indicates that some history dependence is required to accurately represent the observed isothermal cyclic hardening.

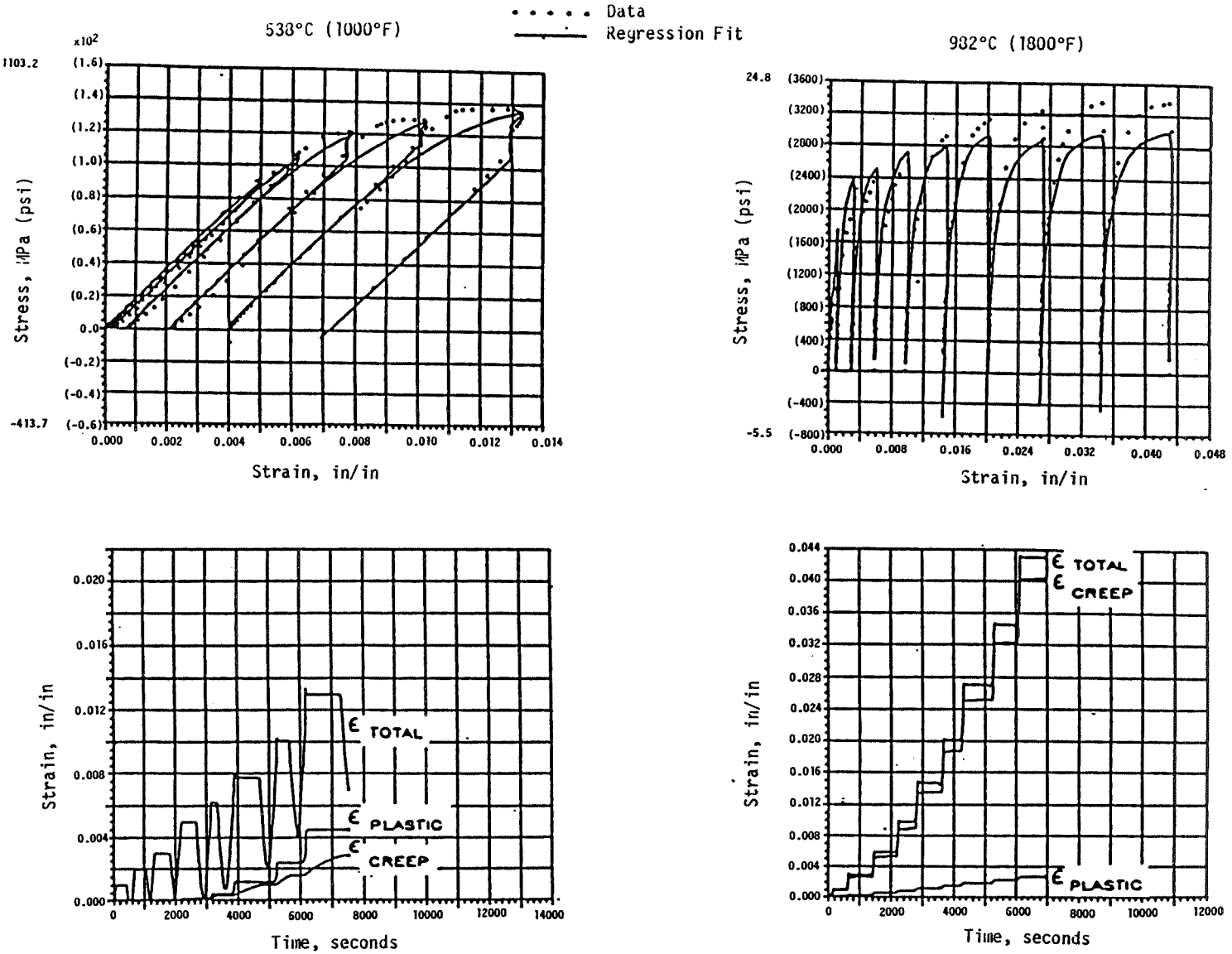

Figure 4-4 Classical Model Regression Fit of Unexposed PWA 286 Stress Relaxation Data

4.1.2 Walker Model

The one-dimensional form used to regress the baseline data was:

$$\dot{\varepsilon}_t = \dot{\varepsilon}_e + \dot{\varepsilon}_{in}$$

$$\dot{\varepsilon}_{in} = \left(\frac{\sigma - \Omega}{K}\right)^n$$

$$K = K_1 - K_2 \exp(-n_7 R)$$

$$\Omega = n_1 \varepsilon_{in} + \Omega_2$$

$$\dot{\Omega}_2 = n_{11} \dot{\varepsilon}_{in} - \Omega_2 \left(\dot{G}_2 - \frac{1}{n_{11}} \frac{\partial n}{\partial \theta} \dot{\theta}\right)$$

$$\dot{G}_2 = n_g \dot{R} + n_{10} \Omega_2^{(m_{0-1})}$$

$$\dot{R} = \left|\dot{\varepsilon}_{in}\right|$$

where: ε_{in} = inelastic strain

$\dot{\varepsilon}_{in}$ = inelastic strain rate

Ω = back stress

K = drag stress

R = effective inelastic strain

$\dot{R}$ = effective inelastic strain rate

n, n_1, n_7, n_9, n_{10}, n_{11}, K_1, K_2, and m_0 are constants.

The two back stress terms (Ω_1 and Ω_2) of the Walker model (Table 3-I) are mathematically similar; therefore, it was felt that one of the terms could be eliminated. A study was conducted to determine the regression capability using Ω_1 and Ω_2 together and separately. The results, presented in Figures 4-5 through 4-7, indicate that no regression capability is lost if either one of the back stress terms were dropped. This is also indicated by the standard deviations of the regressions which are provided in the lower right-hand corner of each figure. Since the Ω_1 term contains more constants than the Ω_2 term, that term was eliminated.

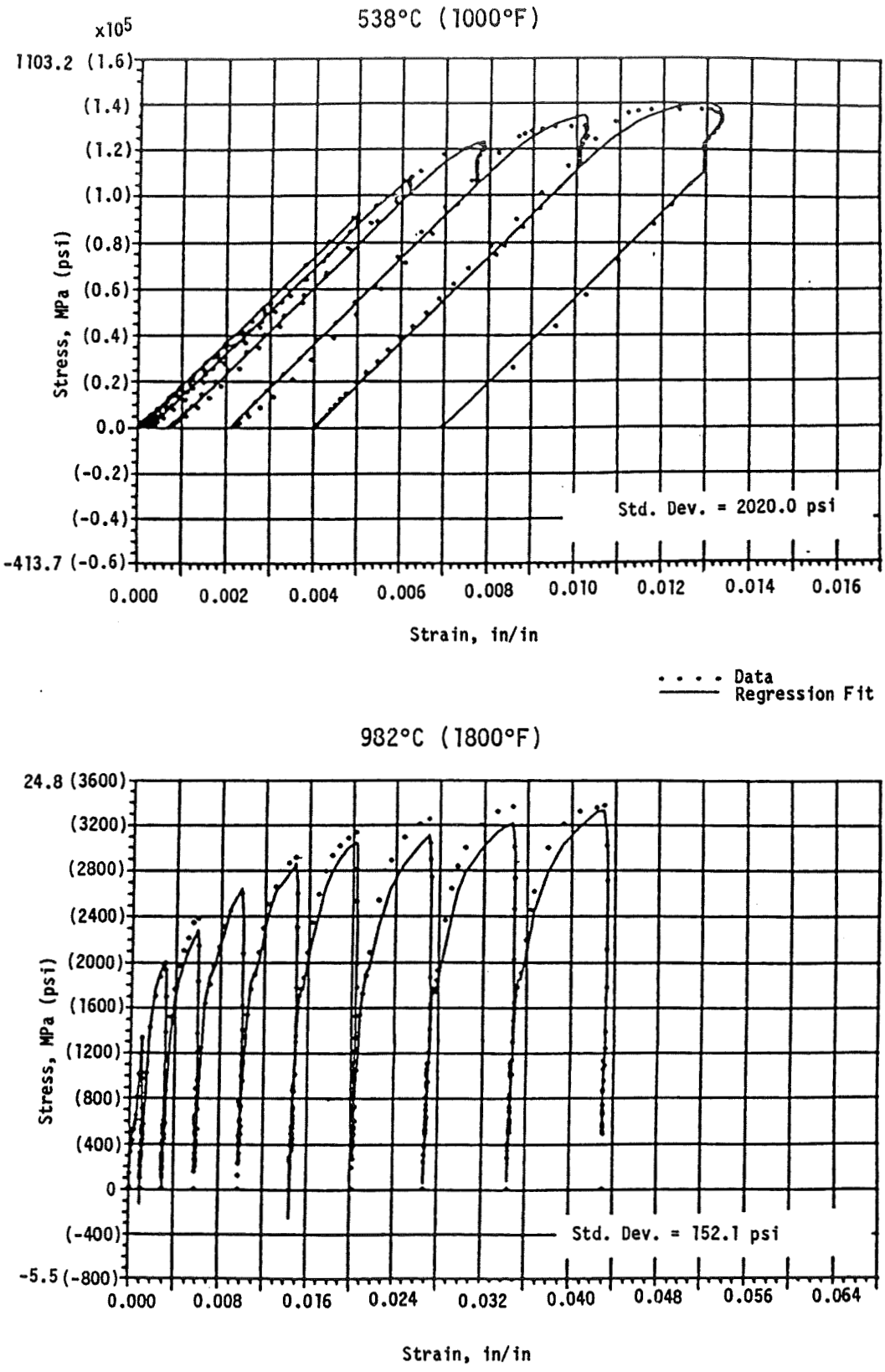

Figure 4-5 Walker Model Regression Fit of Unexposed PWA 286 Stress Relaxation Data Using Ω_1 and Ω_2 Back Stress Terms

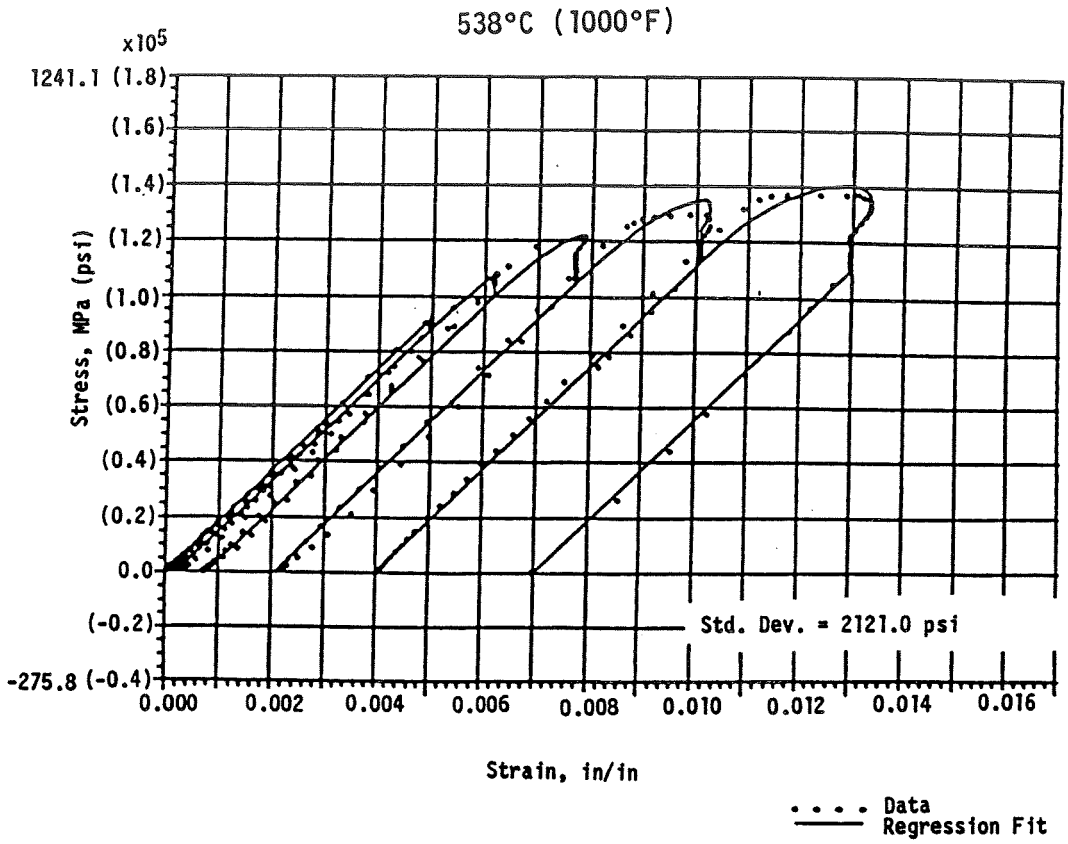

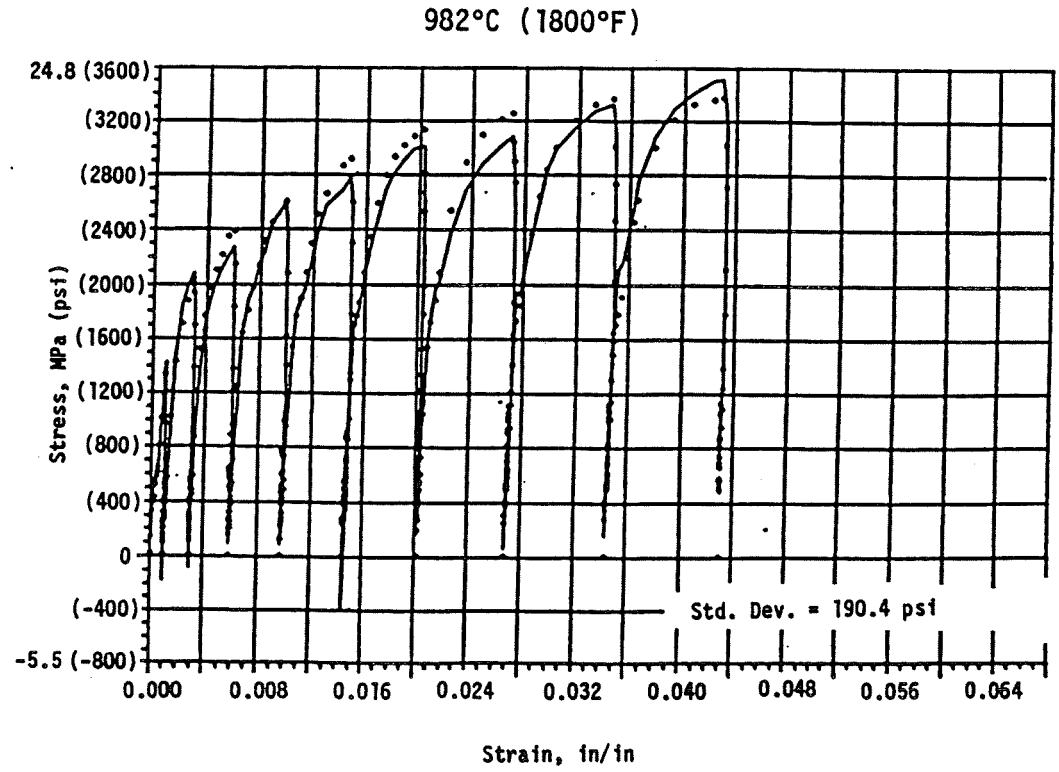

Figure 4-6 Walker Model Regression Fit of Unexposed PWA 286 Stress Relaxation Data Using Ω_1 Back Stress Terms Only

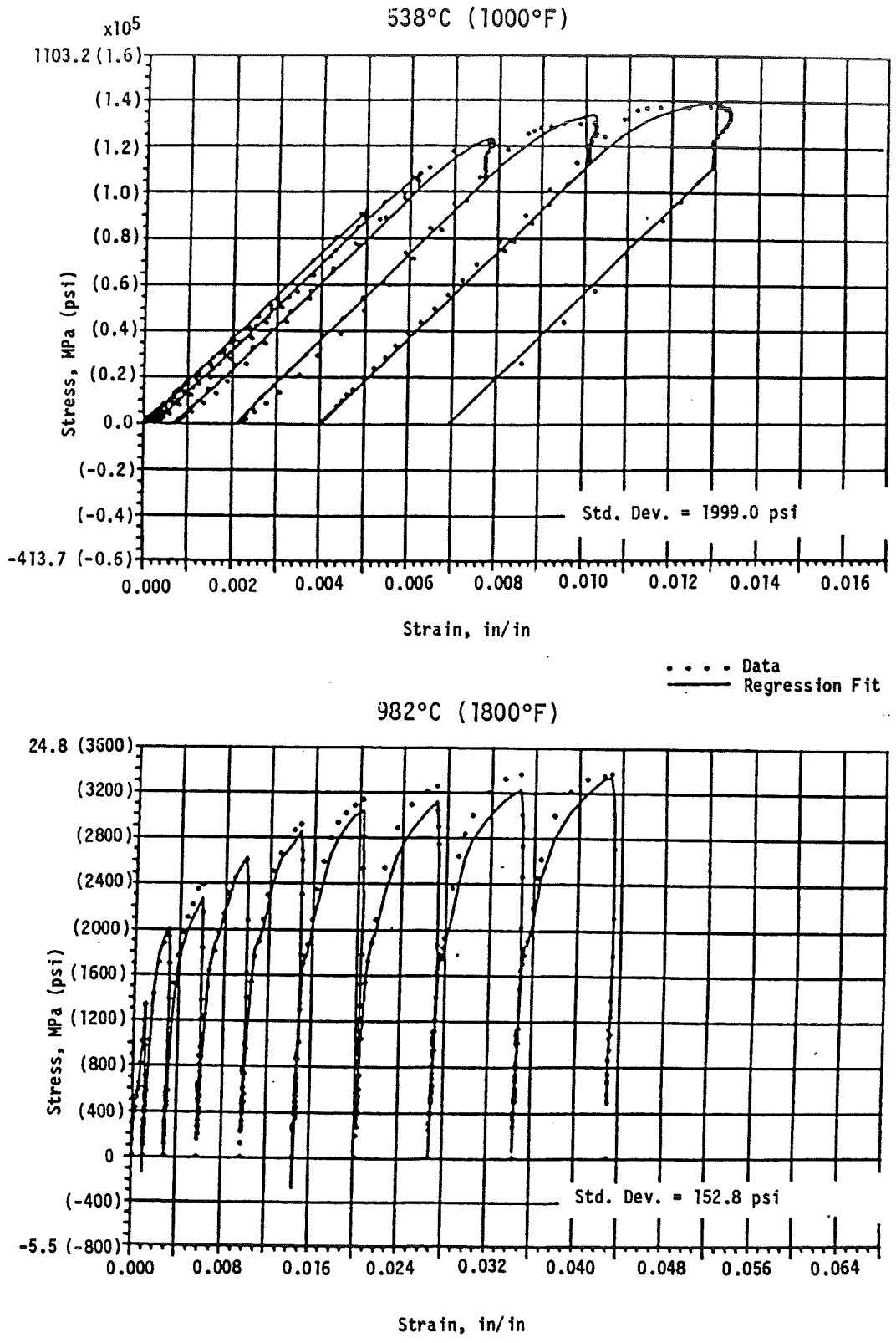

Figure 4-7 Walker Model Regression Fit of Unexposed PWA 286 Stress Relaxation Data Using Ω_2 Back Stress Terms Only

4.1.3 Simplified Walker Model

$$\varepsilon_t = \varepsilon_e + \varepsilon_{in}$$

$$\dot{\varepsilon}_{in} = \left(\frac{\sigma}{K}\right)^n$$

$$K = K_1 - K_2 \exp(-n_7 R)$$

$$\dot{R} = |\dot{\varepsilon}_{in}|$$

The above term descriptions are the same as for the Walker model (see Section 4.1.2).

Figure 4-8 presents the regressions using the Simplified Walker model. Clearly, no gross reduction of regression capability is produced by ignoring back stress.

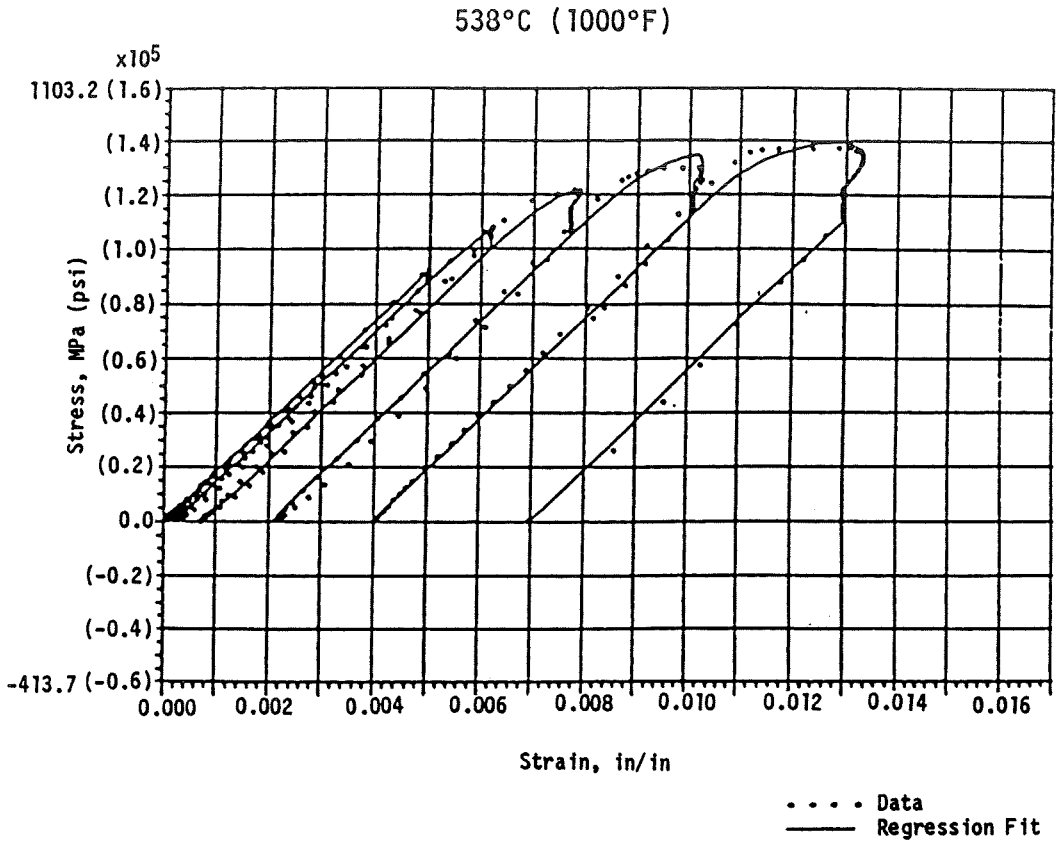

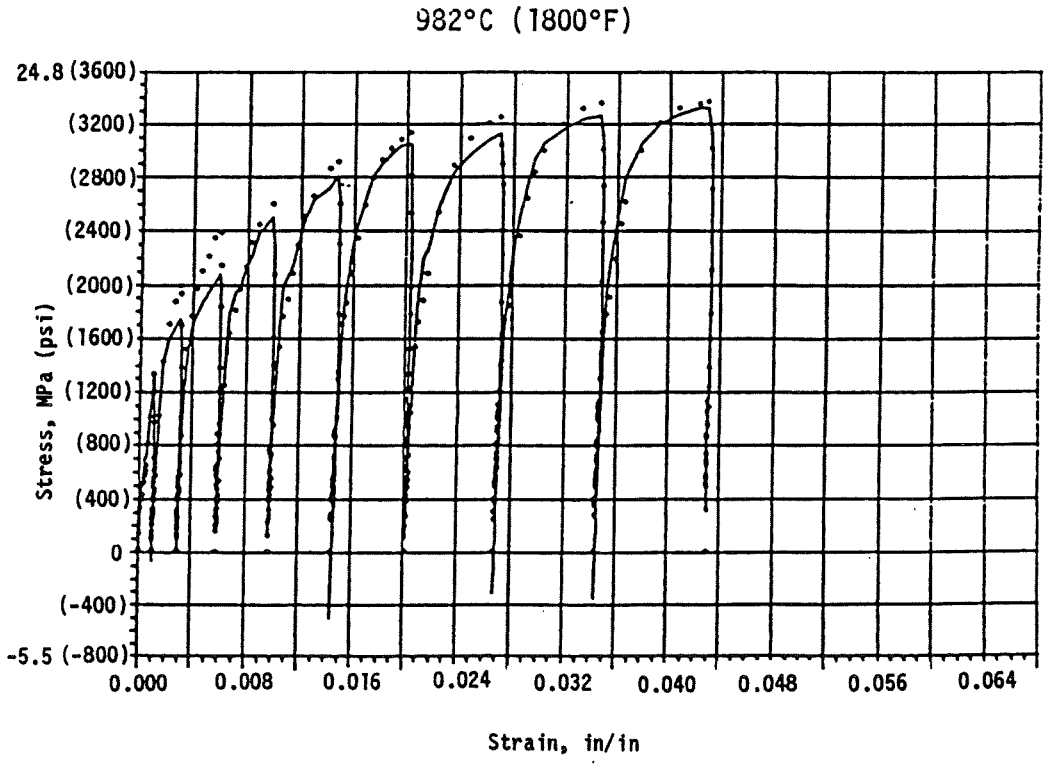

Figure 4-8 Simplified Walker Model Regression Fit of Unexposed PWA 286 Stress Relaxation Data

4.1.4 Simplified Unified Approach

For $\sigma < \sigma_{yi}$,

$$\varepsilon_t = \varepsilon_e + \varepsilon_c$$

$$\varepsilon_t = \frac{\sigma}{E} + A\,\sigma^B\,t$$

For $\sigma_i = \sigma_{yi}$,

$$\Delta\sigma_{plastic} = \sigma_{yi+1} - \sigma_{yi} \text{ ; for } T_{i+1} \geq T_i$$

$$\Delta\sigma_{plastic} = \frac{E_{pi+1} + E_{pi}}{2}\,\Delta\varepsilon_t \text{ ; for } T_{i+1} < T_i$$

where: $\Delta\sigma_{plastic}$ = time independent plastic stress increment

σ_y = yield stress

E_p = strain hardening slope of monotonic σ/ε curve

$\Delta\varepsilon_t$ = total strain increment

A, B are constants

subscripts: i = beginning of increment

i + 1 = end of increment

The Simplified Unified Approach model has not yet been regressed because it is felt that the model cannot adequately represent the baseline isothermal tests. Unlike Hastelloy X, significant isothermal cyclic hardening/softening was observed in PWA 286. Regression of this model is pending evaluation of nonisothermal tests. If those tests indicate that the net cyclic hardening/softening is insignificant, the model will be re-evaluated.

4.1.5 Stowell Model

$$\dot{\varepsilon}_t = \dot{\varepsilon}_e + \dot{\varepsilon}_{in}$$

$$\dot{\varepsilon}_{in} = 2sT \exp\left(\frac{-\Delta H}{RT}\right) \sinh\left(\frac{\sigma}{\sigma_o}\right)$$

where: ΔH = apparent activation energy

T = absolute temperature (°K or °R)

R = gas constant (2 cal/mole.°K or 1545 ft.lb/lb_m-mole.°R)

S, σ_o are constants

The baseline regression data fits using the Stowell model are presented in Figure 4-9. Note that, at 538°C (1000°F), the model is unable to duplicate the observed yielding during loading. This suggests that yielding at low temperature is a nondiffusion process which the Stowell model is not well formulated to correlate.

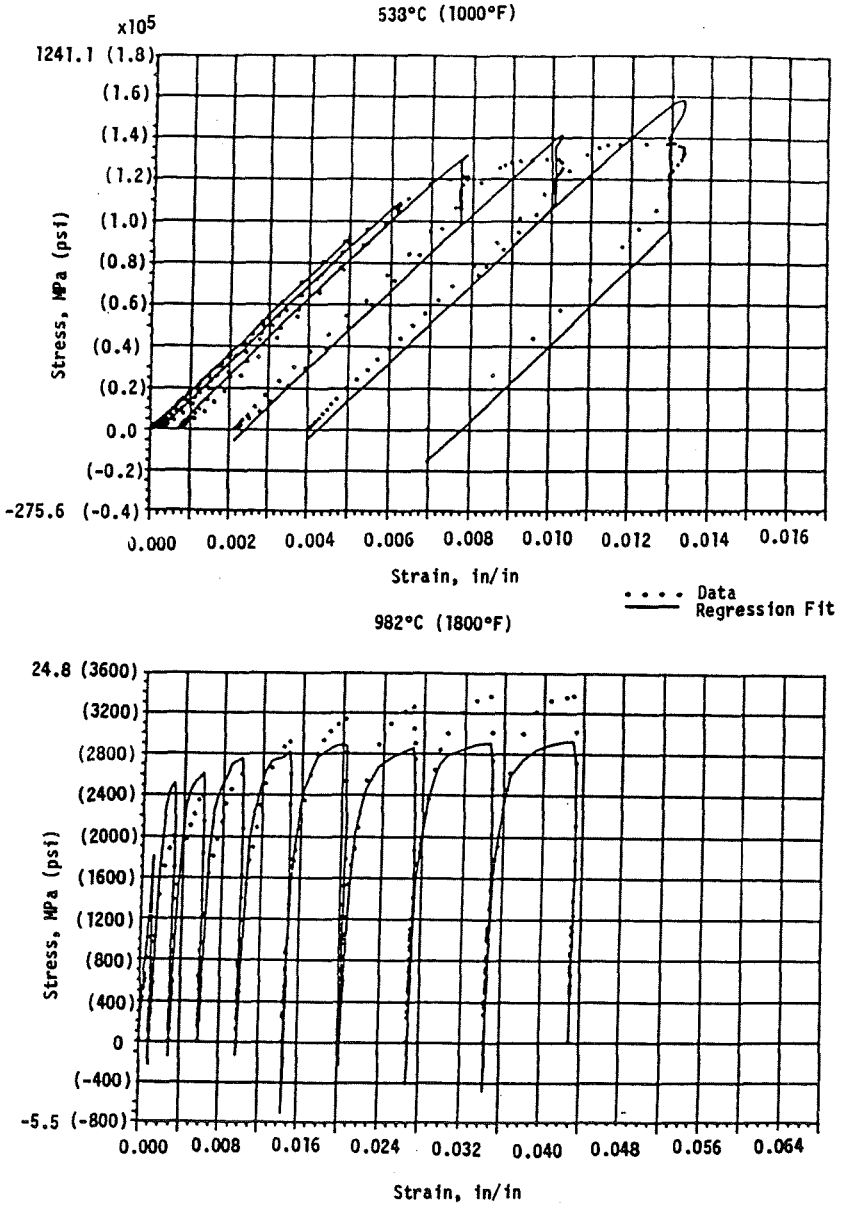

Figure 4-9 Stowell Model Regression Fit of Unexposed PWA 286 Stress Relaxation Data

4.1.6 Summary

Each model considered was regressed on a consistent basis utilizing a computer automated regression system. The standard deviation between the regressed model and the data is used to quantify the regression capability of the model. A constitutive model summary for unexposed PWA 286 is presented in Table 4-III. The results indicate that the various models essentially compare as presented in Figure 3-1.

Table 4-III

Summary of Unexposed PWA 286 Coating Constitutive Models

	Finite Element Code[1]			Standard Deviation of Baseline Data Regressions[2] Temperature °C (°F)				
Model	Speed	Availability	Similar to Substrate	538 (1000)	760 (1400)	871 (1600)	982 (1800)	1093 (2000)
Classical		X		3147.0	1866.0	748.5	310.0	128.0
Walker		X	X	1999.0	1815.0	633.4	152.8	100.7
Simplified Walker	X	X	X	2041.0	1717.0	876.1	220.4	118.5
Simplified Unified Approach	X			-	-	-	-	-
Stowell	X			6521.0	2091.0	1044.0	376.9	139.5

[1] Anticipated finite element code qualities
[2] 1σ; expressed in psi

4.1.7 Future Work

In the remaining period of this task, additional testing, both isothermal and nonisothermal, will be conducted to acquire information for:

1. verification of PWA 286 coating constitutive models, and
2. regression and verification of PWA 273 coating constitutive models. and

4.2 Single Crystal Airfoil Material Constitutive Tests

Cyclic constitutive tests are being conducted on uncoated primary single crystal material (PWA 1480) to develop appropriate constitutive models for turbine airfoil applications. Specimens have been oriented in four crystallographic directions: <100>, <110>, <123>, and <111>. The specimen shown in Figure 2-7(B) has been used for all cyclic tests. To date all cyclic tests have been isothermal push-pull type, completely reversed strain cycles. Each test condition uses a controlled constant strain rate.

Three basic types of constitutive data are being obtained:

1) stabilized hysteresis loops obtained for several different strain ranges;

2) strain rate sensitivity data; and

3) creep and relaxation behavior obtained during hold periods at various points on a given hysteresis loop.

A typical strain rate sensitivity test is illustrated in Figure 4-10. Figures 4-11 and 4-12 show results of a typical test in which creep and relaxation data are obtained. Figure 4-11 shows the locations on the hysteresis loop at which hold periods are imposed. Figure 4-12 shows the decay in the load or strain during each of the hold periods. The "negative" stress relaxation, shown in the curves A and E, was commonly observed in tests to date. This occurs when the stress level is lower than the back stress. After each hold period, the cycling is continued until the hysteresis loop again stabilizes. In all tests to date, the loop stablized to its prior shape after only a few cycles.

Figures 4-10 through 4-12 are the analog traces taken during testing. The data are also being recorded digitally throughout the testing so that virtually every loop and hold period is retrievable for analysis. Appendix E shows a sample of the digital data for a typical test.

A total of 15 cyclic constitutive tests have now been completed. The specimen numbers of tests at each temperature and orientation are summarized in Table 4-IV.

Table 4-IV

Tests Completed as of December 31, 1984

Temperature - °C (°F)

Orientation	427 (800)	760 (1400)	871 (1600)	982 (1800)
<100>	JA61	JA44		JA66
<110>	KA27	KA26		KA22
<111>	LA66	LA67, LA63	LA68	LA64, LA69
<123>	MA26	MA25		MA23

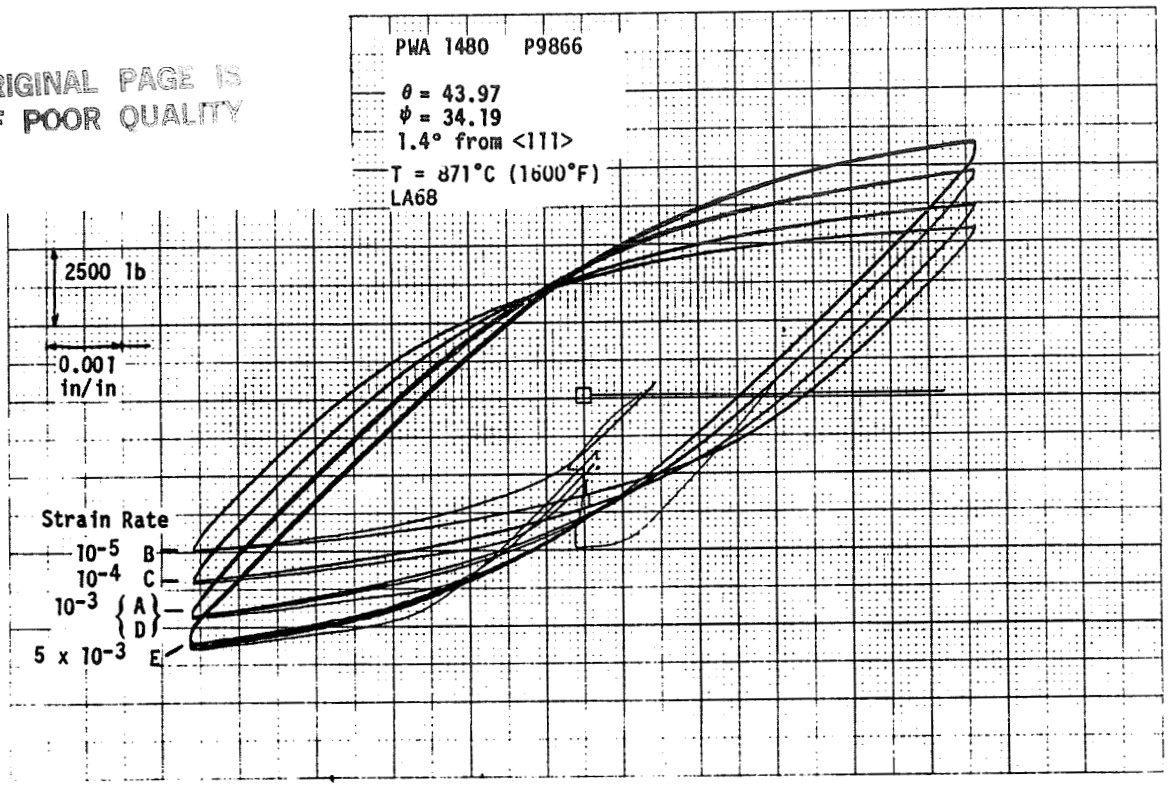

Figure 4-10 Typical Strain Rate Sensitivity Test

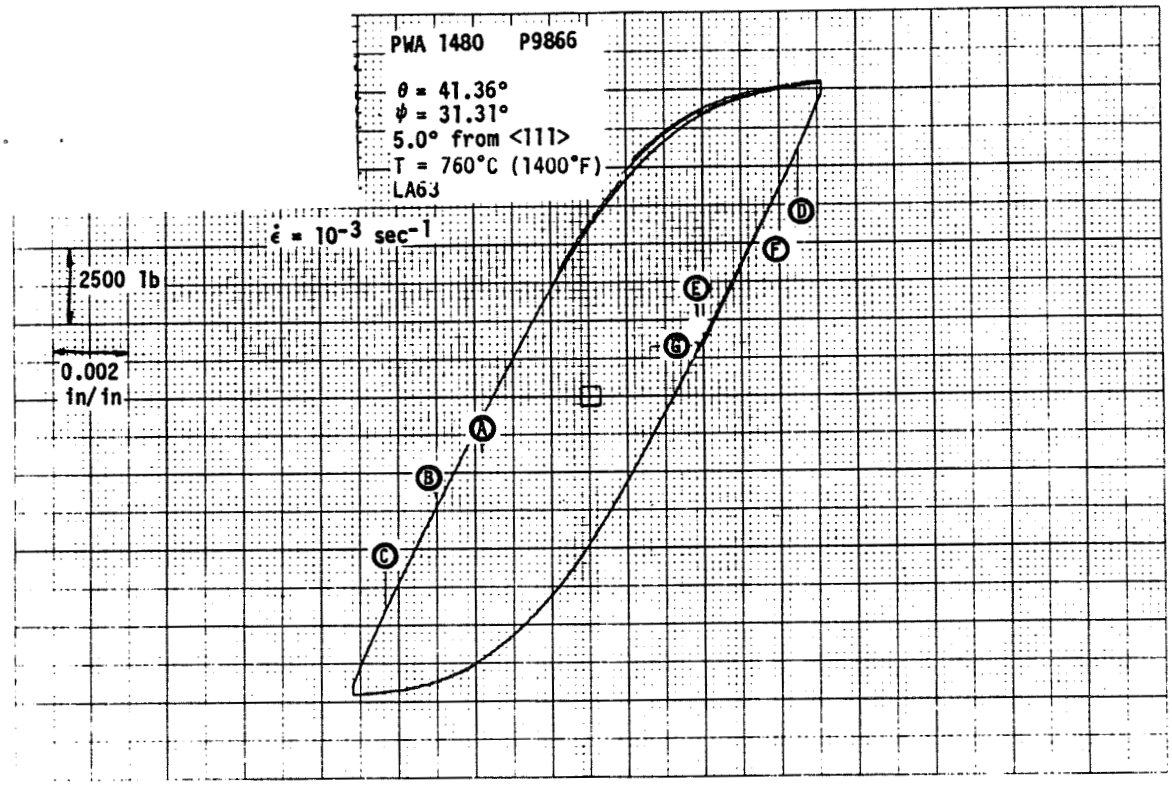

Figure 4-11 Typical Locations on a Hysteresis Loop at Which Relaxation and Creep Data are Obtained

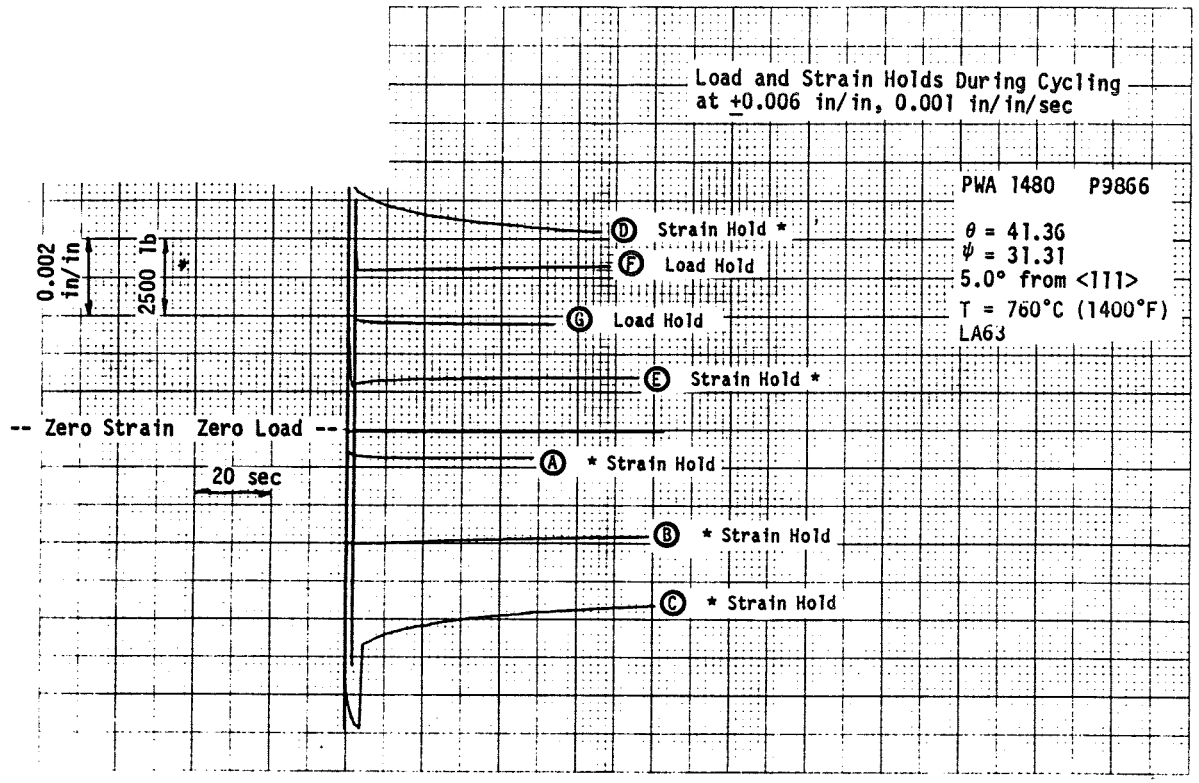

Figure 4-12 Typical Relaxation and Creep Data at Various Points on a Hysteresis Loop

Appendix D presents a detailed list of the loading history for each specimen. The test conditions are presented in the order in which they occurred.

The cyclic stress strain data are being reviewed to provide a general characterization of the material behavior which can serve as a guide to model development and the remaining tests. The general trends observed to date are discussed below.

Figures 4-13 and 4-14 show typical hysteresis loops for all four crystal orientations at 982°C and 427°C (1800°F and 800°F) respectively. The strain rate shown here is 10^{-3} in/in/sec. A strong orientation dependence is obvious at both temperatures. In general, the amount of inelasticity is seen to increase for orientations further away from the crystal axes, <100>. At 982°C (1800°F) the <110> and <123> specimens have nearly identical hysteresis loop shapes. These two orientations also have the same apparent modulus (i.e., $1/S'_{33}$ where S'_{33} is the component of the compliance matrix relating the stress and strain in the tensile direction); therefore, the inelastic portions of their response should be nearly identical. Construction of a stress-inelastic strain curve for the 982°C (1800°F) test, Figure 4-15, shows

this to be true. Figure 4-15 was obtained from a classical cyclic stress-strain curve which joins the tips of the stabilized hysteresis loops for various strain amplitudes. The cyclic stress strain curves for the 982°C (1800°F) tests are shown in Figure 4-16. The apparent modulus values used were taken from the elastic region of the first loading portion of each test. Figure 4-14 shows that at 427°C (800°F), the <110> and <123> orientations do not display such a close similarity as was observed at 982°C (1800°F). This is shown more dramatically in the stress-inelastic strain plot of Figure 4-17.

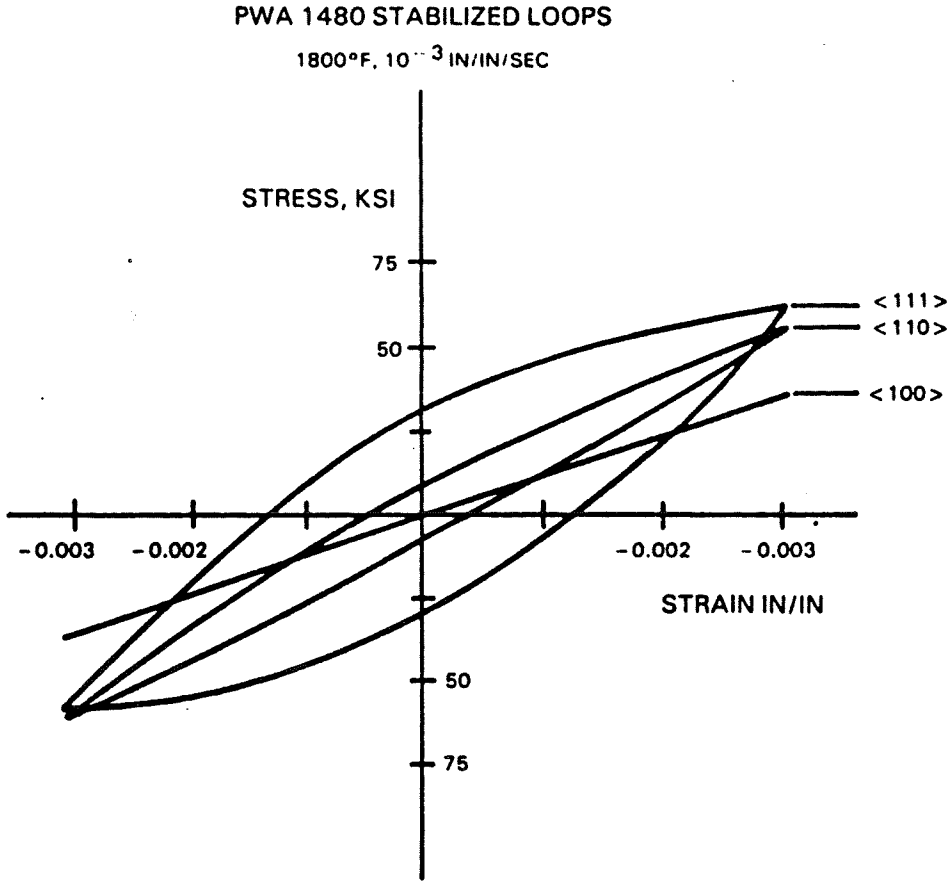

Figure 4-13 Orientation Dependence at 982°C (1800°F)

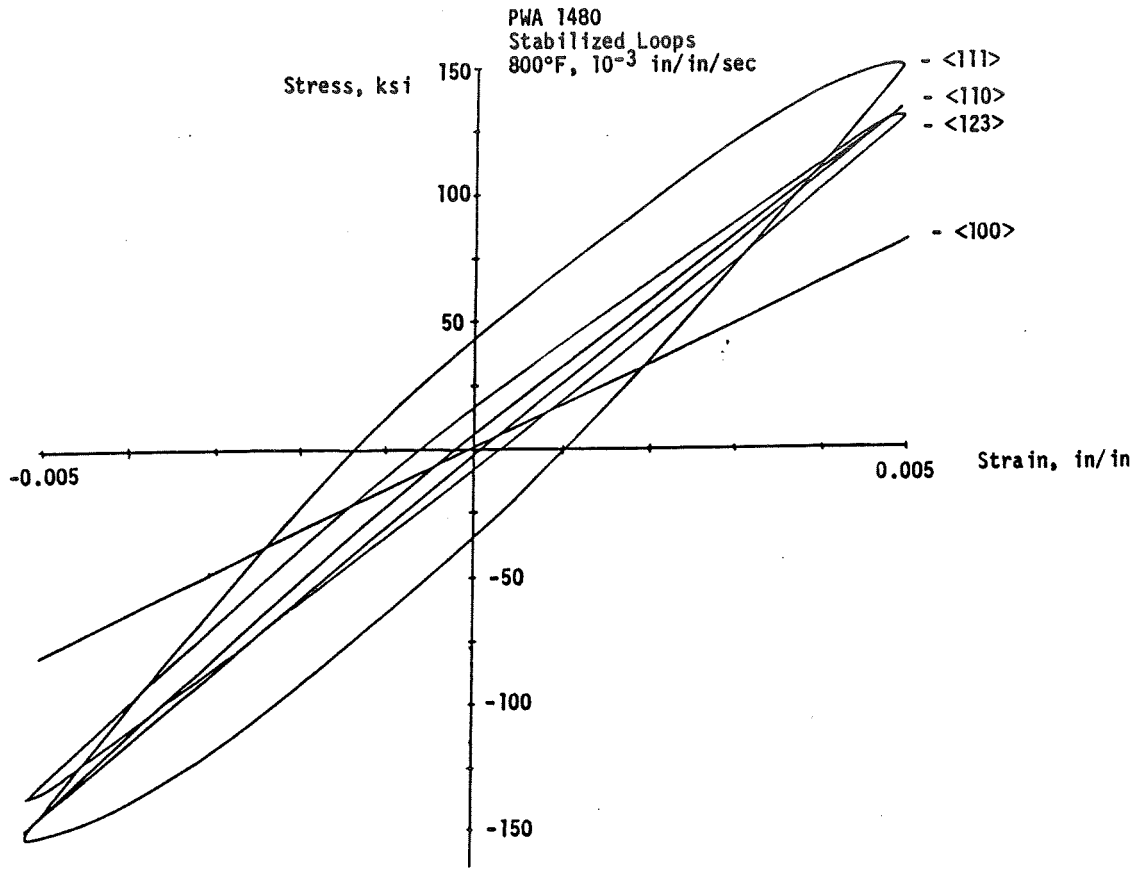

Figure 4-14 Orientation Dependence at 427°C (800°F)

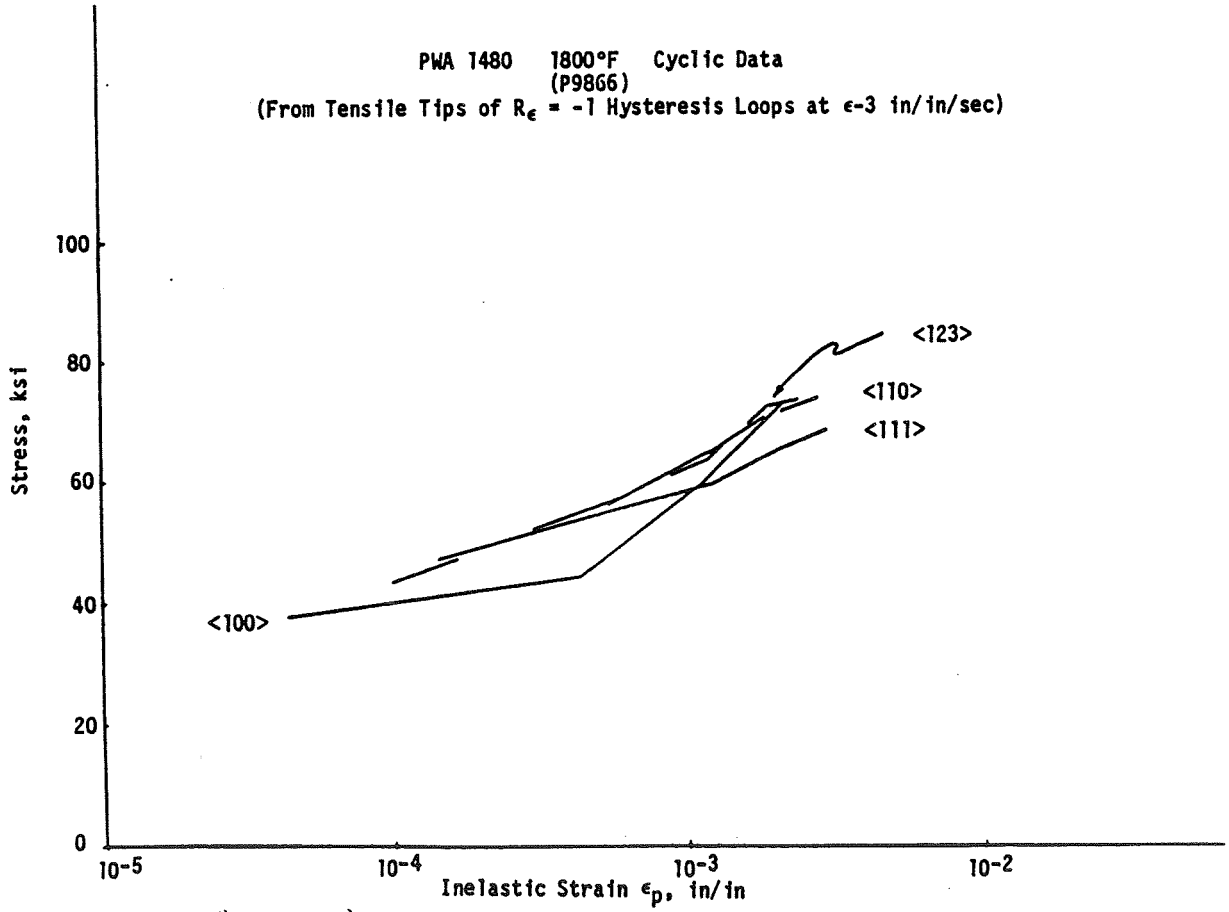

Figure 4-15 982°C (1800°F) Stress Versus Inelastic Strain from Cyclic Stress-Strain Curve

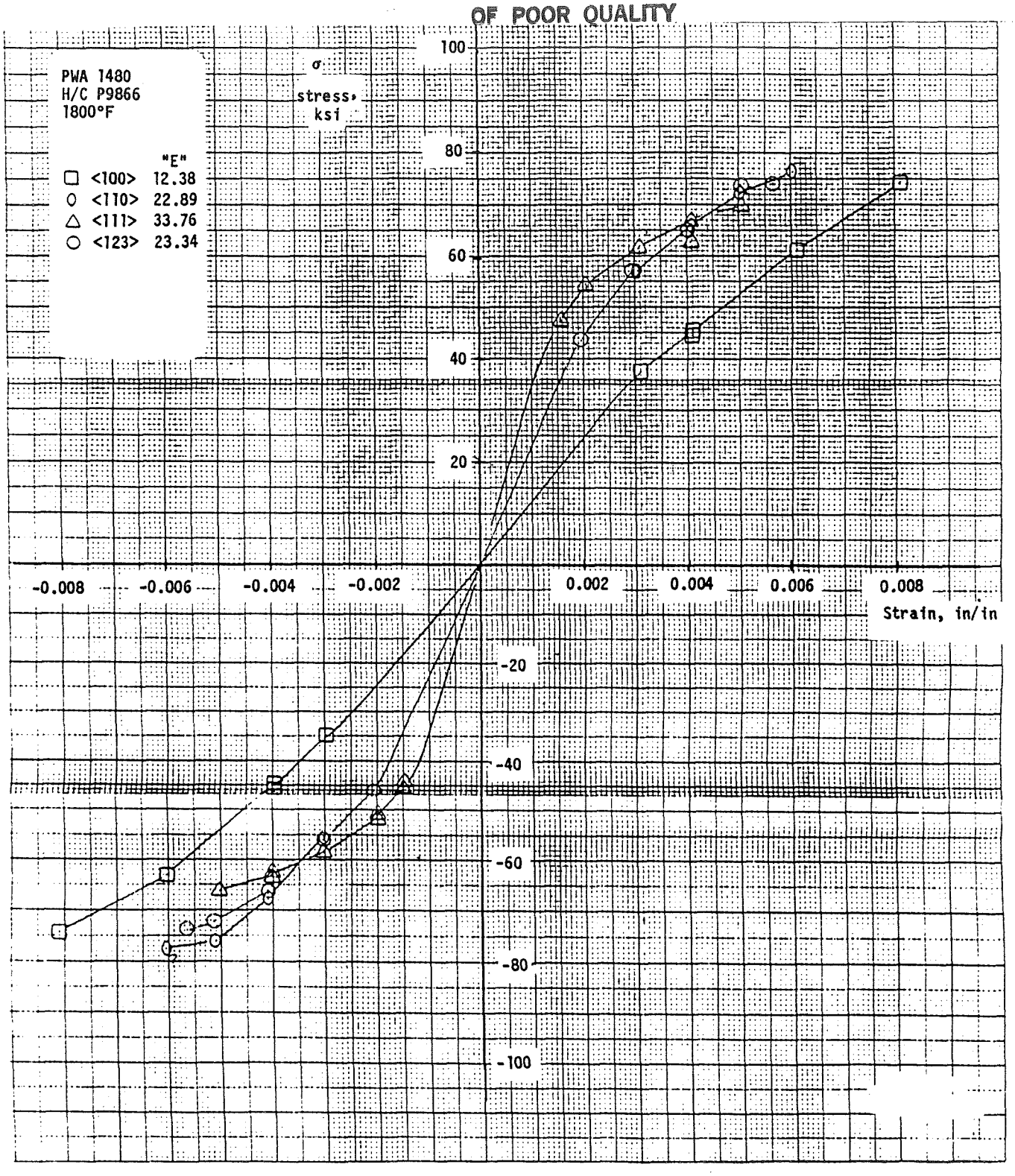

Figure 4-16 Cyclic Stress-Strain Curve at 982°C (1800°F) Constructed of Tips of R_ε: -1 Hysteresis Loops at 10^{-3} in/in/sec

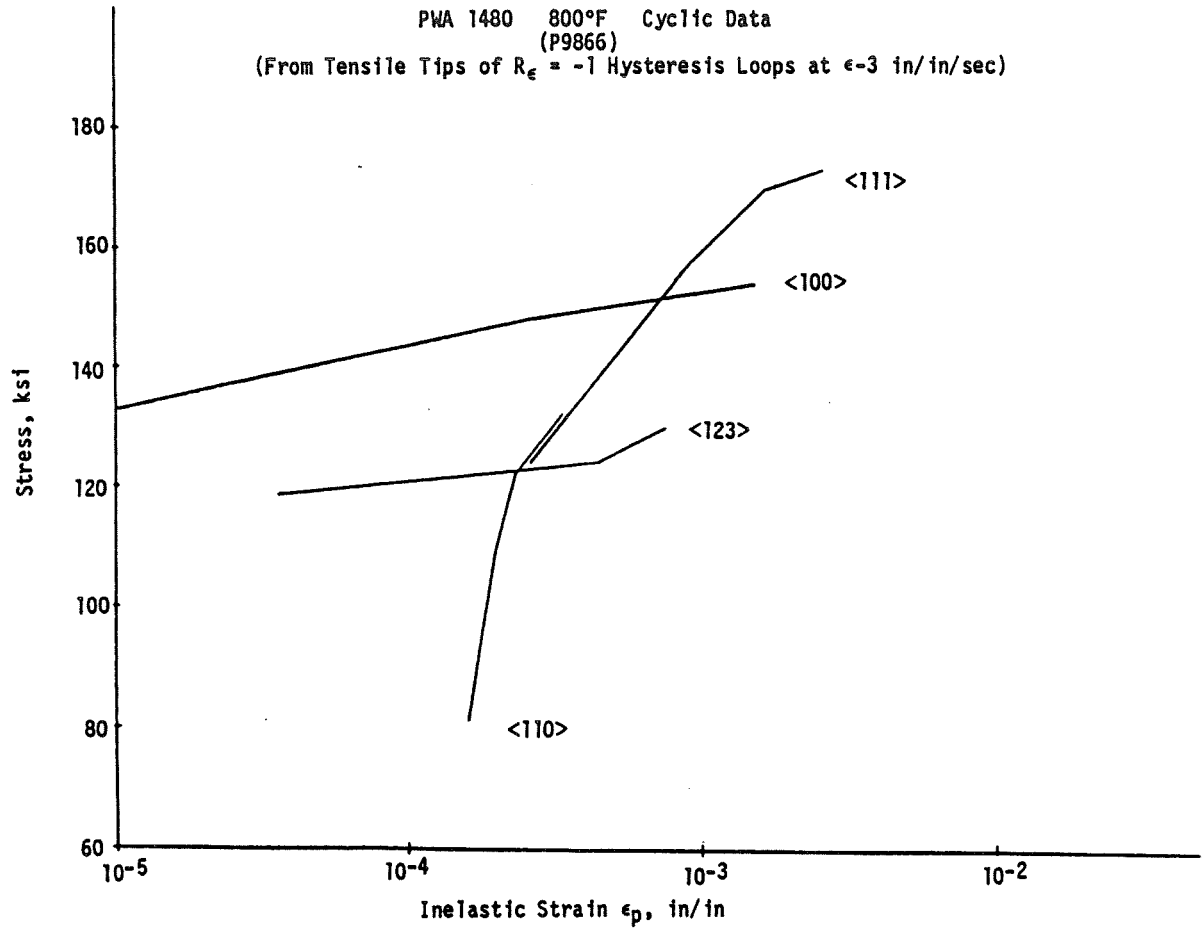

Figure 4-17 Stress Versus Inelastic Strain Curve from Cyclic Stress-Strain Curve

In general it was observed that the orientation dependence diminishes at higher temperature. This is consistent with the notion that noncrystallographic, thermally activated processes dominate at elevated temperatures. Another manifestation of the decreased sensitivity to orientation at elevated temperatures was the behavior of the specimens on initial loading compared to the stabilized behavior. At 427°C and 760°C (800°F and 1400°F) slip bursts were observed during the initial cycles of loading as illustrated in Figure 4-18. This effect was not observed at 982°C (1800°F). The effect was most apparent in the <110> and <123> specimens. These orientations have fewer highly loaded slip systems than do the <100> and <111> specimens so that slip is more likely to be concentrated.

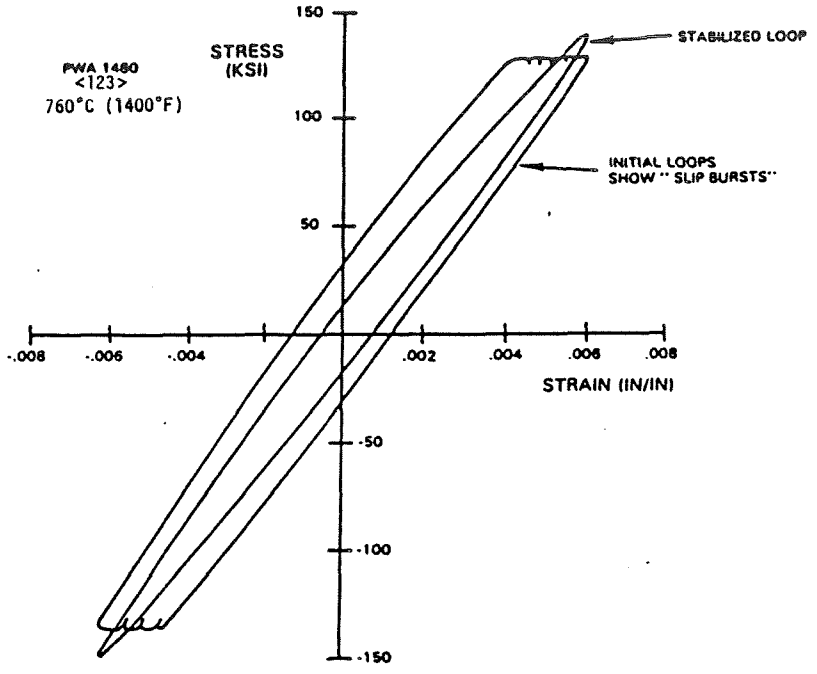

Figure 4-18 Cyclic Hardening Response

The slip bursts are observed at both tensile and compressive ends of the loop. (This behavior is not unlike the Portevin-LeChatelier effect frequently observed in superalloys.) Upon loading in either tension or compression, a critical stress is reached at which the material slips very rapidly. When the material slip burst strain rate is faster than the controlled strain rate at which the test is being conducted, the applied load is reduced until the controlled strain rate is again achieved. This results in the small bumps or serrations in the loop as shown in Figure 4-18. In general, the stress at which these slip bursts occur increases with each subsequent cycle so that a "hardened", stabilized hysteresis loop is achieved after several cycles. The "hardening" is manifested as both an increased stress range and a decreased inelastic strain range (loop width at zero stress). Specimens showing this behavior also show easily observable macroscopic slip bands on the gage section.

The tests conducted to date included an evaluation of strain rate sensitivity with emphasis placed on the higher temperature tests. Figure 4-19 shows the 982°C (1800°F) strain rate sensitivity as measured by the stress amplitude for a given strain range. The data have been normalized to the stress amplitude observed at 10^{-3} in/in/sec. It is clear that the rate dependence is a function of orientation and strain amplitudes, with the effect being more pronounced for higher strain amplitudes and deviation of the <100> orientations. Similarly, the tension-compression assymetry at 982°C (1800°F) was found to be rate dependent and also a function of orientation and strain amplitude as shown in Figure 4-20. In the limits of elastic loading there should be no orientation or strain amplitude dependence. It should be noted that in all the tests to date, the initial loading was compressive. Future tests will include load cycles which produce tensile yielding first.

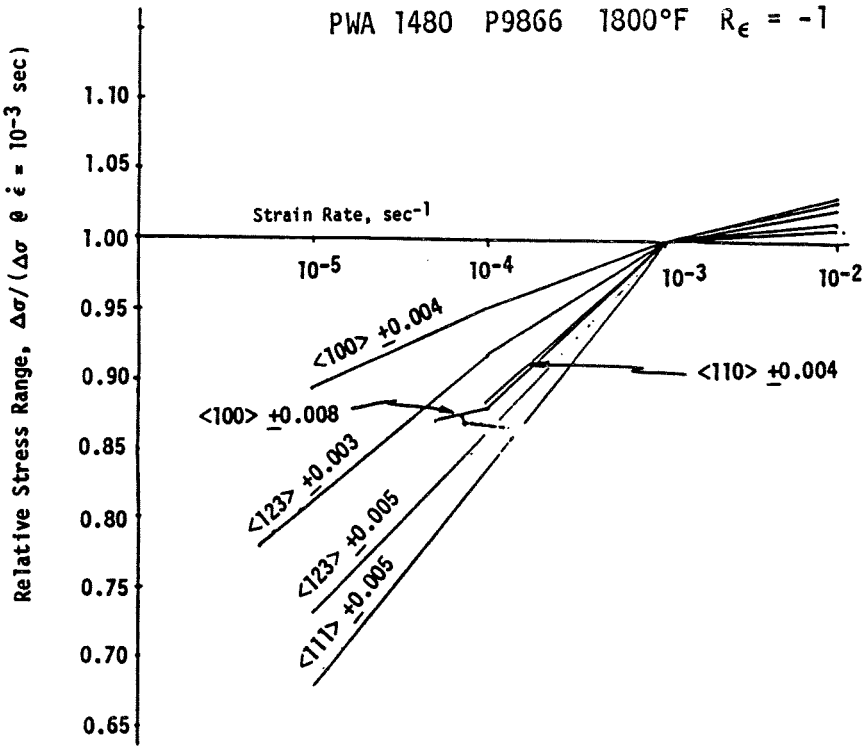

Figure 4-19 Stress Range Dependence on Strain Rate

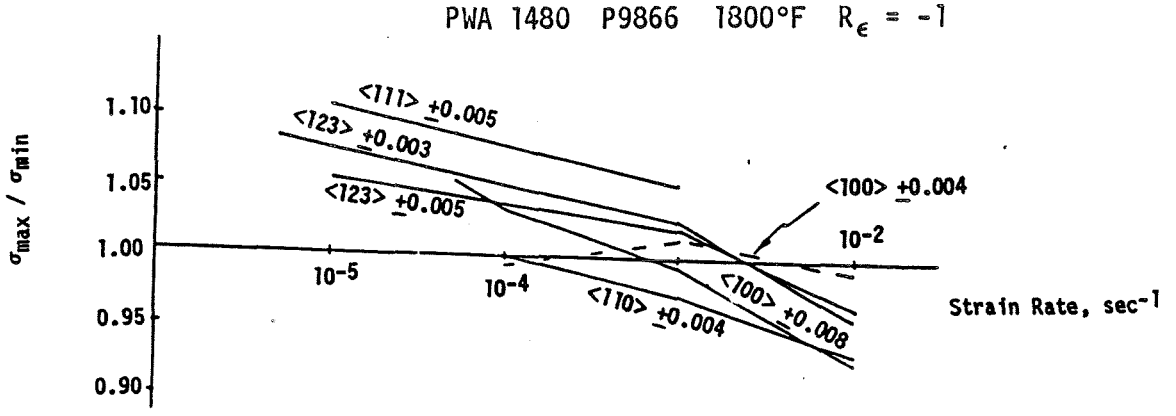

Figure 4-20 Tension-Compression Assymmetry, Strain Rate Sensitivity

4.3 Single Crystal Fatigue Tests

4.3.1 Test Facility

The test facility used for isothermal and thermo-mechanical fatigue (TMF) tests consists of a servo-controlled, closed loop hydraulic testing machine with MTS controllers, a low frequency (10 kHz) 20 kW TOCCO induction heater, and an Ircon model 7000 radiation pyrometer, calibrated over a temperature range of 260°C to 1371°C (500°F to 2500°F), for temperature measurement. Induction heating was selected to accommodate MTS external extensometry and specimen inspection and to provide adequate nonisothermal test heating rates. The quartz rods of the MTS extensometer, which define a 2.54 cm (1.0 in) gage section, are spring loaded against the specimen and did not show any signs of slippage during testing. A typical test setup is illustrated in Figure 4-21.

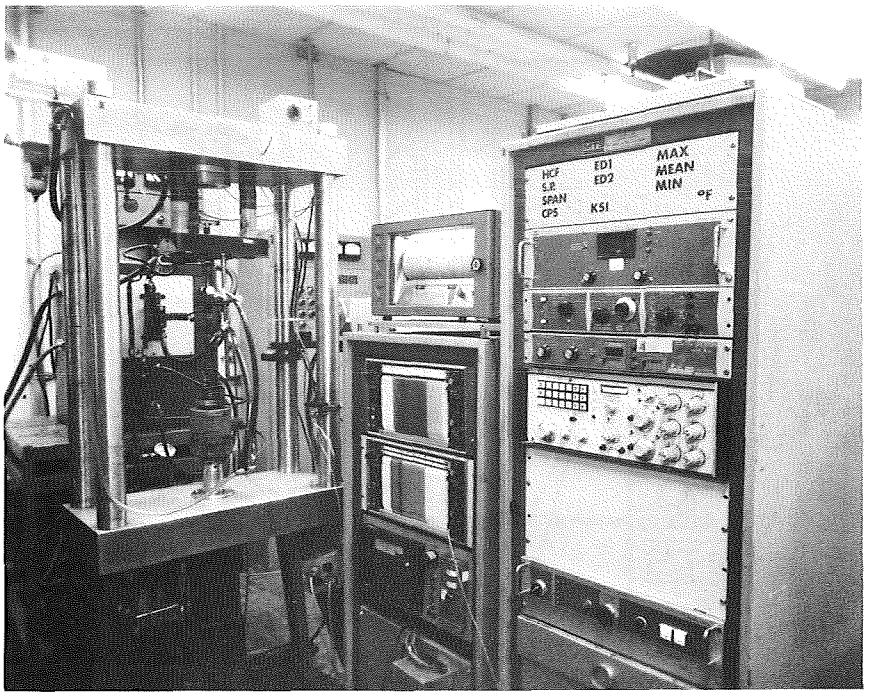

Figure 4-21 Thermo-Mechanical Fatigue Test Rig

4.3.2 Strain Measurement

For this research effort, there are two uniaxial deflection measurement devices (Figure 4-22) available for elevated temperature fatigue testing of hollow specimens: 1) an internal extensometer developed at Pratt & Whitney in the 1960s, and 2) a recently developed MTS external extensometer. As illustrated in the figure, the internal extensometer requires machined internal ridges located at the extremities of the gage section.

Experience with coated specimens controlled via the internal extensometer indicates that thermo-mechanical fatigue (TMF) crack initiation is insensitive to specimen internal geometry since cracking predominantly originates on the coated surface (the O.D.). However, there is a concern that cracking may originate from the internal ridges of uncoated specimens, and that the associated crack initiation life of such tests would be indeterminate. Thus, it is advantageous to remove the internal ridges and rely on external extensometry for deflection measurement.

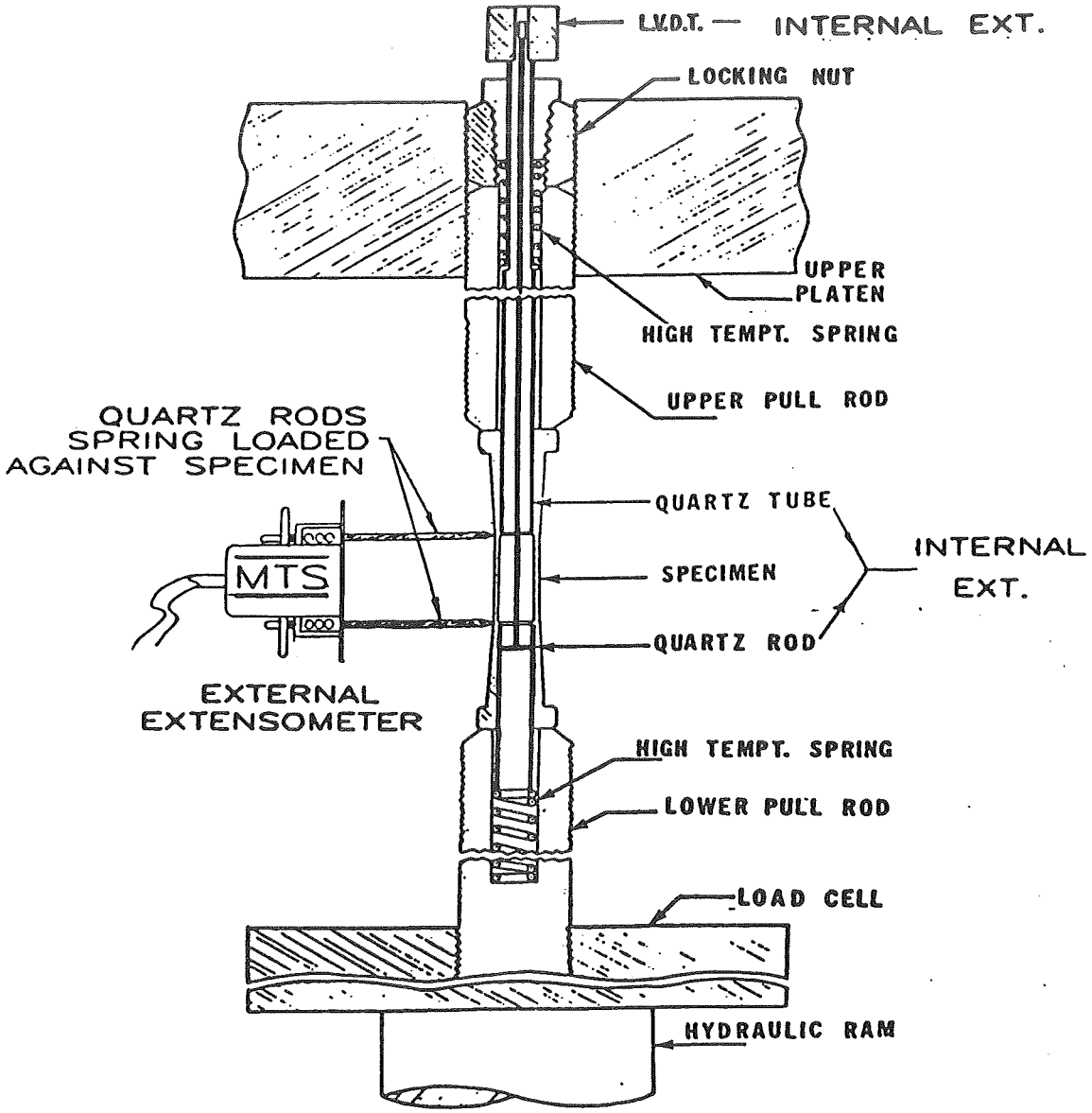

Figure 4-22 Extensometry

To substantiate the measurement accuracy of the external extensometer, a comparison study is being performed between it and the internal extensometer. Deflections from each device are recorded from the same specimen by using the "piggy-back" setup of Figure 4-22. Previous experience from a single PWA 1455 (B1900+Hf) TMF test indicated that significant differences between the two extensometers occurred only when large cracks were present. During that stage of fatigue life, the external extensometer recorded higher deflection ranges than the internal. This was interpreted as a limitation of the external extensometer because it measures a strain which can be influenced by the circumferential location of the dominant crack. The internal extensometer is considered to be insensitive to crack location. For the present study, an initial set of six coated PWA 1480, <100> orientation, single crystal specimens were run at the conditions shown in Figure 4-23. At each test condition, specimens coated with each coating type were tested. Observed deflection results of these tests (Table 4-V) indicate that the external extensometer consistently measures less mechanical strain than the internal.

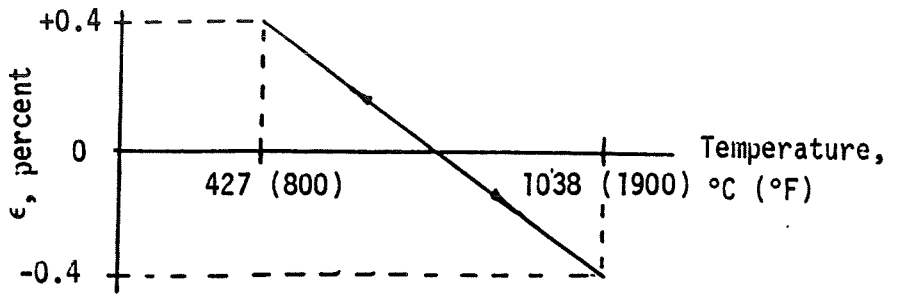

A) HIGH STRAIN: OUT-OF-PHASE

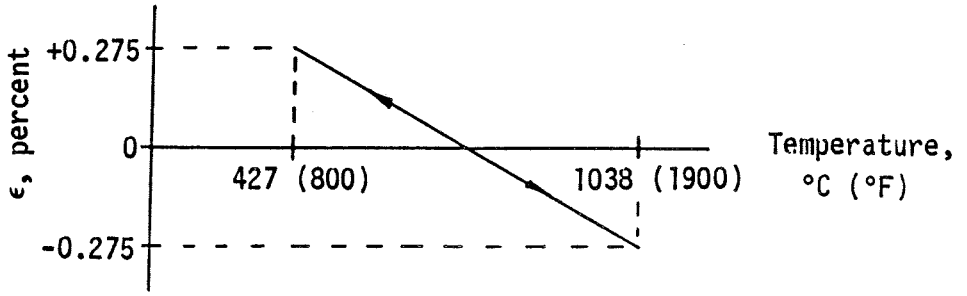

B) LOW STRAIN: OUT-OF-PHASE

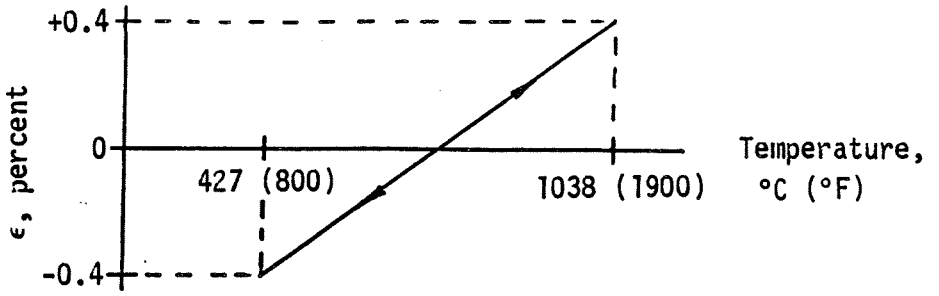

C) HIGH STRAIN: IN-PHASE

Figure 4-23 Initial Thermo-Mechanical Fatigue Test Conditions

Table 4-V

Comparison Summary of Strains Obtained from Internal and External Extensometry During Thermo-Mechanical Fatigue Cycling

Spec ID	Test Condition °C (°F)	Coat Type	Strain Ranges (Percent)					
			Thermal		Total		Mechanical	
			Ext	Int	Ext	Int	Ext	Int
JB-9	427-1038 (800-1900) Out-Of-Phase	286	External Extensometer Quartz Rods Improperly Located On Specimen					
JB-19	427-1038 (800-1900) Out-Of-Phase	273	0.96	0.94	0.13	0.105	0.83	0.84
JB-10	427-1038 (800-1900) Out-Of-Phase	286	0.97	0.96	0.47	0.42	0.50	0.54
JB-22	427-1038 (800-1900) Out-Of-Phase	273	0.95	0.93	0.43	0.36	0.52	0.57
JB-11	427-1038 (800-1900) In-Phase	286	0.97	0.96	1.76	1.76	0.79	0.80
JB-29	427-1038 (800-1900) In-Phase	273	0.97	0.97	1.72	1.76	0.75	0.79

To better understand the observed deflection differences, parametric tests were conducted on uncoated, strain gaged PWA 1480 <100> and PWA 1455 (B1900+Hf) specimens at room temperature. The strain gage locations are shown in Figure 4-24. For these tests, it was assumed that the average strain gage measurement was representative of the true O.D. surface strain and could be used as a reference with which to compare the two extensometers.

The results summarized in Table 4-VI indicate that the external extensometer measured strains more consistent with those of the strain gages.

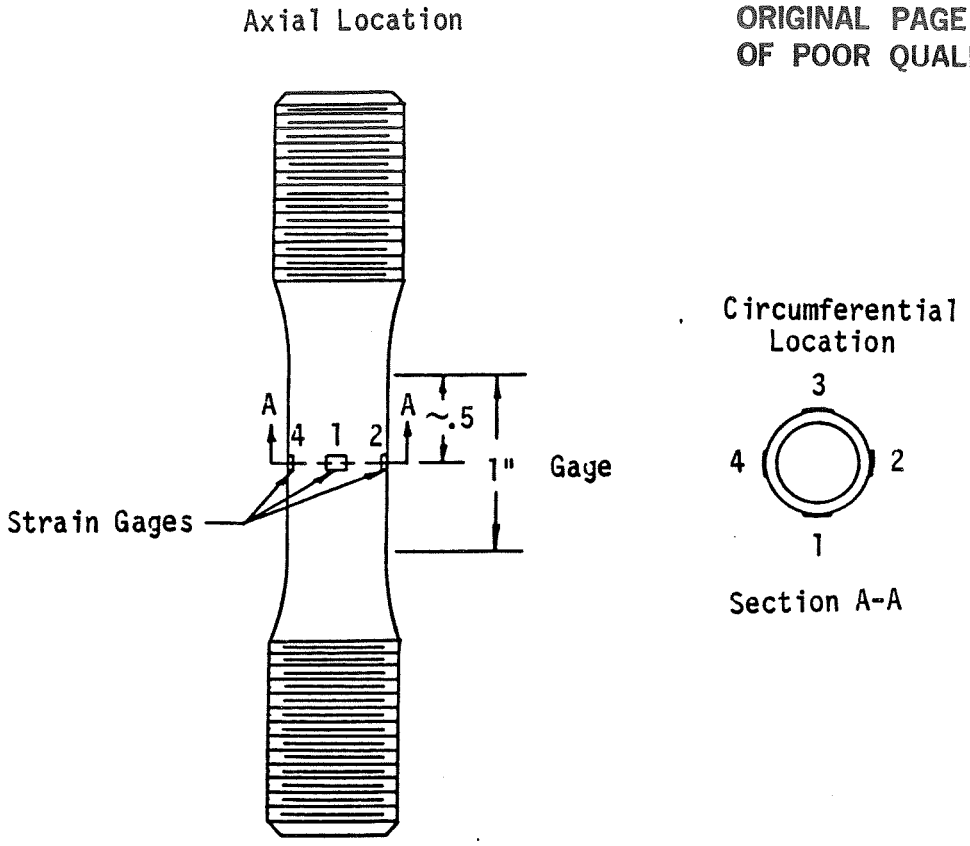

Figure 4-24 Strain Gage Locations on PWA 1480 and PWA 1455 Specimens

Table 4-VI

Comparison Summary of Strains Obtained from Internal and External Extensometry and Strain Gages During Room Temperature Cycling

Spec Material	External Extensometer Location*	Strain Ranges (Percent)		
		Internal	External	Average of Strain Gages
PWA 1480	2	0.324 (0.309)**	0.300	0.298
PWA 1480	1	0.324 (0.309)	0.293	0.296
PWA 1480	1	0.330 (0.315)	0.300	0.302
PWA 1455	4	0.188 (0.177)	0.178	0.178
PWA 1455	3	0.188 (0.177)	0.177	0.178
PWA 1455	3	0.188 (0.177)	0.178	0.178

* Refer to Figure 4-24
** Corrected for calculated distortion

From an elastic two-dimensional finite element analysis of the specimen geometry shown in Figure 2-7(C), it was concluded that both extensometers accurately measure deflections at their respective locations. Further, it was concluded that the observed differences in strain (at least at room temperature) are caused by internal ridge rolling due to the Poisson effect and the specimen thickness increase away from the gage section. When the internal extensometer strain is adjusted to account for these effects (refer to the numbers in parentheses in Table 4-VI), the difference is less than one percent for the PWA 1455 specimen. Since the Poisson ratio of PWA 1480 <100> is greater than PWA 1455, greater ridge deflection will result. Thus, the larger differences of the PWA 1480 specimen can also be explained. Additional finite element analysis using PWA 1480 anisotropic properties will be performed to verify this conclusion.

In light of these findings, there is currently no technical reason why the external extensometer cannot be relied upon to measure hollow specimen strains; however, the decision to remove the internal ridges from future specimens and rely solely on the external extensometer is pending the results of additional testing and analysis at elevated temperature conditions.

4.3.3 Single Crystal Fatigue Tests

Isothermal and thermo-mechanical fatigue (TMF) tests are being conducted to define the crack initiation life of coated PWA 1480 single crystal material and to provide baseline data for life prediction model evaluations. To preclude specimen geometry effects, all fatigue tests (isothermal and TMF) will be conducted on hollow specimens, Figure 2-7(C). Initial testing will be limited to key variables considered relevant to the creep-fatigue life prediction problem. The variables include crystallographic orientation, strain range, strain ratio (R_ε), strain rate, strain dwell periods, and temperature. Both coated and uncoated specimen tests are planned to determine whether uncoated testing is useful for evaluating coated crack initiation life. The applied coatings are of two generic types which are currently used for airfoil oxidations protection: 1) an aluminide diffusion coating (PWA 273), and 2) a NiCoCrAlY overlay coating (PWA 286). In an effort to characterize the material deformation mechanisms which are active during fatigue, several specimens will be selected for transmission electron microscopy (TEM) examination.

To date, fully-reversed (R_ε = -1) TMF tests of coated PWA 1480 <100> have been conducted at the conditions shown in Figure 4-23. These data are summarized in Table 4-VII. Cracking information was obtained by acetate replication of the specimen gage section at various cyclic intervals. Whenever possible, the crack which ultimately led to specimen fracture was identified and traced to its initiation site.

Table 4-VII

Summary of PWA 1480 Thermo-Mechanical Fatigue Results

Spec ID	Orient	Coat Type	Spec[1] Type	Temp °C (°F)	Cycle[2] Type	$\Delta\epsilon_t$ %	Re	Freq CPM	Stress Range MPa (ksi) $\Delta\sigma_0$[3]	Stress Range MPa (ksi) $\Delta\sigma_{1/2}$	Mean Stress MPa (ksi) σ_{m0}	Mean Stress MPa (ksi) $\sigma_{m1/2}$	Cyclic Life 5%[4] Cycles	Cyclic Life 10%[5] Cycles	Cyclic Life SEPR[6] Cycles
JB-9	<100>	286	M44C	427-1038 (800-1900)	I	0.8	-1	1.0	772.9 (112.1)	823.9 (119.5)	120.7 (17.5)	244.1 (35.4)	1820	1875	1878
JB-19	<100>	273	M44C	427-1038 (800-1900)	I	0.8	-1	1.0	744.7 (100.0)	774.3 (112.3)	107.6 (15.6)	220.6 (32.0)	X	X	500
JB-10	<100>	286	M44C	427-1038 (800-1900)	I	0.55	-1	1.0	576.4 (83.6)	611.6 (88.7)	100.7 (14.6)	178.6 (25.9)	3100	4010	4105
JB-22	<100>	273	M44C	427-1038 (800-1900)	I	0.55	-1	1.0	513.0 (74.4)	536.4 (77.8)	66.2 (9.6)	138.6 (20.1)	3600	X	3772
JB-11	<100>	286	M44C	427-1038 (800-1900)	II	0.8	-1	1.0	844.6 (122.5)	862.6 (125.1)	-122.7 (-17.8)	-291.7 (-42.3)	10100	10300	10535
JB-29	<100>	273	M44C	427-1038 (800-1900)	II	0.8	-1	1.0	787.4 (114.2)	760.5 (110.3)	-116.5 (-16.9)	-315.8 (-45.8)	X	X	-Disc @ 10340

Notes:

1: See Figure 2-7
2: I = out-of-phase; II = in-phase
3: 0 = initial values; 1/2 = 1/2 separation life values
4: 5% load range drop
5: 10% load range drop
6: Separation life

For the out-of-phase TMF tests, the two coatings were observed to initiate cracks differently. The diffusion coating tended to generate circumferential cracks, whereas the overlay initiated a multitude of small thumb-nail like cracks. Representative fracture surfaces of these specimens are presented in Figures 4-25 and 4-26. The concentric cracking of the diffusion coating is not unexpected since its fracture ductility is low at temperatures below 649°C (1200°F). From the replica information (Figure 4-27) it is apparent that lower test strain ranges are required to obtain relevant cracking data for this coating type.

In-phase TMF crack initiation of coated specimens is less distinct. The tensile portion of the test occurs at high temperature; therefore, the coatings tend to rumple which makes replication difficult. As can best be determined, in-phase testing generates many small cracks early in the fatigue life of the specimen; however, these cracks do not grow as rapidly as those of out-of-phase testing (Figure 4-28). As a result, the fatigue lives of in-phase TMF tests are significantly longer than those of out-of-phase tests.

A life correlation of the fatigue tests is presented in Figure 4-29. For out-of-phase tests, the fatigue life of the diffusion coated specimens is shown to be more sensitive to total strain range than that of the overlay coated specimens. Thus, at strain ranges below about 0.5 percent, the diffusion coated specimen lives are expected to be higher than those of overlay specimens.

A general matrix of PWA 1480 fatigue test conditions planned for this task is provided in Table 4-VIII.

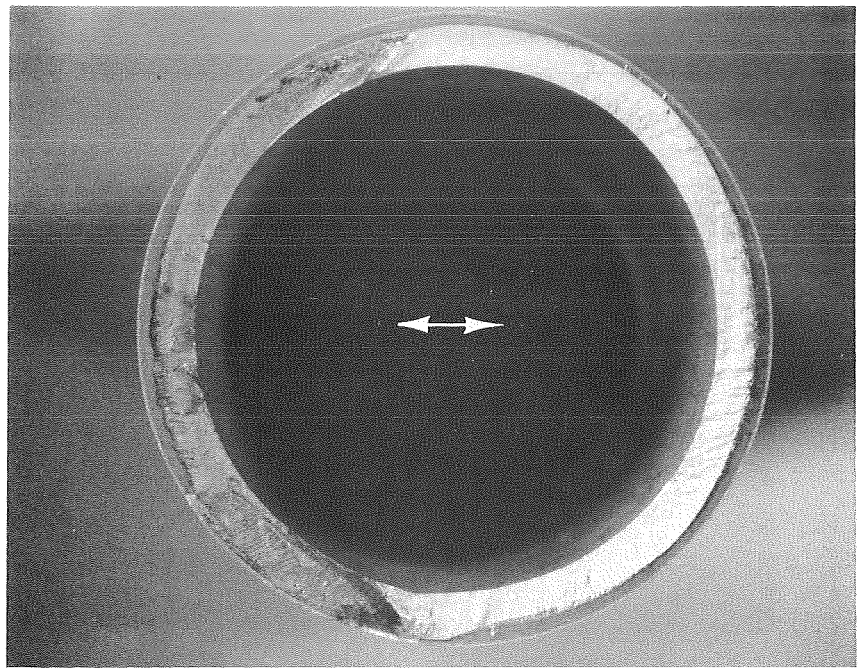

(A) CIRCUMFERENTIAL CRACKING ~6X

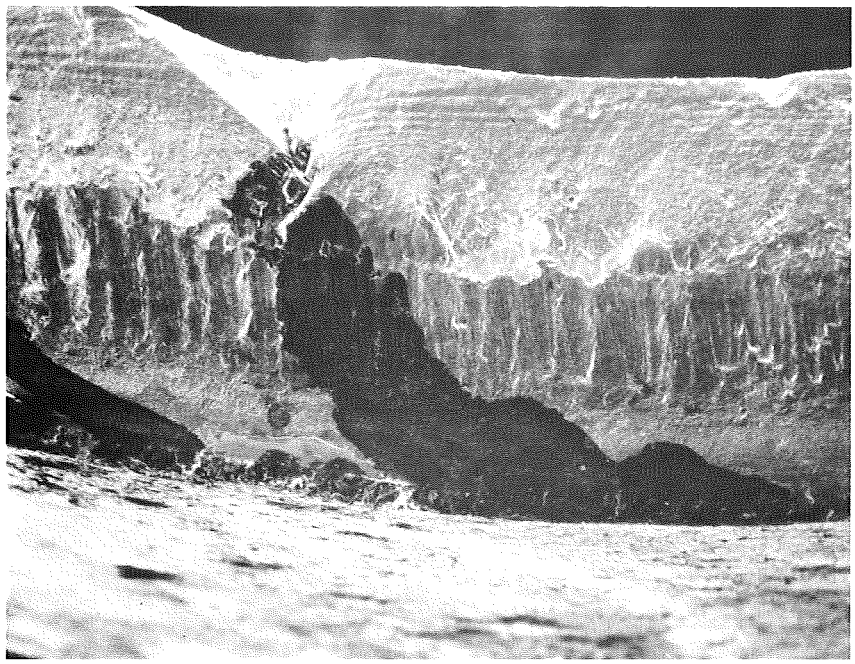

B) FAINT FATIGUE STRIATIONS 50X

Figure 4-25 PWA 273 Coated PWA 1480 <100>; Specimen JB-22; After Being Thermo-Mechanically Fatigue Tested at 427°C - 982°C (800°F - 1900°F) $\Delta\varepsilon_t = \pm 0.275$ Percent, 1 CPM, Out-Of-Phase for 3772 Cycles

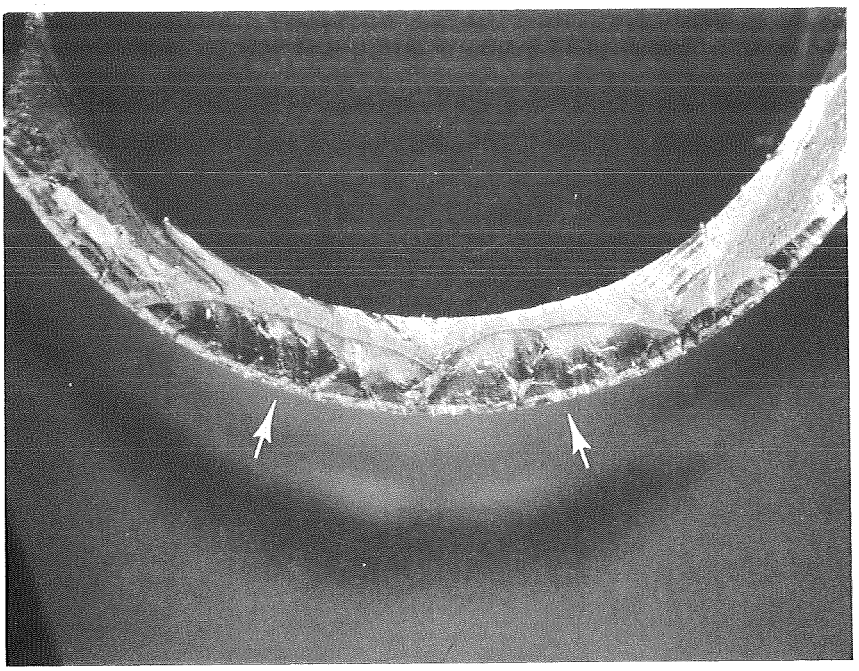

~10X

A) MULTIPLE SMALL THUMB-NAIL LIKE FATIGUE CRACKS

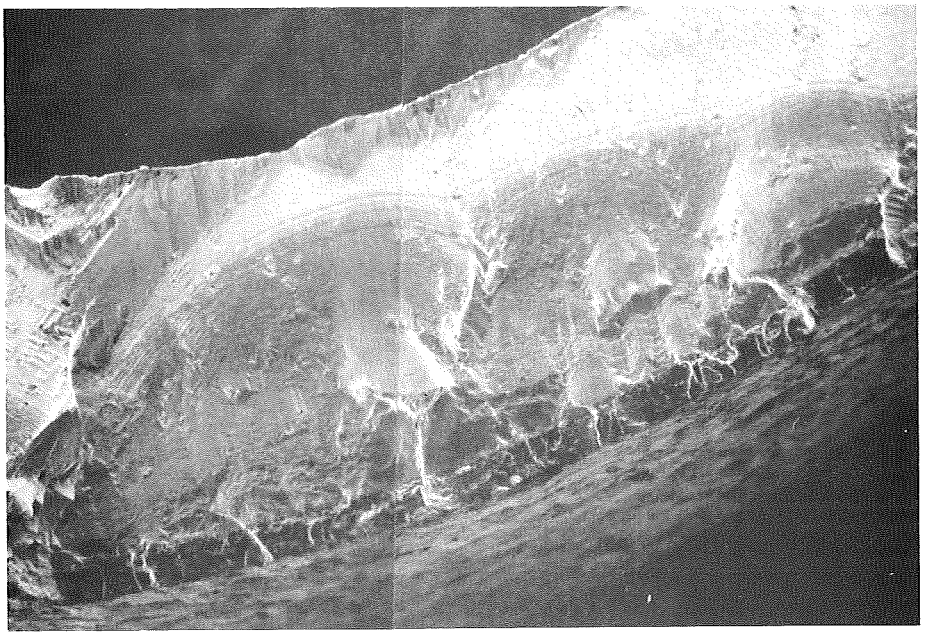

40X

B) FAINT FATIGUE STRIATIONS

Figure 4-26 PWA 286 Coated PWA 1480 <100>; Specimen JB-9; After Being Thermo-Mechanically Fatigue Tested at 427°C - 982°C (800°F - 1900°F) $\Delta\varepsilon_t = \pm 0.4$ Percent, 1 CPM, Out-Of-Phase for 1878 Cycles

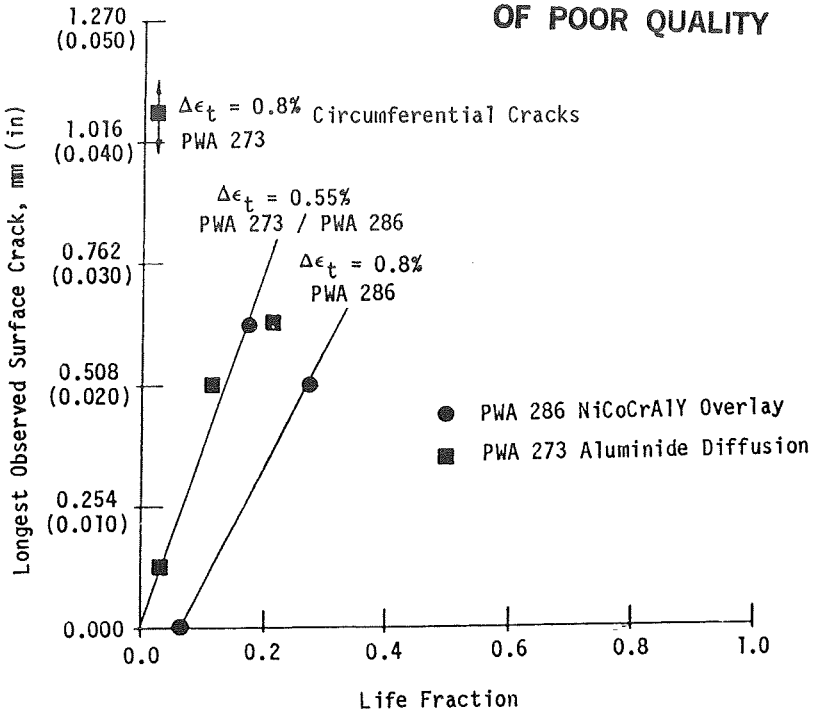

Figure 4-27 Coated PWA 1480 <100> Out-Of-Phase Thermo-Mechanical Fatigue Replica Data

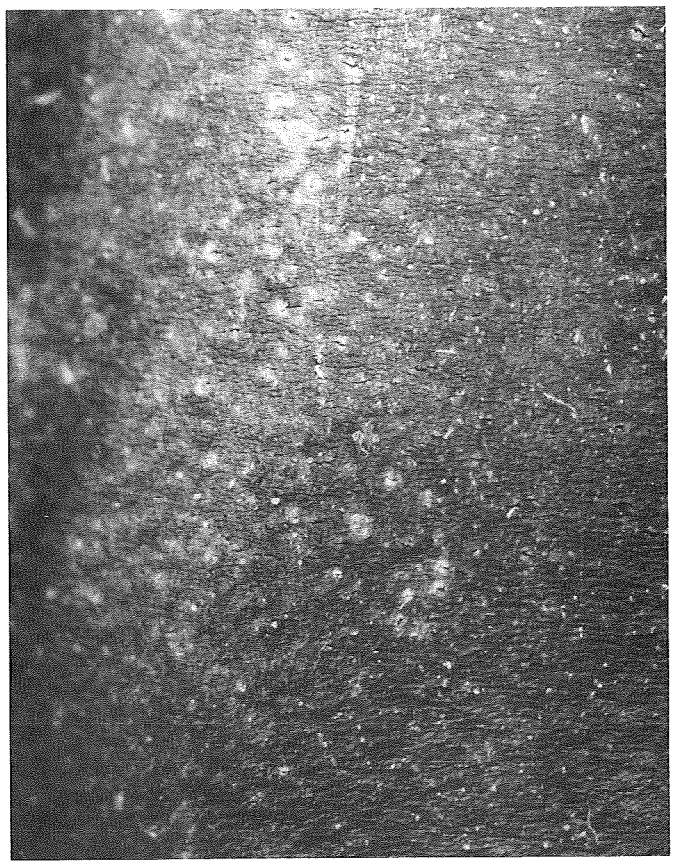

C-2

~10X

Figure 4-28 PWA 273 Coated PWA 1480 <100>; Specimen JB-29; After Being Thermo-Mechanically Fatigue Tested at 427°C - 982°C (800°F - 1900°F) $\Delta\varepsilon_t = \pm 0.4$ Percent, 1 CPM, In-Phase for 10340 Cycles. Coating rumpling and many small cracks are the dominant O.D. surface features.

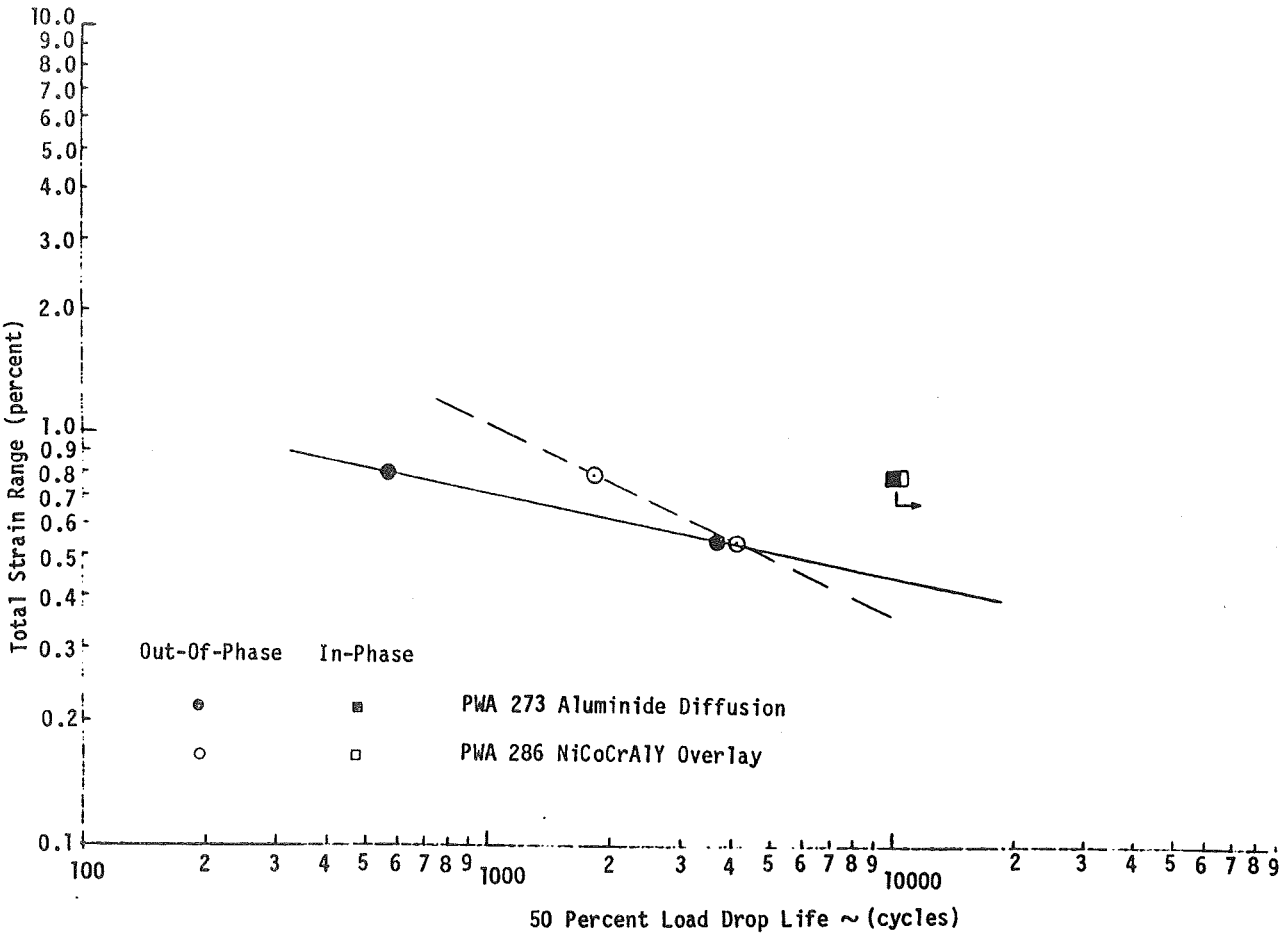

Figure 4-29 Thermo-Mechanical Fatigue Life Versus Strain Range for Coated PWA 1480, 427°C - 1038°C (800°F - 1900°F)

Table 4-VIII

Summary of Planned Task III PWA 1480 Fatigue Tests

Orient[1]				Coat[2,3] Type			Thermo-Mechanical									Isothermal											
							Phase			T Range		Range		Temp			Range		ε Rate		ε Ratio			Dwell				
1	2	3	4	-	C1	C2	In	Out	SP[4]	ΔT1	ΔT2	Δε1	Δε2	T1	T2	T3	Δε1	Δε3	ε̇1	ε̇2	-∞	-1	0	Min	Max			
X		X		X	X	X	X			X		X															
X		X		X	X	X		X		X		X															
X		X		X	X	X		X		X			X														
X		X		X	X	X			X	X		X															
X		X		X	X	X								X	X	X	X		X		X						
X		X		X	X	X										X		X	X		X						
X		X		X	X	X										X	X		X		X			X			
X		X		X	X	X										X	X		X		X				X		
	X		X	X			X			X		X															
	X		X	X				X		X		X															
	X		X	X				X		X			X														
	X		X	X					X	X		X															
	X		X	X										X	X	X	X		X		X						
	X		X	X												X		X	X		X						
	X		X	X												X	X		X		X			X			
	X		X	X												X	X		X		X				X		

Notes: 1: 1 = <100>; 2 = <110>; 3 = <111>; 4 = <123>
2: - = uncoated; C1 = PWA 286 NiCoCrAlY overlay; C2 = PWA 273 aluminide diffusion
3: Emphasis will be on conducting the coated specimen tests
4: Special Cycle

SECTION 5.0

SUMMARY OF RESULTS

During the first year of effort, the following tasks were accomplished and preliminary results obtained.

- The materials selected for the program are as follows: single crystal alloys, PWA 1480 and model Alloy 185, an overlay coating, PWA 286, and aluminide coating, PWA 273. All but the Alloy 185 were selected because they are typical of the most advanced materials being used in gas turbine blades. Alloy 185 was selected because its properties differ greatly from those of PWA 1480 and will be used to test the range of applicability of the constitutive and life prediction models developed in this program.

- Single crystal specimen orientations were chosen to be <100>, <110>, <111> and <123> to represent the full range of slip systems and slip system interaction.

- Physical and thermal property tests on PWA 1480 were completed at Southern Research Institute.

- Specimen preparation is well underway. Casting of all PWA 1480 specimens is complete, and casting of Alloy 185 is underway. Machining of these specimens is in process. Coating specimen fabrication is being paced by the success or failure of exploratory test procedures.

- Literature searches were completed on related constitutive and life prediction models, and are included in the appendices.

- The Walker unified viscoplastic constitutive model has been extended to all the slip systems of a face centered cubic crystal material. The initial mathematical development has been completed and programmed and is being used to correlate initial laboratory data.

- Walker's isotropic constitutive model has been successfully used to correlate limited data obtained for overlay coating, PWA 286. Model constants derived compare reasonably with those from other high temperature alloys.

- Thermal property tests were completed for PWA 1480. Properties included conductivity, coefficient of thermal expansion and specific heat.

- Monotonic tensile and creep data were obtained for PWA 1480 and overlay coating PWA 286.

- PWA 1480 constitutive data were obtained on fifteen of forty specimens. The constitutive models and their constants are being evaluated with these data. From this study the test conditions for the next round of constitutive tests will be determined.

- A modern external MTS extensometer has been evaluated relative to the older and well-established Pratt & Whitney internal extensometer and was found to function accurately and reliably in thermo-mechanical fatigue (TMF) testing. Use of the external extensometer in this program will eliminate the requirement for internal ridges on the test specimens.

- Isothermal and TMF testing of coated and uncoated PWA 1480 has started. Initial out-of-phase cycle TMF tests indicate that at strain ranges greater than 0.5 percent, the overlay coated specimens have longer lives than do those coated with an aluminide. The reverse is true below the 0.5 percent strain range.

SECTION 6.0

FUTURE WORK

During the second year of the base program, the following work will be accomplished:

- Specimen preparation will be completed, including the machining of PWA 1480 specimens, casting and machining of the Alloy 185 specimen, and complete fabrication of all coating specimens.
- Physical property tests will be run on the two coating materials, PWA 286 and PWA 273.
- Level I PWA 1480 experiments will be completed including forty constitutive tests and forty fatigue tests.
- Development of the constitutive and life prediction models will continue in parallel with the above tests. Two models of each will be selected for further evaluation in Task V.

APPENDIX A

EXPERIMENTAL DATA GENERATED FOR COATING CONSTITUTIVE MODEL EVALUATIONS

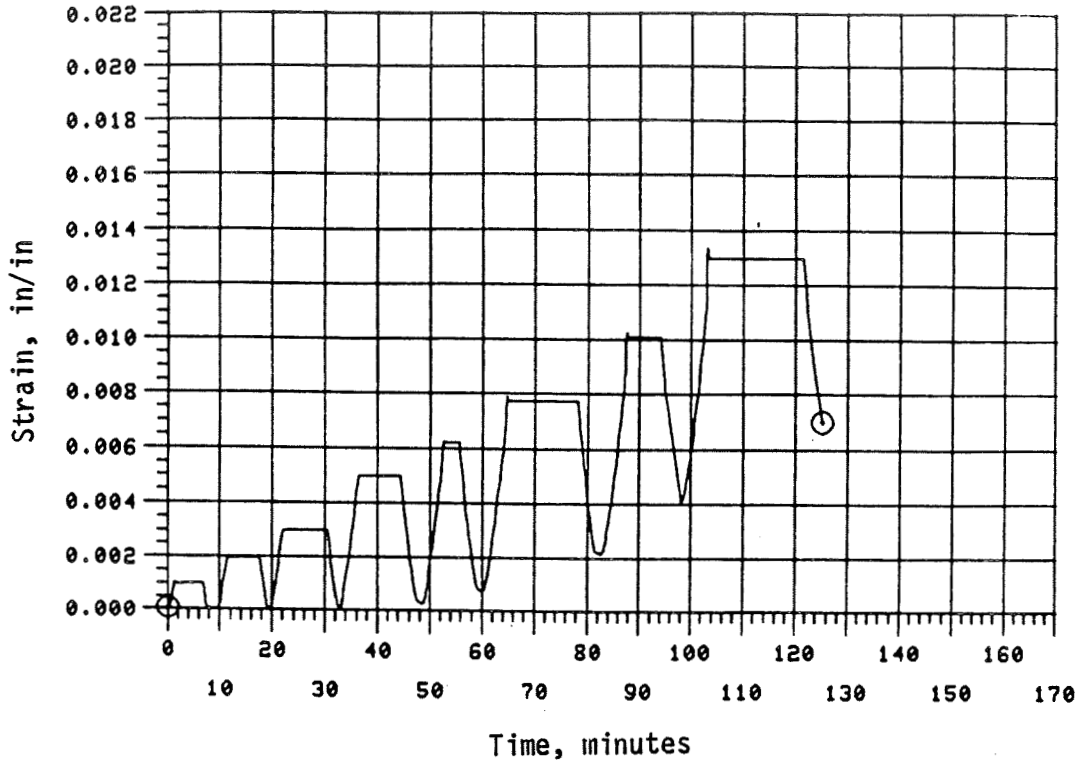

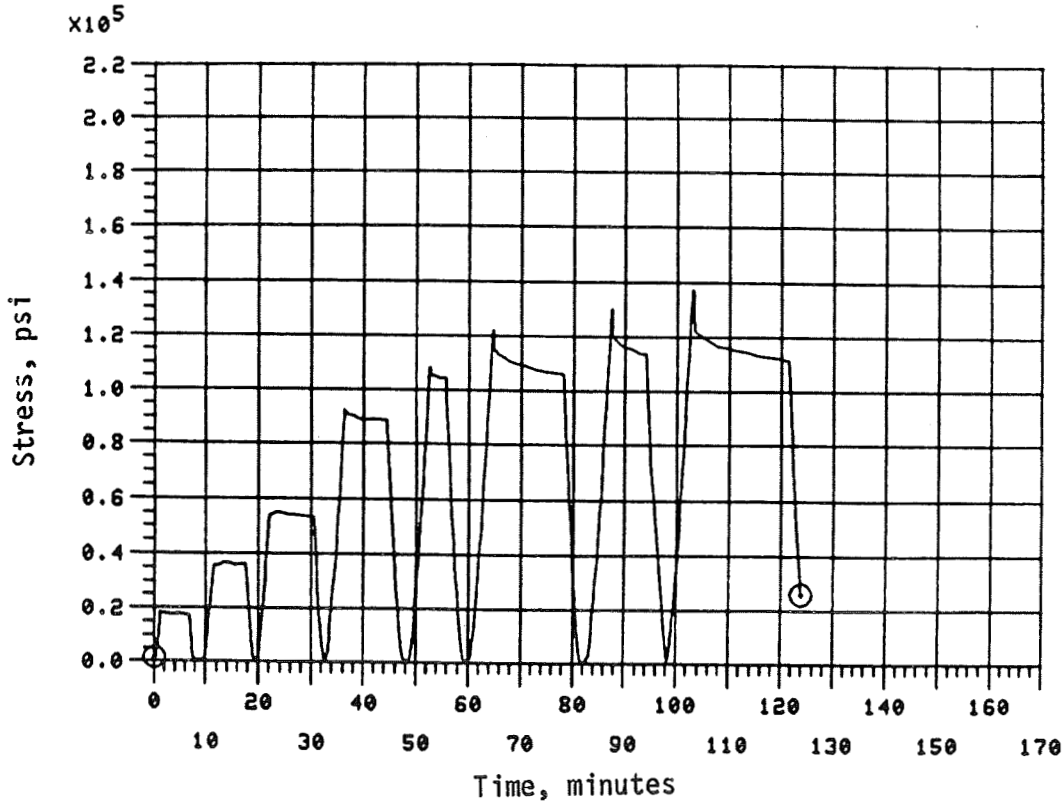

Figure A-1 538°C (1000°F) PWA 286 Bulk (Hot Isostatically Pressed) Relaxation; Unexposed

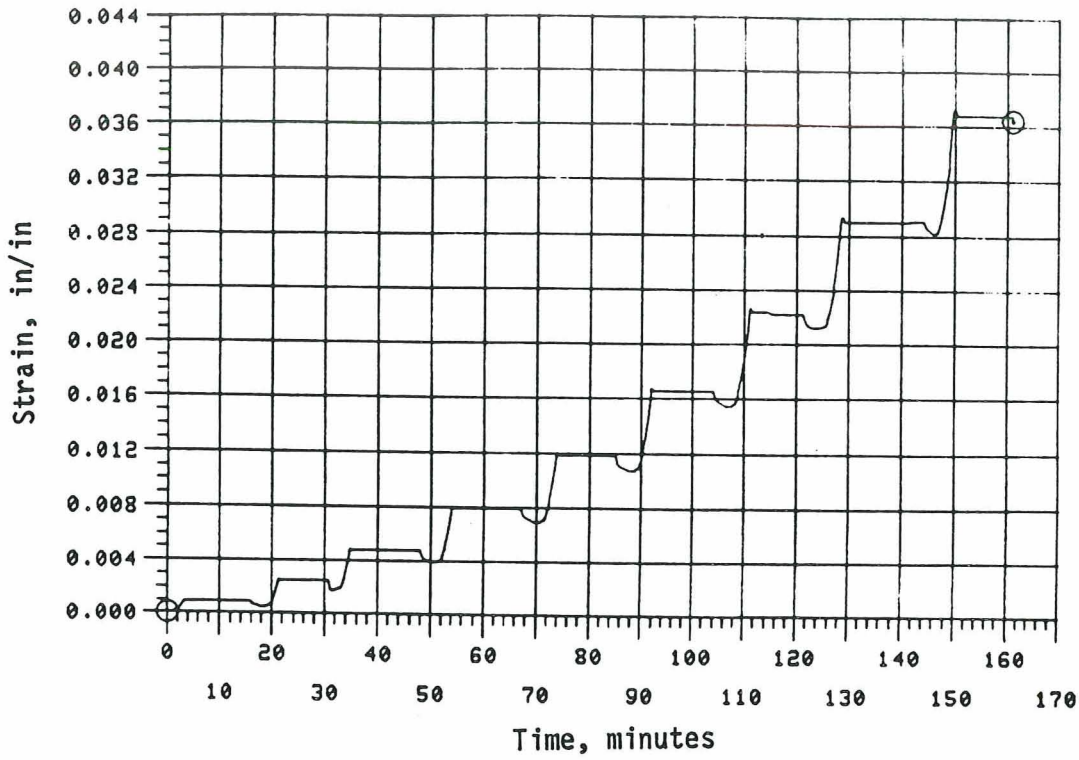

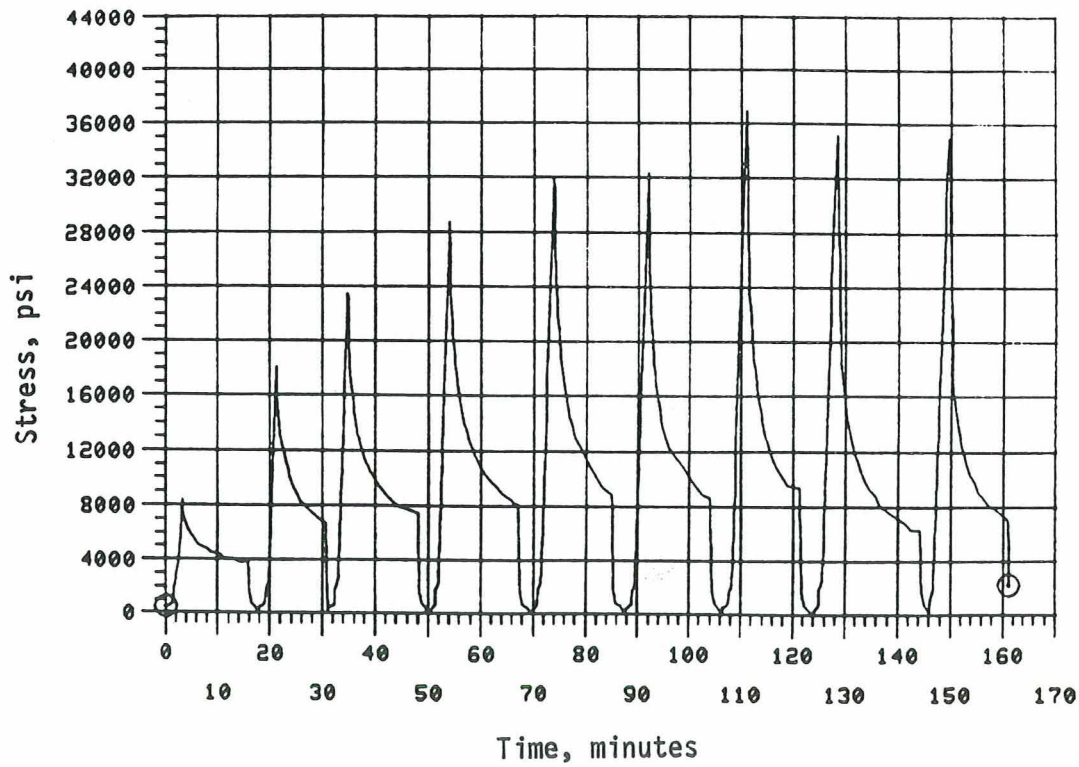

Figure A-2 760°C (1400°F) PWA 286 Bulk (Hot Isostatically Pressed) Relaxation; Unexposed

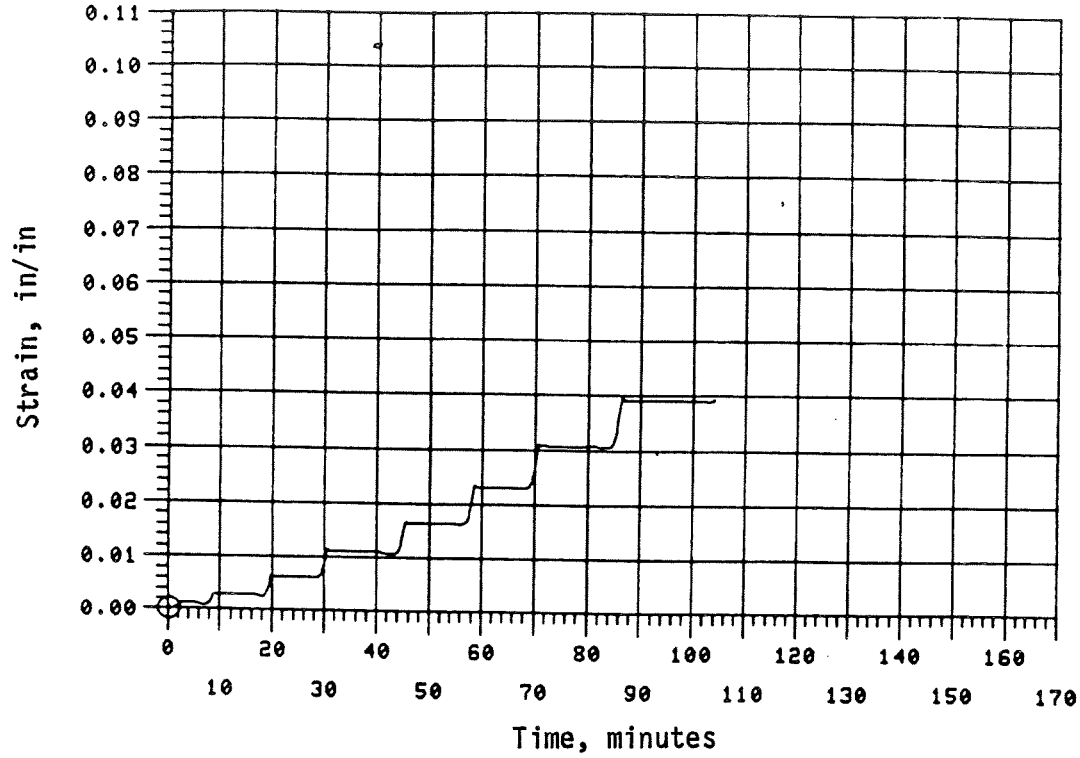

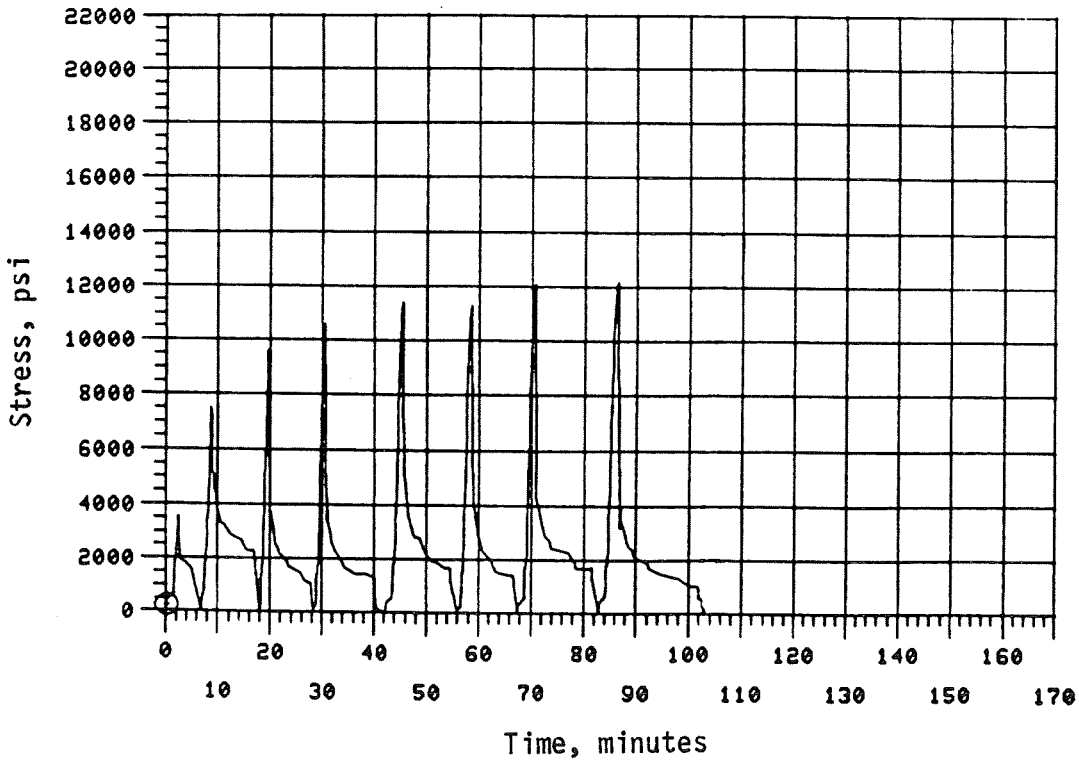

Figure A-3 871°C (1600°F) PWA 286 Bulk (Hot Isostatically Pressed) Relaxation; Unexposed

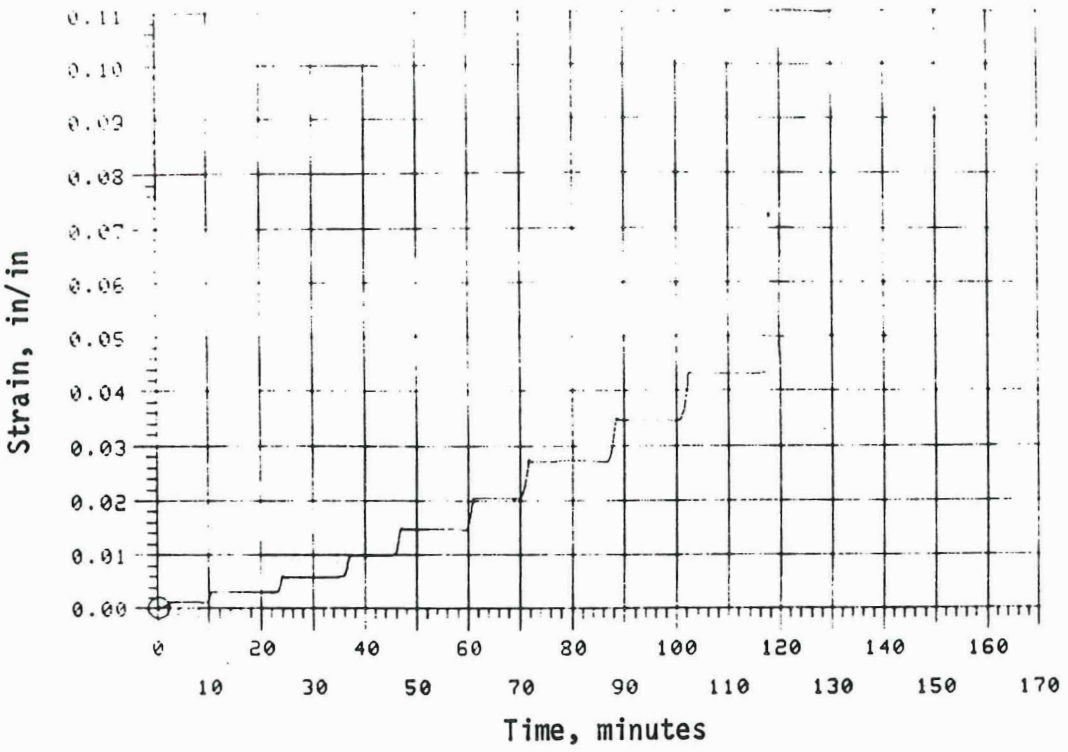

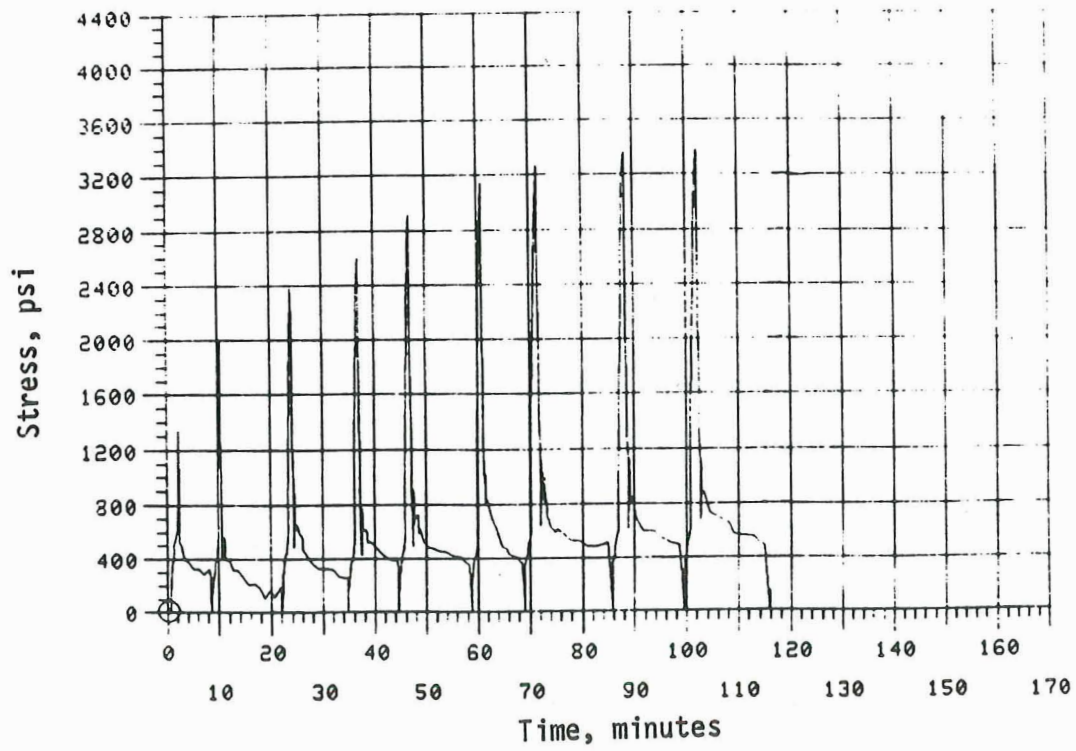

Figure A-4 982°C (1800°F) PWA 286 Bulk (Hot Isostatically Pressed) Relaxation; Unexposed

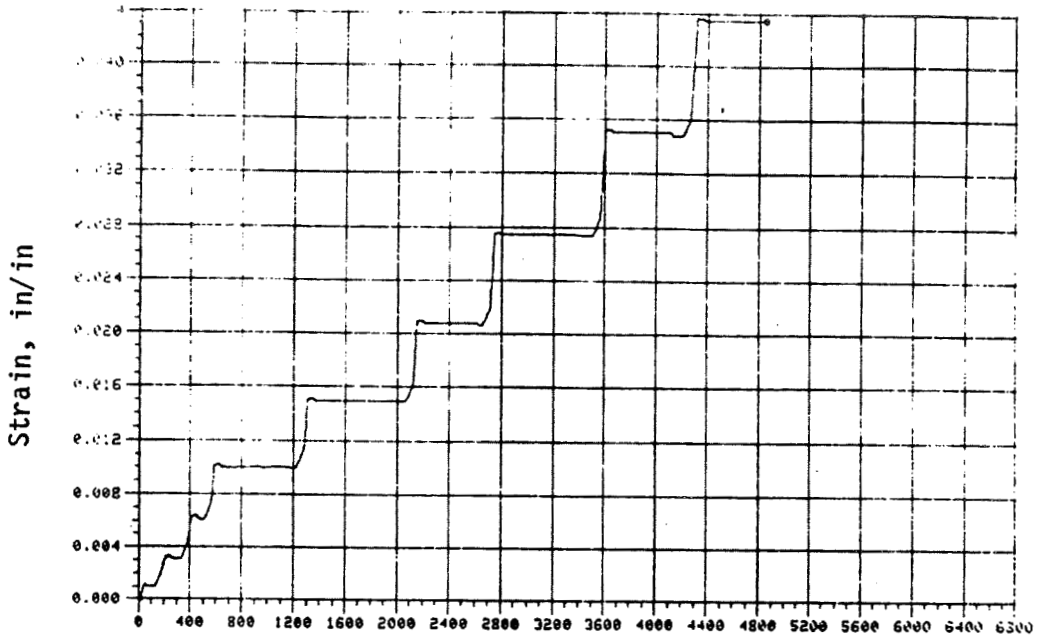

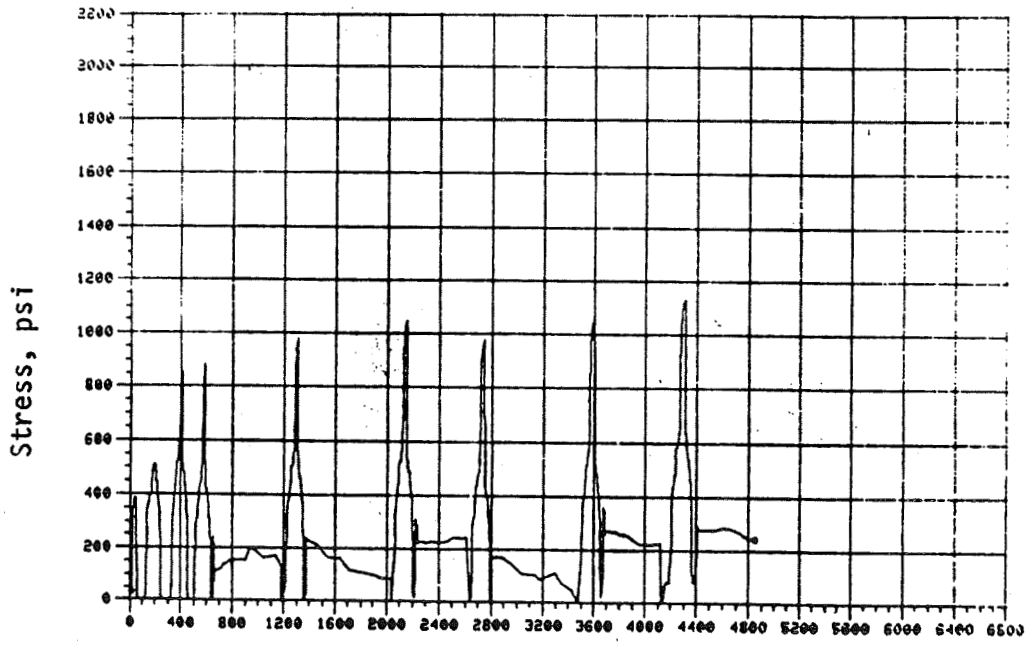

Figure A-5 1093°C (2000°F) PWA 286 Bulk (Hot Isostatically Pressed) Relaxation; Unexposed

APPENDIX B

LITERATURE SURVEY - SINGLE CRYSTAL AIRFOIL MATERIALS CONSTITUTIVE MODELS

This appendix contains a review of constitutive models or modeling approaches which may be applicable to single crystal and transversely isotropic materials. The discussion includes work which has been reported in open literature and likely extensions of this work.

Macroscopic Continuum Theory Formulations

In 1948, Hill (Reference 1) proposed a generalization of the von Mises yield function for states of anisotropy possessing three mutually orthogonal planes of symmetry. Hill's theory remains the most widely used formulation and is currently coded into general purpose nonlinear finite element programs such as MARC and ABAQUS.

Various modifications to Hill's original theory were published in the literature between 1948 and 1977. Theories presented by Edelman and Drucker (Reference 2), Yoshimura (Reference 3), Williams and Svensson (Reference 4), and Baltov and Sawczuk (Reference 5) are basically modifications to Hill's theory to account for Bauschinger effects associated with kinematic hardening. Further work on anisotropic plasticity may be found in References 6 through 11. Hill's original theory allowed the anisotropic yield surface only to expand, whereas the later modifications allowed the anisotropic yield surface to both expand, translate, and change shape in stress space. However, the modifications to Hill's theory employ kinematic shift tensors, α_{ij}, which depend on plastic strain. The various shift tensors therefore vanish in the initial state of the material in which the plastic strain is zero and do not reflect a difference between tensile and compressive loading as observed in experiments with nickel-base single crystal materials. In effect the initial state is governed by Hill's theory.

The yield surface employed by Edelman and Drucker may be written in the form:

$$f = \frac{1}{2} M_{ijkl} (s_{ij} - mc_{ij}) (s_{kl} - mc_{kl}) - k^2$$

where s_{ij} is the deviatoric stress tensor,

c_{ij} is the plastic strain tensor,

k^2 denotes the size of the yield surface, and

M_{ijkl} is a fourth order anisotropy tensor.

If $f < 0$, the material is elastic. If $f = 0$, the yield condition is reached and the stresses are on the yield surface. In this theory, the kinematic shift tensor, α_{ij}, has the form $\alpha_{ij} = mc_{ij}$ and vanishes in the initial virgin state of the material. This tensor translates the yield surface in stress space and therefore introduces kinematic hardening to account for the Bauschinger effect.

Yoshimura employed the yield function:

$$f = \frac{1}{2} M_{ijkl} s_{ij} s_{kl} - B s_{ij} c_{ij} - k^2,$$

in which the yield surface translates through the term $Bs_{ij}c_{ij}$, which also vanishes in the initial virgin state of the material, while that of Williams and Svensson has the form:

$$f = (I_{ijkl} + Ac_{ij}c_{kl}) \left\{\sigma_{ij} + c_{ij} (L_{pqrs}\sigma_{pq}\sigma_{rs} - m)\right\} \left\{\sigma_{kl} + c_{kl} (L_{pqrs}\sigma_{pq}\sigma_{rs} - m)\right\} - K^2.$$

The yield function employed by Williams and Svensson was generalized in 1977 by Lee and Zaverl (References 12 and 13) whose yield surface may be written in the form:

$$f = \frac{1}{3} M_{ijkl} (\sigma_{ij} - \alpha_{ij}) (\sigma_{kl} - \alpha_{kl}) - \frac{1}{3} K^2.$$

This form of the yield surface will now be considered in more detail since this type of formulation is readily adapted for use with the unified viscoplastic models whose employment will be required in the description of the time-dependent anisotropic material behavior of single crystals and directionally solidified materials at elevated temperature. Several aspects of a time-independent formulation will be discussed, including tension/compression asymmetry, flow and hardening rules, the formulation of the elastoplastic stiffness matrix, and finally, the notion of incompressibility. Before proceeding, it will be convenient to adopt a Voigt rotation for the tensor indices so that the fourth rank tensor M_{ijkl} can be written in matrix form. To this end, we introduce the contracted notation for the stress components:

$$\sigma_1=\sigma_{11},\quad \sigma_2=\sigma_{22},\quad \sigma_3=\sigma_{33},\quad \sigma_4=\sigma_{12}=\sigma_{21},\quad \sigma_5=\sigma_{23}=\sigma_{32},\quad \sigma_6=\sigma_{13}=\sigma_{31},$$

and the plastic strain components are:

$$c_1=c_{11},\quad c_2=c_{22},\quad c_3=c_{33},\quad c_4=2c_{12}=2c_{21},\quad c_5=2c_{23}=2c_{32},\quad c_6=2c_{13}=2c_{31}.$$

Any component of the tensor M_{ijkl} may then be written as a two index matrix component. For example, $M_{\underset{4}{12}\ \underset{5}{32}} = M_{45}$ and $M_{\underset{1}{11}\ \underset{2}{22}} = M_{12}$, etc.

Lee and Zaverl's yield surface may now be written in Voigt index notation as:

$$f = M_{ij} (\sigma_i - \alpha_i) (\sigma_j - \alpha_j) - k^2. \tag{B-1}$$

If the material has three orthogonal planes of symmetry (such as the three crystallographic faces in a face centered cubic nickel-base superalloy) and the principal axes of anisotropy coincide with the Cartesian reference axes, the matrix M_{ij} can be written from symmetry arguments in the form:

$$[M] = \begin{bmatrix} M_{11} & M_{12} & M_{13} & 0 & 0 & 0 \\ M_{21} & M_{22} & M_{23} & 0 & 0 & 0 \\ M_{31} & M_{32} & M_{33} & 0 & 0 & 0 \\ 0 & 0 & 0 & M_{44} & 0 & 0 \\ 0 & 0 & 0 & 0 & M_{55} & 0 \\ 0 & 0 & 0 & 0 & 0 & M_{66} \end{bmatrix} \tag{B-2}$$

Equation (B-1) may also be written in the more convenient form:

$$f = M_{ij}\sigma_i\sigma_j - L_i\sigma_i - J, \tag{B-3}$$

where

$$K_i = 2M_{ij}\alpha_j \quad \text{and} \quad J = K^2 - M_{ij}\alpha_i\alpha_j. \tag{B-4}$$

Again, by symmetry, the vector L_i may be written in component form as:

$$[L] = [L_1, L_2, L_3, 0, 0, 0]. \tag{B-5}$$

A physical interpretation of M_{ij}, L_i and J may be made in the following manner. Let Y_{+1}, Y_{+2}, Y_{+3} denote the tensile yield stresses in the x_1, x_2, x_3 directions and let the absolute values of the compressive yield stresses in these directions be denoted by Y_{-1}, Y_{-2}, Y_{-3}, respectively. From equation (B-3), with f=0, we may write for simple uniaxial tension and compression tests in the x_1 direction:

$$M_{11} Y_{+1}^2 - L_1 Y_{+1} = J \text{ in tension,} \tag{B-6}$$

and

$$M_{11} Y_{-1}^2 + L_1 Y_{-1} = J \text{ in compression.} \tag{B-7}$$

Equations (B-6) and (B-7) show that:

$$M_{11} = \frac{J}{Y_{+1}Y_{-1}} , \quad M_{22} = \frac{J}{Y_{+2}Y_{-2}} , \quad M_{33} = \frac{J}{Y_{+3}Y_{-3}} . \tag{B-8}$$

We are at liberty to choose J=1 in equation (B-3) since this merely scales the values associated with M_{ij} and L_i. Hence,

$$M_{11} = (Y_{+1}Y_{-1})^{-1} , \quad M_{22} = (Y_{+2}Y_{-2})^{-1} , \quad M_{33} = (Y_{+3}Y_{-3})^{-1} , \tag{B-9}$$

and the components of M_{ij} are determined from measurements of the tensile and compressive yield stresses along the three crystallographic directions. In pure shear equation (B-3) may also be shown to give:

$$M_{44} = (Y_4)^{-2} , \quad M_{55} = (Y_5)^{-2} , \quad M_{66} = (Y_6)^{-2} , \tag{B-10}$$

where Y_4, Y_5 and Y_6 are the torsional yield stress associated with the stress components σ_{12}, σ_{23} and σ_{13}, respectively. By substituting equation (B-9) into equations (B-6) and (B-7), we find that:

$$L_1 = \frac{1}{Y_{-1}} - \frac{1}{Y_{+1}} , \quad L_2 = \frac{1}{Y_{-2}} - \frac{1}{Y_{+2}} , \quad L_3 = \frac{1}{Y_{-3}} - \frac{1}{Y_{+3}} \tag{B-11}$$

which determines the values of the L_i vector in terms of the measured yield values in tension and compressor. Thus, initial tensile and compressive yield stresses along the crystallographic axes, in addition to torsion tests in the 12, 23 and 31 directions, determine the initial values of the matrix M_{ij} and the vector L_i.

To complete the rate-independent formulation it is necessary to specify a suitable flow rule and to choose suitable hardening rules which determine the subsequent hardening evolution of the variables M_{ij}, α_i and k^2 in the specification of the yield surface in equation (B-3). The equivalent stress, k, is defined by the yield condition in equation (B-3), viz:

$$k = [M_{pq} (\sigma_p - \alpha_p) (\sigma_q - \alpha_q]^{1/2} , \tag{B-12}$$

and the equivalent plastic strain increment, dR, may be defined through the work relation:

$$k dR = \sigma_i \, dc_i . \tag{B-13}$$

If the yield function and the plastic potential are assumed to be identical, the flow rule is obtained by the usual relationship:

$$dc_i = \lambda \frac{\partial f}{\partial \sigma_i} . \tag{B-14}$$

The non-negative function λ is obtained from the usual consistency relation such that when the stress state is on the yield surface,

$$df = \frac{\partial f}{\partial \sigma_i} d\sigma_i + \frac{\partial f}{\partial M_{ij}} dM_{ij} + \frac{\partial f}{\partial \alpha_i} d\alpha_i + \frac{\partial f}{\partial k} dk = 0 . \tag{B-15}$$

The constitutive relation may be written in the form:

$$d\sigma_i = D^*_{ij} \, d\varepsilon_j , \tag{B-16}$$

where the elastoplastic matrix D^*_{ij} is given by:

$$D^*_{ij} = D_{ij} - \frac{1}{d} \frac{k}{\sigma_m \frac{\partial f}{\partial \sigma_m}} D_{ip} \frac{\partial f}{\partial \sigma_p} \frac{\partial f}{\partial \sigma_q} D_{qj} , \tag{B-17}$$

with

$$d = 2k \frac{\partial k}{\partial R} + \frac{K}{\sigma_m \frac{\partial f}{\partial \sigma_m}} \frac{\partial f}{\partial \sigma_i} D_{ij} \frac{\partial f}{\partial \sigma_j} - \frac{\partial f}{\partial M_{ij}} \frac{\partial M_{ij}}{\partial R} - \frac{\partial f}{\partial \alpha_i} \frac{\partial \alpha i}{\partial R} . \tag{B-18}$$

In this relation for d, it is assumed that M_{ij}, α_i and k are functions of the cumulative plastic strain, R, and the matrix D_{ij} in equation (B-17) is the anisotropic elasticity matrix:

$$[D] = \begin{bmatrix} D_{11} & D_{12} & D_{13} & 0 & 0 & 0 \\ D_{21} & D_{22} & D_{23} & 0 & 0 & 0 \\ D_{31} & D_{32} & D_{33} & 0 & 0 & 0 \\ 0 & 0 & 0 & D_{44} & 0 & 0 \\ 0 & 0 & 0 & 0 & D_{55} & 0 \\ 0 & 0 & 0 & 0 & 0 & D_{66} \end{bmatrix} \tag{B-19}$$

when referred to the crystallographic symmetry axes.

We now examine the consequences of assuming that the plastic strain is incompressible. Setting $dc_1 + dc_2 + dc_3 = 0$ in equation (B-14) yields the relations:

$$M_{11} + M_{12} + M_{13} = 0 \quad , \tag{B-20}$$

$$M_{21} + M_{22} + M_{23} = 0 \quad , \tag{B-21}$$

$$M_{31} + M_{32} + M_{33} = 0 \quad , \tag{B-22}$$

$$L_1 + L_2 + L_3 = 0 \quad . \tag{B-23}$$

In a face centered cubic material, such as a nickel-base superalloy single crystal, the properties along each of the crystallographic axes are identical, so that, $M_{11} = M_{22} = M_{33}$ and $M_{12} = M_{23} = M_{13}$.

From the preceding discussion, it is evident that the anisotropy matrix, when specialized to the cubic symmetry appropriate for single crystals, may be written as:

$$[M] = \begin{bmatrix} M_{11} & -\frac{1}{2}M_{11} & -\frac{1}{2}M_{11} & 0 & 0 & 0 \\ -\frac{1}{2}M_{11} & M_{11} & -\frac{1}{2}M_{11} & 0 & 0 & 0 \\ -\frac{1}{2}M_{11} & -\frac{1}{2}M_{11} & M_{11} & 0 & 0 & 0 \\ 0 & 0 & 0 & M_{44} & 0 & 0 \\ 0 & 0 & 0 & 0 & M_{44} & 0 \\ 0 & 0 & 0 & 0 & 0 & M_{44} \end{bmatrix} , \tag{B-24}$$

while the elasticity matrix has the form:

$$[D] = \begin{bmatrix} D_{11} & D_{12} & D_{12} & 0 & 0 & 0 \\ D_{12} & D_{11} & D_{12} & 0 & 0 & 0 \\ D_{12} & D_{12} & D_{11} & 0 & 0 & 0 \\ 0 & 0 & 0 & D_{44} & 0 & 0 \\ 0 & 0 & 0 & 0 & D_{44} & 0 \\ 0 & 0 & 0 & 0 & 0 & D_{44} \end{bmatrix} . \tag{B-25}$$

In order to more clearly investigate the ability of this type of theory to reproduce the orientation dependence of the initial yield stress, we will assume that the material behaves as an anisotropic elastic-perfectly plastic material. Consequently, we may set $\alpha_i = 0$ for the present discussion, since the kinematic shift vector α_i changes only with plastic deformation and we are concerned only with the prediction of the tensile yield stress. Also, since we are interested only in the initial yield stress and not on the subsequent tensile hardening of the stress-strain curve, we may set:

$$M_{ij} = \text{constant}; \; k = \text{constant}; \text{ and } \alpha_i = 0.$$

Consider a uniaxial tensile bar specimen of the single crystal material oriented along the direction ON in Figure B-1. When reduced to one-dimensional form, the elastic-perfectly plastic constitutive relation of Lee and Zaverl appropriate to tensile loading reduces to the following relations:

$$\sigma = E(\theta,\psi) \quad \text{for} \quad \varepsilon < Y_+(\theta,\psi)/E(\theta,\psi) \; , \tag{B-26}$$

$$\sigma = Y_+(\theta,\psi) \quad \text{for} \quad \varepsilon \geq Y_+(\theta,\psi)/E(\theta,\psi) \; . \tag{B-27}$$

In these expressions $E(\theta,\psi)$ is the value of Young's modulus in the direction ON given by the expression:

$$E(\theta,\psi) = \left[\frac{D_{11}+D_{12}}{(D_{11}+2D_{12})(D_{11}-D_{12})} + \left(\frac{1}{D_{44}} \; \frac{2}{D_{11}-D_{12}} \right) (n_x^2 n_y^2 + n_x^2 n_z^2 + n_y^2 n_z^2) \right]^{-1} , \tag{B-28}$$

with

$$n_x = -\sin\psi; \; n_y = \sin\theta \cos\psi; \; n_z = \cos\theta \cos\psi \; . \tag{B-29}$$

The tensile yield value in the direction ON is given by the relation:

$$Y_+(\theta,\psi) = \frac{\left(\frac{Y_+ - Y_-}{Y_+ Y_-} \right) + \sqrt{\left(\frac{Y_+ - Y_-}{Y_+ Y_-} \right)^2 + 4 \left\{ \frac{1}{Y_+ Y_-} + \lambda (n_x^2 n_y^2 + n_x^2 n_z^2 + n_y^2 n_z^2) \right\}}}{2 \left\{ \frac{1}{Y_+ Y_-} + \lambda (n_x^2 n_y^2 + n_x^2 n_z^2 + n_y^2 n_z^2) \right\}} \; , \tag{30}$$

with

$$\lambda = 4M_{44} + 2M_{12} - 2M_{11} = 4M_{44} - 3M_{11} \; . \tag{B-31}$$

The constant λ measures the deviation from isotropy and $\lambda = 0$ in the case of an isotropic material, while the constants Y_+ and Y_- are the tensile and compressive yield stresses along any of the three crystallographic axes, the properties along each axis being assumed to be equivalent.

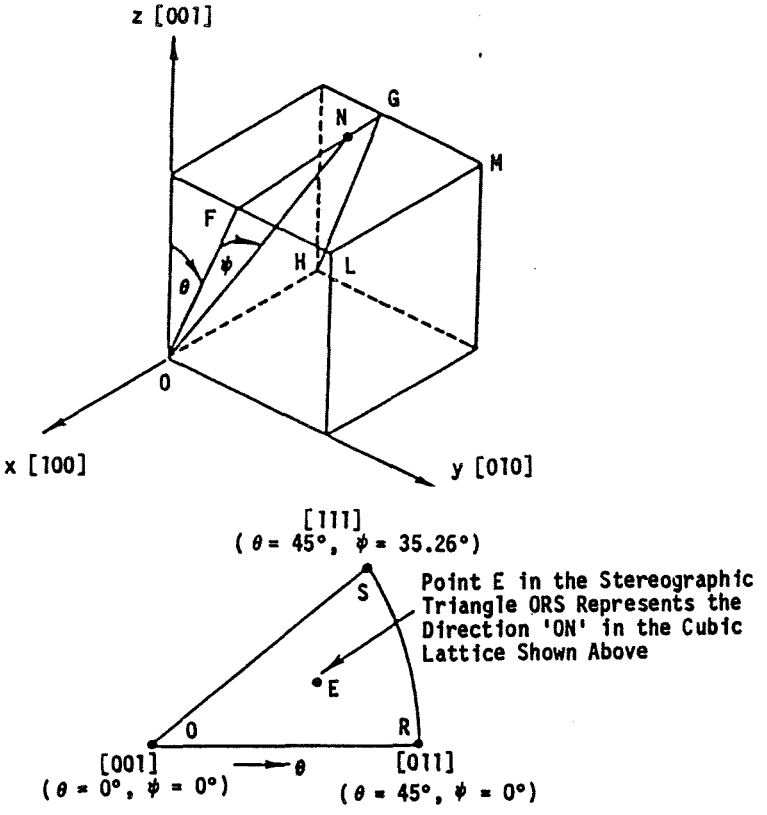

Figure B-1 A Single Crystal Bar Oriented Along ON at Angles θ and ψ With Respect to the Crystal Axes X, Y, Z is Located at Point E in the Stereographic Triangle ORS.

Figures B-2 and B-3 show actual and predicted variation of the tensile yield stress, $Y_+(\theta,\psi)$, as a function of the orientation angles θ and ψ for the case of single crystal PWA 1480 at 593°C (1100°F). It is evident from Figure B-2 that the theoretical prediction of the yield stress variation with θ for the case where $\psi=0^\circ$, i.e., along the [001]-[011] boundary of the stereographic triangle in Figure B-3, shows a yield stress which decreases continually from a maximum at $\theta=0^\circ$ (along the [001] direction) to a minimum at $\theta=45^\circ$ (along the [011] direction). A further decrease in the tensile yield stress occurs as ψ increases towards the [001]-[111] boundary of the stereographic triangle. An absolute minimum in the theoretical prediction occurs in the [111] direction where $\theta=45^\circ$ and $\psi=35.26^\circ$. In the experimental data shown in Figure B-3, the variation of yield stress along the [001]-[011] boundary of the stereographic triangle shows a minimum value around $\theta=35^\circ$.

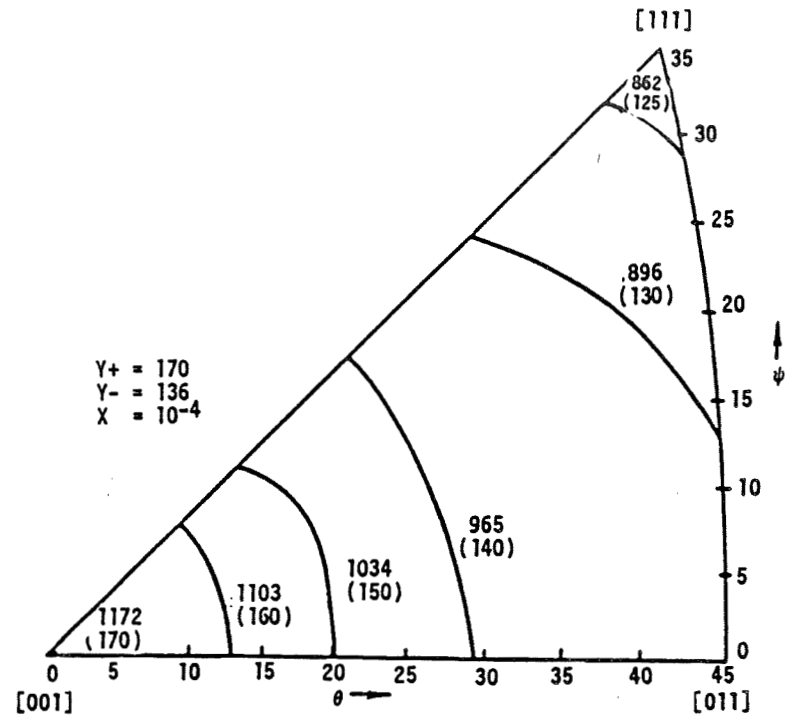

Figure B-2 593°C (1100°F) Tensile Iso - Yield Contours for PWA 1480 Based on Lee and Zaverl's Theory; MPa (ksi)

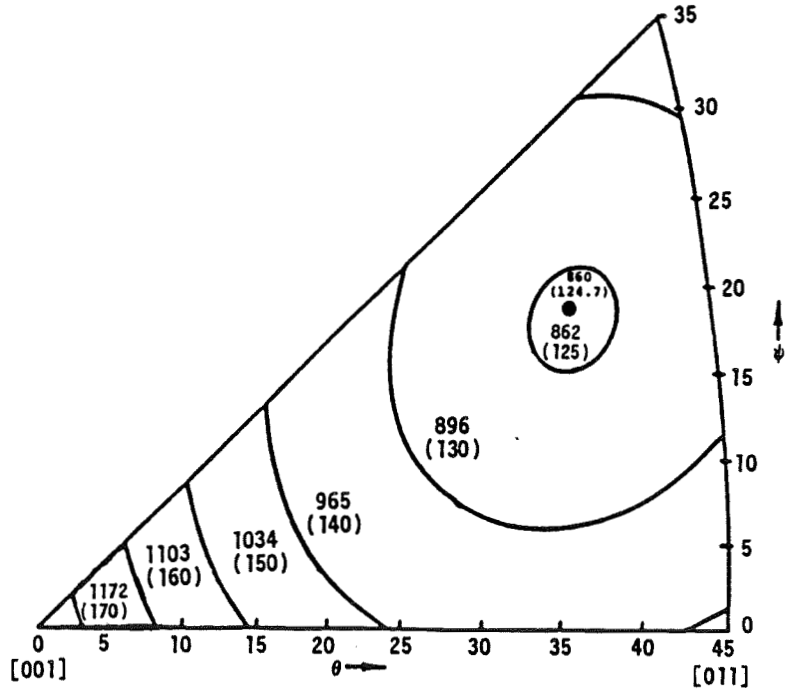

Figure B-3 Experimental Tensile Iso - Yield Contours for PWA 1480

The experimental data are more consistent with the notion that the material yields when the resolved shear stress reaches a critical value in one of the slip directions on one of the crystallographic slip planes. For slip which occurs in the {111} octahedral planes in the <110> type slip directions, the variation of yield stress with angle θ along the [001]-[011] boundary of the stereographic triangle is given by the relation,

$$Y_+(\theta,\psi=0^\circ) = \frac{Y_+ \ (\theta=0^\circ, \ \psi=0^\circ)}{\cos\theta \ (\sin\theta + \cos\theta)} \quad . \qquad \text{(B-32)}$$

This expression is plotted in Figure B-4 and exhibits a "U" shaped curve in which the minimum yield stress occurs at $\theta = 22.5^\circ$. The experimental data are also plotted in this figure for comparison purposes. More will be said concerning the micromechanics of crystalline slip in the next section. The point to be made here is that a minimum is observed in the experimental data which is more consistent with a crystalline slip theory than with a continuum formulation.

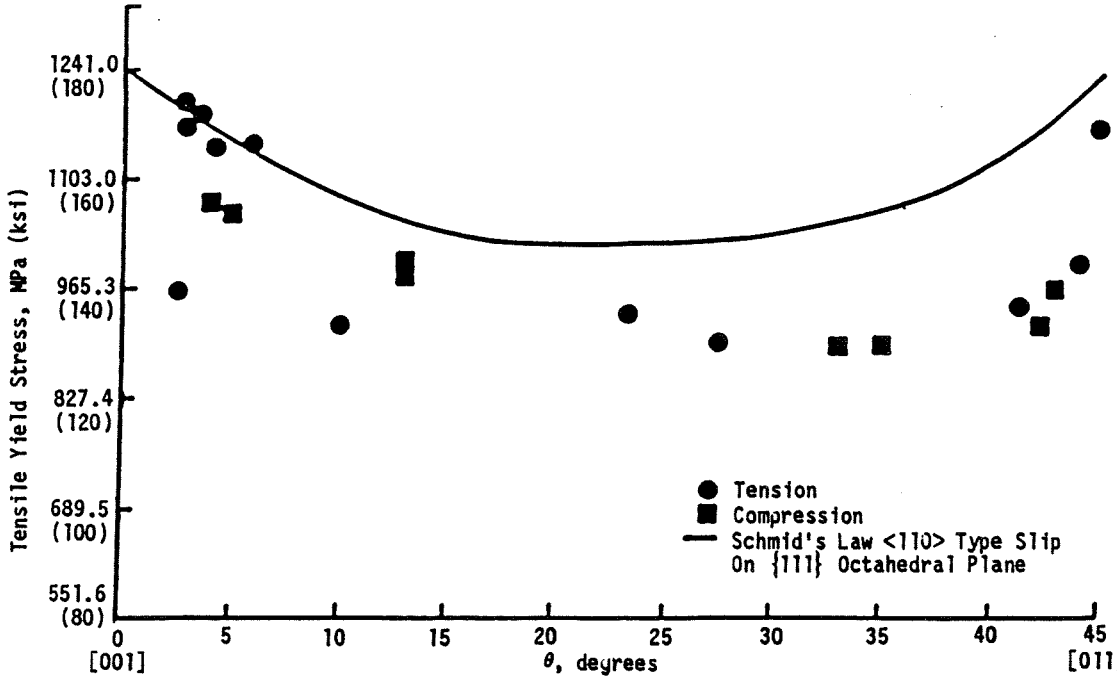

Figure B-4 The Experimental 593°C (1100°F) Yield Strength of PWA 1480 Vs. Orientation Along the [001] - [011] Boundary of the Stereographic Triangle

In general, the as-cast single crystal does not exhibit complete symmetry along the three crystallographic axes. For example, Kear and Piercey (Reference 14) show that creep rupture lives along the [001], [100] and [010] crystallographic axes for single crystals of Mar-M200 are 325, 71 and 82 hours respectively at a stress level of 670 MPa (100 ksi). After heat treatment for one hour at 1232°C (2250°F) and 32 hours at 871°C (1600°F), the creep rupture lives were 459, 365, and 443 hours, respectively. The heat treatment produces equality of behavior along the crystallographic axes. In the as-cast material prior to heat treatment, the inequality of material behavior along the crystallographic axes is attributed to dendrite morphology. Initially, material bars cut parallel to the continuous dendrite arms along the [001] growth axes exhibited a longer creep rupture life than material tested parallel to the discontinuous side arms of the dendrites along the [100] and [010] directions. The significance of this observation is that better correlation with the experimental results may be obtained if the cubic symmetry restriction is relaxed and the matrix M_{ij} is assumed to have the general form depicted in equation (B-2).

Directionally solidified materials consisting of columnar grains of single crystals oriented at random about the grain growth direction may be modeled as transversely isotropic material if a sufficient number of grains are sampled in the transverse plane. In modeling single crystals with cubic symmetry only two independent constants are needed in the matrix M_{ij} and three in the elasticity matrix D_{ij}. The incompressibility of plastic flow reduces the number of independent constants in M_{ij} from three to two. Five constants are required in the matrices D_{ij} and M_{ij} for directionally solidified materials which exhibit transversely isotropic behavior. However, the incompressibility condition for the plastic strain reduces the number of independent constants in M_{ij} from five to three. These transversely isotropic matrices have the form:

$$[D] = \begin{bmatrix} D_{11} & D_{12} & D_{13} & 0 & 0 & 0 \\ D_{12} & D_{11} & D_{13} & 0 & 0 & 0 \\ D_{13} & D_{13} & D_{33} & 0 & 0 & 0 \\ 0 & 0 & 0 & D_{44} & 0 & 0 \\ 0 & 0 & 0 & 0 & D_{44} & 0 \\ 0 & 0 & 0 & 0 & 0 & \frac{1}{2}(D_{11}-D_{12}) \end{bmatrix}, \quad \text{(B-33)}$$

and

$$[M] = \begin{bmatrix} M_{11} & M_{12} & M_{13} & 0 & 0 & 0 \\ M_{12} & M_{11} & M_{13} & 0 & 0 & 0 \\ M_{13} & M_{13} & M_{33} & 0 & 0 & 0 \\ 0 & 0 & 0 & M_{44} & 0 & 0 \\ 0 & 0 & 0 & 0 & M_{44} & 0 \\ 0 & 0 & 0 & 0 & 0 & \frac{1}{2}(M_{11}-M_{12}) \end{bmatrix} , \quad \text{(B-34)}$$

in which x_3 is the columnar growth direction of the single crystal grains. The incompressibility assumption gives:

$$M_{12} = -\frac{1}{2}(2M_{11} - M_{33}) \text{ and } M_{13} = -\frac{1}{2} M_{33} , \quad \text{(B-35)}$$

which reduces the number of independent constants in M_{ij} from five to three.

The requirement of transverse isotropy can be met in practice if the number of grains is large with respect to the reference section (or equivalently the grain size is very small), such as the wall thickness of an airfoil. It is also necessary that the growth axes of the columnar crystals coincide with the growth axes of the composite directionally solidified material and that the secondary crystal orientations about the growth axes are distributed at random. Usually, limitations imposed by both the solidification process and the specimen size make it extremely difficult to meet the preceding theoretical requirements and significant scatter must be expected. Due to this scatter, it may again be necessary to revert to the more general matrices given in equations (B-2) and (B-19) to fit the actual material behavior.

A constitutive equation for modeling secondary creep in directionally solidified eutectic alloys, based on a generalization of the Bailey-Norton creep law to transversely isotropic materials, was proposed by Johnson (Reference 16) in 1977. The theoretical model was developed by assuming that the constitutive equation is:

$$c_{ij} = \frac{\partial \phi}{\partial \sigma_{ij}} , \quad \text{(B-36)}$$

where ϕ is a function of the three invariants of the deviatoric stress tensor s_{ij} in addition to the invariants $I^*_{ij}s_{ji}$ and $s_{ij}I^*_{jk}s_{ki}$, where $I^*_{ij} = d_i d_j$ with d_i denoting a unit vector along the growth direction of the transversely isotropic material. A similar theory, in which the Bailey-Norton creep law is replaced with Robinson's constitutive model, was proposed by Robinson in Reference 17. The matrix M_{ij} which relates the inelastic strain rate to the stress components ($\sigma_{ij} - \Omega_{ij}$ or σ_{ij}) is of the same form in the models of Robinson, Johnson and Lee and Zaverl, and contains three independent constants for the case of transverse material isotropy and two in the case of cubic symmetry.

Stouffer and Bodner (Reference 18) have extended the Prandtl-Reuss flow rule to allow for anisotropy in which the inelastic strain rate is related to the deviatoric stress through the relationship:

$$\dot{c}_i = \lambda_{ij} s_j \,, \tag{B-37}$$

where the matrix λ_{ij} is a function of stress and deformation history and is constrained to satisfy the incompressibility condition. Further work on this model is being pursued by Stouffer.

Micromechanical Slip Theory Formulations

An analysis of single crystal superalloys undergoing steady state creep deformation was presented by Paslay, Wells and Leverant (Reference 19) in 1970 using a theoretical formulation based on crystallographic slip theory of face centered cubic materials. In 1971, the theory was applied by Paslay, Wells, Leverant and Burck (Reference 20) to describe the creep behavior of single crystal nickel-base superalloy tubes under biaxial tension loading conditions. Steady state creep formulations suitable for the analysis of single crystals were used by Brown (Reference 21) in 1970 and by Hutchinson (Reference 22) in 1976 to predict the behavior of polycrystalline materials whose aggregate consists of randomly oriented single crystal grains. Recently, Weng (Reference 23) has developed a single crystal creep formulation which accounts for transient (primary) as well as steady state (secondary) creep. However, in order to describe the combined plastic and creep behavior of polycrystalline materials, Weng combines the rate-independent and rate-dependent components of crystal behavior in such a way that each component is governed by a separate constitutive relation, i.e., plasticity and creep are assumed to be uncoupled phenomena.

A special issue of the ASME Journal of Engineering Materials and Technology published in October, 1984, is devoted entirely to the micro and macro aspects of constitutive equations. This edition contains the latest version of a physical theory of plasticity and creep proposed by Lin (Reference 24) which averages a single crystal model to obtain a stress-strain relationship for an isotropic polycrystalline aggregate. Krempl and Lu (Reference 25) also discuss the latent hardening effects observed in fully annealed AISI type 304 stainless steel under biaxial in-phase and out-of-phase strain cycling at room temperature.

In the decade of the seventies, the creep and plastic responses of materials were combined into unified viscoplastic formulations (Reference 15). These formulations differ from steady state creep theories by introducing history dependent state variables to account for primary creep and plasticity. Most of these unified theories exhibit an elastic response under instantaneous deformation and can be integrated easily using an explicit forward difference method. An anisotropic slip theory formulation suitable for representing viscoplastic material behavior of single crystal materials at elevated

temperature can therefore be obtained by replacing the secondary creep model in Paslay, Wells, Leverant and Burck's formulations with a suitable unified viscoplastic formulation. The single crystal slip model has been embedded in a self-consistent formulation to model the behavior of transversely isotropic directionally solified materials. This work is proceeding under a grant to the University of Connecticut (Reference 26) sponsored by the NASA-Lewis Research Center. Similar work is being undertaken by Stouffer at the University of Cincinatti also under sponsorship from the NASA-Lewis Research Center.

The constitutive formulation represented in Reference 6 has treated the single crystal as if it were a homogeneous single crystal material. In fact, nickel-base superalloys such as PWA 1480 are composed of face centered cubic γ' particles of cuboidal shape embedded in a face centered cubic γ solid solution matrix. Shah and Duhl (Reference 27) have studied the behavior of PWA 1480 in detail and have concluded that the deformation is strongly influenced by the γ-γ' structure. Constitutive equations for the composite γ-γ' mixture could be set up in the manner employed by Nemat-Nasser and his colleagues in References 28 through 30. The work reported in Reference 30 was sponsored by the NASA-Lewis Research Center and can easily be adapted to the modeling of γ-γ' mixtures of single crystal materials. Further references pertinent to the development of viscoplastic slip constitutive models can be found in Reference 26.

References

1. Hill, R., "A Theory of The Yielding and Plastic Flow of Anisotropic Metals," Proc. Royal Society of London, Ser. A, Vol. 193, pp. 281-297, 1948.

2. Edelman, F. and D. C. Drucker, "Some Extensions of Elementary Plasticity Theory," J. Franklin Institute, Vol. 251, pp. 581-605, 1951.

3. Yoshimura, Y., "Hypothetical Theory of Anisotropy and the Bauschinger Effect Due to Plastic Strain History," Report No. 349, Aeronautical Research Institute, University of Tokyo, pp. 221-247, 1959.

4. Williams, J. F. and N. L. Svensson, "A Rationally Based Yield Criterion for Work Hardening Materials," Meccanica, Vol. 6, pp. 104-114, 1971.

5. Baltov, A. and A. Sawczuk, "A Rule of Anisotropic Hardening," Acta Mechanica, Vol. 1, pp. 81-92, 1965.

6. Fisher, J. C., "Anisotropic Plastic Flow," ASME Journal of Applied Mechanics, Vol. 71, No. 4, pp. 349-356, 1949.

7. Hu, L. W. and J. Marin, "Anisotropic Loading Functions for Combined Loading in the Plastic Range," ASME Journal of Applied Mechanics, Vol. 22, pp. 77-85, 1955.

8. Bogue, D. C., "The Yield Stress and Plastic Strain Theory for Anisotropic Materials," Report No. ORNL-TM-1869, Oak Ridge National Laboratory, Oak Ridge, TN, 1967.

9. Shahibi, S. N. and A. Shelton, "The Anisotropic, Yield, Flow and Creep Behavior of Prestrained EN-24 Steel," Journal of Mechanical Engineering Science, Vol. 17, No. 2, pp. 93-104, 1975.

10. Lee, D. and W. A. Backofen, "An Experimental Determination of the Yield Locus for Titanium and Titanium-Alloy Sheet," Trans. AIME, Vol. 236, pp. 1077, 1966.

11. Eisenberg, M. A. and C. F. Yen, "A Theory of Multiaxial Anisotropic Viscoplasticity," ASME Journal of Applied Mechanics, Vol. 48, pp. 276-284, 1981.

12. Lee, D., F. Zaverl, Jr., C. F. Shih and M. D. German, "Plasticity Theories and Structural Analysis of Anisotropic Metals," Report No. 77CRD285, General Electric Corporate Research and Development Center, Schenedtady, NY, 1977.

13. Lee, D., "Anisotropic Yielding Behavior of a Fiber-Reinforce Directionally Solidified Eutectic Alloy," Metallurgical Transactions A, Vol. 9A, pp. 1477-1481, 1978.

14. Kear, B. H. and B. J. Piercey, "Tensile and Creep Properties of Single Crystals of the Nickel-Base Superalloy Mar-M200," Trans. of AIME, Vol. 239, pp. 1209-1215, 1967.

15. Walker, K. P., "Research and Development Program for Nonlinear Structural Modeling with Advanced Time-Temperature Dependence Constitutive Relationships," NASA CR-165533, November 1981.

16. Johnson, A. F., "Creep Characterization of Transversely Isotropic Metallic Materials," J. Mech. Phys. Solids, Vol. 25, pp. 117-126, 1977.

17. Robinson, D. N., "Constitutive Relationships for Anisotropic High-Temperature Alloys," NASA Technical Memorandum 83437, 1983.

18. Stouffer, D. C. and S. R. Bodner, "A Constitutive Model for the Deformation Induced Anisotropic Flow of Metals," Int. J. Engineering Science, Vol. 17, pp. 757-764, 1979.

19. Paslay, P. R., C. H. Wells and G. R. Leverant, "An Analysis of Primary Creep of Nickel-Base Superalloy Single Crystals," ASME Journal of Applied Mechanics, Vol. 37, pp. 759-764, 1970.

20. Paslay, P. R., C. H. Wells, G. R. Leverant and L. H. Burck, "Creep of Single Crystal Nickel-Base Superalloy Tubes under Biaxial Tension," ASME Journal of Applied Mechanics, Vol. 38, pp. 623-626, 1971.

21. Brown, G. M., "A Self-Consistent Polycrystalline Model for Creep Under Combined Stress States," J. Mech. Phys. Solids, Vol. 18, pp. 367-381, 1970.

22. Hutchinson, J. W., "Bounds and Self-Consistent Estimates for Creep of Polycrystalline Materials," Proc. Royal Society of London, Vol. A348, pp. 101-127, 1976.

23. Weng, G. J., "The Influence of Fatigue Stress on the Creep Behavior of Metals," Acta Metallurgical, Vol. 31, pp. 207-212, 1983.

24. Lin, T. H., "A Physical Theory of Plasticity and Creep," ASME Journal of Engineering Materials and Technology, Vol. 106, pp. 290-294, 1984.

25. Krempl, E. and H. Lu, "The Hardening and Rate-Dependent Behavior of Fully Annealed AISI Type 304 Stainless Steel Under Biaxial In-Phase and Out-of-Phase Strain Cycling at Room Temperature," ASME Journal of Engineering Materials and Technology, Vol. 106, pp. 376-382.

26. Walker, K. P. and E. Jordan, "First-Annual Report on NASA Grant NAG-512," 1985.

27. Shah, D. M. and D. N. Duhl, "The Effect of Orientation, Temperature and Gamma Prime Size on the Yield Strength of a Single Crystal Nickel Base Superalloy," Superalloys 1984, Ed. by M. Gell et. al., Met. Soc. AIME, 1984.

28. Nemat-Nasser, S. and M. Taya, "On Effective Moduli of an Elastic Body Containing Periodically Distributed Voids," Quat. Appl. Math, pp. 43-59, 1981.

29. Nemat-Nasser, S. and T. Iwakuna, "Finite Elastic-Plastic Deformation of Composites," Proceedings of IVTAM Symposium on Mechanics of Composite Materials, Blacksburg, VA, August 16-19, 1982.

30. Iwakuna, T. and S. Nemat-Nasser, "Composites with Periodic Microstructure," Computers and Structures, Vol. 16, pp. 13-19, 1983.

APPENDIX C

LITERATURE SURVEY - SINGLE CRYSTAL LIFE PREDICTION

C.1 Introduction

All of the life prediction models published in literature have been developed for conventional multigrained materials which are considered isotropic for analysis purposes. It is generally accepted that structural failures result from subjecting materials to inelastic strains. Applications to anisotropic single crystal material are documented only for a few of these models. The role of coatings on cracking is not modeled although coated specimen data are used by some investigators.

The published life prediction models relate time to failure (life) to the inelastic strain or its time dependent (creep) and time independent (plastic) strain components. Three different approaches are used:

1) life related to macroscopic inelastic strain and cycle parameters (phenomenological models);

2) life related to damage explicitly caused by creep and plasticity (cumulative damage models); and

3) life related to local inelastic strain at a void and/or crack tip (crack growth models).

A number of the existing models which are surveyed in Sections C.2 through C.4.2 of this appendix have potential for extension to hot section anisotropic materials under the current base program. However, methods must be developed to account for the important effects of the base alloy anisotropy and the coatings. In essence, coatings are thin layers of isotropic materials on the surface of the base alloy. A review of published metallographic work on single crystal crack initiation and the role of coatings on crack initiation is included in Section C.5.

C.2 Phenomenological Models

The Coffin-Manson model (References 1 and 2) has been used as the starting point by many investigators interested in predicting cracking life of structures subjected to cyclic loadings. Originally defined for low and intermediate temperature application, this model assumed a logarithmic relationship between plastic strain range and low cycle fatigue life.

$$\Delta\varepsilon_p \, N_f^{\,B} = C \qquad \text{(C-1)}$$

where $\Delta\varepsilon_p$ = plastic strain range,
N_f = number of cycles to crack, and
B, C = material constants.

At high temperature conditions, damage due to both plastic and creep strains can occur. To account for the creep effects, the Coffin-Manson equation has been modified by substituting inelastic strain range ($\Delta\varepsilon_{inel}$) for $\Delta\varepsilon_p$ (Reference 3). This allows the effects of creep to be implicitly included in the model, but only for those load conditions used in material property tests for model development. Using $\Delta\varepsilon_{inel}$ as the single correlation variable does not allow extending this model to other load conditions, i.e., cycle shapes, hold times, strain rates, mean stresses, and temperature cycles which cause different amounts of creep.

The Frequency Modified Life model of Coffin extends the Coffin-Manson model at elevated temperatures by introducing a frequency correction (References 4 and 5). This model is described by the following equation:

$$\Delta\varepsilon_{inel} \cdot (N_f \cdot \nu^{k-1})^{\beta} = C_2 \qquad \text{(C-2)}$$

where ν = cycle frequency, and

$k, \beta, C2$ = material constants.

Frequency correction is important at high temperatures because of strain rate, dwell time at a given stress, and possible environmental interaction effects on low-cycle fatigue (Reference 6). Material property data obtained by specimen testing at elevated temperatures inherently reflect load cycle frequencies used in conducting the tests. The frequency modification provides a single correction to extend data to other frequencies than those used in testing. However, corrections for load and temperature cycle shape variations are not possible by this method.

It is important to note that the frequency correction used in this model distinctly depends on temperature. As stated above, a correction is important at high temperatures while no correction appears necessary at low temperatures where creep cannot occur. This implies that the frequency correction depends on the temperature level, analogous to creep rate, and a single low-cycle fatigue correlation does not apply at all "high" temperatures (Reference 5). However, satisfactory correlations can be achieved for individual isothermal conditions (References 5, 7 and 8).

The Frequency Separation method (References 9 and 10) further improves the two previous models by accounting for the unbalanced tensile and compressive portions of the load cycle and recognizing that compressive and tensile creep damages are different. This model can be described by an equation very similar to that of the Frequency Modified model, except the absolute frequency is replaced by the tension going frequency term and a frequency unbalance correction strain range is used:

$$\Delta\varepsilon'_{inel} \cdot \left[N_f \cdot \left(\frac{\nu_T}{2} \right)^{k-1} \right]^{\beta} = C_2 \qquad \text{(C-3)}$$

where $\Delta\varepsilon'_{inel} = \frac{\Delta\varepsilon_{inel}}{2}\left[\left(\frac{\nu_c}{\nu_T}\right)^{k_1} + 1\right]$, (C-4)

ν_T = tensile going frequency (1/time for $\dot{\varepsilon}_{inel} > 0$),

ν_c = compression going frequency (1/time for $\dot{\varepsilon}_{inel} < 0$), and

k, k_1, β, C_2 = material constants.

This formulation is based on the concept that low cycle fatigue damage is similar to crack growth process where damage occurs mainly when the crack is opening as intense local tensile strains are formed and the crack tip advances by local fracture.

A different frequency separation approach is described in Reference 11, using a modified equation of the following form:

$$\Delta\varepsilon_{inel} \cdot \left[N_f \cdot \nu_T^{k-1}\right]^{\beta} \cdot \left(\frac{\nu_c}{\nu_T}\right)^{k_2} = C'_2 \qquad \text{(C-3A)}$$

Both unbalance corrections account for the relative times in compression and tension but again do not consider stress levels for each. For this reason, this model is sometimes interpreted to be more appropriate for environmental damage than creep effects on low cycle fatigue (Reference 11).

The Tensile Hysteretic Energy model was developed by Ostergren (Reference 12) to account for the observed influence of strain cycle shapes on low cycle cracking life. The model relates cracking life to inelastic tensile strain energy and in this manner includes the combined effects of both unbalanced time and unbalanced loading. This result is yet another formulation very similar to that of Frequency Modified Life, but includes the effects of time, temperatures and loads.

$$\Delta W_T \cdot \left(N_f \cdot \nu^{k-1}\right)^{\beta} = C_1 \qquad \text{(C-5)}$$

where ΔW_T = tensile hysteretic energy,

$$\nu = \begin{cases} \dfrac{1}{\tau_0+\tau_T-\tau_C} & \text{for } \tau_T > \tau_C \\ \dfrac{1}{\tau_0} & \text{for } \tau_T \le \tau_C \end{cases}$$

τ_0 = time per cycle for continuous cycling,

τ_T = tension hold time, and

τ_C = compression hold time.

The basis for this model also is that low cycle fatigue is considered to be essentially a problem of crack propagation from inherent defects or microcracks which initiate in a very small number of cycles. Consequently, it is assumed that the deformation which contributes to damage by propagating the crack occurs during the portion of load cycle when the crack is open. Next, it is recognized that both tensile and compressive hold times increase time dependent inelastic strains. But tensile hold leads to compressive mean stress while compressive hold leads to tensile mean stress and a larger tensile portion for the hysteresis loop. Noting that the compressive hold times were found to be more damaging than tensile hold times in high temperature materials, it followed that the net tensile hysteretic energy is used as the measure of damage.

For computation convenience, it may be assumed in most cases that:

$$\Delta W_T = \alpha \cdot \sigma_T \cdot \Delta\varepsilon_{inel}$$

where α = shape factor for tensile hysteresis loop, and

$$\sigma_T = \bar{\sigma} + \frac{\Delta\sigma}{2} = \text{maximum tensile stress.}$$

Consequently, the model formulation may be changed to:

$$\sigma_T \cdot \Delta\varepsilon_{inel} \cdot (N_f \cdot \nu^{k-1})^{\beta} = C'_1 \qquad \text{(C-6)}$$

The frequency modification term definition used in this model is empirically selected. Modified definitions have been used when environmental instead of time dependent strain effects are modeled (Reference 11). In all cases, the frequency modification may depend on temperature, however.

The tensile hysteretic energy model was recently investigated for application to B-1900+Hf material under high temperature fatigue loads (Reference 3). The results showed consistent under prediction for some data sets, indicating that the total tensile hysteresis area is not equally damaging and/or the damaging portion of hysteresis area was not accurately sized because effects of back stress were not included. A second difficulty was that of accurately determining the area when inelastic strains are small, an important condition for most long life turbine blades. Both of these results are related to modeling the constitutive behavior of the material and reflect the current state of understanding of such behavior.

The Tensile Hysteretic Energy model was recently also applied to limit correlation of isothermal low cycle fatigue (LCF) and thermomechanical fatigue (TMF) data of PWA 1480 single crystal material (References 13 and 14). In order to account for the crystal geometry and loading axis orientations, the hysteretic energy term was normalized by the resolved octahedral normal stress and the modulus in the loading direction. Excellent consolidation of the LCF data was obtained for [001] and [111] specimens in the uncoated condition and including test temperatures of 427°C, 760°C and 980°C (800°F, 1400°F and 1800°F).

The TMF testing involved a very limited test of PWA 273 coated specimens of [001] and [111] orientations. The data were obtained using strain controlled loading in combination with an out-of-phase temperature cycle, for which the maximum compressive load occurs at the maximum temperature and maximum tensile load at the minimum temperature (Cycle I TMF). Although both the applied strain load and temperature had a balanced cycle with respect to time, an unbalanced hysteresis loop resulted because the material properties change with temperature. Since the Young's Modulus changes with temperature, that portion of total strain range which is inelastic was difficult to determine accurately. Although the final correlation for the tests used inelastic strain estimated from isothermal data at cycle mean temperature (Reference 14), the applicability of this to more general and unbalanced cycles needs to be evaluated. The inelastic strains could also be determined by analysis, provided accurate constitutive models can be developed.

The Stress-Strain-Time (SST) model is identical in content to the Hysteretic Energy model except the loading terms are normalized to material strength capabilities (Reference 15).

$$N_f = A \cdot \left(\frac{\Delta\varepsilon}{\varepsilon_f}\right)^b \cdot \left(\frac{\sigma_T}{\sigma_y}\right)^c \cdot \tau^d \qquad \text{(C-7)}$$

where $\Delta\varepsilon$ = strain range,

εf = true strain at fracture,

σT = peak tensile stress,

σy = yield stress,

$$\tau = \begin{cases} \tau_0 + \tau_T + \tau_C & \text{for } \tau_T > \tau_C \\ \tau_0 & \text{for } \tau_T < \tau_C \end{cases}$$

τ_0 = time per cycle spent in cycling,

τ_T = time per cycle spent in tension hold, and

τ_C = time per cycle spent in compression hold.

The SST model was intended to provide a general framework into which the behavior of many different materials and load conditions could be incorporated. This is accomplished by allowing a choice of inelastic, elastic or total strain ranges for the correlating load parameter, depending on which strain provides the best correlation for the material and condition evaluated. Additionally, the stress term is used only when mean stresses are present, and frequency separation methods are permitted, although not recommended, under some conditions.

C.3 Cumulative Damage Models

The cumulative damage approaches assume that the plastic and creep components of inelastic strain cause damage which can be explicitly predicted and which define the state of the material. Damage is considered to be zero in the initial undamaged state and failure occurs when a critical level or limit is reached due to plastic, cyclic creep or monotonic creep deformations. A number of different definitions of damage and approaches for counting damage are used. Nearly all of these require use of a constitutive model to determine the portion of damage caused by a particular load condition. Life prediction models which use this approach are: Linear Time and Cycle Fraction, Ductility Exhaustion, Continuous Damage, Strain Range Partitioning, and Cyclic Damage Accumulation.

C.3.1 Linear Time and Cycle Fraction Method

One of the most widely used and highly developed cumulative damage life prediction schemes is the linear time, cycle fraction damage summation (Reference 16). A number of versions of this method have been employed. One of the most popular is that of code case 1592 of the ASME Boiler and Pressure Vessel Code (Reference 17). The basic equations for this method are shown below.

$$\sum_{j=1}^{p} \left(\frac{n}{N_d}\right)_j + \sum_{m=1}^{q} \left(\frac{t}{t_d}\right)_m \leq D \qquad \text{(C-8)}$$

where n = number of applied cycles at loading condition,

N_d = life in cycles at loading condition,

t = hold time at load and temperature,

t_d = stress-rupture life at load and temperature, and

D = allowable damage before failure.

In some versions of the linear time and cycle fraction method, it was assumed that failure occurs when damage equals 1.0. In the ASME Pressure Vessel and Boiler Code, this assumption is dropped and the damage at failure is a nonlinear function of creep/fatigue life fractions.

In order to use this method, correlations for predicting both N_d and t_d must be available for load ranges of interest. These usually are stress-time to rupture and strain-life relations similar to the Coffin-Manson model described above. Both are usually temperature dependent.

For thermomechanical fatigue (TMF), the temperature is not constant and the prediction of N_d and t_d is complicated. An effective method is not yet available for predicting N_d for thermomechanical conditions, and, therefore, data for the temperature which yields a minimum life at a given strain usually are chosen when TMF data are unavailable. For the creep component of damage, however, the variable temperature can be dealt with using an integral equation (References 16 and 18) shown below.

$$\sum \frac{t}{t_d} = \int_0^t \frac{dt}{t_r(|S|,T)} \qquad \text{(C-9)}$$

where $t_r(|S|,T)$ = stress-rupture life at absolute stress level and temperature.

Using these two methods of dealing with variable temperature, several different thermomechanical fatigue results have been successfully predicted (References 19 and 20). Isothermal results involving hold times also have been predicted (References 21 and 22).

In spite of these successes, there is considerable evidence to suggest that the linear time and cycle fraction method is not satisfactory (References 10, 22 and 23). Manson discussed some reasons for this at a 1978 AGARD conference (Reference 23). These pertain to describing the effects of complex damage histories and assessing damage due to compressive creep. The basic assumption for the linear model is that cyclic fatigue and creep damage components are mutually independent and can be calculated separately (Reference 24). This appears a consequence to the early observation that fatigue failures usually result in transgranular cracking while stress rupture cracks occur in grain boundaries in multigrained materials, and generally is not an accurate assessment of high temperature damage processes.

Finally, since the linear model does not account for the different types of unbalanced creep, modeling effects of the observed tension/compression asymmetry in single crystals would clearly make the use of this model even more difficult. In principle, the directionality of fatigue and tensile properties could be accounted for in this method. But use of this model when the principal fatigue stress directions are not coincident with the creep directions is beyond demonstrated experience.

C.3.2 Ductility Exhaustion

Ductility Exhaustion theory assumes that ductility is a material property and that fatigue and creep use up ductility to produce failure. In a given cycle, the ductility is debited a certain amount for the fatigue damage and a certain amount for the creep damage. The individual damage components are calculated using conventional fatigue life and creep curves and incrementally cumulated cycle by cycle. Failure results when the ductility has been exhausted. One version of this method used by Pratt & Whitney (Reference 24) is described as follows.

The fatigue life is defined as a logarithmic relationship between total strain range and life:

$$\Delta\varepsilon_T \cdot (N_f)^{1/a} = K \qquad \text{(C-10)}$$

where $\Delta\varepsilon_T$ = total strain range,

$$K = \left[\frac{(2\varepsilon_f)^a}{4}\right]^{\frac{1}{a}},$$

ε_f = 1/4 cycle intercept or fracture ductility, and

a = material constant.

The decrease in available ductility produced after n fatigue cycles is then written as:

$$\Delta\varepsilon_f = \varepsilon_f \left[1 - 4n \left(\frac{\Delta\varepsilon_T}{2\varepsilon_f}\right)^a\right]^{\frac{1}{a}} \qquad \text{(C-11)}$$

A decrease in available ductility due to creep is equal to the amount of creep.

Ductility decrements from such cycling and creep can then be accumulated by stepwise progression along a creep-time curve to the point where the initially available ductility is exhausted. The creep curve is selected to be representative of the material behavior. The form of the equation for several current materials can be approximated by a power law.

$$\varepsilon_c = A\, t^b \qquad \text{(C-12)}$$

where t = time, and

A, B = material constants at stress and temperature.

In this method it is assumed the fatigue damage and creep damage are contributors to failure. As originally developed and currently implemented at Pratt & Whitney, thermal mechanical fatigue data are utilized to determine the fatigue ductility equation. Since a "faithful" test cycle could be used for obtaining these data, the cyclic creep strains are directly included in the fatigue data and the ductility exhaustion calculation accounts only for the effects of monotonic creep during hold. This method has been found quite satisfactory for certain cycles, especially those associated with turbine blades. The creep and fatigue damage interaction is nonlinear and depends on the fracture ductility and the creep curve shape (Reference 24).

In a recent investigation (Reference 3), the fatigue data were generated using rapid strain cycling resulting in practically no cyclic creep damage. For subsequent slower cycles and cycles including hold times, cyclic creep effects were added by the ductility exhaustion calculations and resulted in under-predicting life for these test conditions. Life trends observed in additional tests at varying R-ratios were found to be not predicted. These difficulties to account for the cycle shapes are not completely unexpected since: 1) the model has the same limitation to predicting compressive creep effects as the linear fraction method, and 2) no phenomenological correction is provided for maximum and mean stress effects.

C.3.3 Continuous Damage

The Continuous Damage prediction model (References 27 through 30) is a stress based model which assumes that the low cycle fatigue process can be described by a latent internal damage parameter (D) which defines the progressive deterioration process taking place between the initial undamaged state and final failure. The deterioration model is that of the growth of assumed microdefects which are distributed throughout the material volume so that material strength can still be considered to be homogeneous on a macroscopic level. These microdefects may actually include effects of a number of metallurgical phenomena, including slip, ascent of dislocations, and inter- or intragranular microcracks (Reference 28). The failure is considered to be the initiation of larger cracks which affect the local stress distributions.

A characteristic feature of the Continuous Damage model is the definition of damage growth in differential form for both the creep and fatigue damage components.

$$dD = f(\sigma, D, T)\, dt + g(\sigma_M, \overline{\sigma}, D, T)\, dN \qquad \text{(C-13)}$$

where D = damage parameter,

f = creep damage rate,

g = cyclic damage rate,

σ = instantaneous stress,

σ_M = maximum stress for load cycle,

$\bar{\sigma}$ = average stress for load cycle,

T = temperature,

t = time for creep, and

N = fatigue cycles.

When the two damage rate terms, selected to define failure behavior of a particular material, and the loads are simply formulated, this expression can be integrated between suitable bounds and an analytical solution obtained. However, numerical solution techniques will be required when simple formulations are not possible. A nonlinear creep and fatigue life relationship results due to the presence of D in both parts of the differential equation.

In the published work (References 27 through 30), the creep damage is modeled for constant or slowly varying loads using an equation based on those of References 25 and 26, modified to provide a more general nonlinear form dictated by the materials studied. Tensile and compressive anisotropy, if any, could be treated by this form (Reference 30).

$$\frac{dD_c}{dt} = \left[\frac{|\sigma|}{A^{\pm}}\right]^{r} \cdot (1-D)^{k(\sigma)} \qquad \text{(C-14)}$$

where D_c = creep damage,

$A^{\pm}$ = material constants for tensile or compressive creep, and

r, $K(\sigma)$ = material constants.

Similarly, cyclic damage is defined (Reference 28).

$$\frac{dD_F}{d_N} = \left[1 - (1-D)^{\beta+1}\right]^{\alpha(\sigma_M-\bar{\sigma})} \cdot \left[\frac{\sigma_M - \bar{\sigma}}{M(\bar{\sigma}) \cdot (1-D)}\right]^{\beta} \qquad \text{(C-15)}$$

where $\left.\begin{matrix}\alpha \\ \beta \\ M\end{matrix}\right\}$ = material constants.

These equations can be directly integrated between suitable bounds in order obtain life relationships for stress load conditions (References 25 through 27). Applications to strain load conditions require use of constitutive models relating stresses and strains. Solutions for several special case load conditions are presented in Reference 30. The life relationships for strain controlled plastic low cycle fatigue and a saw tooth creep strain loads are identical to those previously described for phenomenological models in equations (C-1) and (C-2).

For the general case of interacting creep and fatigue damage, differential equations (C-14) and (C-15) are substituted into equation (C-13) and solved by numerical methods. When creep and fatigue act simultaneously during each cycle (e.g., cyclic strain loads at high temperature or cyclic loads with strain controlled hold periods) the differential equation which must be solved can be rearranged as follows (Reference 31).

$$dD = \frac{(1-D)^{-k(\sigma)}}{[k(\sigma)+1]\,N_c + (\beta+1)\,[1-\alpha\,(\sigma_M - \bar{\sigma})]\cdot(1-D)^{\beta}\,N_f} + \frac{[1-(1-D)^{\beta+1}]^{\alpha(\sigma_M - \bar{\sigma})}}{[k(\sigma)+1]\,N_c + (\beta+1)\,[1-\alpha\,(\sigma_M - \bar{\sigma})]\cdot(1-D)^{\beta}\,N_f}\,dN \qquad \text{(C-16)}$$

where N_c = cycles to failure under pure creep process, and

N_f = cycles to failure due to pure fatigue.

More recent work on Continuous Damage (References 31 and 32) discusses a general differential damage equation to replace equation (C-13). Use is made of two levels of damage, D_a and D_1 to describe the condition of the material. D_a allows consideration of fatigue damage "incubation" periods during which creep and fatigue damages are accrued separately, followed by a period of interaction.

$$dD_a = g\,(\sigma_M, \bar{\sigma}, D, T)$$

$$dD = f\,(\sigma, D, T)\cdot dt + H\,(1-D_a)\cdot g\,(\sigma_M, \bar{\sigma}, D, T)\cdot dt \qquad \text{(C-17)}$$

where $H\,(1-D_a) = 0$ if $D_a < 1$,

$= 1$ if $D_a \geq 1$.

The Continuous Damage method was successfully applied to IN 100, several stainless steels, and OHFC copper. Using material data determined by pure creep and pure fatigue tests, highly nonlinear interaction effects could be predicted for symmetrical load and strain controlled conditions. An encouraging result was the ability to predict life trends when loading

sequence was changed. However, low frequency test results were consistently under-predicted in subsequent applications of this method to B1900+Hf and Hastelloy X (References 3 and 33), indicating further development may be necessary. Since the determination of material constants for this model is sensitive to the assumed constitutive behavior, constitutive modeling is one area where improvement appears necessary.

Transient loads and temperatures, such as those which may occur during turbine engine acceleration and deceleration, have received only nominal consideration with very limited success in published literature. For such load conditions, damage definition is complicated because the differential damage expression is expected to require an extended form as follows:

$$dD = \frac{\delta D}{\delta t} \cdot dt + \frac{\delta D}{\delta \sigma} \cdot d\sigma + \frac{\delta D}{\delta T} \cdot dT \qquad \text{(C-18)}$$

Equation (C-13), applicable to constant loads, includes only the time rate ($\delta D/\delta t$) portion of creep damage and a corresponding term for cyclic damage. Reference 35 recognizes this and proposes a modification to the differential creep damages in equations (C-13) and (C-14) by including a stress rate term. This approach has not been sufficiently evaluated, however.

Use of continuous damage analysis for modeling thermomechanical fatigue (TMF) life under slow cycles, i.e., negligible temperature rate ($\delta D/\delta T$) effects, has been attempted by some investigators (References 33 and 34). To account for varying temperature effects in model equations, an effective temperature is determined by considering the TMF cycle on an ultimate strength based nondimensional stress basis. The effective temperature is then used for life prediction. It was found that this method did not correctly predict Hastelloy X test results, although the same method had been successfully applied to IN 100. The prediction difference was attributed to the relative strain rate sensitivities of the materials at their respective test conditions.

C.3.4 Strain Range Partitioning (SRP)

Strain Range Partitioning (References 23, and 36 through 39) is an extensively developed cumulative damage model which uses a strain range weighted linear damage cumulation method and results in a nonlinear life relationship that recognizes the differences between plastic and creep deformations, and between tension and compression loading. It had been previously noted that creep reduces cyclic life at elevated temperatures; however, considerable amounts of apparently conflicting evidence concerning the amount of life reduction were noted. This resulted in the conclusion that life reducing effects of creep largely depend on where in the cycle creep occurs, consistent with metallographic findings that tensile and compressive cycle creep causes different types of failure, and evolved in developing SRP (Reference 36).

It is assumed that inelastic strain effects on life can be described by Coffin-Manson type relationships of the form described by equation (C-1), provided the hysteresis loop conforms to a specific form. Four characteristic forms are recognized and assumed to represent four basic components of damage. Life relationships for each are different and can be described using subscripts "p" and "c" to identify terms applicable to plastic and creep strain components respectively, as follows.

$$N_{pp} = C_{pp} \cdot \Delta\varepsilon_{pp}^{M_{pp}}$$

$$N_{cc} = C_{cc} \cdot \Delta\varepsilon_{cc}^{M_{cc}} \qquad \text{(C-19)}$$

$$N_{pc} = C_{pc} \cdot \Delta\varepsilon_{pc}^{M_{pc}}$$

$$N_{cc} = C_{cc} \cdot \Delta\varepsilon_{cc}^{M_{cc}}$$

where pp = loop for high frequency cycling (creep = 0),
cp = loop for tensile hold,
pc = loop for compressive hold,
cc = loop for compressive and tensile holds, and
C and M = material constants.

Loading cycles of most high temperature structures do not exactly conform to one of these four characteristic cycles. Fatigue life for these more complex cycles is calculated by partitioning the inelastic strain range into its four basic components. The partitioning method is defined for isothermal closed hysteresis loops for which the tensile and compressive inelastic strains are equal. In general, actual loading cycles will consist of three components, so that the sum of the components equals the inelastic strain range. Damage for each component is then added according to the interaction damage rule.

$$\frac{1}{N_f} = \frac{f_{pp}}{N_{pp}} + \frac{f_{cc}}{N_{cc}} + \left(\frac{f_{cp}}{N_{cp}} \text{ or } \frac{f_{pc}}{N_{pc}} \right) \qquad \text{(C-20)}$$

where $f_{pp} = \dfrac{\Delta\varepsilon_{pp}}{\Delta\varepsilon_{inel}}$

$f_{cc} = \dfrac{\Delta\varepsilon_{cc}}{\Delta\varepsilon_{inel}}$

$f_{cp} = \dfrac{\Delta\varepsilon_{cp}}{\Delta\varepsilon_{inel}}$

$f_{pc} = \dfrac{\Delta\varepsilon_{pc}}{\Delta\varepsilon_{inel}}$

Strain range partitioning (SRP) has been successful in correlating a large amount of isothermal fatigue data involving unsymmetrical cycles and hold times for different materials, ranging from steels to various generations of nickel alloy (References 29, and 36 through 39). Although material and temperature independence for life relationships is not a requirement for the use of SRP, a method for collapsing data for various materials and temperatures is presented in Reference (40). This procedure provides the obvious advantages of minimizing total requirements for fatigue data.

Further refinements to SRP have been presented in two relatively recent documents (References 41 and 42). The SRP method as presented does not explicitly account for mean stress effects on life, and several investigators found difficulty in applying SRP to strong materials in the presence of mean stress (References 43 and 44). In some cases, it was necessary to use negative damage which resulted in mathematical difficulty. Reference 41 provides a method of explicitly correcting for effects of such mean stresses which can develop with unsymmetrical load cycles or material characteristics.

A total strain range version of SRP is presented in Reference 42 in order to extend predictive capability to very low inelastic strains, prevalent in many practical fatigue problems where long lives are a requirement (e.g., turbine blades). Effectiveness of this version is strongly dependent on constitutive modeling accuracy.

Use of SRP for thermomechanical fatigue (TMF) cycling may present difficulties, first, because of the temperature dependence of fatigue life for some materials (References 29 and 45) and, second, because the strain range partitioning process is not precisely defined for all TMF cycle hysteresis loops. The partitioning process requires that the tensile and compressive going inelastic strains are equal (Reference 36). This requirement is violated for hysteresis loops which are not closed because of monotonic creep strains, such as those in a thermally cycled rotating turbine blade. Another case is the constant strain amplitude TMF cycle.

Applications of SRP to TMF cycling where the basic strain/life relations are temperature independent have been presented for several materials in References 33, 39, and 46 through 48. In some cases (Reference 33), the unequaled compressive going inelastic (plastic) strain was assumed part of $\Delta\varepsilon_{pp}$; in some others, the partitioning details are not explained. Generally, results of these applications were less than satisfactory.

C.3.5 Cycle Damage Accumulation (CDA)

Cycle damage accumulation is the newest cyclic life prediction method and currently still under development for uncoated B1900+Hf nickel base alloy (Reference 3). Cycle damage accumulation presents a new prediction approach which evolved as a result of evaluating various previous life prediction models for use on a typical high strength isotropic material for engine hot section components and is intended to provide improved creep-fatigue predictability.

Fundamentally, CDA follows concepts of both the ductility exhaustion (Reference 24) and continuous damage (References 27 through 30) models. However, the available ductility is redefined as primary creep in a material instead of the quarter cycle intercept. This evolved from metallographic observations that dislocations which ultimately proceed to failure are created early in the load cycle and that the crack initiation process remains primarily transgranular, even though final rupture failure may be intergranular. The primary creep strain is considered indicative of grain deformation during initial creep stage.

The solution technique integrates a damage rate over the loading history similar to that of the continuous damage method; however, a simplified damage rate definition is used. The approach is to determine damage at actual load conditions by applying damage ratios to previously tested reference conditions. This results in the following integral equation.

$$-\bar{\varepsilon}_p - \int_0^{N_f} \left(\frac{dD}{dN_R}\right) \cdot \left\{ \left(\frac{\sigma_T}{\sigma_{TR}}\right)\left(\frac{\Delta\sigma}{\Delta\sigma_R}\right) + \left[\left(\frac{\Delta\sigma_R}{\Delta\sigma}\right)\left(\frac{\sigma_T}{\sigma_{TR}}\right)\right]^{B'} \cdot \left[\left(\frac{t}{t_R}\right)^{C'} - 1\right] \right\} dN = 0 \quad \text{(C-21)}$$

where $\bar{\varepsilon}_p$ = primary creep strain (ductility),

$\frac{dD}{dN_R}$ = reference cyclic damage rate,

$= A\,\Delta\varepsilon_T{}^{B}$,

σ_T = maximum tensile stress,

$\Delta\sigma$ = stress range,

t = time,

N = number of cycles,

A, B, B', C' = material constants, and

subscript R = reference condition.

The initial development of this model was conducted using isothermal conditions at various frequencies, hold times and mean stresses. This resulted in a linear damage relationship as the damage rate is assumed constant through the cycle loading and the damage ratios are linearly added. It is not yet determined whether this relationship is a characteristic of the material tested, unlike most other materials which required nonlinear damage addition (References 24, and 27 through 30), or simply the status of currently incomplete model development. Similarly not determined is how the base metal

primary creep can be used to predict cracks in coated surfaces where the crack starts in the coating. Additional investigations to resolve these questions are currently in progress using variable temperature and TMF cycles and coated specimens.

Although many model details and the general applicability of this model approach are still being determined, the use of the damage ratio concept provides the advantage of not having to evaluate absolute damage increments per cycle. In cycles that include significant amounts of time dependent damage, this is considered important due to the uncertainty associated with relating monotonic creep to the cyclic fatigue process (Reference 23).

C.4 Crack Growth Models

C.4.1 Damage Rate Model

The Damage Rate Model (DRM) assumes that undamaged materials contain two types of microdefects, microcracks and cavities, and that fatigue can be modeled by crack propagation and cavity growth (Reference 49). The model is formulated so that both reversible and irreversible damage can be predicted: microcracks propagate under both tensile and compressive stresses but at different rates, while cavities will enlarge under tensile loads and shrink under compressive loads. The originally defined model was concerned with real transgranular and intergranular cracks, and grain boundary cavities, but actual applications could work with corresponding effective defects, similar to the continuous damage approach (References 27 through 30). This formulation can account for tensile and compressive damage differences.

The growth laws are defined as follows:

$$\frac{da}{dt} = \begin{cases} a \cdot B_T \cdot \left|\varepsilon_{inel}\right|^m \cdot \left|\dot{\varepsilon}_{inel}\right|^k & \text{for tensile stresses} \\ a \cdot B_T \cdot \left|\varepsilon_{inel}\right|^m \cdot \left|\dot{\varepsilon}_{inel}\right|^k & \text{for compressive stresses} \end{cases} \qquad \text{(C-22)}$$

$$\frac{dc}{dt} = \begin{cases} c \cdot G \cdot \left|\varepsilon_{inel}\right|^m \cdot \left|\dot{\varepsilon}_{inel}\right|^{k_c} & \text{for tensile stresses} \\ -c \cdot G \cdot \left|\varepsilon_{inel}\right|^m \cdot \left|\dot{\varepsilon}_{inel}\right|^{k_c} & \text{for compressive stresses} \end{cases} \qquad \text{(C-23)}$$

where a = microcrack length,

c = cavity length,

ε_{inel} = inelastic strain,

$\dot{\varepsilon}_{inel}$ = inelastic strain rate, and

B, G, m, K, K_c = material constants.

Life prediction equations result from integrating these rate equations over the specimen life from the initial microdefect sizes to the critical defect sizes when a macrocrack is formed, and using a microcrack and cavity growth interaction equation. Equation (C-24) defines cyclic life for an ideal cycle (Reference 11) under continuous cycling at constant frequency or strain rate.

$$N_f = \frac{m+1}{4A} \left(\frac{\Delta\varepsilon_{inel}}{2}\right)^{-(m+1)} (\dot{\varepsilon}_{inel})^{k-1} \qquad \text{(C-24)}$$

where $A = \frac{B_c + B_T}{2} / \ln (a_f/a_o)$,

a_o = initial microcrack size, and

a_f = critical microcrack size.

The ideal cycle has been defined as having:

peak tensile stress = peak compressive stress

peak tensile inelastic strain = peak compressive inelastic strain, and

ε_{inel} = constant.

When hold times are present, a linear damage cumulation method is used.

$$\frac{1}{N_f'} = D = \frac{1}{N_f} + D_{a_T} + D_{a_c} + D_{c_T} - D_{c_c} \qquad \text{(C-25)}$$

where N_f' = cycle life with hold times, and

D_{a_T}, D_{a_c}, D_{c_T}, D_{c_c} = tensile and compressive creep damage terms for cracks and cavities (Reference 11).

DRM was applied to two nickel base superalloys, Rene' 95 (Reference 11) and B1900+Hf (Reference 3), at isothermal conditions but did not result in satisfactory solutions. Applications to coatings or coated surfaces under TMF load conditions are not discussed in the surveyed literature.

C.4.2 Fracture Mechanics

Fracture mechanics analysis is generally considered to be an approach to describe life remaining in a part when a macroscopic crack or defect is present (Reference 50). The prediction method usually practiced is that of Linear Elastic Fracture Mechanics (LEFM) which involves describing local loads at the crack tip using stress or strain intensity determined from load distributions on the uncracked part and the crack size and geometry. Also required is the crack propagation law describing crack growth relative to the stress or strain intensity, as follows:

$$\frac{da}{dN} = f(\Delta K) \qquad \text{(C-26)}$$

where ΔK = stress or strain intensity.

For most materials, the propagation law includes a logarithmic linear relation for intermediate levels of ΔK, which can be readily integrated between the initial crack size and failure. However, for turbine blade materials and very long lives, the propagation law must be extended to low ΔK values, where the relation is nonlinear and numerical integration is required. Cook and Rau (Reference 51) reviewed the use of anisotropic fracture mechanics and arrived at a number of conclusions concerning the development of a life prediction method for anisotropic materials. They suggested that a reasonable life prediction model could be developed by utilizing the isotropic stress intensity factor(s) and empirically lumping all of the anisotropic effects into the material's response over the range of grain orientations.

The success of using fracture mechanics for life predictions at elevated temperatures is directly related to knowing the crack growth laws for appropriate load conditions. Limited growth property tests have been reported for vane and blade materials for various temperatures and load cycles (References 52 through 54).

Rau, Gemma and Leverant (Reference 52) found that crack propagation rates for nickel and cobalt base superalloys depend on mean stress, load cycle shape and temperature level. In another paper, Gemma, Langer and Leverant (Reference 53) investigated the effect of orientation on the crack propagation rate for the directionally-solidified nickel-base superalloy MAR M 200 subjected to thermal mechanical fatigue. They found that the crack propagation rate was strongly dependent upon the angle between the axis of loading and the grain growth direction. In addition, they showed that the orientation dependence on crack growth rate could be correlated using a normalized ratio of elastic moduli.

The effects of stress dwells and varying mean strain on crack growth rates during thermal mechanical fatigue also have been investigated by Gemma, Ashland and Masci (Reference 54) for a conventionally cast and directionally-solidified nickel-base superalloy, MAR M 200. They showed that baseline primary creep rates correlated well with cumulative creep rates. They found no correlation of cumulative creep rates with secondary creep rates. In a NASA study, Bizon, Dreshfield and Calfo investigated the thermal fatigue resistance of a coated and uncoated directionally-solidified MAR M 247 superalloy using a MACH 1 burner facility which permitted the leading edge of the specimen to be thermally cycled between room temperature and 1070°C (1926°F), Reference 55. They also found that the thermal fatigue resistance was strongly dependent on the grain orientation, with specimens having higher elastic modulus in the load direction showing correspondingly lower thermal fatigue resistance. Their data were in agreement with that obtained by Gemma et al (Reference 53) on MAR M 200 using crack growth rates under TMF conditions.

At least three applications of LEFM to coated turbine materials have been considered. The first of these involves directionally-solidified turbine blade cracks which develop in the coating early during engine operation and the life is practically all propagation time (Reference 56). Measured crack depths were correlated with predictions. The second application considers actual defects in coatings on laboratory specimens (Reference 57). The defects which were characterized after specimen failure are treated as cracks which propagate initially in the coating and proceed into base metal. Local strain loads were calculated in the coating and used in the initial propagation phase.

The third application also is for specimen analysis. Fifty percent load drop life is predicted in TMF specimens, assuming that coating cracks start early (Reference 58). Time for crack propagation in the base metal is then correlated with specimen life, using strain intensity calculation for observed crack shapes. A very significant result of this study was the correlation of lives for single crystal materials using an approach based on slip behavior of face centered cubic crystals. It was assumed that slip was equally distributed among the available slip directions.

When significant macroscopic inelastic strains are present, LEFM is not applicable and the J-integral, C* or other nonlinear parameters must be used in place of ΔK (References 59 and 60). This has not been found necessary for turbine blade materials in which macroscopic inelastic strains do not occur under normal conditions, but is a requirement for weaker materials such as those used in combustor liners. Meyers (Reference 61) investigated several fracture mechanics analysis methods for predicting crack propagation life for Hastelloy X subjected to inelastic strains. The parameter which showed the most effectiveness in correlating high temperature and variable temperature crack growth data was Crack Opening Displacement calculated from the J-integral.

C.5 Metallographic Investigations

Many metallographic studies have been published which shed light on the mechanisms of fatigue. Some studies concentrate on the 'larger scale' data, such as crack initiation locations, crack orientations, and modes of crack initiation and propagation; while other studies probe the 'finer scale' data of dislocation motion, the development of crystallographic slip bands and the subsequent nucleation of cracks.

C.5.1 Crack Initiation Sites

Many investigators have observed that crack initiation during fatigue is related to the movement of dislocations, and models have been proposed to explain this dislocation behavior and different types for slip in pure metals (Reference 62). Several investigators recently have studied relationships between slip and crack nucleation in model superalloys at room temperature (References 63 and 64). Crack nucleation and slip were observed at the surface of a smooth wall test specimen in one experiment (Reference 63). Crystallographic slip bands developed on the surface early during loading. Shallow microcracks were found in the slip bands even after a few cycles. After subsequent cycling, the slip line cracks became deeper and grew due to both extension and linking. A second type of microcrack also developed at an angle to the slip and normal to the applied stress load. This crack grew along a zigzag path due to extension only.

Fatigue crack initiation in hot section anistropic superalloys (both single crystal and columnar grain) has been almost always associated with defects in the microstructure. These may be brittle phases, internal porosity, surface defects or environmental attack sites (References 13, and 65 through 72). The cracks initiate at the defects and propagate to failure under continued loading. Increased defect sizes cause shorter lives (References 65, 67 and 68), but determining which particular defect initiates the crack depends on the material and on loading conditions.

These results made use of uncoated specimen tests, similar to those used to obtain data for life prediction correlations. When tests were conducted on coated specimens, the cracking origin generally moved to the coating (References 13, 63, 66, 67 and 73). The limited published data on actual hot section cracking (References 13 and 56) and Pratt & Whitney experience also indicate that, in components using advanced anisotropic materials, cracks initiate in the coating. However, coated conventional multigrained (isotropic) materials may initiate cracks either in the coating or in the grain boundaries underneath the coating (Reference 68).

The following table presents an overview of the initiation sites for the various materials which were included in this survey.

Crack Initiation Site Summary

Material	Initiation Site: Carbides	Porosity	Oxidation	Coating	Grain Boundary	Reference
B1900+Hf	X	X			X	3
Coated B1900+Hf	X	X			X	68
Mar-M-200					X	78
Mar-M-200 DS	X	X	X			65-68
Coated Mar-M-200 DS	X	X		X		66-67
Low C Mar-M-200 DS		X	X			68-69
PWA 1480 SC		X				13
Coated PWA 1480 SC				X		13, 73
Rene' 80					X	81
Rene' 120, 150 DS		X	X			70
Rene' N4 SC		X	X			71-72, 77
Coated Rene' N4 SC				X		71, 77

DS = Directionally Solidified
SC = Single Crystal

C.5.2 Initiated Crack Orientations

Both crystallographic and noncrystallographic transgranular cracks occur due to fatigue in anisotropic superalloys (References 65 and 68). The crystallographic cracks (sometimes termed stage I cracks) tend to form at low temperatures and high strain rates and are directly related to both material orientation and load orientation. The noncrystallographic cracks (termed stage II cracks) are usually associated with high temperatures and low strain rates. Stage II crack direction is perpendicular to the applied stress direction but independent of material orientation.

Planar bands of dislocations are generated at discontinuities (defects or previously initiated cracks) at all temperatures and strain rates (References 65, 68 and 69). At the high temperatures/low strain rates, these dislocation bands disperse before stage I cracks can form, and subsequently stage II cracks are nucleated in a homogeneous dislocation array. The initiated stage II cracks propagate and subsequently transition to stage I cracking, depending on loading conditions (Reference 69). However, at low temperatures/high strain rates, stage I cracks initiate within the slip bands before dislocations can disperse.

In room temperature tests of single crystal Mar-M-200, crack initiation sites nearly always were MC type carbides oriented normal to the stress axis. These cracks formed when a tensile stress was applied. As the stress was increased, localized crystallographic slip occurred in the metal at both ends of the carbides and was followed by cracking after repeated loading. Similar slip and cracking were also observed at a limited number of micropores present, but the cracking from micropores tended to be less severe (Reference 65). At higher temperatures, crack initiation generally continued at both carbides and micropores; however, there was a greater tendency for cracking at the micropores (Reference 68). At the higher temperatures, slip became more homogeneous (References 68 and 74) and the initiated cracks were perpendicular to the load axis, particularly at slow strain rates. The cracks that led to failure continued to initiate internally at carbides and micropores in directionally solidified Mar-M-200 even when tested with an aluminide coating (References 65 and 68), although extensive cracking initiated in the coating and propagated a short distance into the base alloy. The coating cracks initiated and propagated normal to the stress axis again.

In uncoated advanced single crystal superalloys, such as PWA 1480 and Rene' N4, fatigue cracks also initiate at defects (References 13, 71, 72, and 75). However, while the crack initiation in PWA 1480 occurred at subsurface or near-surface microporosity, the initiated cracks involved some amount of stage II type cracking adjacent to the microporosity at all temperatures (Reference 13). The initiated cracks were perpendicular to the load direction independent of the material orientation for the <100> and <111> orientations tested. But the number of cycles to crack strongly depended on the material orientation. Similar results were reported for Rene' N4 (References 71 and 72) and an advanced model superalloy (Reference 76). At both 1400°F and 1800°F test temperatures, all six tested orientations of Rene' N4 involved a small region of stage II cracking associated with the crack origin, except the <111> orientation at 1400°F, which showed an area of stage I planar cracking or cube slip planes. Also, Rene' N4 crack initiation at high temperatures occurred at the surface and was environmentally driven.

Cracks in both PWA 1480 and Rene' N4 initiated in the coating and were perpendicular to the applied load direction (References 13, 71, 72, and 77) when these alloys were tested in the coated condition.

These results were previously observed in directionally solidified Mar-M-247 material tested using wedge shaped test specimens in a burner rig (Reference 55). Both coated and uncoated specimens cracked perpendicular to the specimen edge independent of the material orientation in the specimen, which ranged from 0 to 30 degrees. However, the number of cycles to crack depended on the base alloy orientation; i.e., cycles to crack decreased as the angle between the specimen axis and the <001> direction increased.

Environmental effects on fatigue cracking of superalloys are important in superalloys, for not only does surface oxidation present detrimental effects, but it can also provide advantageous effects on life (References 64, 67 and 68). Experiments at moderate temperatures have shown that surface slip is more uniform and surface shear displacements smaller because of a thin oxide film formation on surface slip offsets which leads to greater surface work hardening. At the higher temperatures, of course, the thin oxide benefits are overcome by local penetration of oxidation pitting which can act as crack initiation sites (References 68, 77 and 78).

C.5.3 Coating Effects on Cracking

Oxidation retardant coatings are used on hot section components mainly to provide protection against oxidation or corrosion during high temperature operation. However, the coatings also significantly influence the formation of cracks in the coated base alloy system and usually change the crack initiation site from the base alloy to the coating (References 68 and 79).

The presence of the coating causes a bimetallic structure on the coated component surface which changes the surface deformation characteristics. The stresses developed in the coating can differ from those in the base alloy because of both constitutive behavior differences and thermal expansion property differences (References 56, 57, 79 and 80).

Several investigators have considered the mechanical aspects of coatings. Reference 57 reported propagation of cracks in the coating and into the base alloy, resulting from thermalmechanical loads mainly due to coating and base alloy property differences. The cracks had initiated at coating defects believed inherent to the coating application method used. An experimental and analytical study (Reference 80) evaluated stresses in several coatings on an Armco iron bar under tensile load. The stresses caused coating failure along the coating grain boundaries. In another study (Reference 79), effects of strain resulting from coating application and subsequent service loads were considered.

Other effects of a coating, previously mentioned, are eliminating environment related surface pitting from which cracks can initiate and crack initiation becoming controlled by coating instead of base metal fatigue properties (Reference 68).

Two distinct coating cracking modes have been observed, which indicate that two failure mechanisms may be important (References 13 and 71). Both modes result in cracks normal to the applied stress. The first mode is characterized by long cracks, completely or partially around the cylindrical test specimen circumference, which were found to initiate in aluminide coatings in isothermal fatigue at low temperatures and in-phase thermalmechanical fatigue at low temperature. These cracks are similar in appearance to limited ductility fractures and exhibited little evidence of inelastic deformation in the coating. At higher temperatures, a second mode is observed where both the aluminide and overlay coatings initiated small cracks locally. These cracks are thumbnail-shaped and are preceded by coating deformation.

C.5.4 Crack Initiation Criteria

A wide range of cracking life criteria have been used in past investigations depending on material tested, test purpose and conditions. Specimen data, used in previous cracking life correlations, nearly always represented time to failure or impending failure indicated by a load drop. This circumstance was dictated at least in part by the internally initiated cracking which caused specimen failure but which could not be detected without destructive inspections. Experience shows, however, that a substantial amount of time is expended between crack initiation and final failure, controlled by crack propagation (References 13, 68, 71 and 75). Since including the propagation time with initiation life can lead to significant error, several investigators used periodic test interruption and replication to document surface conditions of specimens. When failure occurs from an externally initiated crack, initiation time for the critical crack can then be determined from the replicas (References 3, 13 and 77).

References

1. Manson, S. S., "Behavior of Materials Under Conditions of Thermal Stress," NACA TN-2933, 1953.

2. Coffin, L. F., "A Study of the Effects of Cyclic Thermal Stress in a Ductile Metal," Trans. ASME, Vol. 76, 1954, p. 931.

3. Moreno, V., D. N. Nissley and L. S. Lin, "Creep Fatigue Life Prediction for Engine Hot Section Materials (Isotropic), Second Annual Report," NASA CR-174844, 1984.

4. Coffin, L. F., "The Effect of Frequency on High-Temperature Low-Cycle Fatigue," Proceedings of Conf. on Fatigue and Fracture of Aircraft Structures and Materials, TR 70-144, AFFDL, 1970, pp. 301-310.

5. Coffin, L. F., "Fatigue at High Temperature," Fatigue at Elevated Temperatures, STP 520, ASTM, 1973, pp. 5-34.

6. McEvily, A. J. and S. R. Crosby, "Lifetime Prediction Methods for Elevated Temperature Fatigue," Proceedings, Specialists Meeting on Low Cycle High Temperature Fatigue, CP-155 AGARD, 1974, pp. 6.1-6.18.

7. Coffin, L. F., "The Effect of Frequency on the Cyclic Strain and Low-Cycle Fatigue of Cast U-500 at Elevated Temperature," Metallurgical Transactions, Vol. 2, 1971, pp. 3105-3113.

8. Coffin, L. F., "The Effect of Frequency on the Cyclic Strain and Fatigue Behavior of Cast Rene' at 1600°F," Metallurgical Transactions, Vol. 5, 1974, pp. 1053-1060.

9. Coffin, L. F., "The Concept of Frequency Separation in Life Prediction for Time Dependent Fatigue," Symposium on Creep-Fatigue Interaction, MPC-3, ASME, 1976, pp. 349-364.

10. Coffin, L. F., "Time Dependent Fatigue-Phenomenology and Life Prediction," Time Dependent Fatigue of Materials at Elevated Temperature, U. S. Dept. of Energy, 1979, pp. 41-59.

11. Bernstein, H. L., "An Evaluation of Four Current Models to Predict the Creep-Fatigue Interaction in Rene' 95," Technical Report TR-79-4075, AFMC, 1979.

12. Ostergren, W. J., "A Damage Function and Associated Failure Equations for Predicting Hold Time and Frequency Effects in Elevated-Temperature Low-Cycle Fatigue," Jl. of Testing and Evaluation, Vol. 4, No. 5, Sept. 1976, pp. 327-339.

13. DeLuca, D. P. and B. A. Cowles, "Fatigue and Fracture of Advanced Blade Materials," Final Report to AFWAL, FR-18518, P&W, 1984.

14. Pejsa, P. N. and B. A. Cowles, "TMF Behavior of a Cast Single Crystal Alloy," TMF Workshop at NASA-Lewis Research Center, Nov. 15/16, 1984.

15. Bernstein, H. L., "A Stress-Strain-Time (SST) Model for High-Temperature Low-Cycle Fatigue," Methods for Predicting Material Life in Fatigue, AFML-TR-79-4114, 1979.

16. Taira, S., "Lifetime of Structures Subjected to Varying Load and Temperature," Creep in Structures, N. J. Hoff, ed., Academic Press, New York, 1962, pp. 96-124.

17. Class I Components in Elevated Temperature Service, ASME Boiler and Pressure Vessel Code, Section III, Code Case 1592, ASME.

18. Robinson, E. L., "Effects of Temperature Variation on the Long-Time Rupture Strength of Steels," Trans. ASME, Vol. 74, 1952, pp. 777-781.

19. Spera, D. A., "Comparison of Experimental and Theoretical Thermal Fatigue Lives for Nickel Base Alloys," Fatigue at Elevated Temperature, STP520, American Society for Testing and Materials, 1973, pp. 648-657.

20. Spera, D. A. and E. C. Cox, "Description for Computerized Method for Predicting Thermal Fatigue Life of Metals," Thermal Fatigue Life of Materials and Components, STP612, D. A. Spera and D. F. Mowbrey, Eds., American Society for Testing and Materials, 1976, pp. 69-85.

21. Kitagawa, M. and R. W. Weeks, "Analysis of Hold Time Fatigue Test Results of AISI 304 Stainless Steel by Five Existing Methods," Proceedings of the Symposium on Mechanical Behavior of Materials, Koyto, Japan, 1973, pp. 233-238.

22. Blass, J. J., "Multiaxial Creep and Fatigue Damage Estimation for Type 304 Stainless Steel," Oakridge National Laboratory, ORNL/TM-6438.

23. Manson, S. S., "The Development and Application of Strain Range Partitioning as a Tool for High Temperature Metal Fatigue," AGARD CP-243, 1978, pp. K.1-K.11.

24. Polhenus, J. F., C. E. Spaeth and W. H. Vogel, "Ductility Exhaustion Model for Prediction of Thermal Fatigue and Creep Interaction," Fatigue at Elevated Temperatures, STP-520, 1973, pp. 625-636.

25. Kachanov, L. M., "Time of the Rupture Process Under Creep Conditions," Izv. Akademii Nauk SSSR, OTN, No. 8, 1958, pp. 26-31.

26. Rabotnov, Y. N., Creep Problem in Structural Members, North Holland Publ. Comp., Amsterdam - London, 1969, pp. 372-382.

27. Lemaitre, J. and J. L. Chaboche, "A Non-Linear Model for Creep Fatigue Damage Cumulation and Interaction," Mechanics of Viscoplastic Media and Bodies, J. Hult, Ed., Springer - Verlag, 1975, pp. 291-301.

28. Lemaitre, J., "Phenomenological Relations for the Prediction of Low-Cycle Fatigue," European Space Agency Technical Translation, ESA-TT-402, July, 1977.

29. Chabocne, J. L., H. Policella and H. Kaczmarek, "Applicability of the SRP Method and Creep-Fatigue Damage Approach to the LCHTF Life Prediction in In-100 Alloy," AGARD CP-243, 1978, pp. 4.1-4.20.

30. Lemaitre, J. and A. Plumtree, "Application of Damage Concepts to Predict Creep Fatigue Failures," J. Eng. Materials and Technology, Vol. 10, ASME, 1979, pp. 284-292.

31. Chaboche, J. L., "Lifetime Prediction and Cumulative Damage Under High Temperature Conditions," Low Cycle Fatigue and Life Prediction, STP-770, ASTM, 1982, pp. 81-104.

32. Savalle, S. and G. Cailletaud, "Microinitiation, Micropropagation and Damage," La Recherche Aerospatiale, No. 1982-6, ONERA, pp. 17-32.

33. Moreno, V., "Combustor Liner Durability Analysis," NASA CR-165250, 1981.

34. Chaboche, J. L., "Thermodynamic and Phenomenological Description of Cyclic Viscoplasticity With Damage," European Space Agency Technical Translation, May, 1979.

35. Chrzanowski, M., "Use of the Damage Concept in Describing Creep-Fatigue Interaction Under Prescribed Stress," Intl. J. Mech. Sci., Vol. 18, 1976, pp. 69-73.

36. Manson, S. S., G. R. Halford and M. H. Hirschberg, "Creep-Fatigue Analysis by Strain-Range Partitioning," NASA TMX-67838, 1971.

37. Coffin, L. F., A. E. Carden, S. S. Manson, L. K. Severud and W. F. Greenstreet, "A General Assessment of Time Dependent Fatigue of Structural Alloys," Oakridge National Laboratory, ORNL-5073, 1977.

38. Halford, G. R. and A. J. Nachtigall, "Strain-Range Partitioning Behavior of the Nickel-Base Superalloys Rene' 80 and In100," NASA TM-7828, 1978.

39. Halford, G. R., M. H. Hirschberg and S. S. Manson, "Temperature Effects on the Strain-Range Partitioning Approach for Creep-Fatigue Analysis," Fatigue at Elevated Temperatures, STP-520, ASTM, 1973, pp. 658-667.

40. Halford, G. R., J. F. Saltsman and M. H. Hirschberg, "Ductility Normalized Strain-Range Partitioning Life Relations for Creep-Fatigue Life Prediction," Proceedings of the Conf. on Environmental Degradation of Engineering Materials, NASA TM-73737, 1977.

41. Halford, G. R. and A. J. Nachtigall, "The Strainrange Partitioning Behavior of an Advanced Gas Turbine Disk Alloy," AIAA/SAE/ASME 15th Joint Propulsion Conference, June 18-20, 1979.

42. Halford, G. R. and J. F. Saltsman, "Strainrange Partitioning - A Total Strain Range Version," NASA Technical Memorandum 83023, 1983.

43. Day, M. F. and G. B. Thomas, "Creep-Fatigue Interaction in Alloy IN738LC," AGARD CP-243, 1978, pp. 10.1-10.13.

44. Hyzak, J. M. and H. L. Bernstein, "An Analysis of the Low Cycle Fatigue Behavior of Rene' 95 by Strainrange Partitioning," AGARD CP-243, 1978, pp. 11.1-11.25.

45. Antunes, V. T. A. and P. Hancock, "Strainrange Partitioning of MARM002 Over the Temperature Range 750-1040°C," AGARD CP-243, 1978, pp. 5.1-5.9.

46. McKnight, R. L., J. H. Laflen and G. T. Spamer, "Turbine Blade Tip Durability Analysis," NASA CR-165268, General Electric, 1981.

47. Hirschberg, M. H. and G. R. Halford, "Use of Strain Range Partitioning to Predict High-Temperature Low-Cycle Fatigue Life," NASA TN D-8072, 1976.

48. Halford, G. R. and S. S. Manson, "Life Prediction of Thermal-Mechanical Fatigue Using Strain Range Partitioning," Thermal Fatigue of Materials and Components, STP-612, ASTM, 1976, pp. 239-254.

49. Majumdar, S. and P. S. Maiya, "A Unified and Mechanistic Approach to Creep-Fatigue Damage," ANL-76-58, Argonne National Laboratory, 1976.

50. Ewalds, H. L. and R. J. H. Wanhill, Fracture Mechanics, Ewald Arnold (Publishing) Ltd., 1984, pp. 28-116.

51. Cook, T. S. and C. A. Rau, "A Critical Review of Anisotropic Fracture Mechanics," Prospects of Fracture Mechanics, G. Sih et al eds., Proceedings of an Int. Conf., Delft, Holland, June, 1974.

52. Rau, C. A., A. E. Gemma and G. R. Leverant, "Thermal-Mechanical Crack Propagation in Nickel- and Cobalt-Base Superalloys Under Various Strain-Temperature Cycles," Fatigue at Elevated Temperatures, STP-520, ASTM, 1973, pp. 166-178.

53. Gemma, A. E., B. S. Langer and G. R. Leverant, "Thermomechanical Fatigue Crack Propagation in an Anisotropic Nickel-Base Superalloy," Thermal Fatigue of Material and Components, STP-612, ASTM, 1976, pp. 199-213.

54. Gemma, A. E., F. X. Ashland and R. M. Masci, "The Effects of Stress Dwells and Varying Mean Strain on Crack Growth During Thermomechanical Fatigue," Journal of Testing and Evaluation, Vol. 9, No. 4, July, 1981, pp. 209-215.

55. Bizon, P. T., R. L. Dreshfield and F. D. Calfo, "Effect of Grain Orientation and Coating on Thermal Fatigue Resistance of a Directionally Solidified Superalloy (MAR M 247)," NASA Technical Memorandum 79129, 1979.

56. Linask, I. and J. Dierberger, "A Fracture Mechanics Approach to Turbine Airfoil Design," ASME Gas Turbine Conference and Products Show, March 2-6, 1975.

57. Strangman, T. E., "Thermal Fatigue of Oxidation Resistant Overlay Coatings," Ph.D. Thesis, University of Connecticut, 1978.

58. Gemma, A. E., Unpublished research, 1981.

59. Rice, J. R., "A Path Independent Integral and the Approximate Analysis of Strain Concentration by Notches and Cracks," Journal of Applied Mechanics, Vol. 35, ASME, 1968, pp. 379-386.

60. Stonesifer, R. B. and S. N. Atluri, "On a Study of the $(\Delta T)_C$ and C* Integrals for Fracture Mechanics Analysis Under Non-Steady Creep," Engineering Fracture Mechanics, Vol. 16, No. 5, 1982, pp. 625-643.

61. Meyers, G. J., "Fracture Mechanics Criteria for Turbine Engine Hot Section Components," NASA CR-167896, P&WA, 1982.

62. Laird, C., "Mechanisms and Theories of Fatigue," Fatigue and Microstructure, American Society for Metals, 1978, pp. 149-203.

63. Anton, D. L. and Fine, M. E., "Fatigue Crack Evolution in Overaged Ni-14.4 at %Al Alloy with Coherent Precipitates," Materials Science and Engineering, Vol. 58, 1983, pp. 135-142.

64. Pangborn, R. N., Weissman, S. and Kramer, I. R., "Dislocation Distribution and Prediction of Fatigue Damage," Metallurgical Transactions A, Vol. 12A, 1981, pp. 109-120.

65. Gell, M. and Leverant, G. R., "The Fatigue of the Nickel-Base Superalloy, Mar-M200, in Single Crystal and Columnar Grained Forms at Room Temperature," Trans. Metallurgical Society of AIME, Vol. 242, 1968, pp. 1869-1879.

66. Leverant, G. R. and Gell, M., "The Elevated Temperature Fatigue of a Nickel-Base Superalloy, Mar-M200," Trans. Metallurgical Society of AIME, Vol. 245, 1969, pp. 1167-1173.

67. Gell, M., Leverant, G. R. and Wells, C. H., "The Fatigue Strength of Nickel-Base Superalloys," Achievement of High Fatigue Resistance in Metals and Alloys, STP 467, ASTM, 1970, pp. 113-153.

68. Gell, M. and Leverant, G. R., "Mechanisms of High-Temperature Fatigue," Fatigue at Elevated Temperatures, STP 520, ASTM, 1973, pp. 37-67.

69. Leverant, G. R. and Gell, M., "The Influence of Temperature and Cyclic Frequency on the Fatigue Fracture of Cube Oriented Nickel-Base Superalloys," Metallurgical Transactions A, Vol. 6A, 1975, pp. 367-371.

70. Wright, P. K. and Anderson, A. F., "The Influence of Orientation on the Fatigue of Directionally Solidified Superalloys," Superalloys 1980, ASM, 1980, pp. 689-698.

71. Wright, P. K., "TMF Failure Modes in Single Crystal Rene' N4," NASA TMF Workshop, November 15-16, 1984.

72. Gabb, T. P., Gayder, J. and Miner, R. V., "Orientation and Temperature Dependence of Some Mechanical Properties of the Single-Crystal Nickel-Base Superalloy Rene'N4: Part II Low Cycle Fatigue Behavior," Submitted for Publication in Metallurgical Transaction, 1985.

73. Barkalow, R. H., "Effect of Cyclic Strain/Temperature Exposure on Fatigue Life of Coated Turbine Alloys," Interim Report to AFWAL/ML, FR-18605, Pratt & Whitney, September, 1984.

74. Leverant, G. R., Gell, M. and Hopkins, S. W., "The Effect of Strain Rate on the Flow Stress and Dislocation Behavior of a Precipitation-Hardened Nickel-Base Alloy," Materials Sci. and Eng., Vol. 8, 1971, pp. 125-133.

75. Anton, D. L., "Fatigue Crack Growth in Anisotropic Superalloy Single Crystals," Fatigue 84, pp. 1361-1369.

76. Anton, D. L., Low Cycle Fatigue Characteristics of <001> and Randomly Aligned Superalloy Single Crystals," Acta Metallurgica, Vol. 32, 1984, pp. 1669-1679.

77. Wright, P. K., "Environmental Effects on the Low Cycle Fatigue of a Single-Crystal Superalloy," Final Report to Naval Air Systems Command, R84AEB648, GE, October, 1984.

78. Milligan, W. W. and Bill, R. C., "Low Cycle Fatigue Behavior of Conventionally Cast Mar M-200 at 1000°C," NASA Tech. Memorandum 83769, 1984.

79. Schneider, K. and Grunling, H. W., "Mechanical Aspects of High Temperature Coatings," Thin Solid Films, Vol. 107, 1983, pp. 395-416.

80. Shatinskii, V. F., Safarov, Y. S. and Garlinskii, R. N., "Determination of Stresses in a Diffusion Coating Applied to a Rod Under Tension," Strength of Materials, Vol. 14, Plenum Publishing Co., 1983, pp. 654-663.

81. Antolovich, S. D., Liu, S. and Baur, R., "Low Cycle Fatigue Behavior of Rene'80 at Elevated Temperature," Metallurgical Transactions A, Vol. 12A, 1981, pp. 473-481.

APPENDIX D

TEST SEQUENCE OF CYCLIC CONSTITUTIVE TESTS

The sequence of load for each test is listed in this appendix. The orientation of each specimen is also given in terms of deviation from the nominal crystal orientation and in terms of their Eulerian angles θ and ψ which are defined in Figure 3-7.

Specimen Number = JA61

Nominal Orientation = <100>

Deviation from Nominal Orientation = 6.7°

Actual Orientation θ = 6.50°, ψ = 0.68°

Test Temperature = 427°C (800°F)

Test Conditions

Order of Test	Strain Rate (in/in/sec)	Nominal Strain Limits (in/in)	Number of Creep and Relaxation Test Conditions
1	10^{-3}	$\pm$ .006	
2	10^{-3}	$\pm$ .008	
3	10^{-3}	$\pm$ .009	
4	10^{-3}	$\pm$ .010	

Specimen Number = KA27

Nominal Orientation = <110>

Deviation from Nominal Orientation = 1.5°

Actual Orientation $\theta = 43.60°$, $\psi = 0.50°$

Test Temperature = 427°C (800°F)

Test Conditions

Order of Test	Strain Rate (in/in/sec)	Nominal Strain Limits (in/in)	Number of Creep and Relaxation Test Conditions
1	10^{-3}	$\pm$ .003	
2	10^{-3}	$\pm$ .004	
3	10^{-3}	$\pm$ .0045	
4	10^{-3}	$\pm$ .005	
5	10^{-4}	$\pm$ .005	
6	10^{-4}	$\pm$ .0053	

Specimen Number = LA66

Nominal Orientation = <111>

Deviation from Nominal Orientation = 2.8°

Actual Orientation $\theta = 42.56°$, $\psi = 33.28°$

Test Temperature = 427°C (800°F)

Test Conditions

Order of Test	Strain Rate (in/in/sec)	Nominal Strain Limits (in/in)	Number of Creep and Relaxation Test Conditions
1	10^{-3}	$\pm$ .003	
2	10^{-3}	$\pm$ .0035	
3	10^{-3}	$\pm$ .004	
4	10^{-3}	$\pm$ .0045	
5	10^{-3}	$\pm$ .005	
6	10^{-3}	$\pm$ .0053	
7	10^{-3}	$\pm$ .0056	
8	10^{-3}	$\pm$ .0061	
9	10^{-3}	$\pm$ .0070	
10	10^{-3}	$\pm$ .004	
11	10^{-3}	$\pm$ .007	
12	10^{-3}	$\pm$ .005	
13	10^{-3}	$\pm$ .007	
14	10^{-3}	$\pm$ .006	
15	10^{-3}	$\pm$ .005	
16	10^{-3}	$\pm$ .0035	

Specimen Number = MA27

Nominal Orientation = <123>

Deviation from Nominal Orientation = 1.2°

Actual Orientation θ = 34.93°, ψ = 15.40°

Test Temperature = 427°C (800°F)

Test Conditions

Order of Test	Strain Rate (in/in/sec)	Nominal Strain Limits (in/in)	Number of Creep and Relaxation Test Conditions
1	10^{-3}	$\pm$ .003	
2	10^{-3}	$\pm$ .004	
3	10^{-3}	$\pm$ .0045	2
4	10^{-3}	$\pm$ .005	
5	10^{-3}	$\pm$ .0053	1

Specimen Number = JA44

Nominal Orientation = <100>

Deviation from Nominal Orientation = 5.7°

Actual Orientation $\theta = 4.89°$, $\psi = 2.59°$

Test Temperature = 760°C (1400°F)

Test Conditions

Order of Test	Strain Rate (in/in/sec)	Nominal Strain Limits (in/in)	Number of Creep and Relaxation Test Conditions
1	10^{-3}	$\pm$ .006	
2	10^{-3}	$\pm$ .007	
3	10^{-3}	$\pm$ .008	5
4	10^{-3}	$\pm$ .009	
5	10^{-3}	$\pm$ .010	
6	10^{-3}	$\pm$ .011	5
7	5×10^{-5}	$\pm$ .011	
8	10^{-3}	$\pm$ .013	

Specimen Number = KA26

Nominal Orientation = <110>

Deviation from Nominal Orientation = 2.1°

Actual Orientation $\theta = 43.20°$, $\psi = 1.03°$

Test Temperature = 760°C (1400°F)

Test Conditions

Order of Test	Strain Rate (in/in/sec)	Nominal Strain Limits (in/in)	Number of Creep and Relaxation Test Conditions
1	10^{-3}	$\pm$ .003	
2	10^{-3}	$\pm$ .003	
3	10^{-3}	$\pm$ .004	
4	10^{-3}	$\pm$ .005	
5	10^{-3}	$\pm$ .006	
6	10^{-4}	$\pm$ .006	
7	10^{-3}	$\pm$ .006	10
8	10^{-3}	$\pm$ .007	
9	10^{-3}	$\pm$ .008	

Specimen Number = LA63

Nominal Orientation = <111>

Deviation from Nominal Orientation = 5.0°

Actual Orientation $\theta = 41.36°$, $\psi = 31.31°$

Test Temperature = 760°C (1400°F)

Test Conditions

Order of Test	Strain Rate (in/in/sec)	Nominal Strain Limits (in/in)	Number of Creep and Relaxation Test Conditions
1	10^{-3}	$\pm$ .004	10
2	10^{-4}	$\pm$ .004	
3	10^{-2}	$\pm$ .004	
4	10^{-3}	$\pm$ .004	
5	10^{-3}	$\pm$ .005	
6	10^{-3}	$\pm$ .006	7

Specimen Number = LA67

Nominal Orientation = <111>

Deviation from Nominal Orientation = 3.2°

Actual Orientation $\theta = 42.21°$, $\psi = 33.00°$

Test Temperature = 760°C (1400°F)

Test Conditions

Order of Test	Strain Rate (in/in/sec)	Nominal Strain Limits (in/in)	Number of Creep and Relaxation Test Conditions
1	10^{-3}	$\pm$ .004	Buckled on Loading

Specimen Number = MA25

Nominal Orientation = <123>

Deviation from Nominal Orientation = 2.0°

Actual Orientation $\theta = 35.75°$, $\psi = 15.36°$

Test Temperature = 760°C (1400°F)

Test Conditions

Order of Test	Strain Rate (in/in/sec)	Nominal Strain Limits (in/in)	Number of Creep and Relaxation Test Conditions
1	10^{-3}	$\pm$ .004	
2	10^{-3}	$\pm$ .005	
3	10^{-3}	$\pm$ .006	11

Specimen Number = JA66

Nominal Orientation = <100>

Deviation from Nominal Orientation = 5.3°

Actual Orientation $\theta = 3.90°$, $\psi = 2.79°$

Test Temperature = 982°C (1800°F)

Test Conditions

Order of Test	Strain Rate (in/in/sec)	Nominal Strain Limits (in/in)	Number of Creep and Relaxation Test Conditions
1	10^{-3}	$\pm$ .003	
2	10^{-3}	$\pm$ .004	10
3	10^{-2}	$\pm$ .004	
4	10^{-4}	$\pm$ .004	
5	10^{-5}	$\pm$ .004	
6	10^{-3}	$\pm$ .004	
7	10^{-3}	$\pm$ .006	
8	10^{-3}	$\pm$ .008	12
9	10^{-2}	$\pm$ .008	
10	10^{-4}	$\pm$ .008	3
11	5×10^{-5}	$\pm$ .008	

Specimen Number = KA22

Nominal Orientation = <110>

Deviation from Nominal Orientation = 5.4°

Actual Orientation $\theta = 41.55°$, $\psi = 4.15°$

Test Temperature = 982°C (1800°F)

Test Conditions

Order of Test	Strain Rate (in/in/sec)	Nominal Strain Limits (in/in)	Number of Creep and Relaxation Test Conditions
1	10^{-3}	$\pm$ .003	
2	10^{-3}	$\pm$ .004	12
3	10^{-2}	$\pm$ .004	
4	10^{-4}	$\pm$ .004	
5	10^{-3}	$\pm$ .005	
6	10^{-3}	$\pm$ .006	10
7	10^{-5}	$\pm$ .006	

Specimen Number = LA68

Nominal Orientation = <111>

Deviation from Nominal Orientation = 1.4°

Actual Orientation $\theta = 43.97°$, $\psi = 34.19°$

Test Temperature = 871°C (1600°F)

Test Conditions

Order of Test	Strain Rate (in/in/sec)	Nominal Strain Limits (in/in)	Number of Creep and Relaxation Test Conditions
1	10^{-3}	$\pm$ .002	
2	10^{-3}	$\pm$ .003	9
3	10^{-3}	$\pm$ .004	
4	10^{-3}	$\pm$ .005	9
5	10^{-5}	$\pm$ .005	
6	10^{-4}	$\pm$ .005	
7	10^{-3}	$\pm$ .005	
8	5×10^{-3}	$\pm$ .005	
9	10^{-3}	$\pm$ .005	
10	10^{-3}	$\pm$ .006	12
11	10^{-3}	$\pm$ .010	

Specimen Number = LA69

Nominal Orientation = <111>

Deviation from Nominal Orientation = 2.0°

Actual Orientation θ = 43.11°, ψ = 34.02°

Test Temperature = 982°C (1800°F)

Test Conditions

Order of Test	Strain Rate (in/in/sec)	Nominal Strain Limits (in/in)	Number of Creep and Relaxation Test Conditions
1	10^{-3}	$\pm$ .0015	7
2	10^{-3}	$\pm$ .002	6
3	10^{-3}	$\pm$ .003	7
4	10^{-3}	$\pm$ .004	12
5	10^{-3}	$\pm$ .005	9
6	10^{-3}	$\pm$ .004	
7	10^{-3}	$\pm$ .003	
8	10^{-3}	$\pm$ .002	3
9	10^{-3}	$\pm$ .0015	
10	10^{-5}	$\pm$ .005	

Specimen Number = LA64

Nominal Orientation = <111>

Deviation from Nominal Orientation = 3.4°

Actual Orientation $\theta = 41.86°$, $\psi = 33.07°$

Test Temperature = 982°C (1800°F)

Test Conditions

Order of Test	Strain Rate (in/in/sec)	Nominal Strain Limits (in/in)	Number of Creep and Relaxation Test Conditions
1	10^{-3}	$\pm$ .003	7
2	10^{-4}	$\pm$ .003	1
3	10^{-5}	$\pm$ .003	
4	10^{-4}	$\pm$ .003	5

Specimen Number = MA23

Nominal Orientation = <123>

Deviation from Nominal Orientation = 5.1°

Actual Orientation $\theta = 35.60°$, $\psi = 10.76°$

Test Temperature = 982°C (1800°F)

Test Conditions

Order of Test	Strain Rate (in/in/sec)	Nominal Strain Limits (in/in)	Number of Creep and Relaxation Test Conditions
1	10^{-3}	$\pm$ .002	
2	10^{-3}	$\pm$ .003	8
3	10^{-4}	$\pm$ .003	
4	10^{-2}	$\pm$ .003	
5	10^{-4}	$\pm$ .003	
6	10^{-3}	$\pm$ .004	
7	10^{-3}	$\pm$ .005	
8	10^{-5}	$\pm$ .005	
9	10^{-3}	$\pm$ .005	10
10	10^{-2}	$\pm$ .005	
11	10^{-3}	$\pm$ .0055	
12	10^{-3}	$\pm$ .004	
13	10^{-3}	$\pm$ .003	3
14	5×10^{-6}	$\pm$ .003	

APPENDIX E

SAMPLE DIGITAL FORMAT OF CYCLIC CONSTITUTIVE DATA

Data from the cyclic constitutive tests are being recorded digitally as the testing proceeds so that virtually every cycle and hold period are preserved. The following is a sample of the format in which these data are being stored and will be reported. The data used in this example are taken from the stabilized response of specimen LA68, a <111> specimen tested at 871°C (1600°F).

The format consists of two major "files", a HEADER file and a TRAILER file. The HEADER file gives a general description of the material and specimen geometry as well as the sequence of loading conditions imposed on the specimen. The TRAILER file gives the actual specimen response as stress-strain-time triplets for each "cycle" of each block of loading. The format has been designed so that keywords (e.g., MATL and SPECID) signal the type of data to follow. This format is more flexible and easier to read than strict card column formats. A more detailed description of the keywords follows.

Keyword	Description
HEADER	Signals the beginning of the HEADER file
TITLE	General description of test
ANISO	Signals that anisotropic material description follows
THETA, PSI, GAMMA	Eulerian angles describing the specimen orientation
COMMENT	Descriptive comment
MATL	Signals that general material data follows
CODE	Material specification
HCODE	Heat code
HTSPEC	Heat treatment specification
GEOMETRY	Signals that specimen geometry follows
CONFIG	Specimen part number
GEOMUNIT	Units used to describe the specimen dimensions
OD	Outer diameter
GAGELN	Gage length
JOB	Signals that project identification follows
JOBID	Project identification
SPECID	Specimen identification (serial or specimen number)
DATE	Date of test
BLOCi	Signals that loading conditions for the ith block of loading will follow. A new BLOCi (sequentially numbered) is used each time the imposed loading conditions are changed.

Keyword	Description
NCYC	The generic "cycle" number at which this loading condition begins. The "cycle" number corresponds to CYCLE in the TRAILER file describing the response under BLOCi loading conditions. Note that load or strain hold periods are also considered to be generic "cycles" in this format.
ISOTEMP	Signals that the test was isothermal and is followed by the test temperature
TESTTYP	Signals that the test is a constitutive test
UNITS	Signals that the units for reporting the data follow. These units remain in effect for all tests and are specified only in the BLOCi description.
STRN1UNIT	Strain units
STRS1UNIT	Stress units
TUNIT	Temperature units
TIMUNIT	Time units
CONVERT STRN1CON STRS1CON TCON TIMCON	These data are included to facilitate subsequent conversion of the data to other units. These conversion factors are specified only in the BLOC1 description.
TRAILER	Signals the beginning of the TRAILER file
CYCLE	The generic cycle number for the stress-strain-time triplets that follow
BEGTIME	The actual test time at the beginning of the cycle
STRESS 1 * *	Signals that stress values will follow in free field format
STRAIN 1 * *	Signals that strain values will follow in free field format
TIME * *	Signals that time values will follow in free field format

```
HEADER
TITLE  CONSTITUTIVE TEST  PWA 1480 < 111 > NOMINAL
ANISO
     THETA      =  43.97
     PSI        =  34.19
     GAMMA      =  0
COMMENT    2  FROM < 111 > UNCOATED
MATL
     CODE       = PWA1480
     HCODE      = P9866
     HTSPEC     = 1975F/4HR+1600F/32HR
GEOMETRY
     CONFIG     = LED 41784
     GEOMUNIT   = INCHES
     OD         =  .3
     GAGELN     =  1
JOB
     JOBID      = NAS3-23929
     SPECID     = LA-68,T-724-84
     DATE       = 08/30/84
BLOC1
     NCYC       =  1
     ISOTEMP    =  1600
     TESTYP     = C
COMMENT MINSTRAIN   = -5.00000E-03 MAXSTRAIN= 5.00000E-03
COMMENT STRAIN RATE = 1.00000E-05
UNITS
     STRN1UNIT =  IN/IN
     STRS1UNIT =  PSI
     TUNIT     =  F
     TIMUNIT   =  SEC
CONVERT
     STRN1CON  =  1.0
     STRS1CON  =  1.0
     TCON      =  1.0
     TIMCON    =  1.0
BLOC2
     NCYC       =  2
     ISOTEMP    =  1600
     TESTYP     = C
COMMENT MINSTRAIN   = -5.00000E-03 MAXSTRAIN= 5.00000E-03
COMMENT STRAIN RATE = 1.00000E-04
BLOC3
     NCYC       =  3
     ISOTEMP    =  1600
     TESTYP     = C
COMMENT MINSTRAIN   = -5.00000E-03 MAXSTRAIN= 5.00000E-03
COMMENT STRAIN RATE = 1.00000E-03
BLOC4
     NCYC       =  4
     ISOTEMP    =  1600
     TESTYP     = C
COMMENT STRAIN HOLD AT  3.90816E-03
COMMENT
BLOC5
```

```
     NCYC      = 5
     ISOTEMP   = 1600
     TESTYP    = C
COMMENT LOAD HOLD AT  15722.9
COMMENT
CYCLE =  1          BEGTIME =  2047.4
TRAILER
STRESS 1 * *
-46131.9 -48032.5 -49414.7 -51488.1 -52524.7
-54252.5 -55462 -57189.7 -58572 -59435.9
-60990.9 -61682 -62718.7 -63755.3 -64792
-65655.9 -66519.8 -67210.9 -67556.5 -68593.1
-68938.7 -69802.6 -69975.4 -70839.3 -70839.3
-71357.6 -60990.9 -53043.1 -45268 -38356.9
-31100.2 -24361.8 -17450.6 -10885.1 -4665.02
 1382.23  6738.37  12094.5  16932.3  21597.3
 25571.2  29717.9  33000.7  36283.5  39566.3
 41985.2  44922.5  47168.6  49587.5  51488.1
 53561.4  55462  56844.2  58572  60127
 61509.2  62891.4  64100.9  64964.8  65828.7
 67038.1  67729.2  68765.9  69457  70320.9
 71012  71530.4  72048.7  72394.3  72912.6
 73258.2  74122.1  74294.8  74986  75158.7
 75504.3  65828.7  58226.4  51142.5  44231.3
 37493  31100.2  24016.2  17623.4  11576.2
 5356.14 -345.557 -5874.48 -10712.3 -15895.6
-19869.6 -24016.2 -27299 -30236.3 -33173.5
-35592.4 -38184.1 -40084.7 -42330.8 -44058.6
STRAIN 1 * *
 4.39668E-05 -1.66097E-04 -3.51734E-04 -5.76453E-04 -7.66976E-04
-9.77039E-04 -1.17733E-03 -1.38251E-03 -1.59746E-03 -1.79775E-03
-2.00293E-03 -2.18857E-03 -2.40840E-03 -2.60870E-03 -2.81676E-03
-3.01417E-03 -3.22423E-03 -3.42941E-03 -3.63459E-03 -3.84954E-03
-4.04983E-03 -4.25989E-03 -4.45530E-03 -4.66048E-03 -4.86566E-03
-5.05129E-03 -4.87543E-03 -4.67513E-03 -4.46507E-03 -4.25989E-03
-4.05471E-03 -3.85442E-03 -3.65413E-03 -3.45872E-03 -3.25354E-03
-3.03859E-03 -2.83830E-03 -2.63312E-03 -2.43283E-03 -2.22276E-03
-2.01759E-03 -1.80752E-03 -1.61700E-03 -1.41182E-03 -1.19687E-03
-1.00147E-03 -7.96287E-04 -6.05765E-04 -3.90816E-04 -1.90523E-04
 2.44260E-05  2.19834E-04  4.20127E-04  6.25305E-04  8.40254E-04
 1.04055E-03  1.24573E-03  1.45579E-03  1.64631E-03  1.84172E-03
 2.06155E-03  2.26185E-03  2.48168E-03  2.67709E-03  2.88227E-03
 3.07279E-03  3.28285E-03  3.50269E-03  3.69321E-03  3.90327E-03
 4.10357E-03  4.31363E-03  4.51392E-03  4.71910E-03  4.91939E-03
 5.12457E-03  4.94382E-03  4.74353E-03  4.53835E-03  4.33317E-03
 4.12799E-03  3.92281E-03  3.71275E-03  3.51246E-03  3.32193E-03
 3.10210E-03  2.89204E-03  2.69663E-03  2.50122E-03  2.27162E-03
 2.09086E-03  1.88569E-03  1.67562E-03  1.48510E-03  1.27504E-03
 1.06986E-03  8.64680E-04  6.59502E-04  4.54323E-04  2.58915E-04
    TIME      * *
 0  20.474  40.948  61.422  81.896
 102.37  122.844  143.318  163.792  184.266
 204.74  225.214  245.688  266.162  286.636
 307.11  327.584  348.058  368.532  389.006
 409.48  429.954  450.428  470.902  491.376
```

```
 511.85   532.324   552.798   573.272   593.746
 614.22   634.694   655.168   675.642   696.116
 716.59   737.064   757.538   778.012   798.486
 818.96   839.434   859.908   880.382   900.856
 921.33   941.804   962.278   982.752   1003.23
 1023.7   1044.17   1064.65   1085.12   1105.6
 1126.07  1146.54   1167.02   1187.49   1207.97
 1228.44  1248.91   1269.39   1289.86   1310.34
 1330.81  1351.28   1371.76   1392.23   1412.71
 1433.18  1453.65   1474.13   1494.6    1515.08
 1535.55  1556.02   1576.5    1596.97   1617.45
 1637.92  1658.39   1678.87   1699.34   1719.82
 1740.29  1760.76   1781.24   1801.71   1822.19
 1842.66  1863.13   1883.61   1904.08   1924.56
 1945.03  1965.5    1985.98   2006.45   2026.93
CYCLE =  2          BEGTIME =  409.2
STRESS 1 * *
-51488.1 -53907   -55980.3  -58053.6  -59781.4
-61682   -63409.8 -64964.8  -66692.6  -68247.6
-69802.6 -71357.6 -72567    -73949.3  -75331.5
-76368.2 -77577.6 -78614.3  -79823.8  -80514.9
-81551.5 -82415.4 -83279.3  -84143.2  -84834.3
-85525.5 -76195.4 -67210.9  -59263.1  -51833.6
-44749.7 -37493   -30581.8  -23497.9  -16759.5
-10366.7 -3801.13  2418.9    8120.6    13822.3
 19005.7  24016.2  28681.3   33173.5   37320.2
 40775.8  44231.3  46823     50105.8   52697.5
 55289.2  57362.5  59608.6   61854.8   63409.8
 65310.3  67038.1  68420.4   70320.9   71530.4
 73085.4  74122.1  75504.3   76368.2   77577.6
 78959.9  79996.5  80687.6   81551.5   82588.2
 83279.3  83970.4  84834.3   85525.5   86043.8
 86562.1  78441.5  70148.1   62373.1   55289.2
 48205.3  41466.9  34383     27471.8   20906.2
 14340.6  7947.82  2073.34  -3973.91  -9675.61
-15204.5 -20215.1 -24880.1  -29199.6  -33519.1
-37147.4 -40430.2 -43540.2  -46477.5  -49241.9
STRAIN 1 * *
 7.32780E-05 -1.27015E-04 -3.32193E-04 -5.42257E-04 -7.37665E-04
-9.42843E-04 -1.14802E-03 -1.35320E-03 -1.55838E-03 -1.75379E-03
-1.96873E-03 -2.17391E-03 -2.37909E-03 -2.57450E-03 -2.78456E-03
-2.98974E-03 -3.20469E-03 -3.39033E-03 -3.60528E-03 -3.81045E-03
-4.01563E-03 -4.21593E-03 -4.42599E-03 -4.63117E-03 -4.82658E-03
-5.02198E-03 -4.91451E-03 -4.70933E-03 -4.49927E-03 -4.29897E-03
-4.09868E-03 -3.89839E-03 -3.68344E-03 -3.48803E-03 -3.28285E-03
-3.08256E-03 -2.86761E-03 -2.66732E-03 -2.46702E-03 -2.26673E-03
-2.05667E-03 -1.85638E-03 -1.66097E-03 -1.44602E-03 -1.24084E-03
-1.04055E-03 -8.40254E-04 -6.35076E-04 -4.29897E-04 -2.24719E-04
-1.95408E-05  1.75867E-04  3.85931E-04  6.00879E-04  8.01172E-04
 9.96580E-04  1.21153E-03  1.42159E-03  1.60723E-03  1.80752E-03
 2.02736E-03  2.23254E-03  2.42306E-03  2.63312E-03  2.83830E-03
 3.04348E-03  3.24866E-03  3.44895E-03  3.64436E-03  3.86419E-03
 4.06448E-03  4.25989E-03  4.47484E-03  4.68002E-03  4.88520E-03
 5.08061E-03  4.98290E-03  4.78261E-03  4.57254E-03  4.37225E-03
 4.16219E-03  3.96678E-03  3.76180E-03  3.54665E-03  3.34636E-03
```

```
3.15584E-03  2.95066E-03  2.74060E-03  2.54030E-03  2.33512E-03
2.13483E-03  1.92477E-03  1.72447E-03  1.52418E-03  1.31900E-03
1.10405E-03  9.08647E-04  7.08354E-04  5.03175E-04  2.93112E-04
    TIME      * *
0  2.046  4.092  6.138  8.184
10.23  12.276  14.322  16.368  18.414
20.46  22.506  24.552  26.598  28.644
30.69  32.736  34.782  36.828  38.874
40.92  42.966  45.012  47.058  49.104
51.15  53.196  55.242  57.288  59.334
61.38  63.426  65.472  67.518  69.564
71.61  73.656  75.702  77.748  79.794
81.84  83.886  85.932  87.978  90.024
92.07  94.116  96.162  98.208  100.254
102.3  104.346  106.392  108.438  110.484
112.53  114.576  116.622  118.668  120.714
122.76  124.806  126.852  128.898  130.944
132.99  135.036  137.082  139.128  141.174
143.22  145.266  147.312  149.358  151.404
153.45  155.496  157.542  159.588  161.634
163.68  165.726  167.772  169.818  171.864
173.91  175.956  178.002  180.048  182.094
184.14  186.186  188.232  190.278  192.324
194.37  196.416  198.462  200.508  202.554
CYCLE =  3           BEGTIME =  60
STRESS 1 * *
-52351.9 -55980.3 -59608.6 -63064.2 -66174.2
-68938.7 -71875.9 -74294.8 -76541 -78959.9
-80860.4 -83106.5 -84834.3 -86389.3 -88289.9
-89672.1 -91054.4 -92609.4 -93991.6 -95373.8
-96410.5 -97792.7 -98829.4 -99693.3 -100730
-101594 -102285 -95028.3 -84316 -75677.1
-67556.5 -59954.2 -52697.5 -45440.8 -38184.1
-31100.2 -24361.8 -17277.9 -10539.5 -3801.13
 2591.68  8984.49  14686.2  20387.9  26780.7
 31964.1  36801.9  41466.9  45959.1  50278.6
 54252.5  57880.9  61336.4  64619.2  67729.2
 70493.7  73085.4  75677.1  77750.4  79651
 81378.8  83279.3  85007.1  86562.1  88117.1
 89326.6  90708.8  92091  93473.3  94509.9
 95719.4  96928.8  98138.3  98829.4  99866.1
 100730  101767  96410.5  86216.6  77923.2
 70493.7  62891.4  55980.3  49069.1  41985.2
 35246.9  28508.5  21597.3  15031.7  8466.16
 2073.34 -4146.69 -9848.39 -16414 -22115.7
-27817.4 -32655.2 -37665.8 -42158 -46477.5
STRAIN 1 * *
 2.83341E-04  7.81632E-05 -1.41671E-04 -3.41964E-04 -5.47142E-04
-7.47435E-04 -9.42843E-04 -1.15779E-03 -1.35809E-03 -1.55838E-03
-1.76844E-03 -1.96873E-03 -2.17880E-03 -2.37909E-03 -2.57450E-03
-2.78456E-03 -2.98974E-03 -3.19003E-03 -3.40010E-03 -3.60528E-03
-3.80557E-03 -4.01075E-03 -4.21104E-03 -4.40645E-03 -4.62140E-03
-4.82658E-03 -5.02198E-03 -4.97802E-03 -4.73376E-03 -4.52369E-03
-4.31851E-03 -4.10845E-03 -3.91304E-03 -3.70787E-03 -3.50269E-03
-3.29751E-03 -3.10210E-03 -2.88715E-03 -2.68686E-03 -2.49145E-03
```

```
-2.29116E-03 -2.09086E-03 -1.89546E-03 -1.70005E-03 -1.47044E-03
-1.26527E-03 -1.06986E-03 -8.69565E-04 -6.59502E-04 -4.54323E-04
-2.49145E-04 -4.39668E-05  1.61212E-04  3.66390E-04  5.61798E-04
 7.66976E-04  9.81925E-04  1.18222E-03  1.37763E-03  1.58280E-03
 1.78798E-03  1.99805E-03  2.19345E-03  2.39375E-03  2.60870E-03
 2.80410E-03  3.01417E-03  3.21935E-03  3.42452E-03  3.61505E-03
 3.82511E-03  4.03517E-03  4.23058E-03  4.43576E-03  4.64094E-03
 4.84612E-03  5.05618E-03  5.06106E-03  4.84123E-03  4.64094E-03
 4.42599E-03  4.22570E-03  4.02052E-03  3.81045E-03  3.60528E-03
 3.40498E-03  3.19980E-03  2.99463E-03  2.78945E-03  2.59404E-03
 2.38886E-03  2.17880E-03  1.99805E-03  1.77821E-03  1.56815E-03
 1.36786E-03  1.16756E-03  9.67269E-04  7.52320E-04  5.47142E-04
     TIME      * *
  0   .2   .4   .6   .8
  1  1.2  1.4  1.6  1.8
  2  2.2  2.4  2.6  2.8
  3  3.2  3.4  3.6  3.8
  4  4.2  4.4  4.6  4.8
  5  5.2  5.4  5.6  5.8
  6  6.2  6.4  6.6  6.8
  7  7.2  7.4  7.6  7.8
  8  8.2  8.4  8.6  8.8
  9  9.2  9.4  9.6  9.8
 10 10.2 10.4 10.6 10.8
 11 11.2 11.4 11.6 11.8
 12 12.2 12.4 12.6 12.8
 13 13.2 13.4 13.6 13.8
 14 14.2 14.4 14.6 14.8
 15 15.2 15.4 15.6 15.8
 16 16.2 16.4 16.6 16.8
 17 17.2 17.4 17.6 17.8
 18 18.2 18.4 18.6 18.8
 19 19.2 19.4 19.6 19.8
     CYCLE =  4          BEGTIME =  263.2
     STRESS 1 * *
52179.2 52179.2 52351.9 52351.9 52351.9
52351.9 52351.9 52179.2 52179.2 52179.2
52006.4 52006.4 52006.4 51833.6 51833.6
51833.6 51833.6 51660.8 51660.8 51833.6
51660.8 51660.8 51315.3 51315.3 51488.1
51488.1 51488.1 51315.3 51488.1 51315.3
51488.1 51142.5 51315.3 51142.5 50969.7
51142.5 50969.7 50969.7 50969.7 50969.7
50969.7 50969.7 50796.9 50624.2 50796.9
50796.9 50624.2 50796.9 50624.2 50451.4
50451.4 50624.2 50624.2 50451.4 50451.4
50451.4 50451.4 50278.6 50278.6 50451.4
50278.6 50278.6 50278.6 50278.6 50105.8
50278.6 50105.8 49933  50105.8 49933
49933  49933  49933  50105.8 49933
49933  49933  50105.8 49933  49933
49933  49933  49760.3 49933  49933
49760.3 49760.3 49587.5 49587.5 49587.5
49760.3 49414.7 49587.5 49587.5 49760.3
49587.5 49587.5 49587.5 49587.5 49587.5
```

49587.5	49414.7	49587.5	49241.9	49414.7
49414.7	49414.7	49414.7	49414.7	49414.7
49414.7	49414.7	49414.7	49414.7	49241.9
49069.2	49241.9	49414.7	49241.9	49414.7
49069.2	49069.2	49069.2	49069.2	49069.2
49069.2	49069.2	49069.2	49241.9	49069.2
48896.4	49069.2	49069.2	48896.4	48896.4
48896.4	49069.2	48896.4	48896.4	49069.2
48896.4	48896.4	48896.4	48896.4	48896.4
48723.6	49069.2	48896.4	48896.4	49069.2
48896.4	48896.4	48896.4	48896.4	48896.4
48723.6	48723.6	48896.4	48723.6	48723.6
48896.4	49069.2	48723.6	48723.6	48723.6
48723.6	48550.8	48723.6	48723.6	48723.6
48550.8	48550.8	48550.8	48550.8	48550.8
48550.8	48550.8	48550.8	48378	48550.8
48550.8	48550.8	48550.8	48550.8	48550.8
48550.8	48723.6	48378	48378	48378
48378	48550.8	48378	48550.8	48378
48550.8	48378	48378	48378	48378
48378	48378	48378	48550.8	48205.3
48378	48378	48205.3	48205.3	48205.3
48378	48378	48205.3	48205.3	48378
48378	48205.3	48205.3	48378	48378
48378	48205.3	48378	48205.3	48205.3
48205.3	48205.3	48205.3	48205.3	48205.3
48205.3	48378	48032.5	48205.3	48032.5
48205.3	48032.5	48032.5	48205.3	48032.5
48205.3	48032.5	47859.7	48032.5	

STRAIN 1 * *

3.90816E-03	3.91304E-03	3.91304E-03	3.91793E-03	3.91793E-03
3.91304E-03	3.91793E-03	3.91304E-03	3.91304E-03	3.91793E-03
3.92281E-03	3.92281E-03	3.91304E-03	3.92281E-03	3.91793E-03
3.91304E-03	3.91304E-03	3.91793E-03	3.90816E-03	3.91793E-03
3.91304E-03	3.91793E-03	3.91793E-03	3.91304E-03	3.90816E-03
3.91793E-03	3.91304E-03	3.91793E-03	3.91304E-03	3.90816E-03
3.91304E-03	3.91793E-03	3.91793E-03	3.92281E-03	3.91793E-03
3.91304E-03	3.91793E-03	3.91304E-03	3.91304E-03	3.91304E-03
3.91304E-03	3.91304E-03	3.91304E-03	3.91304E-03	3.91793E-03
3.91793E-03	3.91793E-03	3.91304E-03	3.91304E-03	3.91793E-03
3.90816E-03	3.91304E-03	3.91793E-03	3.91304E-03	3.91304E-03
3.91793E-03	3.91793E-03	3.91304E-03	3.91793E-03	3.91304E-03
3.91304E-03	3.91304E-03	3.91304E-03	3.92281E-03	3.91304E-03
3.91304E-03	3.90816E-03	3.90816E-03	3.90816E-03	3.91304E-03
3.91793E-03	3.90816E-03	3.91793E-03	3.91304E-03	3.90327E-03
3.91304E-03	3.90327E-03	3.91304E-03	3.91793E-03	3.90327E-03
3.90816E-03	3.91304E-03	3.90816E-03	3.91304E-03	3.91304E-03
3.90816E-03	3.91304E-03	3.90816E-03	3.91793E-03	3.91304E-03
3.91304E-03	3.90816E-03	3.90816E-03	3.91304E-03	3.90816E-03
3.91304E-03	3.91304E-03	3.91304E-03	3.90816E-03	3.91304E-03
3.91304E-03	3.91793E-03	3.91304E-03	3.90816E-03	3.90327E-03
3.90816E-03	3.91793E-03	3.90327E-03	3.91304E-03	3.91304E-03
3.91793E-03	3.91304E-03	3.92281E-03	3.91304E-03	3.91304E-03
3.91793E-03	3.90816E-03	3.90327E-03	3.91304E-03	3.91793E-03
3.90816E-03	3.90816E-03	3.91304E-03	3.91304E-03	3.90327E-03

3.91793E-03	3.90816E-03	3.90816E-03	3.90816E-03	3.91304E-03
3.90816E-03	3.90816E-03	3.91304E-03	3.91304E-03	3.90816E-03
3.90816E-03	3.91304E-03	3.91304E-03	3.91304E-03	3.90816E-03
3.90816E-03	3.91304E-03	3.90816E-03	3.90816E-03	3.90816E-03
3.90327E-03	3.91304E-03	3.91304E-03	3.91304E-03	3.91793E-03
3.91793E-03	3.91304E-03	3.91304E-03	3.90816E-03	3.90816E-03
3.91304E-03	3.91304E-03	3.91304E-03	3.90816E-03	3.91304E-03
3.91304E-03	3.91304E-03	3.91793E-03	3.91793E-03	3.91304E-03
3.91304E-03	3.91304E-03	3.91793E-03	3.91793E-03	3.91793E-03
3.91304E-03	3.91793E-03	3.91304E-03	3.92281E-03	3.91304E-03
3.92281E-03	3.92281E-03	3.91304E-03	3.90816E-03	3.91793E-03
3.92281E-03	3.91304E-03	3.91793E-03	3.91304E-03	3.91793E-03
3.91304E-03	3.91793E-03	3.91793E-03	3.92281E-03	3.92281E-03
3.91793E-03	3.91793E-03	3.91793E-03	3.91793E-03	3.92281E-03
3.92281E-03	3.92281E-03	3.91793E-03	3.91793E-03	3.90816E-03
3.91793E-03	3.92281E-03	3.91793E-03	3.90816E-03	3.91793E-03
3.91304E-03	3.92281E-03	3.91793E-03	3.91793E-03	3.92281E-03
3.91304E-03	3.91304E-03	3.91793E-03	3.91793E-03	3.91304E-03
3.91793E-03	3.91793E-03	3.91304E-03	3.91304E-03	3.92281E-03
3.91793E-03	3.91304E-03	3.91304E-03	3.92770E-03	3.92281E-03
3.91793E-03	3.92281E-03	3.91793E-03	3.91304E-03	3.91793E-03
3.91304E-03	3.90816E-03	3.91304E-03	3.90816E-03	3.91793E-03
3.91793E-03	3.91304E-03	3.90816E-03	3.91793E-03	3.91793E-03
3.91304E-03	3.91304E-03	3.91304E-03	3.90816E-03	

TIME * *

0	.2	.4	.6	.8	
1	1.2	1.4	1.6	1.8	
2	2.2	2.4	2.6	2.8	
3	3.2	3.4	3.6	3.8	
4	4.2	4.4	4.6	4.8	
5	5.2	5.4	5.6	5.8	
6	6.2	6.4	6.6	6.8	
7	7.2	7.4	7.6	7.8	
8	8.2	8.4	8.6	8.8	
9	9.2	9.4	9.6	9.8	
10	10.2	10.4	10.6	10.8	
11	11.2	11.4	11.6	11.8	
12	12.2	12.4	12.6	12.8	
13	13.2	13.4	13.6	13.8	
14	14.2	14.4	14.6	14.8	
15	15.2	15.4	15.6	15.8	
16	16.2	16.4	16.6	16.8	
17	17.2	17.4	17.6	17.8	
18	18.2	18.4	18.6	18.8	
19	19.2	19.4	19.6	19.8	
20	20.2	20.4	20.6	20.8	
21	21.2	21.4	21.6	21.8	
22	22.2	22.4	22.6	22.8	
23	23.2	23.4	23.6	23.8	
24	24.2	24.4	24.6	24.8	
25	25.2	25.4	25.6	25.8	
26	26.2	26.4	26.6	26.8	
27	27.2	27.4	27.6	27.8	
28	28.2	28.4	28.6	28.8	
29	29.2	29.4	29.6	29.8	

```
 30  30.2  30.4  30.6  30.8
 31  31.2  31.4  31.6  31.8
32.0001  32.2001  32.4001  32.6001  32.8001
33.0001  33.2001  33.4001  33.6001  33.8001
34.0001  34.2001  34.4001  34.6001  34.8001
35.0001  35.2001  35.4001  35.6001  35.8001
36.0001  36.2001  36.4001  36.6001  36.8001
37.0001  37.2001  37.4001  37.6001  37.8001
38.0001  38.2001  38.4001  38.6001  38.8001
39.0001  39.2001  39.4001  39.6001  39.8001
40.0001  40.2001  40.4001  40.6001  40.8001
41.0001  41.2001  41.4001  41.6001  41.8001
42.0001  42.2001  42.4001  42.6001  42.8001
43.0001  43.2001  43.4001  43.6001  43.8001
44.0001  44.2001  44.4001  44.6001  44.8001
45.0001  45.2001  45.4001  45.6001  45.8001
46.0001  46.2001  46.4001  46.6001  46.8001
47.0001  47.2001  47.4001  47.6001  47.8001
48.0001  48.2001  48.4001  48.6001
    CYCLE =  5              BEGTIME =  599.6
    STRESS 1 * *
15722.9  15895.6  15722.9  15722.9  15895.6
15722.9  15895.6  15895.6  15895.6  15895.6
15895.6  15722.9  15895.6  15895.6  15722.9
15895.6  15722.9  15895.6  15895.6  15895.6
15895.6  15722.9  15895.6  15895.6  15895.6
16068.4  15895.6  15895.6  15722.9  15895.6
15895.6  15722.9  15895.6  15722.9  15895.6
15895.6  15895.6  15895.6  15895.6  15722.9
15895.6  15895.6  15895.6  15895.6  15895.6
15895.6  15895.6  15895.6  15895.6  15895.6
15722.9  15895.6  15895.6  15895.6  15895.6
15895.6  16068.4  15895.6  15895.6  15895.6
15895.6  15895.6  15722.9  15895.6  16068.4
15895.6  16068.4  15895.6  15895.6  15895.6
15895.6  15895.6  16068.4  15895.6  15895.6
16068.4  15895.6  15895.6  16068.4  15895.6
15895.6  16068.4  15895.6  15722.9  16068.4
15895.6  15895.6  15895.6  16068.4  15722.9
15722.9  15895.6  15895.6  15895.6  16068.4
15895.6  15895.6  15895.6  15895.6  15895.6
15895.6  15895.6  15895.6  15895.6  15895.6
15895.6  15895.6  15895.6  15895.6  16068.4
16068.4  15895.6  15895.6  15722.9  15895.6
16068.4  15895.6  16068.4  15895.6  15895.6
15895.6  15895.6  16068.4  15722.9  15895.6
16068.4  15895.6  15895.6  15895.6  15895.6
15895.6  15895.6  15895.6  15722.9  15895.6
15895.6  15895.6  16068.4  15895.6  15895.6
15895.6  15895.6  15895.6  15895.6  16068.4
15895.6  15895.6  15895.6  15895.6  16068.4
```

15895.6	15895.6	15895.6	15895.6	15895.6
15895.6	15895.6	15895.6	15895.6	15895.6
15895.6	16068.4	15895.6	15895.6	15895.6
16068.4	16068.4	15722.9	15895.6	16068.4
16068.4	16068.4	15895.6	15895.6	15895.6
15722.9	15895.6	16068.4	15895.6	16068.4
15895.6	15895.6	15895.6	15895.6	15895.6
15895.6	15895.6	15895.6	16068.4	15895.6
15722.9	15895.6	15895.6	15895.6	15895.6
15895.6	15722.9	15895.6	15895.6	15895.6
15722.9	15895.6	15895.6	15722.9	15895.6
15895.6	15895.6	15895.6	15895.6	15895.6
15895.6	15895.6	15895.6	15722.9	15722.9
15895.6	15895.6	15895.6	15895.6	15895.6
15895.6	15895.6	15895.6	15722.9	15722.9
15895.6	16068.4	15895.6	15895.6	15895.6
15895.6	15895.6			

STRAIN 1 * *

2.81876E-03	2.81387E-03	2.80899E-03	2.79433E-03	2.79433E-03
2.79433E-03	2.78456E-03	2.78456E-03	2.78945E-03	2.77968E-03
2.77479E-03	2.77479E-03	2.76991E-03	2.77479E-03	2.76991E-03
2.76502E-03	2.76991E-03	2.77968E-03	2.76991E-03	2.76502E-03
2.76991E-03	2.76502E-03	2.76502E-03	2.75525E-03	2.76014E-03
2.76502E-03	2.76014E-03	2.75525E-03	2.75037E-03	2.76014E-03
2.74548E-03	2.76502E-03	2.75525E-03	2.75037E-03	2.75525E-03
2.75037E-03	2.74060E-03	2.75525E-03	2.74060E-03	2.74060E-03
2.74548E-03	2.75037E-03	2.75037E-03	2.75037E-03	2.74548E-03
2.74548E-03	2.75037E-03	2.74548E-03	2.75037E-03	2.75525E-03
2.74548E-03	2.74548E-03	2.75037E-03	2.74060E-03	2.73571E-03
2.74548E-03	2.74060E-03	2.74060E-03	2.74060E-03	2.75037E-03
2.73571E-03	2.74548E-03	2.74060E-03	2.74060E-03	2.74060E-03
2.74548E-03	2.73571E-03	2.74060E-03	2.73571E-03	2.74060E-03
2.73571E-03	2.73571E-03	2.74060E-03	2.74548E-03	2.73083E-03
2.73571E-03	2.73083E-03	2.73571E-03	2.74060E-03	2.73571E-03
2.74060E-03	2.73571E-03	2.73571E-03	2.73571E-03	2.73571E-03
2.73083E-03	2.73571E-03	2.73571E-03	2.73083E-03	2.73083E-03
2.74548E-03	2.74060E-03	2.73571E-03	2.73571E-03	2.73571E-03
2.72594E-03	2.73571E-03	2.73083E-03	2.73571E-03	2.73083E-03
2.73083E-03	2.73083E-03	2.73083E-03	2.72594E-03	2.73083E-03
2.73083E-03	2.72594E-03	2.72105E-03	2.72594E-03	2.73083E-03
2.73083E-03	2.73083E-03	2.73571E-03	2.73083E-03	2.73083E-03
2.73083E-03	2.73571E-03	2.73571E-03	2.73571E-03	2.73083E-03
2.73083E-03	2.74060E-03	2.73571E-03	2.73083E-03	2.73083E-03
2.73083E-03	2.73083E-03	2.73083E-03	2.73571E-03	2.73571E-03
2.72594E-03	2.73571E-03	2.74060E-03	2.74060E-03	2.73571E-03
2.72594E-03	2.73571E-03	2.73083E-03	2.73571E-03	2.72594E-03
2.73083E-03	2.73083E-03	2.73083E-03	2.72105E-03	2.73083E-03
2.72594E-03	2.73083E-03	2.72594E-03	2.73083E-03	2.72594E-03
2.72594E-03	2.72594E-03	2.73083E-03	2.73083E-03	2.72105E-03
2.72594E-03	2.72594E-03	2.73083E-03	2.73083E-03	2.72594E-03
2.72594E-03	2.73571E-03	2.72594E-03	2.73083E-03	2.73571E-03
2.73571E-03	2.72105E-03	2.72594E-03	2.72594E-03	2.72594E-03
2.73083E-03	2.72594E-03	2.72594E-03	2.72594E-03	2.72594E-03
2.73083E-03	2.72594E-03	2.73083E-03	2.72594E-03	2.73083E-03
2.72594E-03	2.73571E-03	2.72594E-03	2.72594E-03	2.72594E-03

2.73083E-03 2.72105E-03 2.73083E-03 2.72594E-03 2.72594E-03
2.73083E-03 2.73083E-03 2.72594E-03 2.72594E-03 2.72594E-03
2.73571E-03 2.73083E-03 2.73083E-03 2.72594E-03 2.73083E-03
2.73083E-03 2.72594E-03 2.73083E-03 2.72594E-03 2.73083E-03
2.72594E-03 2.72594E-03 2.72594E-03 2.72594E-03 2.73083E-03
2.72594E-03 2.72594E-03 2.72105E-03 2.72594E-03 2.72594E-03
2.73083E-03 2.72594E-03 2.72594E-03 2.71617E-03 2.72105E-03
2.72594E-03 2.72594E-03 2.72594E-03 2.72594E-03 2.72594E-03
2.72105E-03 2.72594E-03 2.71617E-03 2.71617E-03 2.71617E-03
2.72105E-03 2.72105E-03 2.72105E-03 2.72105E-03 2.71128E-03
2.72105E-03 2.71617E-03 2.71617E-03 2.71617E-03 2.72105E-03
2.71617E-03 2.71617E-03 2.71617E-03 2.71617E-03 2.72105E-03
2.72594E-03 2.71617E-03 2.71617E-03 2.71617E-03 2.72594E-03
2.71617E-03 2.71617E-03

TIME * *

0 .2 .4 .6 .8
1 1.2 1.4 1.6 1.8
2 2.2 2.4 2.6 2.8
3 3.2 3.4 3.6 3.8
4 4.2 4.4 4.6 4.8
5 5.2 5.4 5.6 5.8
6 6.2 6.4 6.6 6.8
7 7.2 7.4 7.6 7.8
8 8.2 8.4 8.6 8.8
9 9.2 9.4 9.6 9.8
10 10.2 10.4 10.6 10.8
11 11.2 11.4 11.6 11.8
12 12.2 12.4 12.6 12.8
13 13.2 13.4 13.6 13.8
14 14.2 14.4 14.6 14.8
15 15.2 15.4 15.6 15.8
16 16.2 16.4 16.6 16.8
17 17.2 17.4 17.6 17.8
18 18.2 18.4 18.6 18.8
19 19.2 19.4 19.6 19.8
20 20.2 20.4 20.6 20.8
21 21.2 21.4 21.6 21.8
22 22.2 22.4 22.6 22.8
23 23.2 23.4 23.6 23.8
24 24.2 24.4 24.6 24.8
25 25.2 25.4 25.6 25.8
26 26.2 26.4 26.6 26.8
27 27.2 27.4 27.6 27.8
28 28.2 28.4 28.6 28.8
29 29.2 29.4 29.6 29.8
30 30.2 30.4 30.6 30.8
31 31.2 31.4 31.6 31.8
32.0001 32.2001 32.4001 32.6001 32.8001
33.0001 33.2001 33.4001 33.6001 33.8001
34.0001 34.2001 34.4001 34.6001 34.8001
35.0001 35.2001 35.4001 35.6001 35.8001
36.0001 36.2001 36.4001 36.6001 36.8001
37.0001 37.2001 37.4001 37.6001 37.8001
38.0001 38.2001 38.4001 38.6001 38.8001
39.0001 39.2001 39.4001 39.6001 39.8001
40.0001 40.2001 40.4001 40.6001 40.8001
41.0001 41.2001 41.4001 41.6001 41.8001
42.0001 42.2001 42.4001 42.6001 42.8001
43.0001 43.2001 43.4001 43.6001 43.8001
44.0001 44.2001 44.4001 44.6001 44.8001
45.0001 45.2001 45.4001 45.6001 45.8001
46.0001 46.2001 46.4001 46.6001 46.8001
47.0001 47.2001 47.4001 47.6001 47.8001
48.0001 48.2001 48.4001 48.6001 48.8001
49.0001 49.2001 49.4001 49.6001 49.8001
50.0001 50.2001

Distribution List for NASA CR-174952
Life Prediction and Constitutive Models for Engine
Hot Section Anisotropic Materials Program

Aerojet Liquid Rocket
Attn: V. Frick
Mgr, Matl's Eng
Box 13222
Sacramento, CA 95813

AFOSR/NA
Attn: Maj. David Glasgow
Mgr, Aerospace Sci
Bolling AFB
Washington, DC 20332

Wright Patterson Air Force Base
Attn: Ted Nicholas
AFWAL/MLLN
Wright Patterson Air Force Base,
OH 45433

Wright Patterson Air Force Base
Attn: Library
AFWAL/MLLAM
Wright Patterson Air Force Base,
OH 45433

Airesearch Mfg. Co.
Attn: Richard Graves
2525 W. 190th St.
Torrance, CA 90509

Univ. of Alabama
Attn: Dr. A.. E. Carden
AME Dept.
Box 2908
University, AL 35486

Allison Gas Turbine Oper.
Attn: Mehmet Doner W8
P. O. Box 420
Indianapolis, IN 46206

Allison Gas Turbine Oper.
Attn: Frank Walters
P. O. Box 894
Indianapolis, IN 46206

Allison Gas Turbine Oper.
Attn: Donald Vaccari T10
P. O. Box 420
Indianapolis, IN 46206

Univ. of Arizona
Attn: Dr. Paul H. Wirsching
Dept Aero & Mech Eng.
Tucson, AZ 85721

Army Applied Tech Lab
Attn: Jan Lane
DAVDL-ATL-ATP
Fort Eustis, VA 23604

Army Applied Tech Lab
Attn: Library
Fort Eustis, VA 23604

AVCO - Space Systems Div.
Attn: Library
Lowell Industrial Pk.
Lowell, MA 01851

AVCO - Lycoming Div.
Attn: Jerry Walters
550 S. Main St.
Stratford, CT 06497

Battelle Columbus Lab
Attn: Brian Leis
505 King Ave.
Columbus, OH 43201

Boeing
Attn: Library
3801 S. Oliver
Wichita, KS 67210

Carnegie-Mellon University
Attn: Dr. Mel Bernstein
Schaife Hall
Pittsburg, PA 15213

Case Western Reserve Univ.
Attn: Prof. S. S. Manson
619 Glennan Bldg.
10900 Euclid Ave.
Cleveland, OH 44106

Univ. of Cincinnati
Attn: Dr. Donald Stouffer
Rm. 833 Rhodes Hall
Dept. Eng. Sci.
Cincinnati, OH 45221

Univ. of Connecticut
Attn: Dr. Eric Jordan
Mech. Eng. Dept. U-139
Storrs, CT 06268

Curtiss Wright
Attn: Jerome Mogul
Dir - Matl's Eng.
1 Rotary Dr.
Wood-Ridge, NJ 07075

Univ. of Dayton
Attn: Dr. Joseph Gallagher
Research Institute
Rm. 563 Kettering Bldg.
Dayton, OH 45469

Defense Documentation Ctr.
Cameron Station
5010 Duke St.
Alexandria, VA 22314

DeLaval Turbine
Attn: Harry Gayley
Nottingham Way
Trenton, NJ 08602

Failure Analysis Assoc.
Attn: Dr. Clifford Wells
2225 E. Bayshore Rd.
Palo Alto, CA 94303

Garrett Turbine Eng. Co.
Attn: Joe Adams (503-4Z)
111 S. 34th St.
Box 5217
Phoenix, AZ 85010

Garrett Turbine Eng. Co.
Attn: Lee Matsch
111 S. 34th St.
Box 5217
Phoenix, AZ 85010

Gen. Elec. Co. - AEBG
Attn: Dr. Len Beitch K-221
Mgr, EM & LM
Evandale, OH 45215

Gen. Elec. Co. - AEBG
Attn: J. H. Laflen
Mail Drop G-60
Evandale, OH 45215-6301

Gen. Elec. Co.
Attn: Library
1000 Western Ave.
Lynn, MA 01905

Gen. Elec. Co.
Attn: Library
Box 8
Schenectady, NY 12301

Gen. Elec. Co. - AEBG
Attn: Joe McKenzie
Technical Programs
Mail Drop H-9
Evandale, OH 45215

Gen. Elec. Co.
Attn: Donald Mowbray
Bldg. 55-219
1 River Rd.
Schenectady, NY 12345

Gen. Elec. Co. - AEBG
Attn: Dr. Mel Roberts
Mail Drop K-69
Evandale, OH 45215

Gen. Elec. Co. - R&D Ctr.
Attn: Dr. David Woodford
Bldg. K-1, Rm 231M
Schenectady, NY 12301

Gen. Elec. Co. - AEBG
Attn: Kennard Wright
Evandale, OH 45215-6301

Gen. Elec. Co. - AEBG
Attn: T. Cook
Evandale, OH 45215-6301

Georgia Inst. of Tech.
Attn: Prof. S. Antolovich
Fracture & Fatigue Lab
Bunger-Henry Bldg.
Atlanta, GA 30332

Hamilton Standard
Attn: Gerald Molter
Mail Stop 1-1-6
Bradley Field Rd.
Windsor Locks, CT 06096

Hibbitt, Karlsson & Sorensen, Inc.
Attn: Dr. Kevin Walker
35 South Angell St.
Providence, RI 02906

Univ. of Illinois
Attn: Prof. D. Socie
Dept. Mech Engrng.
1206 W. Green St
Urbana, IL 61801

I. I. T. Research Inst.
Attn: Humphries
10 W. 35th St.
Chicago, Il 60616

Int'l Harvester Co. - Solar
Attn: Library
2200 Pacific Hwy.
San Diego, CA 92101

Lockheed California
Attn: Library
Burbank, CA 91503

Lockheed Huntsville
Attn: W. H. Armstrong
Mgr, Struct & Mech
Huntsville, AL 35806

MIT
Attn: Prof. Regi Pelloux
Rm 8-237
77 Mass Ave.
Cambridge, MA 02139

McDonnell Douglas
Attn: Library
Missiles & Space Div.
5301 Bolsa Ave.
Huntington Beach, CA 92647

Michigan State Univ.
Attn: Dr. John Martin
MMM Dept.
330 Engineering Bldg.
E. Lansing, MI 48824

NASA-AFWAL Tech Liaison
Attn: Everett Bailey
AFWAL/DO
Wright Patterson Air Force Base,
OH 45433

NASA Headquarters
Attn: Dr. M. Greenfield
RTM-6, M&S Div.
Washington, DC 20546

NASA Langley Research Ctr.
Attn: Library
MS-185
Hampton, VA 23665

NASA - LeRC
Attn: Dr. Robert Bill
Head, Fatigue Res. Sect
MS 49-7
Cleveland, OH 44135

NASA - LeRC
Attn: D. E. Sokoloski
Mail Stop 49-1
Cleveland, OH 44135

NASA - LeRC
Attn: T. J. Miller
Mail Stop 49-3
Cleveland, OH 44135

NASA - LeRC
Attn: HOST Proj. Off.
Mail Stop 49-7
Cleveland, OH 44135

NASA - LeRC
Attn: R. H. Johns
Mail Stop 49-6
Cleveland, OH 44135

NASA - LeRC
Attn: Carl Stearns
Mail Stop 106-1
Cleveland, OH 44135

NASA - LeRC
Attn: D. B. Ercegovic
Mail Stop 6-11
Cleveland, OH 44135

NASA - LeRC
Attn: D.R. Englund
Mail Stop 77-1
Cleveland, OH 44135

NASA - LeRC
Attn: J. E. Rohde
Mail Stop 6 - 10
Cleveland, OH 44135

NASA - LeRC
Attn: N. T. Saunders
Mail Stop 3-8
Cleveland, OH 44135

NASA - LeRC
Attn: J. A. Ziemianski
Mail Stop 49-6
Cleveland, OH 44135

NASA - LeRC
Attn: A. Kaufman
Mail Stop 49-7
Cleveland, OH 44135

NASA - LeRC
Attn: Dr. R. L. Thompson
Mail Stop 49-6
Cleveland, OH 44135

NASA - LeRC
Attn: M. A. McGaw
Mail Stop 49-7
Cleveland, OH 44135

NASA - LeRC
Attn: T. W. Orange
Mail Stop 49-6
Cleveland, OH 44135

NASA - LeRC
Attn: Dr. L. Berke
Mail Stop 49-6
Cleveland, OH 44135

NASA - LeRC
Attn: Dr. D. A. Robinson
Mail Stop 49-6
Cleveland, OH 44135

NASA - LeRC
Attn: Dr. R. Ellis
Mail Stop 49-6
Cleveland, OH 44135

NASA - LeRC
Attn: Dr. R. L. Dreshfield
Mail Stop 49-1
Cleveland, OH 44135

NASA - LeRC
Attn: S. J. Grisaffe
Mail Stop 49-1
Cleveland, OH 44135

NASA - LeRC
Attn: Marv Hirschberg
Chief, Fatigue & Fracture
MS 49-6
Cleveland, OH 44135

NASA - LeRC
Attn: Dr. R. V. Miner
Mail Stop 49-3
Cleveland, OH 44135

NASA - LeRC
Attn: Report Control
MS 5-5
Cleveland, OH 44135

NASA - LRC
Attn: M. V. Nathal
Mail Stop 49-1
Cleveland, OH 44135

NASA - LeRC
Attn: Library
MS 60-3
Cleveland, OH 44135

NASA - LeRC
Attn: B. McKay
Mail Stop 49-3
Cleveland, OH 44135

NASA - LeRC
Attn: S&T Section
MS 501-11
Cleveland, OH 44135

NASA - LeRC
Attn; Dr. J. Gayda
Mail Stop 49-3
Cleveland, OH 44135

NASA - LeRC
Attn: AR&TL Office
MS 77-5
Cleveland, OH 44135

NASA - LeRC
Attn: Dr. Gary Halford
MS 49-7
Cleveland, OH 44135

NASA - LeRC
Attn: AFSC Liaison Office
MS 501-3
Cleveland, OH 44135

NASA Marshall Space Ctr.
Attn: Library
Huntsville, AL 35812

NASA Marshall Space Ctr.
Attn: Carmelo Bianca
EP42, Bldg 4610
Huntsville, AL 35812

NASA Marshall Space Ctr.
Attn: Larry Salter
EP46, Bldg 4610
Huntsville, AL 35812

NASA Marshall Space Ctr.
Attn: Bryan McPherson
Huntsville, AL 35812

NASA Marshall Space Ctr.
Attn: B Bhat
Huntsville, AL 35812

NASA Marshall Space Ctr.
Attn: P. Munafo
EH22, Bldg 4612
Huntsville, AL 35812

NASA Sci. & Tech. Info
Attn: Accessioning Dept.
Box 8757
Balt/Washington International Airport
Maryland 21240

Naval Ship R&D Ctr
Attn: Library
Code 522.1
Bethesda, MD 20084

Northwestern Univ.
Attn: Dr. Julia Weertman
Dept. Matl's Sci
Evanston, IL 60201

O R N L Box X
Attn: Dr. Charles Brinkman
Metals & Ceramics Div.
Oak Ridge, TN 37830

O'Donnell & Assoc.
Attn: Dr. W. O'Donnell
241 Curry Hollow Rd.
Pittsburgh, PA 15232

Pennsylvania State Univ.
Attn: Dr. Sam Zamrik
121 Hammond Bldg.
University Park, PA 16802

Rensselaer Polytech Inst.
Attn: Prof. Norman Stoloff
Dept. of Matl's Eng.
Troy, NY 12181.

Rockwell Int'l
Attn: Dr. Mike Mitchell
Rockwell Science Ctr.
P.O. Box 1085
Thousand Oaks, CA 91360

Rocketdyne
Attn: Dr. Bob Jewett AC10
6633 Canoga Ave.
Canoga Park, CA 91304

Rocketdyne
Attn: Ed Larson AC10
6633 Canoga Ave.
Canoga Park, CA 91304

Rocketdyne
Attn: Jack Lewis AC10
6633 Canoga Ave.
Canoga Park, CA 91304

Rockwell Int'l
Attn: Library
6633 Canoga Ave.
Canoga Park, CA 91304

Rolls Royce, Inc.
Attn: Dr. Ashok Thakker
1895 Phoenix Blvd.
Atlanta, GA 30349

Sandia Labs
Attn: Jack Hyzak
Division 8314
Box 969
Livermore, CA 94550

Sandia Labs
Attn: Library
Albuquerque, NM 87115

Southern Research Inst.
Attn: Library
2000 9th Ave. S.
Birmingham, AL 35205

Southwest Research
Attn: Dr. Gerald Leverant
P. O. Drawer 28510
San Antonio, TX 78284

Southwest Research
Attn: Dr. U. S. Lindholm
P. O. Drawer 285
San Antonio, TX 78284

Southwest Research
Attn: Library
8500 Culebra Rd.
San Antonio, TX 78284

Stanford Univ.
Attn: Prof. Alan K. Miller
Dept. Matl's Sci & Eng
Stanford, CA 94305

Syracuse Univ.
Attn: Dr. H. W. Liu
409 Link Hall
Syracuse, NY 13210

T R W Inc.
Attn: Dr. C. Kortovich
T/M-3357
23555 Euclid Ave.
Cleveland, OH 44117

Teledyne CAE
Attn: Hugh Gaylord
Mgr., Explor. Dev. Appl.
1330 Laskey Rd.
Toledo, OH 43612

Teledyne CAE
Attn: Bryon L. Lewis
1330 Laskey Rd.
Toledo, OH 43612

Teledyne CAE
Attn: Tom Moyer
Box 6971
Toledo, OH 43612

Teledyne CAE
Attn: Jerry Walcher
Box 6971
Toledo, OH 43612

Univ. of Tennessee
Attn: Dr. V. Smith
Space Institute
Tullahoma, TN 37388

V. P. I. & State Univ.
Attn: Dr. Norm Dowling
Eng. Sci. & Mech. Dept.
Blacksburg, VA 24061

Williams Research
Attn: Peter Nagy
2280 W. Maple Rd.
Walled Lake, MI 48088

Westinghouse - R&D Ctr.
Attn: Robert Johnson
Bldg. 401, Rm. 2X9G
Pittsburgh, PA 15235

Westinghouse - ARD
Attn: Alfred Snow
Box 158
Madison, PA 15663

Argonne Nat. Lab.
Attn: S. Majumdar
9700 S. Cass Ave.
Argonne, IL 60439

NASA Headquarters
Attn: Charles Bersch
RTM-6, M&S Div.
Washington, DC 20546

AVCO - Lycoming Div
Attn: Louis Fiedler
Chief, Matl's Eng & Dev
550 S Main St
Stratford, CT 06497

N. A. P. C.
Attn: A. Martino
P. O. Box 7176
Mgr. R&T Div.
Trenton, NJ 08628

Case Western Reserve Univ
Attn: Prof. A. Chudnovski
205 Bingham Bldg.
10900 Euclid Ave.
Cleveland, OH 44106

Wright Patterson Air Force Base
Attn: Richard Hill
AFWAL/POTC
Area B, Bldg 18
Wright Patterson Air Force Base,
OH 45433

Eng Science Software Inc
Attn: Dr. Kevin Walker
P 65 Log Road
Smithfield, RI 02917

Airesearch Mfg. Co.
Attn: Dr. Tekal Nath
Mail T-42, Dept 93-3
2525 W 190th St
Torrance, CA 90509

Exxon Res & Eng Co
Attn: R P Gangloff
Box 45
Linden, NJ 07036

University of Akron
Attn: Prof. Padovan
Dept. Civil Eng.
Akron, OH 44325

FAA - New England Reg.
Attn: Dan Salvano
12 New England Exec. Park
Burlington, MA 01803

Failure Analysis Assoc.
Attn: Dr. Jerrell Thomas
2225 E. Bayshore Rd
Palo Alto, CA 94303

McDonnell Douglas
Attn: F. C. Claser
Dept 243
Box 516
St Louis, MO 63166

Grumman Aerospace
Attn: R. Friedman
Mail Stop B-43/35
Bethpage, NY 11714

McDonnell Douglas
Attn: R. T. Kawai (36-41)
3852 Lakewood Blvd
Long Beach, CA 90801

General Electric Co
Attn: Ted Russell G-25
Turbine Division
Schenectady, NY 12345

Univ. of Minnesota
Attn: Dr. W. W. Gerberich
Dept Chem Eng & Matl Sci
Minneapolis, MN 55455

NASA - LeRC
Attn: J. Acurio, Director
USAR&TL Propulsion Lab
Cleveland, OH 44135

NASA - LeRC
Attn: R. E. Gaugler
Mail Stop 6-10
Cleveland, OH 44135

John Hopkins Univ.
Attn: Prof. W. N. Sharpe
Chairman, Dept of Mech
123 LaTrobe Hall
Baltimore, MD 21218

NASA - LeRC
Attn: T. W. Orange
Mail Stop 49-7
Cleveland, OH 44135

Lockheed Georgia
Attn: H. S. Sweet
Marietta, GA 30060

NASA - LeRC
Attn: J. F. Saltsman
Mail Stop 49-7
Cleveland, OH 44135

NASA - LeRC
Attn: R. J. Simoneau
Mail Stop 6-10
Cleveland, OH 44135

Northwestern Univ.
Attn: Prof S. Nemat-Nasser
Dept of Civil Eng
Evanston, IL 60201

NASA - LeRC
Attn: S&MT Div. Files
MS 49-6
Cleveland, OH 44135

O R N L Box X
Attn: J. McGowan
Oak Ridge, TN 37830

Rensselaer Polytech Inst
Attn: Dr. Erhard Krempl
Mech & Aero Eng Dept
Troy, NY 12181

Rocketdyne
Attn: Dr. D. Matejczk/AC10
6633 Canoga Ave
Canoga Pk, CA 91304

Rockwell Int'l
Attn: Dr. Mike Mitchell
Rockwell Science Ctr
P. O. Box 1085
Thousand Oaks, CA 91360

Rocketdyne
Attn: Jim Newell AC10
6633 Canoga Ave
Canoga Pk, CA 91304

Sandia Labs
Attn: D. W. Lobitz
Div 1541
Box 5800
Albuquerque, NM 87115

Southwest Research Inst
Attn: Dr. Thomas Cruse
PO Drawer 28510
San Antonio, TX 78284

Southwest Research
Attn: Dr. C. S. Chan
P O Drawer 285
San Antonio, TX 78284

Texas A & M University
Attn: Dr. W. L. Bradley
College Station, TX 77843

Texas A & M University
Attn: Dr. Walter Haisler
Aerospace Eng Dept
College Station, TX 77843

NASA-AFWAL Tech Liaison
Attn: Everett Bailey
AFWAL/DO
Wright Patterson Air Force Base,
OH 45433

William Research
Attn: R. L. Maxwell
2280 W Maple Rd
Walled Lake, MI 48088

Scientific Info Service
Attn: Ref. USZ
7 Woodland Ave
Larchmont, NY 10538

Westinghouse - Hanford
Attn: L. K. Severud
Mgr, Plant Analysis
Box 1970
Richland, WA 99352

O R N L Box X
Attn: Dr. Robert Swindeman
Metals & Ceramics Div
Oak Ridge, TN 37830

Cummins Engine
Attn: Justin Drake
Tech Ctr
500 S Poplar St
Columbus, IN 47201

NASA - LeRC
Attn: N. T. Saunders
Mail Stop 3-8
Cleveland, OH 44135

University of Dayton
Attn: Dr. Joseph Gallagher
Research Institute
Rm 563 Kettering Bldg
Dayton, OH 45469

Scientific Info. Service
Attn: Ref USZ
7 Woodland Ave.
Larchmont, NY 10538

Defense Documentation Ctr
Cameron Station
5010 Duke St
Alexandria, VA 22314

Bradord A. Cowles
MS 707-22

Glenn Folsom
MS 118-19

Donald E. Jensen
MS 161-15

David N. Duhl
MS 165-37

I. Linask
MS 165-14

Maurice L. Gell
MS 162-04

Harry L. Lemasters
MS 163-09

J. Magowan
MS 165-03

Thomas G. Meyer
MS 163-09

Jeffrey T. Hill
MS 163-09

Vito Moreno
MS 163-09

Dave Nissley
MS 165-14

A. Giamei, UTRC
East Hartford, CT 06108

Richard S. Nelson
MS 163-09

Pratt & Whitney
Attn: Art Leiser
24500 Center Ridge Road, Suite 280
Westlake, OH 44145

Robert R. Sellers
MS 713-37

C. G. Phippen
MS 402-12

Gustav A. Swanson
MS 165-03

H. J. Kocar
MS 118-19

Paul Norris
MS 165-37

I. Gould
MS 104-08

RETURN ORIGINALS TO:
D. L. Avery
MS 118-35